



# Universidad de Oviedo

Programa de doctorado en Diseño, Construcción y Fabricación  
en la Ingeniería Mecánica

TESIS DOCTORAL

## **Influencia de las teorías de gradientes de deformación plástica en los modelos de daño y fractura**

Emilio Martínez Pañeda

Director:

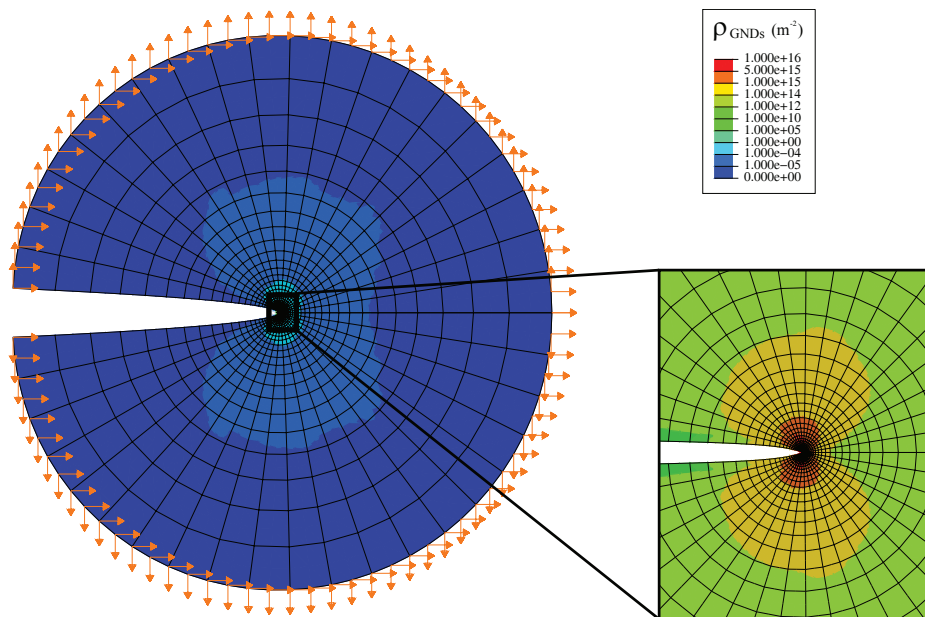
Covadonga Betegón Biempica

*Junio, 2016*



# Strain gradient plasticity-based modeling of damage and fracture

EMILIO MARTÍNEZ PAÑEDA



Emilio Martínez Pañeda: *Strain gradient plasticity-based modeling of damage and fracture*, PhD Dissertation © University of Oviedo 2016. All rights reserved.

All men by nature desire to know.

— Aristotle

It would have been virtually impossible, indeed, to have achieved any success with the idea of the *Autogiro* unless I had been able to calculate its basic design by mathematics before I began to build it.

Success by mere experiment would have been as unlikely as the successful construction of a cantilever bridge without any previous engineering experience.

— Juan de la Cierva

I am, and ever will be, a white-socks, pocket-protector, nerdy engineer — born under the second law of thermodynamics, steeped in the steam tables, in love with free-body diagrams, transformed by Laplace, and propelled by compressible flow.

— Neil Armstrong



## ABSTRACT

---

Experiments have consistently shown that metallic materials display strong size effects at the micron scale, with smaller being harder. As a result, a significant body of research has been devoted to model this size dependent plastic phenomenon. At the continuum level, phenomenological strain gradient plasticity (SGP) formulations have been developed to extend plasticity theory to small scales. Grounded on the physical notion of geometrically necessary dislocations (GNDs, associated with non-uniform plastic deformation), SGP theories relate the plastic work to both strains and strain gradients, introducing a length scale in the constitutive equations.

While growing interest in micro-technology motivated at first the development of SGP models, the influence of GNDs goes beyond micron-scale applications, as strains vary over microns in a wide range of engineering designs. Particularly, gradient-enhanced modeling of fracture and damage appears imperative - independently of the size of the specimen - as the plastic zone adjacent to the crack tip is physically small and contains strong spatial gradients of deformation. In this work a general framework for damage and fracture assessment accounting for the role of GNDs is provided. Different classes of gradient plasticity theories with *ad hoc* novel numerical schemes are employed. Emphasis is given to develop robust computational tools to predict and understand material failure mechanisms.

Results show a very strong influence of GNDs, revealing the need to incorporate gradient effects to adequately characterize behavior at the small scales involved in crack tip deformation. Encouraging quantitative agreement with experimental data is achieved by incorporating features of the underlying microstructure (GNDs). The richer continuum characterization of stress and hydrogen concentration in the fracture process zone leads to particularly promising results in hydrogen environmental assisted cracking modeling, a field of great engineering interest that continues to plague applications of high strength metals.

## RESUMEN

---

Las observaciones experimentales han puesto de manifiesto la existencia, a nivel micrométrico, de un fuerte efecto tamaño en los materiales metálicos (*smaller is harder*). Se ha destinado por consiguiente un significativo esfuerzo investigador a la modelización de este efecto plástico de escala. En el medio continuo se han desarrollado formulaciones fenomenológicas de gradientes de deformaciones plásticas (SGP) para extender la plasticidad convencional al dominio micrométrico. Basadas en el concepto físico de las dislocaciones geométricamente necesarias (GNDs, asociadas a deformación plástica no uniforme), las teorías SGP relacionan el trabajo plástico con la deformación y los gradientes de deformación, introduciendo así una longitud de escala en las ecuaciones constitutivas.

Aunque el desarrollo de modelos SGP estuvo motivado en primer lugar por un creciente interés en la microtecnología, la influencia de las GNDs va más allá del desarrollo de micro-componentes, ya que las deformaciones varían significativamente en distancias micrométricas en un amplio rango de aplicaciones ingenieriles. En particular, la modelización de la fractura y el daño considerando los gradientes parece indispensable - independientemente del tamaño del componente estructural - ya que la zona plástica adyacente a la punta de la grieta es físicamente pequeña y contiene fuertes gradientes espaciales de deformación. En este trabajo se desarrolla un marco generalizado para la evaluación del daño y la fractura incorporando la influencia de las GNDs. Para ello se emplean diferentes clases de teorías SGP con novedosas implementaciones numéricas *ad hoc*, haciendo especial énfasis en el desarrollo de herramientas computacionales robustas para predecir y comprender los mecanismos de fallo.

Los resultados muestran una importante influencia de las GNDs, revelando la necesidad de incorporar el efecto gradiente para modelizar adecuadamente el comportamiento en las diferentes escalas que caracterizan la deformación en la punta de la grieta. Así, cuando se consideran ciertas características de la microestructura (GNDs), se aprecia una alentadora concordancia cuantitativa con los datos experimentales. Esta caracterización enriquecida en el medio continuo de las tensiones y la concentración de hidrógeno en la zona de proceso de fractura lleva a unos resultados particularmente prometedores en la modelización del agrietamiento asistido por hidrógeno, un campo de gran interés ingenieril que continúa limitando las aplicaciones de metales de alta resistencia.

## PUBLICATIONS

---

The research conducted during the present doctoral thesis has been disseminated, as of June 2016, through the following journal articles and oral presentations:

### JOURNAL PUBLICATIONS

Martínez-Pañeda, E., Natarajan, S., Bordas, S., 2016. Gradient plasticity crack tip characterization by means of the extended finite element method (*submitted*).

Martínez-Pañeda, E., Niordson, C.F., Gangloff, R.P., 2016. Strain gradient plasticity-based modeling of hydrogen environment assisted cracking. *Acta Materialia* **117**, 321-332.

Martínez-Pañeda, E., Niordson, C.F., Bardella, L., 2016. A finite element framework for distortion gradient plasticity with applications to bending of thin foils. *International Journal of Solids and Structures* **96**, 288-299.

Martínez-Pañeda, E., del Busto, S., Niordson, C.F., Betegón, C., 2016. Strain gradient plasticity modeling of hydrogen diffusion to the crack tip. *International Journal of Hydrogen Energy* **41**, 10265-10274.

Martínez-Pañeda, E., Niordson, C.F., 2016. On fracture in finite strain gradient plasticity. *International Journal of Plasticity* **80**, 154-167.

Martínez-Pañeda, E., Betegón, C., 2015. Modeling damage and fracture within strain-gradient plasticity. *International Journal of Solids and Structures* **59**, 208-215.

### INTERNATIONAL CONFERENCES

Martínez-Pañeda, E., Crack tip modeling of hydrogen assisted cracking: the role of strain gradients. *VII European Congress on Computational Methods in Applied Sciences and Engineering*. Crete Island (Greece), June 2016.

Martínez-Pañeda, E. [invited speaker], Fracture in strain gradient plasticity. *Aifantis International Symposium - SIPS2015*. Antalya (Turkey), October 2015.

Martínez-Pañeda, E., Niordson, C.F., Bardella, L., A finite element basis for distortion gradient plasticity. *XIII International Conference on Computational Plasticity (COMPLAS XIII)*. Barcelona (Spain), September 2015.

Martínez-Pañeda, E., Betegón, C., Modeling damage and fracture accounting for size effects. *9th European Solid Mechanics Conference (ESMC 2015)*. Madrid (Spain), July 2015.

Martínez-Pañeda, E., Niordson, C.F., The role of Geometrically Necessary Dislocations in the fracture process of metallic materials. *12th International Conference on the Mechanical Behavior of Materials (ICM 12)*. Karlsruhe (Germany), May 2015.

#### INVITED SEMINARS

*Strain gradient plasticity: numerical modelling and fracture assessment*. University of Cambridge, Micromechanics Seminar Series. March 2016

*Numerical modeling of size effects in metal plasticity*. University of Granada, Seminars on Science and Engineering of Structures. February 2016

*Modeling size effects in metal plasticity with particular emphasis on fracture*. University of Luxembourg, Legato Computational Mechanics Team Seminar Series. June 2015

## ACKNOWLEDGMENTS

---

First and foremost I wish to express my gratitude to my supervisor, Prof. Covadonga Betegón, for her unconditional support, endless forbearance, constant backing and friendship. She has played an essential role in the success of this thesis. I am also very grateful to all faculty members, administrative staff and laboratory technicians of the Continuum Mechanics and Structures section of the University of Oviedo for their help and encouraging remarks. Particularly, I would like to thank Prof. Cristina Rodríguez, for always having her office doors open to me, and Prof. Alfonso Fernández-Canteli, for being a role model. Feedback and advice from faculty members from other sections, such as Dr. Inés Peñuelas and Dr. Rocío Fernandez (Mechanical Engineering) or Dr. Inés Pariente and Prof. Javier Belzunce (Materials Science), is also very much acknowledged. The working atmosphere has been amazing and I would like to thank all my young colleagues who have played a key role in this. From the veterans (Dr. Pelayo Fernández, Dr. Carlos López-Colina and Dr. Marta García) to the newcomers; with special gratitude to my friends from the VIP room (Dr. Tomás García, Miguel Muñoz and Susana del Busto) for all the interesting discussions that we had.

My research stays in several universities across Europe have given me the opportunity to learn from very bright scientists; their valuable advice cannot be acknowledged enough. The Technical University of Denmark (DTU), which I had the fortune of visiting on three occasions, has always been a second home for me. I will never forget the kindness and politeness of all the members of the Solid Mechanics section. Among the many friendships established, I must undoubtedly highlight the one with my host, Prof. Christian Niordson; he has been a great scientific mentor to whom I will be eternally grateful. My research career has been also particularly influenced by Prof. Stéphane Bordas and his very active group at the Universities of Cardiff and Luxembourg. It was a magnificent experience to learn from him and his coworkers and I look forward to continuing collaborating for years to come. And last, but certainly not least, my 3-month research stay at Cambridge University was strongly rewarding, having the opportunity to conduct research under the guidance of Prof. Norman Fleck and Prof. Vikram Deshpande, well-known experts in mechanics. The very enriching discussions with my colleagues at the Cambridge Centre for Micromechanics further enhanced my scientific skills. Highly useful input and guidance from other collaborators, such as Prof. Lorenzo

Bardella (University of Brescia) or Prof. Richard Gangloff (University of Virginia), has also played a very important role in the success of this thesis. Besides, during this 3-year PhD I had the chance to meet many academics at numerous scientific events, with whom I have shared opinions and enjoyable moments; their valuable advice and encouraging remarks are very much acknowledged. I am also very grateful to Prof. Rafael Gallego (University of Granada) for guiding my first steps into the wonderful world of science.

A special acknowledgement goes to my family, the constant encouragement of my parents and brother has been an invaluable asset to me. Particular mention deserves the endless patience and continuous help from my partner Sandra during hard working evenings and weekends: a million thanks; things would have been very different without your support.

# CONTENTS

---

<b>I</b>	<b>NUMERICAL FRAMEWORK</b>	<b>1</b>
1	INTRODUCTION	3
1.1	Background	3
1.2	Objectives	9
1.3	Thesis outline	10
2	GRADIENT PLASTICITY FORMULATIONS	13
2.1	Mechanism-based gradient plasticity	15
2.2	Fleck-Hutchinson 2001 theory	17
2.3	Advanced gradient plasticity theories	20
2.4	Distortion gradient plasticity	25
3	NUMERICAL IMPLEMENTATION	31
3.1	CMSG plasticity: FEM and X-FEM	31
3.2	Phenomenological higher order SGP	48
3.3	Numerical modeling of energetic and dissipative size effects	52
3.4	A finite element basis for DGP	61
<b>II</b>	<b>RESULTS</b>	<b>67</b>
4	MECHANISM-BASED CRACK TIP CHARACTERIZATION	69
4.1	Introduction	69
4.2	Crack tip fields with infinitesimal strains	70
4.3	Crack tip fields with finite strains	75
4.4	Discussion	79
4.5	Conclusions	81
5	ON FRACTURE IN FINITE STRAIN GRADIENT PLASTICITY	83
5.1	Introduction	83
5.2	Numerical results	84
5.3	Conclusions	97
6	THE ROLE OF ENERGETIC AND DISSIPATIVE LENGTH PARAMETERS	99
6.1	Introduction	99
6.2	Stationary crack tip fields	100
6.3	Steady-state crack growth and work of fracture	105
6.4	Conclusions	114
7	HYDROGEN DIFFUSION TOWARDS THE FRACTURE PROCESS ZONE	117
7.1	Introduction	117
7.2	Numerical framework	118
7.3	Finite element results	119

7.4	The role of hydrogen trapping	130
7.5	Conclusions	132
8	SGP-BASED MODELING OF HEAC	135
8.1	Introduction	135
8.2	Objective	137
8.3	Experimental procedure	137
8.4	Modeling procedure	138
8.5	Results	142
8.6	Discussion	152
8.7	Conclusions	160
9	CONCLUSIONS	161
9.1	Achievements	161
9.2	Concluding remarks	162
9.3	Future work	163
9	CONCLUSIONES	165
9.1	Logros	165
9.2	Conclusiones	166
9.3	Trabajo futuro	168
	BIBLIOGRAPHY	171

## LIST OF FIGURES

---

Figure 1.1	Size effects in nanoindentation	3
Figure 1.2	Size effects in torsion of thin copper wires	4
Figure 1.3	Size effects in bending of thin nickel foils	5
Figure 1.4	GNDs in a plastically bent metal beam	6
Figure 1.5	Plastic strain gradients ahead of a crack tip	9
Figure 3.1	Numbering scheme adopted for the plane strain element	36
Figure 3.2	Verification of the numerical framework for MSG plasticity: crack tip fields	38
Figure 3.3	Schematic diagram of the different domains surrounding the crack tip	41
Figure 3.4	Typical X-FEM mesh with an arbitrary crack	41
Figure 3.5	Single edge cracked plate	43
Figure 3.6	FEM normalized opening stress distribution ahead of the crack tip for different mesh densities	44
Figure 3.7	Representative FE mesh	45
Figure 3.8	X-FEM mesh	45
Figure 3.9	Topological enrichment results	46
Figure 3.10	Geometrical enrichment results	47
Figure 3.11	Verification of the numerical framework for Phenomenological SGP - small strains	51
Figure 3.12	Verification of the numerical framework for Phenomenological SGP - large strains	52
Figure 3.13	Outline of the staggered numerical procedure	56
Figure 3.14	Schematic of a finite slab constrained between rigid platens	57
Figure 3.15	Verification of the numerical framework for advanced SGP models: tensile loading of a clamped slab	59
Figure 3.16	Schematic of a thin foil under bending	60
Figure 3.17	Verification of the numerical framework for advanced SGP models: microbending	61
Figure 3.18	Verification of the numerical framework for DGP: simple shear	66

Figure 4.1	FE mesh for the boundary layer formulation - Small strains	71
Figure 4.2	Opening stress distribution under CMSG plasticity - small strains	72
Figure 4.3	Parametric study under CMSG plasticity - small strains	74
Figure 4.4	Finite element mesh for the boundary layer formulation under large deformations	76
Figure 4.5	Opening stress distribution under CMSG plasticity - large strains	77
Figure 4.6	Parametric study under CMSG plasticity - large strains	78
Figure 4.7	Opening stress ratio between CMSG and classic plasticity as a function of $K_I$	80
Figure 5.1	Opening stress distribution for both MSG and phenomenological SGP models - Small strains	85
Figure 5.2	Opening stress distribution for both MSG and phenomenological SGP models - Large strains	87
Figure 5.3	Crack tip blunting for both MSG and phenomenological SGP models	88
Figure 5.4	Ratio of stress elevation for both MSG and phenomenological SGP models	90
Figure 5.5	Gradient-dominated length for both MSG and phenomenological SGP models	91
Figure 5.6	Opening stress distribution for both MSG and phenomenological SGP models under different load levels	92
Figure 5.7	Hydrostatic stress distribution for both MSG and phenomenological SGP models	93
Figure 5.8	Influence on crack tip fields of varying one length parameter	95
Figure 5.9	Influence on crack tip fields of varying two length parameters	96
Figure 6.1	Finite element mesh employed in the boundary layer model	100
Figure 6.2	Stationary crack tip fields for different values of $\ell$ and $L$	101
Figure 6.3	Stationary crack tip fields for different values of $\ell$ and $L$ and different loads	102
Figure 6.4	Stationary crack tip fields for different values of $\ell$ and $L$ and different loads for DGP	104
Figure 6.5	Stationary crack tip fields for different values of $\chi$	105

Figure 6.6	Schematic of the SENT specimen configuration	106
Figure 6.7	Finite element mesh employed for the SENT specimen	109
Figure 6.8	Traction-separation cohesive law	110
Figure 6.9	Outline of the mixed FE-Rayleigh-Ritz method	112
Figure 6.10	Crack growth resistance curves	113
Figure 7.1	Boundary conditions in the stress and diffusion models	120
Figure 7.2	Hydrostatic stress distribution in impure iron	122
Figure 7.3	Lattice hydrogen concentration in impure iron	123
Figure 7.4	Finite element model for the duplex stainless steel study	125
Figure 7.5	Experimental and numerical predictions of the crack mouth opening displacement	126
Figure 7.6	Lattice hydrogen concentration in duplex stainless steel	127
Figure 7.7	Hydrostatic stress distribution in X80 pipeline steel	129
Figure 7.8	Experimental and numerical hydrogen concentration in X80 pipeline steel	130
Figure 7.9	Equivalent plastic strain distribution ahead of the crack tip in an iron-based material	132
Figure 8.1	Hydrostatic stress distribution for Monel K-500	143
Figure 8.2	Dislocation density and crack tip blunting predictions for Monel K-500	144
Figure 8.3	Model $K_{TH}$ and $da/dt_{II}$ versus $E_{APP}$ predictions for Monel K-500	146
Figure 8.4	Hydrostatic stress distribution for AerMet <sup>TM</sup> <sub>100</sub>	147
Figure 8.5	Model $K_{TH}$ versus $E_{APP}$ predictions for AerMet <sup>TM</sup> <sub>100</sub> (upper bound $C_{H,Diff}$ )	149
Figure 8.6	Model $K_{TH}$ versus $E_{APP}$ predictions for AerMet <sup>TM</sup> <sub>100</sub> (lower bound $C_{H,Diff}$ )	150
Figure 8.7	Model $da/dt_{II}$ versus $E_{APP}$ predictions for AerMet <sup>TM</sup> <sub>100</sub> (upper bound $C_{H,Diff}$ )	151
Figure 8.8	Model $da/dt_{II}$ versus $E_{APP}$ predictions for AerMet <sup>TM</sup> <sub>100</sub> (lower bound $C_{H,Diff}$ )	152

## LIST OF TABLES

---

Table 1	Literature review of experimentally reported length scales	14
Table 2	Finite element predictions of $\sigma_H/\sigma_Y$	145

## ACRONYMS

---

CMSG	Conventional Mechanism-based Strain Gradient
DGP	Distortion Gradient Plasticity
FE	Finite Element
FPZ	Fracture Process Zone
GNDs	Geometrically Necessary Dislocations
HEAC	Hydrogen Environment Assisted Cracking
HEDE	Hydrogen Enhanced Decohesion
HELP	Hydrogen Enhanced Localized Plasticity
IHAC	Internal Hydrogen Assisted Cracking
MSG	Mechanism-based Strain Gradient
SGP	Strain Gradient Plasticity
SSDs	Statistically Stored Dislocations
X-FEM	Extended Finite Element Method

Part I

NUMERICAL FRAMEWORK



INTRODUCTION

1.1 BACKGROUND

In recent years there has been an increasing interest in characterizing the behavior of metallic materials at the micrometer scale. Examples are found in micro-electromechanical systems (MEMS), microelectronic components and thin film applications. A wide array of micron scale experiments have revealed that metals display strong size effects when deformed non-uniformly into the plastic range. Particularly representative examples are: (i) indentation (Fig. 1.1), (ii) torsion (Fig. 1.2) and (iii) bending (Fig. 1.3).

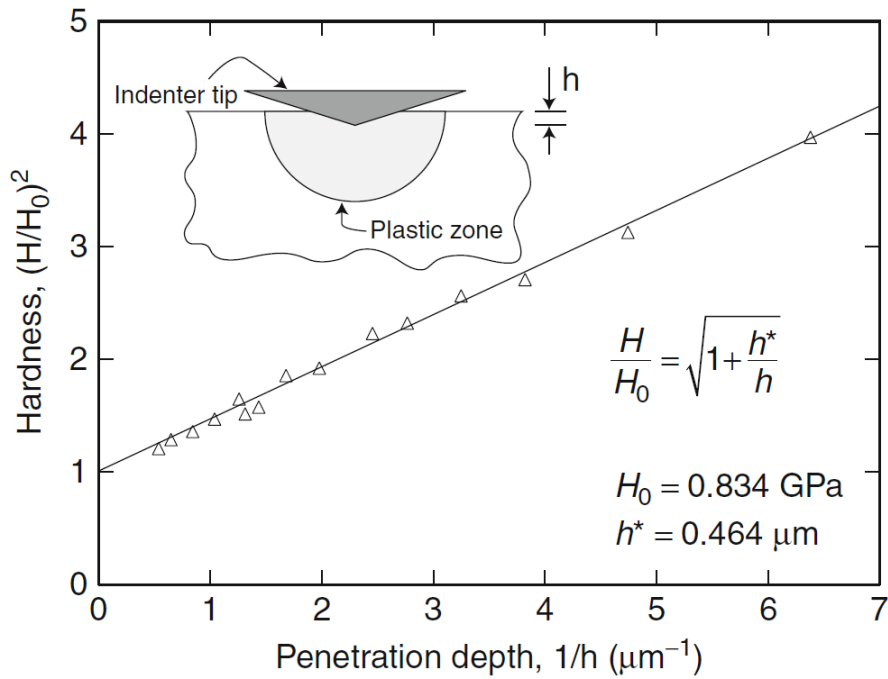


Figure 1.1: Indentation depth dependence of the hardness of polycrystalline copper [1]. Taken from [2].

From a series of careful nanoindentation experiments, Nix and Gao [1] found a linear relation between the indentation depth and the hardness of single crystal and cold worked polycrystalline copper. This size effect becomes negligible as the indentation depth is increased beyond a characteristic length of the order of micrometers.

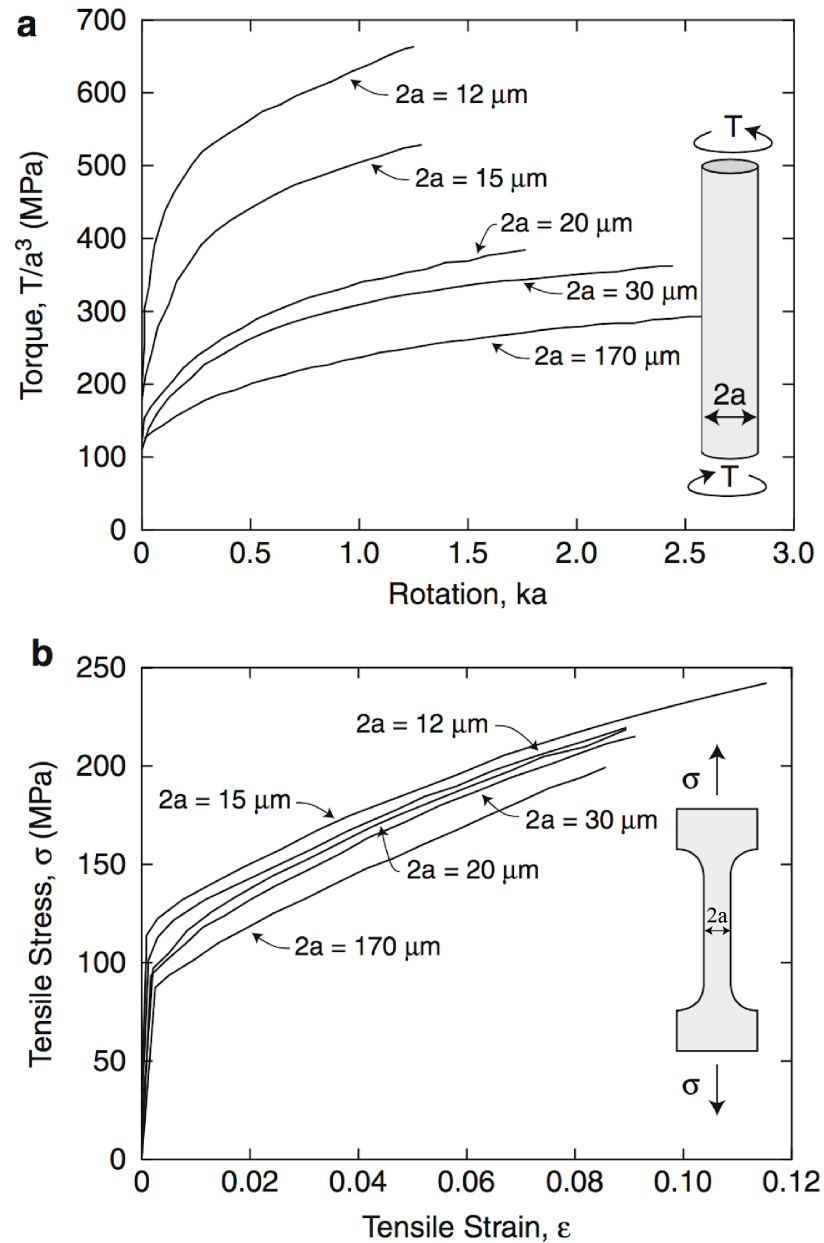


Figure 1.2: Experimental data on thin copper wires reveals a significant gradient effect under (a) torsion, where non-uniform strains arise, while nearly no size effect is observed in (b) uniaxial tension. Adapted from [2, 3].

Fleck and co-workers [3] tested very thin copper wires (with radius  $a$  varying from 6 to 85  $\mu\text{m}$ ) under both uniaxial tension and torsion. Results reveal only a minor influence of specimen size on tensile behavior but a systematic increase in torsional hardening with decreasing wire diameter. As described in [3], the torsion data in Fig. 1.2 (a) is displayed in the form  $T/a^3$  vs  $\kappa a$ , with  $T$  being the torque and  $\kappa$  the twist per unit length. The non-dimensional group  $\kappa a$  may

be interpreted as the magnitude of the shear strain at the surface of the wire while the group  $T/a^3$  gives a measure of the shear stress across the section of the wire in some averaged sense. Dimensional analysis establishes that  $T/a^3$  is a function of  $\kappa a$  but is otherwise independent of the wire radius, such that the curves should superpose for any constitutive law which does not contain a length scale.

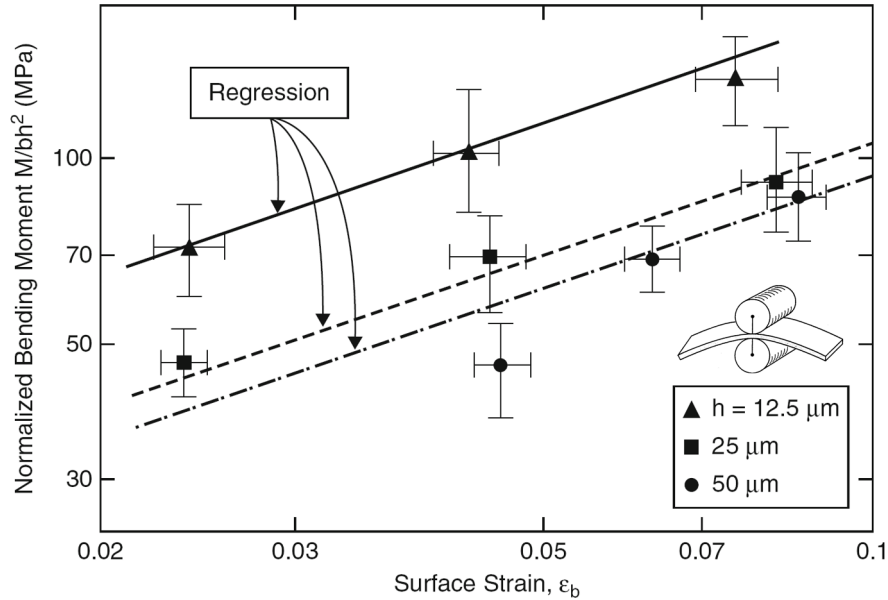


Figure 1.3: Microbending tests on nickel foils reveal substantial strengthening with diminishing thickness, which is not observed in tension. Adapted from [2, 4].

By means of a novel experimental setup, Stölken and Evans [4] were able to perform micro-bending tests on nickel foils of different thicknesses. Scaling arguments based on conventional plasticity predict that, for foils of thickness  $h$  and width  $b$ , the normalized bending moment  $M/bh^2$  should depend uniquely on the plastic strain at the surface  $\epsilon_b = h/2R_0$  (with  $R_0$  being the mandrel radius) [2]. However, results reveal that thinner specimens are stronger and strain harden more than thicker ones. Uniaxial tension tests were also conducted and, as in the work by Fleck et al. [3], almost no influence of specimen size is observed. Thus, the *smaller is harder* or *smaller is stronger* trends observed in the aforementioned micron scale experiments are intrinsically associated with the presence of strain gradients.

In terms of the underpinning dislocation phenomena, work hardening is controlled by the total density of dislocations, part of which is related to the gradients of plastic strain. Thereby, dislocation storage governing material hardening is due to: (i) dislocations that trap each other in a random way and (ii) dislocations required for compatible

deformation of various parts of the crystal [3]. The latter are referred to as Geometrically Necessary Dislocations (**GNDs**) while the former are named Statistically Stored Dislocations (**SSDs**). The physical notion of **GNDs** is further elucidated in the paradigmatic benchmark of a plastically bent metal beam. As depicted in Fig. 1.4, an extra storage of dislocations is required to accommodate the lattice curvature that arises due to non-uniform plastic deformation [5]. **GNDs** do not contribute to plastic strain but to material work hardening by acting as obstacles to the motion of **SSDs**. This extra storage of dislocations associated with gradients of plastic strain will manifest its influence when the characteristic length of deformation becomes sufficiently small.

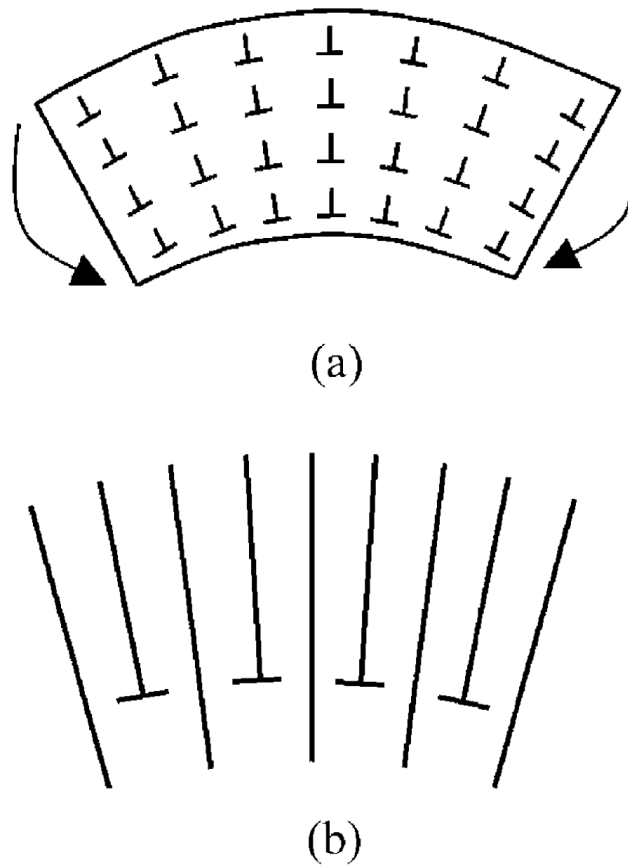


Figure 1.4: (a) Under pure bending a periodic array of dislocations with Burgers vector  $b$  and spacing  $L$  will generate a lattice curvature equal to  $b/L^2$ , (b) a schematic view of **GNDs** in a plastically bent lattice. Adapted from [5].

Depending on the scale of interest, different approaches can be adopted to model small scale plastic deformation [6]. Thus, *ab initio* or molecular dynamics calculations may be appropriate for studies of dislocation cores and interactions between individual dislocations. However, these models would be prohibitively expensive from a

computational point of view if a larger material volume is considered. An alternative is to apply dislocation mechanics and to model the motion of a large number of individual dislocations in a crystal. This so-called discrete dislocation dynamics simulations average out the atomistic nature of the material by reducing the direct atomic interactions to linear continuum elasticity. Another option is to address the evolution of crystallographic texture by modeling anisotropic plastic flow in single crystals, with crystal plasticity models being able to explicitly determine the density of GNDs as a function of the plastic slip tensor (see, e.g., [7]). While dislocation dynamics and crystal plasticity constitute very useful tools to gain insight into the fundamental mechanisms of plasticity, current computational capabilities significantly limit the size of the volume that can be handled through these approaches. Hence, plastic deformation at the engineering component scale will continue to be modeled using continuum-level isotropic plasticity for many years. However, such size-scale dependent plastic phenomena cannot be captured by classic plasticity theory, as the constitutive model includes no material length parameters and hence predicts results independent of sample dimensions.

Since the earlier works of Berdichevskii [8] and Aifantis [9, 10], a number of formulations - referred to as Strain Gradient Plasticity (SGP) models - have been proposed to extend plasticity theory to small scales (see, e.g., [6, 11–18] and references therein). Grounded on the physical notion of GNDs, associated with incompatibility due to strain gradients, SGP theories relate the plastic work (or, in some cases, the yield strength) to both strains and strain gradients; thereby introducing a length scale in the material description. These models are cast in a form which reduces to classic plasticity when the length scales of the imposed deformation gradients are large compared to the material length parameters [13].

Isotropic gradient plasticity formulations can be classified according to different criteria. For example, as a function of their approach (i), either *phenomenological* [11, 13] or *mechanism-based* [12, 14]; as a function of their order (ii), i.e., with (*higher order*) or without (*lower order*) additional stress quantities and boundary conditions (see [19]); or as a function of the theoretical treatment of higher order terms (iii), namely *work-conjugate* or *non-work-conjugate* types (see [20]). One of the most widely used SGP models is that of Fleck and Hutchinson [13], which employs the displacement components and the effective plastic strain as the primary variables in the variational statement of boundary value problems. Unlike its predecessors [11], only the primary variables and their first gradients enter the variational formulation, leading itself nicely to numerical implementation.

However, this attractive higher order phenomenological formulation was found, under some non-proportional straining histories, to violate the thermodynamic requirement that plastic dissipation must be non-negative [6, 21]. Positive plastic work was later ensured by employing dissipative higher order stresses constitutively related to increments of strain [6, 15, 16]. But it has been very recently noticed that this *non-incremental* formulation may lead to a delay in plastic flow under certain non-proportional loading conditions [18, 22, 23]. It is therefore manifest that continuum modeling of size effects in metal plasticity is under continuous development. The presently available constitutive models are far from being firmly established and uncertainties remain regarding the constitutive prescriptions that best capture increased GNDs density associated with a plastic strain gradient. Further progress in the search of a consistent theory that yields realistic model predictions is expected in the years to come, as valuable insight will likely be gained from critical experiments and multi-scale modeling. The situation is not unlike that in the early days of the development of conventional plasticity models, when there was uncertainty about descriptions of yield surfaces and the connection between phenomenological and physically-based theories [24].

Remaining uncertainties and the complexity associated with their numerical implementation have hindered a comprehensive embrace of SGP theories in many engineering problems where GNDs play a major role. This is particularly true in large scale applications that demand a robust and efficient computational framework but, at the same time, require a very accurate description of certain phenomena governing the design criteria where strains vary over microns. Structural integrity assessment is a very representative example of the applicability of SGP models beyond micron scale specimens. Since the earlier days of the development of SGP theories it has been widely believed that GNDs must have a profound influence in fracture problems; independently of the size of the specimen, the plastic zone adjacent to the crack tip is physically small and contains strong spatial gradients of deformation (see Fig. 1.5). The experimental observation of cleavage fracture in the presence of significant plastic flow [25, 26] has encouraged significant interest in the role of plastic strain gradients in fracture and damage assessment. Studies conducted in the framework of phenomenological [27–31] and mechanism-based theories [32–35] have shown that GNDs near the crack tip promote local strain hardening and lead to a much higher stress level as compared with classic plasticity predictions. These studies have highlighted the need to account for the influence of strain gradients in the modeling of a wide range of fracture problems, being particularly relevant in hydrogen assisted cracking due to the central role that the stress field close

to the crack tip plays on both hydrogen diffusion and interface decohesion [36]. Consequently, there is a need to identify and quantify the relation between material parameters and the physical length over which gradient effects prominently enhance crack tip stresses. However, fracture assessment within SGP is a very demanding problem from the computational perspective; an appropriate characterization of gradient effects requires the use of extremely refined meshes, with a characteristic element length of a few micrometers in the vicinity of the crack. This leads to convergence problems as the element distortion becomes large or elements lose bearing capacity. It is therefore a challenge to develop robust numerical schemes for state-of-the-art SGP formulations that are able to handle load levels of interest from an engineering perspective, where large strains and crack tip blunting are of significant relevance.

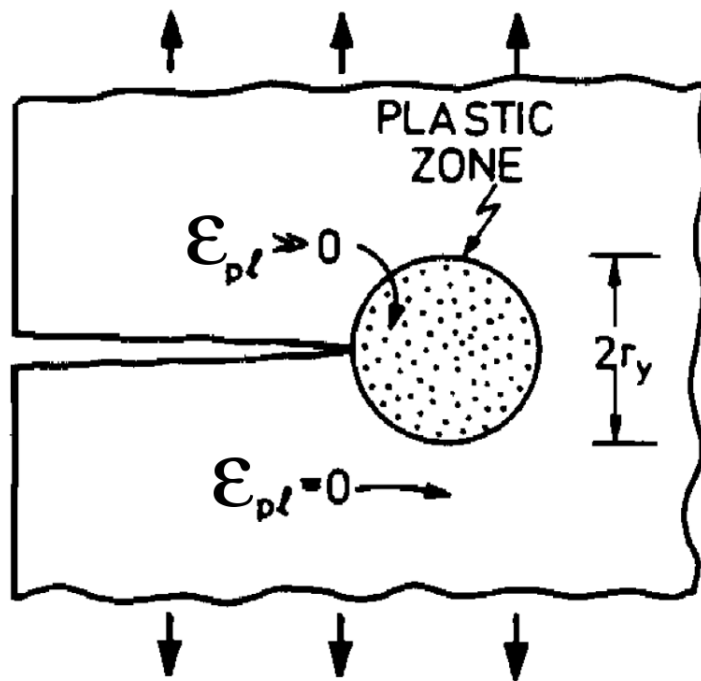


Figure 1.5: Plastic strain gradients caused by local boundary conditions ahead of a crack tip. Adapted from [3].

## 1.2 OBJECTIVES

Understanding material failure mechanisms and developing powerful predictive computational tools for structural integrity assessment is a field of great interest for industrial and engineering applications. Consequently, the key objective of the present PhD thesis is to develop an efficient and reliable numerical framework to quantitatively model fracture and damage at the engineering scale by incorpora-

ting enhanced microstructural features (GNDs). While a number of fracture studies accounting for gradient effects have been conducted, several aspects have yet to be incorporated into the modeling to properly characterize behavior at the small scales involved in crack tip deformation. Namely,

- Identify the conditions where gradient effects should be incorporated in crack tip damage modeling by relating material properties, constraint scenarios and applied loads with the physical distance ahead of the crack tip where GNDs significantly influence the stress distribution.
- Account for large strains and rotations in the gradient-enhanced crack tip fields characterization.
- Compare predictions from different classes of SGP formulations, examining the existing differences and discussing the physical implications.
- Incorporate state-of-the-art gradient plasticity formulations, elucidating the role of energetic and dissipative contributions.
- Quantify gradient effects in hydrogen transport towards the fracture process zone.
- Gain insight into the fracture mechanisms by correlating numerical predictions with available experimental data.
- Estimate hydrogen cracking thresholds and subcritical crack growth rates under different environmental conditions with SGP-based models.

A wide range of gradient plasticity formulations must be examined to assess the role of strain gradients in crack tip mechanics. Consequently, different numerical solutions must be employed to accommodate the peculiarities of each class of SGP theories.

### 1.3 THESIS OUTLINE

This work is divided in two main parts.

Part I covers the first three chapters. In the first introductory chapter the motivations and objectives of this work have been exposed, size effects in metals have been described and the main modeling efforts have been reviewed.

Chapter 2 introduces the compatibility, balance and constitutive equations of the different classes of SGP formulations employed in

the present work.

In chapter 3 the proposed *ad hoc* Finite Element (FE) - based solutions for each gradient plasticity model are described. Emphasis is placed on the original contributions of this work and their numerical verification.

Part II includes the outcome of several novel studies of particular interest from the fracture and damage assessment perspective.

In chapter 4 crack tip fields are thoroughly examined by means of mechanism-based strain gradient plasticity for both infinitesimal and finite deformation theories. An extensive parametric study is conducted and differences in the stress distributions ahead of the crack tip, as compared with conventional plasticity, are quantified.

In chapter 5 the higher order phenomenological theory by Fleck and Hutchinson [13] is employed to characterize crack tip fields within a finite strains framework. Results are compared with the predictions from the mechanism-based strain gradient plasticity theory and differences between the two approaches within continuum SGP modeling are highlighted and discussed.

Chapter 6 is devoted to fracture assessment by means of advanced SGP models [6, 15]. The role of energetic and dissipative higher order contributions is elucidated and gradient effects are quantified by previously fitting experimental micro-tests data. Crack growth initiation and subsequent resistance is computed using a cohesive zone model and a special mixed FE-Rayleigh-Ritz method [37].

In chapter 7 hydrogen diffusion towards the fracture process zone is examined accounting for local hardening due to GNDs by means of phenomenological higher order SGP. Finite element computations are performed within the finite deformation theory to characterize the gradient-enhanced stress elevation and subsequent diffusion of hydrogen towards the crack tip.

In chapter 8 finite element analysis of crack tip fields, emphasizing finite strain and SGP, is integrated with electrochemical assessment of occluded-crack tip hydrogen solubility and two decohesion-based damage models to predict hydrogen environment assisted crack growth properties.

The main achievements, conclusions and future work are presented in chapter 9.



A theoretical framework that has potential to cover a large range of gradient plasticity effects in isotropic materials is presented. Four classes of [SGP](#) theories are considered, aiming to span a wide domain of gradient plasticity formulations. The models considered as most representative of the state-of-the-art are the Mechanism-based Strain Gradient ([MSG](#)) plasticity theory [[12](#)], the phenomenological [SGP](#) theory re-formulated by Fleck and Hutchinson [[13](#)], the advanced model by Gudmundson [[6](#)], incorporating dissipative and energetic terms, and the more general theory by Gurtin [[15](#)], which is generally referred to as Distortion Gradient Plasticity ([DGP](#)). The compatibility, balance and constitutive equations of the aforementioned [SGP](#) models are respectively described in sections [2.1](#), [2.2](#), [2.3](#) and [2.4](#).

Gradient plasticity formulations introduce one or several length parameters to capture the experimentally-observed size effects. Despite the efficiency of [SGP](#) theories, a unified interpretation of these internal length scales is still lacking and its relationship with the material microstructure has not been clearly understood [[38](#)]. By fitting experimental measurements of micro-tests through a specific [SGP](#) theory (in a way that resembles the fitting of the strain hardening exponent by means of a specific power law) the observed range of the magnitude of these length parameters roughly falls within 1-10  $\mu\text{m}$ , as depicted in [Table 1](#).

Finally, it is necessary to remark that [SGP](#) theories are continuously being enriched and modified; as the field evolves the role of novel formulations on crack tip mechanics must be assessed.

Table 1: Compilation of experimentally reported length scales with their associated [SGP](#) formulation.

Work	Material	Experiment	Length scale - <a href="#">SGP</a> model
Fleck et al. (1994) [3]	Cu	Torsion	3.7 $\mu\text{m}$ - Fleck & Hutchinson (1993) [39]
Nix and Gao (1998) [1]	Cu (cold worked)	Indentation	5.84 $\mu\text{m}$ - Nix & Gao (1998) [1]
	Single crystal Cu (annealed)	Indentation	12 $\mu\text{m}$ - Nix & Gao (1998) [1]
Stölken and Evans (1998) [4]	Ni	Bending	5.2 $\mu\text{m}$ - Fleck & Hutchinson (1993) [39]
Shrotriya et al. (2003) [40]	Ni	Bending	5.6 $\mu\text{m}$ - Fleck & Hutchinson (1993) [39]
Haque and Saif (2003) [41]	Al	Bending	4.5 $\mu\text{m}$ - Gao et al. (1999) [12]
Ro et al. (2006) [42]	Al2024	Indentation	0.2 $\mu\text{m}$ - Nix & Gao (1998) [1]
Qian et al. (2014) [43]	Steel S355	Indentation	7 $\mu\text{m}$ - Gao et al. (1999) [12]
	Steel S690	Indentation	7 $\mu\text{m}$ - Gao et al. (1999) [12]
Guo et al. (2017) [44]	Cu	Torsion	3 $\mu\text{m}$ - Fleck & Hutchinson (1993) [39]
Iliev et al. (2017) [45]	In	Indentation	85.21 $\mu\text{m}$ - Nix & Gao (1998) [1]
	In	Bending	93.34 $\mu\text{m}$ - Fleck & Hutchinson (1993) [39]

## 2.1 MECHANISM-BASED GRADIENT PLASTICITY

The mechanism-based theory of strain gradient plasticity was proposed by Gao and co-workers [12, 46] based on a multiscale framework linking the microscale concept of SSDs and GNDs to the mesoscale notion of plastic strains and strain gradients. Unlike other SGP formulations, MSG plasticity introduces a linear dependence of the square of plastic flow stress on strain gradient. This linear dependence was largely motivated by the nano-indentation experiments of Nix and Gao [1] and comes out naturally from Taylor's dislocation model [47], on which MSG plasticity is built. Therefore, while all continuum formulations have a strong phenomenological component, MSG plasticity differs from all existing phenomenological theories in its mechanism-based guiding principles. The constitutive equations common to mechanism-based theories are summarized below, more details can be found in the original articles [12, 46].

In MSG plasticity, since the Taylor model is adopted as a founding principle, the shear flow stress  $\tau$  is formulated in terms of the dislocation density  $\rho$  as

$$\tau = \alpha \mu b \sqrt{\rho} \quad (2.1)$$

Here,  $\mu$  is the shear modulus,  $b$  is the magnitude of the Burgers vector and  $\alpha$  is an empirical coefficient which takes values between 0.3 and 0.5. The dislocation density is composed of the sum of the density  $\rho_S$  for SSDs and the density  $\rho_G$  for GNDs as

$$\rho = \rho_S + \rho_G \quad (2.2)$$

The GND density  $\rho_G$  is related to the effective plastic strain gradient  $\eta^P$  by:

$$\rho_G = \bar{r} \frac{\eta^P}{b} \quad (2.3)$$

where  $\bar{r}$  is the Nye-factor which is assumed to be 1.90 for face-centered-cubic (fcc) polycrystals. Following Fleck and Hutchinson [11], Gao et al. [12] used three quadratic invariants of the plastic strain gradient tensor to represent the effective plastic strain gradient  $\eta^P$  as

$$\eta^P = \sqrt{c_1 \eta_{iik}^P \eta_{jjk}^P + c_2 \eta_{ijk}^P \eta_{ijk}^P + c_3 \eta_{ijk}^P \eta_{kji}^P} \quad (2.4)$$

The coefficients were determined to be equal to  $c_1 = 0$ ,  $c_2 = 1/4$  and  $c_3 = 0$  from three dislocation models for bending, torsion and void growth, leading to

$$\eta^P = \sqrt{\frac{1}{4} \eta_{ijk}^P \eta_{ijk}^P} \quad (2.5)$$

where the components of the strain gradient tensor are obtained by  $\eta_{ijk}^p = \varepsilon_{ik,j}^p + \varepsilon_{jk,i}^p - \varepsilon_{ij,k}^p$ . The tensile flow stress  $\sigma_{\text{flow}}$  is related to the shear flow stress  $\tau$  by:

$$\sigma_{\text{flow}} = M\tau \quad (2.6)$$

where  $M$  is the Taylor factor, taken to be 3.06 for fcc metals. Rearranging Eqs. (2.1-2.3) and Eq. (2.6) yields

$$\sigma_{\text{flow}} = M\alpha\mu b \sqrt{\rho_S + \bar{r} \frac{\eta^p}{b}} \quad (2.7)$$

The SSD density  $\rho_S$  can be determined from (2.7) knowing the relation in uniaxial tension between the flow stress and the material stress-strain curve as follows

$$\rho_S = [\sigma_{\text{ref}} f(\varepsilon^p) / (M\alpha\mu b)]^2 \quad (2.8)$$

Here  $\sigma_{\text{ref}}$  is a reference stress and  $f$  is a non-dimensional function of the plastic strain  $\varepsilon^p$  determined from the uniaxial stress-strain curve. Substituting back into (2.7),  $\sigma_{\text{flow}}$  yields:

$$\sigma_{\text{flow}} = \sigma_{\text{ref}} \sqrt{f^2(\varepsilon^p) + l\eta^p} \quad (2.9)$$

where  $l$  is the intrinsic material length based on parameters of elasticity ( $\mu$ ), plasticity ( $\sigma_{\text{ref}}$ ) and atomic spacing ( $b$ ). Such that, for fcc metals,

$$l = M^2 \bar{r} \alpha^2 \left( \frac{\mu}{\sigma_{\text{ref}}} \right)^2 b = 18\alpha^2 \left( \frac{\mu}{\sigma_{\text{ref}}} \right)^2 b \quad (2.10)$$

Several observations on the flow stress (2.9) must be remarked: [14]

(i) If the characteristic length of plastic deformation is much larger than the intrinsic material length  $l$ , the GNDs-related term  $l\eta^p$  becomes negligible, such that the flow stress degenerates to  $\sigma_{\text{ref}} f(\varepsilon^p)$ , as in conventional plasticity.

(ii) The flow stress in Eq. (2.9) is based on the Taylor dislocation model, which represents an average of dislocation activities and is therefore only applicable at a scale much larger than the average dislocation spacing. For a typical dislocation density of  $10^{15}/\text{m}^2$ , the average dislocation spacing is around 30 nm such that the flow stress in (2.9) holds at a scale above 100 nm.

(iii) Even though the intrinsic material length  $l$  in (2.10) depends on the choice of the reference stress  $\sigma_{\text{ref}}$ , the flow stress in (2.9) is, in fact, independent of  $\sigma_{\text{ref}}$ . This is because both terms inside the square root in (2.9) are independent of  $\sigma_{\text{ref}}$ .

## 2.2 FLECK-HUTCHINSON 2001 THEORY

The 2001 re-formulation by Fleck and Hutchinson [13] of their earlier phenomenological higher order SGP model [11] is one of the most widely used gradient plasticity theories. Of similar form to that proposed by Aifantis [9, 10], the novel formulation enjoys distinct computational advantages that makes it attractive for applications requiring the generation of numerical solutions. There are two important differences with its predecessors: (i) plastic strains are treated as primary variables, placing them on a footing similar to the displacements and (ii) length parameters are only present in the plastic range.

### 2.2.1 Infinitesimal deformation framework

Within a small strain setup, where the elastic and plastic strains are respectively denoted as  $\varepsilon_{ij}^e$  and  $\varepsilon_{ij}^p$ , the total strain is given by

$$\varepsilon_{ij} = \varepsilon_{ij}^e + \varepsilon_{ij}^p \quad (2.11)$$

The conventional effective plastic strain rate is  $\dot{\varepsilon}_p = \sqrt{\frac{2}{3} \dot{\varepsilon}_{ij}^p \dot{\varepsilon}_{ij}^p}$ , with  $\varepsilon_p = \int \dot{\varepsilon}_p dt$ . In Fleck-Hutchinson [13] theory hardening effects due to plastic strain gradients are included through the gradient of the plastic strain rate

$$\dot{\varepsilon}_{ij,k}^p = (m_{ij} \dot{\varepsilon}_p)_{,k} \quad (2.12)$$

where  $m_{ij} = \frac{3}{2} \sigma'_{ij} / \sigma_e$  is the direction of the plastic strain increment, with  $\sigma'_{ij}$  denoting the stress deviator, and  $\sigma_e$  the von Mises effective stress. Variations of the displacements  $u_i$ , the effective plastic strain  $\varepsilon_p$  and the gradient of the effective plastic strain  $\varepsilon_{p,i}$  appear in the variational principles underlying the formulation and a higher order stress vector quantity  $\tau_i$  arises naturally as work conjugate to  $\varepsilon_{p,i}$ . The internal virtual work increment takes the form

$$\delta W_i = \int_V (\sigma_{ij} \delta \varepsilon_{ij}^e + Q \delta \varepsilon_p + \tau_i \delta \varepsilon_{p,i}) dV \quad (2.13)$$

Here  $\sigma_{ij}$  denotes the Cauchy stress tensor,  $Q$  is defined as the work conjugate to  $\varepsilon_p$  and  $\tau_i \delta \varepsilon_{p,i}$  is the contribution due to the plastic strain gradients. Since  $\dot{\varepsilon}_{ij}^p = \dot{\varepsilon}_p m_{ij}$ , and consequently  $\sigma_{ij} \delta \varepsilon_{ij}^p = \sigma_e \delta \varepsilon_p$ , integrating by parts (2.13) renders

$$\begin{aligned} \delta W_i = & \int_V [-\sigma_{ij,j} \delta u_i + (Q - \sigma_e - \tau_{i,i}) \delta \varepsilon_p] dV \\ & + \int_S (\sigma_{ij} n_j \delta u_i + \tau_i n_i \delta \varepsilon_p) dS \end{aligned} \quad (2.14)$$

where  $n_i$  is the unit outward normal to  $S$ . In the absence of body forces, the volume integral on the right-hand side of (2.14) vanishes, resulting in the conventional equilibrium relation

$$\sigma_{ij,j} = 0 \quad \text{on } V \quad (2.15)$$

and its higher order counterpart

$$Q = \sigma_e + \tau_{i,i} \text{ on } V \quad (2.16)$$

Consequently, the principle of virtual work follows as

$$\int_V (\sigma_{ij} \delta \varepsilon_{ij} + \tau_{i,i} \delta \varepsilon_p + \tau_i \delta \varepsilon_{p,i}) dV = \int_S (T_i \delta u_i + t \delta \varepsilon_p) dS \quad (2.17)$$

with the traction quantities  $T_i$  and  $t$  satisfying the natural boundary conditions

$$T_i = \sigma_{ij} n_j \text{ on } S \quad (2.18)$$

$$t = \tau_i n_i \text{ on } S \quad (2.19)$$

The third order plastic strain gradient tensor  $\dot{\varepsilon}_{ij,k}^p$  can be decomposed, via orthogonal decomposition, into three independent tensors  $\dot{\varepsilon}_{ij,k}^{p(G)}$ , with  $G = 1, 3$  [28, 48]. Such that a gradient-enhanced effective plastic strain rate,  $\dot{E}^p$  can be defined in terms of three unique, non-negative invariants of  $\dot{\varepsilon}_{ij,k}^p$ , which are homogeneous of degree two:

$$\dot{E}^p = \sqrt{\dot{\varepsilon}_p^2 + l_1^2 \dot{\varepsilon}_{ij,k}^{p(1)} \dot{\varepsilon}_{ij,k}^{p(1)} + 4l_2^2 \dot{\varepsilon}_{ij,k}^{p(2)} \dot{\varepsilon}_{ij,k}^{p(2)} + \frac{8}{3} l_3^2 \dot{\varepsilon}_{ij,k}^{p(3)} \dot{\varepsilon}_{ij,k}^{p(3)}} \quad (2.20)$$

where,  $l_1$ ,  $l_2$  and  $l_3$  are material length parameters. The effective plastic strain rate can be expressed explicitly in terms of  $\dot{\varepsilon}_p$  and  $\dot{\varepsilon}_{p,i}$ :

$$\dot{E}^p = \sqrt{\dot{\varepsilon}_p^2 + A_{ij} \dot{\varepsilon}_{p,i} \dot{\varepsilon}_{p,j} + B_i \dot{\varepsilon}_{p,i} \dot{\varepsilon}_p + C \dot{\varepsilon}_p^2} \quad (2.21)$$

where the coefficients  $A_{ij}$ ,  $B_i$  and  $C$  depend on the three material length parameters as well as on the spatial gradients of the plastic strain increment direction,

$$A_{ij} = l_1^2 \left( \frac{1}{2} \delta_{ij} + \frac{2}{5} m_{ip} m_{jp} \right) + \varepsilon_{pir} m_{qr} (L_2^2 \varepsilon_{pjqv} m_{qv} + L_3^2 \varepsilon_{qjiv} m_{pv}) \quad (2.22)$$

$$B_i = l_1^2 \left( \frac{4}{3} m_{pq} m_{pi,q} - \frac{8}{15} m_{ip} m_{pq,q} \right) + 2\varepsilon_{pir} m_{qr} (L_2^2 \varepsilon_{puv} m_{qv,u} + L_3^2 \varepsilon_{quv} m_{pv,u}) \quad (2.23)$$

$$C = l_1^2 \left[ \frac{1}{3} m_{ij,k} (m_{ij,k} + 2m_{jk,i}) - \frac{4}{15} m_{ki,i} m_{kj,j} \right] + \varepsilon_{pir} m_{qr,i} (L_2^2 \varepsilon_{puv} m_{qv,u} + L_3^2 \varepsilon_{quv} m_{pv,u}) \quad (2.24)$$

with  $L_2^2 = \frac{4}{3} l_2^2 + \frac{8}{5} l_3^2$  and  $L_3^2 = \frac{4}{3} l_2^2 - \frac{8}{5} l_3^2$ . Here,  $\delta_{ij}$  is the Kronecker delta and  $\varepsilon_{ijk}$  is the permutation tensor.

By the alternative definitions  $A_{ij} = l^{*2} \delta_{ij}$ ,  $B_i = 0$  and  $C = 0$  a single length scale parameter theory closely related to the strain gradient

theory of Aifantis [9] can be formulated using a new length parameter  $l^*$  with

$$\dot{\epsilon}^P = \sqrt{\dot{\epsilon}_p^2 + l^{*2} \dot{\epsilon}_{p,i} \dot{\epsilon}_{p,i}} \quad (2.25)$$

The stresses are related to the strains through the following incremental relations

$$\dot{\sigma}_{ij} = C_{ijkl} (\dot{\epsilon}_{kl} - \dot{\epsilon}_p m_{kl}) \quad (2.26)$$

$$\dot{Q} = h(E^P) \left( \dot{\epsilon}_p + \frac{1}{2} B_i \dot{\epsilon}_{p,i} + C \dot{\epsilon}_p \right) \quad (2.27)$$

$$\dot{\tau}_i = h(E^P) \left( A_{ij} \dot{\epsilon}_{p,j} + \frac{1}{2} B_i \dot{\epsilon}_p \right) \quad (2.28)$$

where  $C_{ijkl}$  is the elastic stiffness tensor in an isotropic solid and  $h(E^P) = d\sigma/d\epsilon_p$  is the tangent hardening quantity, evaluated from uniaxial tensile data of stress  $\sigma$  versus plastic strain  $\epsilon_p$ , as in the case of classic plasticity. For the one-parameter version (2.25) the constitutive relations yield

$$\dot{Q} = h(E^P) \dot{\epsilon}_p \quad (2.29)$$

$$\dot{\tau}_i = l^{*2} h(E^P) \dot{\epsilon}_{p,i} \quad (2.30)$$

The yield condition is specified in terms of the generalized effective stress  $Q_y = Q$ , with the evolution of  $Q_y$  being respectively given by  $Q_y = h(\dot{\epsilon}_p + \frac{1}{2} B_i \dot{\epsilon}_{p,i} + C \dot{\epsilon}_p)$  and  $Q_y = h(\dot{\epsilon}_p)$  for the multiple and single length parameter versions.

### 2.2.2 Finite deformation framework

The phenomenological SGP theory by Fleck and Hutchinson [13] is generalized following the work by Niordson and Redanz [49], where a thorough description can be found (see also the work by Niordson and Tvergaard [50]). An updated Lagrangian configuration is adopted and by means of Kirchhoff stress measures the incremental principle of virtual work, Eq. (2.17), can be expressed as:

$$\int_V \left( \tilde{\zeta}_{ij} \delta \dot{\epsilon}_{ij} - \sigma_{ij} (2 \dot{\epsilon}_{ik} \delta \dot{\epsilon}_{kj} - \dot{\epsilon}_{kj} \delta \dot{\epsilon}_{ki}) + (\dot{q} - \dot{\sigma}_e^c) \delta \dot{\epsilon}^P + \check{\varrho}_i \delta \dot{\epsilon}_{p,i}^P \right) dV = \int_S (\dot{T}_{0i} \delta \dot{u}_i + \dot{t}_0 \delta \dot{\epsilon}^P) dS \quad (2.31)$$

Here,  $\tilde{\zeta}_{ij}$  is the Jaumann rate of the Kirchhoff stress,  $\dot{q}$  is the rate of the Kirchhoff variant of the effective stress,  $\check{\varrho}_i$  is the convected derivative of the higher order Kirchhoff stress and the velocity gradient is denoted by  $\dot{\epsilon}_{ij}$ .  $\dot{T}_{0i}$  and  $\dot{t}_0$  are the nominal traction and the nominal higher order traction, respectively, with the subscript 0 referring to the reference configuration. The Kirchhoff quantities are related to

their Cauchy counterparts in Eq. (2.17) by the determinant,  $J$ , of the deformation gradient:  $\varsigma_{ij} = J\sigma_{ij}$ ,  $\varrho_i = J\zeta_i$ ,  $\mathbf{q} = J\mathbf{Q}$  and  $\sigma_e^s = J\sigma_e$ . The finite strain generalization, for a hardening modulus  $h$  [ $E^P$ ], of the constitutive equations for the stress measures corresponding to the total strain, the plastic strain, and the plastic strain gradient, respectively, are given by:

$$\tilde{\varsigma}_{ij} = C_{ijkl} (\dot{\epsilon}_{kl} - \dot{\epsilon}^P m_{kl}) = \dot{\varsigma}_{ij} - \dot{\omega}_{ik} \sigma_{kj} - \sigma_{ik} \dot{\omega}_{jk} \quad (2.32)$$

$$\dot{\mathbf{q}} - \dot{\sigma}_{(e)}^s = h \left( \dot{\epsilon}^P + \frac{1}{2} B_i \dot{\epsilon}_{,i}^P + C \dot{\epsilon}^P \right) - m_{ij} \tilde{\varsigma}_{ij} \quad (2.33)$$

$$\check{\varrho}_i = h \left( A_{ij} \dot{\epsilon}_{,j}^P + \frac{1}{2} B_i \dot{\epsilon}^P \right) = \dot{\varrho}_i - \dot{\epsilon}_{ik} \varrho_k \quad (2.34)$$

where the elastic stiffness tensor is given by

$$C_{ijkl} = \frac{E}{1+\nu} \left( \frac{1}{2} (\delta_{ik} \delta_{jl} + \delta_{il} \delta_{jk}) + \frac{\nu}{1-2\nu} \delta_{ij} \delta_{kl} \right) \quad (2.35)$$

and  $\dot{\omega}_{ij} = \frac{1}{2} (\dot{\epsilon}_{ij} - \dot{\epsilon}_{ji})$  is the anti-symmetric part of the velocity gradient. Here  $\delta_{ij}$  is the Kronecker delta while  $E$  and  $\nu$  denote Young's modulus and the Poisson ratio, respectively.

Fleck-Hutchinson (2001) [13] higher order phenomenological *SGP* theory has been consistently employed to model size effects in metal plasticity. The influence of the strain gradients is accurately captured in a number of numerical experiments, such as simple shear, torsion, void growth or nanoindentation [13, 51]. As detailed before, this is achieved by defining the flow stress as a function of a gradient-enhanced effective plastic strain  $\sigma_{\text{flow}} = f(E^P)$ , where  $f$  is an increasing function determined from a macroscopic uniaxial stress-strain test. Motivated by Taylor-based hardening, wherein increases in dislocation density underlie strain hardening, Fleck and Hutchinson [13] define  $E^P$  to include contributions from plastic strain gradients. Thus, as described in [28], dislocation density increases in the presence of severe plastic strain gradients: this is manifest as an increase in effective plastic strain and a subsequent increase in flow stress through the macroscopically determined strain hardening description.

### 2.3 ADVANCED GRADIENT PLASTICITY THEORIES

Gudmundson [6] was the first to note that the widely accepted phenomenological model by Fleck and Hutchinson [13] does not always satisfy thermodynamic requirements on plastic dissipation. With the aim of overcoming this deficiency, Gudmundson [6] and Gurtin and Anand [16] put forward a novel class of *SGP* theories that incorporates both energetic (or recoverable) and dissipative (or unrecoverable) higher order stresses.

### 2.3.1 Principle of virtual work and governing equations

Employing a small strain formulation, the total strain rate is determined from the gradients of the displacement rates:  $\dot{\varepsilon}_{ij} = (\dot{u}_{i,j} + \dot{u}_{j,i})/2$ , and decomposes into an elastic part,  $\dot{\varepsilon}_{ij}^e$ , and a plastic part,  $\dot{\varepsilon}_{ij}^p$ , so that:  $\dot{\varepsilon}_{ij} = \dot{\varepsilon}_{ij}^e + \dot{\varepsilon}_{ij}^p$ . For a solid of volume  $V$  and external surface  $S$ , the principle of virtual work reads [6]

$$\int_V \left( \sigma_{ij} \delta \varepsilon_{ij}^e + q_{ij} \delta \varepsilon_{ij}^p + \tau_{ijk} \delta \varepsilon_{ij,k}^p \right) dV = \int_S \left( T_i \delta u_i + t_{ij} \delta \varepsilon_{ij}^p \right) dS \quad (2.36)$$

where  $\sigma_{ij}$  denotes the Cauchy stress,  $q_{ij}$  the so-called micro-stress tensor (work conjugate to the plastic strain,  $\varepsilon_{ij}^p$ ) and  $\tau_{ijk}$  the higher order stress tensor (work conjugate to the plastic strain gradients  $\varepsilon_{ij,k}^p$ ), being the prime symbol omitted from  $q_{ij}$  and  $\tau_{ijk}$  although only their deviatoric parts contribute to the principle of virtual work. The right-hand side of Eq. (2.36) includes both conventional tractions,  $T_i = \sigma_{ij} n_j$ , and higher order terms,  $t_{ij} = \tau_{ijk} n_k$ , with  $n_k$  denoting the outward normal to the surface  $S$ . The principle of virtual work can alternatively be stated as

$$\int_V \left( \sigma_{ij} \delta \varepsilon_{ij} + (q_{ij} - \sigma'_{ij}) \delta \varepsilon_{ij}^p + \tau_{ijk} \delta \varepsilon_{ij,k}^p \right) dV = \int_S \left( T_i \delta u_i + t_{ij} \delta \varepsilon_{ij}^p \right) dS \quad (2.37)$$

Here,  $\sigma'_{ij}$  is the deviatoric part of the Cauchy stress:  $\sigma'_{ij} = \sigma_{ij} - \delta_{ij} \sigma_{kk}/3$ . Applying the product rule and Gauss' divergence theorem to the internal virtual work - left hand side of Eq. (2.37) - renders

$$\delta W_i = \int_S \left( \sigma_{ij} n_j \delta u_i + \tau_{ijk} n_k \delta \varepsilon_{ij}^p \right) dS - \int_V \left( \sigma_{ij,j} \delta u_i + (\tau_{ijk,k} + s_{ij} - q_{ij}) \delta \varepsilon_{ij}^p \right) dV \quad (2.38)$$

Since the second integral on the right-hand side of Eq. (2.38) should vanish for arbitrary variations, two sets of equilibrium equations can be obtained

$$\sigma_{ij,j} = 0 \quad (2.39)$$

$$\tau_{ijk,k} + s_{ij} - q_{ij} = 0 \quad (2.40)$$

Where the first integral on the right hand side of (2.38) may be identified as part of the external virtual work. Thus, by accounting for the right hand side of (2.36), the corresponding conventional  $T_i = \sigma_{ij} n_j$  and higher order  $t_{ij} = \tau_{ijk} n_k$  boundary conditions can be obtained.

### 2.3.2 Thermodynamically consistent constitutive equations

The first two laws of thermodynamics for a given domain  $\Omega$  of a continuum body within a dynamical process of specific internal energy  $\mathcal{E}$  and specific entropy  $\Lambda$  read [52, 53]

$$\overline{\int_{\Omega} \mathcal{E} dV} = W_e(\Omega) - \int_{\partial\Omega} q_i n_i dS + \int_{\Omega} q dV \quad (2.41)$$

$$\overline{\int_{\Omega} \Lambda dV} \geq \int_{\partial\Omega} \frac{q_i}{\Theta} n_i dS + \int_{\Omega} \frac{q}{\Theta} dV \quad (2.42)$$

with  $\overline{(\cdot)}$  denoting a total time derivative and where  $W_e$  is the external work,  $q_i$  is the heat flux,  $q$  is the heat absorption and  $\Theta$  the absolute temperature. Within an isothermal process ( $\Theta = \Theta_0$ ) the thermodynamic laws can be readily combined by considering the free energy  $\Psi = \mathcal{E} - \Theta_0 \Lambda$ , such that [21]

$$\overline{\int_{\Omega} \Psi dV} \leq W_e(\Omega) \quad (2.43)$$

which is generally referred to as Clausius-Duhem inequality or the principle of dissipation. Given (2.36), and since  $\overline{\int_{\Omega} \Psi dV} = \int_{\Omega} \dot{\Psi} dV$  (with  $\Omega$  being an arbitrary domain), the local free-energy inequality takes the form

$$\sigma_{ij} \dot{\varepsilon}_{ij}^e + q_{ij} \dot{\varepsilon}_{ij}^p + \tau_{ijk} \dot{\varepsilon}_{ij,k}^p - \dot{\Psi} \geq 0 \quad (2.44)$$

Within a generalized setting, the time derivative of the Helmholtz free energy is given by

$$\dot{\Psi} = \frac{\partial \Psi}{\partial \varepsilon_{ij}^e} \dot{\varepsilon}_{ij}^e + \frac{\partial \Psi}{\partial \varepsilon_{ij}^p} \dot{\varepsilon}_{ij}^p + \frac{\partial \Psi}{\partial \varepsilon_{ij,k}^p} \dot{\varepsilon}_{ij,k}^p \quad (2.45)$$

Accordingly, appropriate constitutive relations must be considered in order to fulfill the following imbalance:

$$\left( \sigma_{ij} - \frac{\partial \Psi}{\partial \varepsilon_{ij}^e} \right) \dot{\varepsilon}_{ij}^e + \left( q_{ij} - \frac{\partial \Psi}{\partial \varepsilon_{ij}^p} \right) \dot{\varepsilon}_{ij}^p + \left( \tau_{ijk} - \frac{\partial \Psi}{\partial \varepsilon_{ij,k}^p} \right) \dot{\varepsilon}_{ij,k}^p \geq 0 \quad (2.46)$$

It is possible to prescribe arbitrary values of  $\dot{\varepsilon}_{ij}^e$  such that the inequality is violated [54]. Thus, the elastic contribution is understood to be purely energetic and the first term within brackets must vanish, leading to the constitutive equation for the Cauchy stress,

$$\sigma_{ij} = \frac{\partial \Psi}{\partial \varepsilon_{ij}^e} \quad (2.47)$$

The dissipative components of the microstress  $q_{ij}^D$  and the higher order stress  $\tau_{ijk}^D$  are given by,

$$q_{ij}^D = \left( q_{ij} - \frac{\partial \Psi}{\partial \varepsilon_{ij}^p} \right) \quad \text{and} \quad \tau_{ijk}^D = \left( \tau_{ijk} - \frac{\partial \Psi}{\partial \varepsilon_{ij,k}^p} \right) \quad (2.48)$$

and the dissipation inequality (2.46) takes the form,

$$q_{ij}^D \dot{\varepsilon}_{ij}^p + \tau_{ijk}^D \dot{\varepsilon}_{ij,k}^p \geq 0 \quad (2.49)$$

The first term in (2.49) does not constitute a problem from the thermodynamic perspective as the effective plastic strain rate is inherently positive. Plastic deformation is generally considered to be a dissipative process and consequently the free energy is usually defined independently of the plastic strain, implying  $q_{ij} = q_{ij}^D$  (this is, nevertheless, not always the case, c.f. [55]). However, the second term may be negative for strongly non-proportional histories when the stored energy associated with the plastic gradients is being released (see [21, 54]). This is the case of Fleck and Hutchinson (2001) theory [13] where the higher order stress - given by (2.28) - is purely dissipative.

One way of ensuring positive plastic work is to adopt a purely energetic formulation, implying:

$$\tau_{ijk}^E = \tau_{ijk} = \frac{\partial \Psi}{\partial \varepsilon_{ij,k}^p} \quad \text{and} \quad \tau_{ijk}^D = 0 \quad (2.50)$$

such that the second term in (2.49) vanishes. The earlier works of Aifantis and co-workers [9, 56, 57] fall within this approach, as the higher order stress is given by

$$\tau_i = \ell^2 H \varepsilon_{p,i} \varepsilon_{p,i} \quad (2.51)$$

such that it can be determined from a free energy,

$$\Psi = \frac{\ell^2}{2} H \varepsilon_{p,i} \varepsilon_{p,i} \quad (2.52)$$

where  $H$  is the tangent modulus, which is assumed to be a positive constant. However, as discussed by Hutchinson [22], this interpretation requires the input tensile curve to have a constant tangent modulus, which is not a realistic restriction for a general plasticity model. Moreover, from a physical standpoint it seems likely that some of the work associated with  $\tau_{ijk}$  should be dissipative. The source of dissipative effects may be attributed to the movement of dislocations, a resulting resistance to dislocation motion that translates into an increase of the yield strength; while energetic effects may be associated to dislocation networks that lead to an

increase in strain hardening [55, 58].

Dissipative higher order contributions can be incorporated - in a thermodynamically consistent manner - by employing higher order stress quantities that are related to increments of strain, as postulated by Gudmundson [6] and Gurtin and Anand [16]. The pivotal step in constructing this class of constitutive relations is to define an effective stress  $\Sigma$  work conjugate to the gradient-enhanced effective plastic strain rate  $\dot{\mathbf{E}}^P$ , ensuring that the plastic work rate,

$$\Sigma \dot{\mathbf{E}}^P = q_{ij} \dot{\varepsilon}_{ij}^p + \tau_{ijk}^D \dot{\varepsilon}_{ij,k}^p \quad (2.53)$$

is always positive. Such that, for a quadratic form of the gradient enhanced effective plastic strain rate,

$$\dot{\mathbf{E}}^P = \sqrt{\frac{2}{3} \dot{\varepsilon}_{ij}^p \dot{\varepsilon}_{ij}^p + L^2 \dot{\varepsilon}_{ij,k}^p \dot{\varepsilon}_{ij,k}^p} \quad (2.54)$$

where  $L$  is the dissipative length scale; a work conjugate effective stress can be defined

$$\Sigma = \sqrt{\frac{2}{3} q_{ij}^D q_{ij}^D + L^{-2} \tau_{ijk}^D \tau_{ijk}^D} \quad (2.55)$$

and the corresponding dissipative stress quantities (in terms of *increments* of strain) can be readily obtained:

$$q_{ij}^D = \frac{2}{3} \frac{\Sigma}{\dot{\mathbf{E}}^P} \dot{\varepsilon}_{ij}^p \quad \text{and} \quad \tau_{ijk}^D = \frac{\Sigma}{\dot{\mathbf{E}}^P} L^2 \dot{\varepsilon}_{ij,k}^p \quad (2.56)$$

Following [6], the energetic contributions are obtained from the free energy, with a quadratic form being assumed,

$$\Psi = \frac{1}{2} (\varepsilon_{ij} - \varepsilon_{ij}^p) C_{ijkl} (\varepsilon_{kl} - \varepsilon_{kl}^p) + \frac{1}{2} \mu \ell^2 \varepsilon_{ij,k}^p \varepsilon_{ij,k}^p \quad (2.57)$$

Here,  $C_{ijkl}$  is the isotropic elastic stiffness tensor,  $\mu$  the shear modulus and  $\ell$  the energetic constitutive length parameter. The conventional stresses are given through the elastic relationship:

$$\sigma_{ij} = \frac{\partial \Psi}{\partial \varepsilon_{ij}^e} = C_{ijkl} (\varepsilon_{kl} - \varepsilon_{kl}^p) \quad (2.58)$$

And the energetic higher order stresses are derived as:

$$\tau_{ijk}^E = \frac{\partial \Psi}{\partial \varepsilon_{ij,k}^p} = \mu \ell^2 \varepsilon_{ij,k}^p \quad (2.59)$$

This novel class of advanced *SGP* theories [6, 16] is therefore able to incorporate both energetic and dissipative higher order contributions within a consistent thermodynamic framework. The seminal theory by Fleck and Hutchinson [13] has been recently reformulated

by Hutchinson [22] to meet the aforementioned thermodynamic requirements. Thus, the works by Gudmundson [6] and Gurtin and Anand [16] established a milestone in the development of gradient plasticity models. However, a number of open research issues remain to be addressed. Very recently Fleck, Hutchinson and Willis [18, 22, 23] noted that *non-incremental* dissipative higher order terms may lead to a delay in plastic flow under certain non-proportional loading conditions. This has been numerically corroborated by Bardella and Panteghini [59] and by Martínez-Pañeda et al. [60]. This physically uncertain response may favor the *incremental* modeling approach suggested by Hutchinson [22] where increments of all stress magnitudes are expressed in terms of increments of strain. However, a thermodynamically-consistent formulation with incremental constitutive relations for dissipative gradient contributions has not been proposed yet.

## 2.4 DISTORTION GRADIENT PLASTICITY

In recent years, increased attention has been focused on the need to account for the plastic spin, as proposed by Gurtin [15], to properly describe the plastic flow incompatibility and associated dislocation densities. It has been consistently shown (see, e.g., [59, 61, 62]) that the use of phenomenological higher order models that involve the whole plastic distortion (here referred to as Distortion Gradient Plasticity, DGP) leads to superior modeling capabilities. Hence, a distinct feature of Gurtin 2004 DGP [15] is the constitutive inclusion of the plastic rotation through the prescription of a free energy dependent on Nye's dislocation density tensor [63].

The equations in this section refer to the mechanical response of a body occupying a volume  $V$  with external surface  $S$  of outward normal  $n_i$ . More details about the higher order theory of distortion gradient plasticity can be found in [15].

### 2.4.1 Variational principles and balance equations

Within a small strain formulation, the displacement gradient  $u_{i,j}$  can be decomposed into its elastic and plastic parts:

$$u_{i,j} = \gamma_{ij}^e + \gamma_{ij}^p \quad (2.60)$$

Where  $\gamma_{ij}^p$ , the plastic distortion, which characterizes the evolution of dislocations and other defects through its structure, may in turn be decomposed into its symmetric and skew parts:

$$\gamma_{ij}^p = \varepsilon_{ij}^p + \vartheta_{ij}^p \quad (2.61)$$

Unlike the plastic strain field  $\varepsilon_{ij}^p$ , the plastic rotation  $\vartheta_{ij}^p$  is essentially irrelevant in the conventional theory. However, as pointed out by Gurtin [15], phenomenological models of isotropic SGP involving Nye's dislocation density tensor  $\alpha_{ij}$  as primal higher order kinematic variable,

$$\alpha_{ij} = \varepsilon_{jkl} \gamma_{il,k}^p \quad (\alpha = \text{curl } \gamma^p) \quad (2.62)$$

must account for the plastic spin since the macroscopic characterization of the Burgers vector involves both the symmetric and skew parts of the plastic distortion

$$\varepsilon_{jkl} \gamma_{il,k}^p = \varepsilon_{jkl} \varepsilon_{il,k}^p + \varepsilon_{jkl} \vartheta_{il,k}^p \quad (\text{curl } \gamma^p = \text{curl } \varepsilon^p + \text{curl } \vartheta^p) \quad (2.63)$$

with  $\varepsilon_{jkl}$  denoting the alternating symbol. Thus, in the absence of higher order surface tractions, the principle of virtual work can be expressed as:

$$\int_V \left( \sigma_{ij} \delta \varepsilon_{ij}^e + \zeta_{ij} \delta \alpha_{ij} + S_{ij} \delta \gamma_{ij}^p + \tau_{ijk} \delta \varepsilon_{ij,k}^p \right) dV = \int_S T_i \delta u_i dS \quad (2.64)$$

where the Cauchy stress is denoted by  $\sigma_{ij}$ . In addition to conventional stresses, the principle of virtual work incorporates the so-called micro-stress tensor,  $S_{ij}$  (work conjugate to the plastic distortion,  $\gamma_{ij}^p$ ), the defect stress  $\zeta_{ij}$  (work conjugate to Nye's tensor  $\alpha_{ij}$ , the curl of the plastic distortion) and the higher order stress tensor,  $\tau_{ijk}$  (work conjugate to the plastic strain gradients  $\varepsilon_{ij,k}^p$ ). By taking into account that the micro-stress tensor can be decomposed into its symmetric and skew parts:  $S_{ij} = q_{ij} + \omega_{ij}$ , the virtual work statement can be expressed as:

$$\int_V \left( \sigma_{ij} \delta \varepsilon_{ij} + \zeta_{ij} \delta \alpha_{ij} + (q_{ij} - \sigma'_{ij}) \delta \varepsilon_{ij}^p + \omega_{ij} \delta \vartheta_{ij}^p + \tau_{ijk} \delta \varepsilon_{ij,k}^p \right) dV = \int_S T_i \delta u_i dS \quad (2.65)$$

with  $\sigma'_{ij}$  being the deviatoric part of the Cauchy stress. Applying the product rule and Gauss' divergence theorem to Eq. (2.65) renders:

$$\begin{aligned} & \int_V \left( -\sigma_{ij,j} \delta u_i + (q_{ij} - \sigma'_{ij} - \tau_{ijk,k} + \eta'_{ij}) \delta \varepsilon_{ij}^p + (\omega_{ij} + \varphi_{ij}) \delta \vartheta_{ij}^p \right) dV \\ & = \int_S \left( (T_i - \sigma_{ij} n_j) \delta u_i - (\Upsilon'_{ij} + \tau_{ijk} n_k) \delta \varepsilon_{ij}^p - (\Delta_{ij}) \delta \vartheta_{ij}^p \right) dS \end{aligned} \quad (2.66)$$

where  $\eta_{ij}$  and  $\varphi_{ij}$  are, respectively, the symmetric and skew-symmetric parts of the curl of the defect stress  $\xi_{ij} = \varepsilon_{jkl} \zeta_{il,k} = \eta_{ij} + \varphi_{ij}$ ; and equivalently,  $\Upsilon_{ij}$  and  $\Delta_{ij}$  respectively denote the symmetric and skew-symmetric parts of the cross product of the defect stress and the outward normal  $\Gamma_{ij} = \varepsilon_{jkl} \zeta_{il} n_k = \Upsilon_{ij} + \Delta_{ij}$ , with the

prime symbol ' denoting deviatoric quantities. By means of the fundamental lemma of calculus of variations, the governing equations

$$\sigma_{ij,j} = 0 \quad (2.67)$$

$$q_{ij} - \sigma'_{ij} - \tau_{ijk,k} + \eta'_{ij} = 0 \quad (2.68)$$

$$\omega_{ij} + \varphi_{ij} = 0 \quad (2.69)$$

and the natural boundary conditions

$$T_i = \sigma_{ij} n_j \quad (2.70)$$

$$\Upsilon'_{ij} + \tau_{ijk} n_k = 0 \quad (2.71)$$

$$\Delta_{ij} = 0 \quad (2.72)$$

readily follow.

#### 2.4.2 Energetic contributions

In order to account for the influence of GNDs, the free energy is chosen to depend on both the elastic strain  $\varepsilon_{ij}^e$  and Nye's tensor  $\alpha_{ij}$ :

$$\Psi = \frac{1}{2} C_{ijkl} \varepsilon_{ij}^e \varepsilon_{kl}^e + \Phi(\alpha_{ij}) \quad (2.73)$$

with  $C_{ijkl}$  being the elastic stiffness and  $\Phi(\alpha_{ij})$  the defect energy that accounts for the recoverable mechanisms associated with the development of GNDs. The widely used quadratic form of the defect energy is adopted

$$\Phi(\alpha_{ij}) = \frac{1}{2} \mu \ell^2 \alpha_{ij} \alpha_{ij} \quad (2.74)$$

but one should note that exploring other options may lead to further modeling capabilities (see [59, 61]), with recoverable gradient effects contributing to both hardening and strengthening. Accordingly, the defect stress equals:

$$\zeta_{ij} = \frac{\partial \Phi(\alpha_{ij})}{\partial \alpha_{ij}} = \mu \ell^2 \alpha_{ij} \quad (2.75)$$

with  $\mu$  being the shear modulus and  $\ell$  an energetic length scale.

#### 2.4.3 Dissipative contributions

A gradient-enhanced phenomenological effective plastic flow rate is defined,

$$\dot{E}^p = \sqrt{\frac{2}{3} \dot{\varepsilon}_{ij}^p \dot{\varepsilon}_{ij}^p + \chi \dot{\vartheta}_{ij}^p \dot{\vartheta}_{ij}^p + \frac{2}{3} L^2 \dot{\varepsilon}_{ij,k}^p \dot{\varepsilon}_{ij,k}^p} \quad (2.76)$$

where  $L$  is a dissipative length parameter and  $\chi$  is the parameter governing the dissipation due to the plastic spin. Bardella [64] has analytically identified the value of  $\chi$  that captures the mechanical response of a crystal subjected to multislip under simple shear:

$$\chi = \left[ \frac{3}{2} + \frac{\sigma_0}{\mu \varepsilon_0} \left( \frac{L}{\ell} \right)^2 \right]^{-1} \quad (2.77)$$

being  $\sigma_0$  and  $\varepsilon_0$  non-negative material parameters, which implies a value for  $\chi$  bounded between 0 and 2/3. The flow resistance  $\Sigma$ , work conjugate to  $\dot{E}^P$ , is given by

$$\Sigma = \sqrt{\frac{3}{2} q_{ij} q_{ij} + \frac{1}{\chi} \omega_{ij} \omega_{ij} + \frac{3}{2L^2} \tau_{ijk} \tau_{ijk}} \quad (2.78)$$

Such that the unrecoverable stresses equal

$$q_{ij} = \frac{2}{3} \frac{\Sigma}{\dot{E}^P} \dot{\varepsilon}_{ij}^P \quad (2.79)$$

$$\omega_{ij} = \chi \frac{\Sigma}{\dot{E}^P} \dot{\vartheta}_{ij}^P \quad (2.80)$$

$$\tau_{ijk} = \frac{2}{3} L^2 \frac{\Sigma}{\dot{E}^P} \dot{\varepsilon}_{ij,k}^P \quad (2.81)$$

And consequently the second law of thermodynamics is fulfilled by relating finite stress measures with rates of plastic deformation in what is referred to as a *non-incremental* form:

$$q_{ij} \dot{\varepsilon}_{ij}^P + \omega_{ij} \dot{\vartheta}_{ij}^P + \tau_{ijk} \dot{\varepsilon}_{ij,k}^P \equiv \Sigma \dot{E}^P > 0 \quad (2.82)$$

While higher order energetic and dissipative contributions are a common feature among the majority of the most advanced phenomenological *SGP* theories (see, e.g., [6, 16, 21, 65]), the need to constitutively account for the plastic spin, as proposed about ten years ago by Gurtin [15], has been mostly neglected in favor of simpler models. However, the use of phenomenological higher-order formulations that involve the whole plastic distortion has attracted increasing attention in recent years due to its superior modeling capabilities. The studies of Bardella and Giacomini [66] and Bardella [61, 64] have shown that, even for small strains, the contribution of the plastic spin plays a fundamental role in order to provide a description closer to the mechanical response predicted by strain gradient *crystal* plasticity. This has been further assessed by Poh and Peerlings [62], who, by comparing to a reference crystal plasticity solution given by [67], showed that the plastic rotation must be incorporated to capture the essential features of crystal plasticity. Moreover, Poh and Peerlings [62] numerically elucidated that the localization phenomenon that takes place in Bittencourt et al. [68] composite unit cell benchmark problem can only be reproduced by *DGP*. Gurtin [15] theory has also

been employed by Poh and co-workers [69, 70] through a novel homogenization formulation to describe the behavior of each grain in a polycrystal where grain boundaries are modeled to describe effects of dislocation blockage or transmittal.



## NUMERICAL IMPLEMENTATION

---

While solving analytically (or semi-analytically) simple problems, such as pure bending or shear of an infinite layer, has been particularly useful to compare and benchmark [SGP](#) theories, quantitative assessment of gradient effects in engineering applications requires the use of numerical methods. Particularly, the finite element method is by far the most commonly adopted approach to characterize size effects in metal plasticity.

The numerical implementation of each class of [SGP](#) formulations is significantly influenced by the theoretical framework. Thus, a wide range of *ad hoc* numerical solutions have been proposed for each gradient plasticity model, ranging from the relatively easy to implement lower order theories to the more complicated gradient plasticity formulations falling within the mathematical framework of Cosserat–Koiter–Mindlin theories of higher order elasticity. Aiming to cover a large spectrum of numerical methodologies, focus is placed on: a numerical solution without higher order stresses for [MSG](#) plasticity, including both the standard [FE](#) case and a new enriched scheme (Section [3.1](#)), a higher order monolithic procedure for Fleck–Hutchinson phenomenological theory (Section [3.2](#)), a staggered approach for advanced [SGP](#) theories with energetic and dissipative contributions (Section [3.3](#)), and a novel higher order [FE](#) basis for [DGP](#) (Section [3.4](#)). As detailed below, verification of each numerical implementation is performed by solving different boundary value problems and comparing the output with numerical results from other authors.

### 3.1 CMSG PLASTICITY: FEM AND X-FEM

As a function of their order, two different classes of [SGP](#) theories can be identified. One involves higher order stresses and therefore requires extra boundary conditions; the other one does not involve higher order terms, and gradient effects come into play via the incremental plastic moduli. With the aim of employing mechanism-based [SGP](#) formulations within a lower order setup, Huang et al. [[14](#)] developed what is referred to as the Conventional Mechanism-based Strain Gradient ([CMSG](#)) plasticity theory. It is also based on Taylor’s dislocation model (i.e., [MSG](#) plasticity), but it does not involve higher order terms and therefore falls into the [SGP](#) framework that preserves the structure of classic plasticity. Consequently, the plastic strain

gradient appears only in the constitutive model, and the equilibrium equations and boundary conditions are the same as the conventional continuum theories [14]. This lower order scheme is adopted in the present work to characterize gradient effects from a mechanism-based approach, as it does not suffer convergence problems when addressing numerically demanding problems, such as crack tip deformation under large strains, unlike its higher order counterpart (see [71, 72]). In MSG plasticity the differences between the higher order and the lower order versions are restricted to a very thin boundary layer ( $\approx 10$  nm) [14, 73].

### 3.1.1 Finite element implementation

#### 3.1.1.1 A Taylor-based viscoplastic-like constitutive relation

As discussed in [74], the Taylor dislocation model gives the flow stress dependent on both the equivalent plastic strain  $\varepsilon^P$  and effective plastic strain gradient  $\eta^P$

$$\dot{\sigma} = \frac{\partial \sigma}{\partial \varepsilon^P} \dot{\varepsilon}^P + \frac{\partial \sigma}{\partial \eta^P} \dot{\eta}^P \quad (3.1)$$

such that, for a plastic strain rate  $\dot{\varepsilon}_{ij}^P$  proportional to the deviatoric stress  $\sigma'_{ij}$ , a self contained constitutive model cannot be obtained due to the term  $\dot{\eta}^P$ . In order to overcome this situation without employing higher order stresses, Huang et al. [14] adopted a viscoplastic formulation to obtain  $\dot{\varepsilon}^P$  in terms of the effective stress  $\sigma_e$  rather than its rate  $\dot{\sigma}_e$

$$\dot{\varepsilon}^P = \dot{\varepsilon} \left[ \frac{\sigma_e}{\sigma_{\text{flow}}} \right]^{(1/m)} \quad (3.2)$$

The viscoplastic-limit approach developed by Kok et al. [75] is used to suppress strain rate and time dependence by replacing the reference strain rate  $\dot{\varepsilon}_0$  with the effective strain rate  $\dot{\varepsilon}$ . The exponent is taken to fairly large values ( $m \leq 0.05$ ), which in Kok and co-workers' [75] scheme is sufficient to reproduce the rate-independent behavior given by the viscoplastic limit in a conventional power law (see [14]). Taking into account that the volumetric ( $\dot{\varepsilon}_{kk}$ ) and deviatoric ( $\dot{\varepsilon}'_{ij}$ ) strain rates are related to the stress rate in the same way as in classic plasticity, the constitutive equation yields:

$$\dot{\sigma}_{ij} = K \dot{\varepsilon}_{kk} \delta_{ij} + 2\mu \left\{ \dot{\varepsilon}'_{ij} - \frac{3\dot{\varepsilon}}{2\sigma_e} \left[ \frac{\sigma_e}{\sigma_{\text{flow}}} \right]^{(1/m)} \dot{\sigma}'_{ij} \right\} \quad (3.3)$$

Where, as described in Section 2.1 of Chapter 2, the flow stress includes an additional term to account for the influence of GNDs:

$$\sigma_{\text{flow}} = \sigma_{\text{ref}} \sqrt{f^2 (\varepsilon^P) + l \eta^P} \quad (3.4)$$

With  $K$  being the bulk modulus,  $\mu$  the shear modulus,  $\delta_{ij}$  the Kronecker delta,  $\sigma_{ref}$  a reference stress,  $f(\varepsilon^P)$  a non-dimensional function determined from the uniaxial stress-strain curve,  $l$  the intrinsic material length,  $\varepsilon_{ij}$  the total strain and  $\sigma_{ij}$  the Cauchy stress tensor.

### 3.1.1.2 Consistent tangent modulus

Since higher order terms are not involved, the governing equations of CMSG plasticity are essentially the same as those in conventional plasticity and the FE implementation is relatively straightforward. As in classic plasticity, the plastic strain rate  $\dot{\varepsilon}_{ij}^P$  is proportional to the deviatoric stress  $\sigma'_{ij}$

$$\dot{\varepsilon}_{ij}^P = \frac{3\dot{\varepsilon}^P}{2\sigma_e} \sigma'_{ij} \quad (3.5)$$

with the usual definitions of the effective stress

$$\sigma_e = \sqrt{\frac{3}{2} \sigma'_{ij} \sigma'_{ij}} \quad (3.6)$$

and the equivalent strain rate

$$\dot{\varepsilon} = \sqrt{\frac{2}{3} \dot{\varepsilon}'_{ij} \dot{\varepsilon}'_{ij}} \quad (3.7)$$

The deviatoric stresses at the end of the increment can be readily obtained from the elastic relation with the deviatoric strains

$$\sigma'_{ij} = 2\mu \left( \varepsilon'_{ij}|_t + \Delta\varepsilon'_{ij} - \Delta\varepsilon_{ij}^P \right) \quad (3.8)$$

Where, following the notation by Qu [74],  $\Delta$  refers to the incremental value and  $|_t$  denotes the value at the beginning of the increment. Substituting the incremental version of (3.5) into (3.8) renders

$$\sigma'_{ij} = 2\mu \left( \varepsilon'_{ij}|_t + \Delta\varepsilon'_{ij} - \frac{3\Delta\varepsilon^P}{2\sigma_e} \sigma'_{ij} \right) \quad (3.9)$$

Defining  $\hat{\varepsilon}'_{ij} = \varepsilon'_{ij}|_t + \Delta\varepsilon'_{ij}$  and rearranging,

$$\left( 1 + \frac{3\mu}{\sigma_e} \Delta\varepsilon^P \right) \sigma'_{ij} = 2\mu \hat{\varepsilon}'_{ij} \quad (3.10)$$

Taking the inner part of (3.10)

$$\sigma_e + 3\mu\Delta\varepsilon^P = 3\mu\hat{\varepsilon} \quad (3.11)$$

where  $\hat{\varepsilon} = \sqrt{\frac{2}{3} \hat{\varepsilon}'_{ij} \hat{\varepsilon}'_{ij}}$ . Reformulating (3.11) and substituting (3.2) and (3.4) renders,

$$\sigma_e - 3\mu \left( \hat{\varepsilon} - \Delta\varepsilon \left( \frac{\sigma_e}{\sigma_{flow}} \right)^{(1/m)} \right) = 0 \quad (3.12)$$

Which is a non-linear equation that can be solved by Newton–Raphson method

$$\sigma_e = \sigma_e + \frac{3\mu \left( \hat{\varepsilon} - \Delta\varepsilon \left( \frac{\sigma_e}{\sigma_{\text{flow}}} \right)^{(1/m)} \right) - \sigma_e}{1 + 3\mu h} \quad (3.13)$$

with  $h$  being

$$h = m\Delta\varepsilon \left( \frac{\sigma_e}{\sigma_{\text{flow}}} \right)^{\left(\frac{1}{m}-1\right)} \frac{1}{\sigma_{\text{flow}}} \quad (3.14)$$

Once convergence has been achieved the incremental effective plastic strain is obtained from

$$\Delta\varepsilon^p = \hat{\varepsilon} - \frac{\sigma_e}{3\mu} \quad (3.15)$$

Such that  $\sigma'_{ij}$  can be obtained from (3.10) and  $\Delta\varepsilon^p_{ij}$  from the incremental version of (3.5). The consistent material Jacobian  $\partial\Delta\sigma_{ij}/\partial\Delta\varepsilon_{ij}$  is then computed by taking the variation of (3.10) with respect to all quantities at the end of the increment

$$\left( 1 + \frac{3\mu}{\sigma_e} \Delta\varepsilon^p \right) \partial\sigma'_{ij} + \sigma'_{ij} \frac{3\mu}{\sigma_e} \left( \partial\Delta\varepsilon^p - \frac{\Delta\varepsilon^p}{\sigma_e} \partial\sigma_e \right) = 2\mu \partial\hat{\varepsilon}'_{ij} \quad (3.16)$$

And (3.11) leads to

$$\partial\sigma_e + 3\mu\partial\Delta\varepsilon^p = 3\mu\partial\hat{\varepsilon} \quad (3.17)$$

Substituting (3.15) and rearranging,

$$\partial\sigma_e = \frac{3\mu}{1 + 3\mu h} \partial\hat{\varepsilon} \quad (3.18)$$

Accounting for the definition of  $\hat{\varepsilon}$  renders,

$$\partial\sigma_e = \frac{2}{3\hat{\varepsilon}} \frac{3\mu}{1 + 3\mu h \hat{\varepsilon}'_{ij} \partial\hat{\varepsilon}'_{ij}} \quad (3.19)$$

Substituting in (3.16) and rearranging leads to:

$$\partial\sigma'_{ij} = \left( \frac{2\sigma_e}{3\hat{\varepsilon}} I_{ijkl} - \frac{1}{\sigma_e \hat{\varepsilon}} \left( h - \frac{\Delta\varepsilon^p}{\sigma_e} \right) \frac{3\mu}{1 + 3\mu h} \sigma'_{ij} \sigma'_{ij} \right) \partial\hat{\varepsilon}'_{ij} \quad (3.20)$$

with  $I_{ijkl}$  being the fourth-order unit tensor. Such that, by considering the relation between the stress and strain tensors with their deviatoric quantities, the material stiffness Jacobian can be expressed as:

$$\begin{aligned} \partial\sigma_{ij} = & \left( \frac{2\sigma_e}{3\hat{\varepsilon}} I_{ijkl} + \left( K - \frac{2\sigma_e}{9\hat{\varepsilon}} \right) I_{ij} \right. \\ & \left. - \frac{1}{\sigma_e \hat{\varepsilon}} \left( h - \frac{\Delta\varepsilon^p}{\sigma_e} \right) \frac{3\mu}{1 + 3\mu h} \sigma'_{ij} \sigma'_{ij} \right) \partial\varepsilon_{ij} \end{aligned} \quad (3.21)$$

### 3.1.1.3 Computation of the effective plastic strain gradient

The effective plastic strain gradient  $\eta^P$  is obtained at the element level: the plastic strain increment is interpolated through its values at the Gauss points in the isoparametric space and afterwards the increment in the plastic strain gradient is calculated by differentiation of the shape functions. Here focus is placed on the particular case of a plane strain quadrilateral element with 8 nodes and 4 integration points, extension to other types of elements can be performed in a relatively straightforward manner.

Thus, the incremental value of the components of the plastic strain  $\Delta\varepsilon_{ij}^P$  within the element can be readily obtained from its values at the Gauss integration points  $(\Delta\varepsilon_{ij}^P)_k$

$$\Delta\varepsilon_{ij}^P = \sum_{k=1}^4 N'_k(x, y) (\Delta\varepsilon_{ij}^P)_k \quad (3.22)$$

where  $N'_k(x, y)$  is the interpolation function in global coordinates. By performing the classic isoparametric mapping, the coordinate transformation is:

$$x = \sum_{k=1}^4 N_k(\xi, \eta) x_k \quad (3.23)$$

$$y = \sum_{k=1}^4 N_k(\xi, \eta) y_k \quad (3.24)$$

where  $N_k(\xi, \eta)$  is the shape function vector. For convenience, the interpolation function in local coordinates takes the same form as the shape functions and (3.22) becomes:

$$\Delta\varepsilon_{ij}^P = \sum_{k=1}^4 N_k(\xi, \eta) (\Delta\varepsilon_{ij}^P)_k \quad (3.25)$$

Accordingly, linear shape functions are adopted,

$$N_i = \frac{1}{4} (1 + \xi_i \xi) (1 + \eta_i \eta) \quad (3.26)$$

with  $\xi_i$  and  $\eta_i$  denoting the integration point coordinates in the isoparametric space.

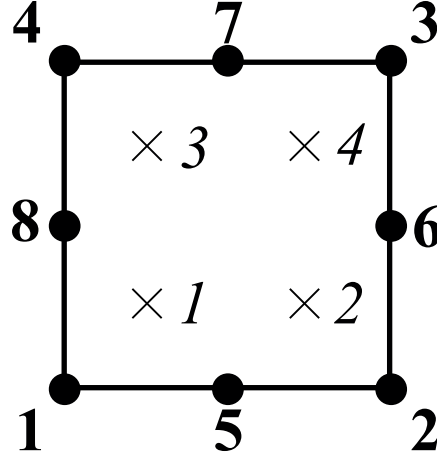


Figure 3.1: Nodal and integration point numbering adopted for a quadrilateral plane strain quadratic finite element

The numbering scheme in this Gauss point-based interpolation is depicted in Fig. 3.1. The differentiation of the shape functions readily follows:

$$\frac{\partial N_i}{\partial \xi} = \frac{1}{4} \xi_i (1 + \eta \eta_i) \quad (3.27)$$

$$\frac{\partial N_i}{\partial \eta} = \frac{1}{4} \eta_i (1 + \xi \xi_i) \quad (3.28)$$

Which, by means of the chain rule, can be easily converted to the global coordinate system,

$$\begin{bmatrix} \frac{\partial N_k}{\partial x} \\ \frac{\partial N_k}{\partial y} \end{bmatrix} = J^{-1} \begin{bmatrix} \frac{\partial N_k}{\partial \xi} \\ \frac{\partial N_k}{\partial \eta} \end{bmatrix} \quad (3.29)$$

with J being the Jacobian matrix:

$$J = \frac{\partial(x, y)}{\partial(\xi, \eta)} = \begin{bmatrix} \frac{\partial x}{\partial \xi} & \frac{\partial y}{\partial \xi} \\ \frac{\partial x}{\partial \eta} & \frac{\partial y}{\partial \eta} \end{bmatrix} = \begin{bmatrix} \sum_{k=1}^4 \frac{\partial N_k}{\partial \xi} x_k & \sum_{k=1}^4 \frac{\partial N_k}{\partial \xi} y_k \\ \sum_{k=1}^4 \frac{\partial N_k}{\partial \eta} x_k & \sum_{k=1}^4 \frac{\partial N_k}{\partial \eta} y_k \end{bmatrix} \quad (3.30)$$

With the plastic strain gradient being computed in MSG plasticity from: [12]

$$\Delta \eta_{ijk}^p = \Delta \varepsilon_{ik,j}^p + \Delta \varepsilon_{jk,i}^p - \Delta \varepsilon_{ij,k}^p \quad (3.31)$$

And the effective strain gradient increment being:

$$\Delta \eta^p = \frac{1}{4} \frac{\eta_{ijk}^p \Delta \eta_{ijk}^p}{\eta^p} \quad (3.32)$$

With  $\eta_{ijk}^p$  being computed in the same way as  $\Delta\eta_{ijk}^p$ . Under rate-proportional loading  $\Delta\eta^p$  can be computed as

$$\Delta\eta^p = \sqrt{\frac{1}{4}\Delta\eta_{ijk}^p\Delta\eta_{ijk}^p} \quad (3.33)$$

This non-local approach can be easily implemented in commercial FE software. For example, in the case of the well-known package ABAQUS, *modules* may be used within a UMAT subroutine to store the plastic strain components at each Gauss point.

#### 3.1.1.4 Verification

Since higher order boundary conditions have essentially no effect on the stress distribution at a distance of more than 10 nm away from the crack tip in MSG plasticity [33, 73], the outcome of the present numerical implementation will be compared to available results for the higher order version [32]. While not relevant to the present work, it must be remarked that lower order theories are not able to model effects of dislocation blockage at impermeable boundaries (see [19]), of particular interest in many small scale problems.

Following Jiang et al. [32], two dimensional plane strain crack tip fields are evaluated by means of a boundary layer formulation, where the crack region is contained by a circular zone and the Mode I load is applied at the remote circular boundary through a prescribed displacement:

$$u(r, \theta) = K_I \frac{1+\nu}{E} \sqrt{\frac{r}{2\pi}} \cos\left(\frac{\theta}{2}\right) (3-4\nu-\cos\theta) \quad (3.34)$$

$$v(r, \theta) = K_I \frac{1+\nu}{E} \sqrt{\frac{r}{2\pi}} \sin\left(\frac{\theta}{2}\right) (3-4\nu-\cos\theta) \quad (3.35)$$

Here,  $u$  and  $v$  are the horizontal and vertical components of the displacement boundary condition,  $r$  and  $\theta$  the radial and angular coordinates in a polar coordinate system centered at the crack tip,  $E$  is Young's modulus,  $\nu$  is the Poisson ratio of the material and  $K_I$  is the applied stress intensity factor, which quantifies the remote load. Small strain conditions are assumed and only the upper half of the circular domain is modeled due to symmetry. An outer radius of  $R = 42$  mm is defined and the entire specimen is discretized by means of eight-noded quadrilateral elements with reduced integration. Different mesh densities were used to study convergence behavior, and it was found that 1600 elements were sufficient to achieve mesh-independent results. With the aim of accurately characterizing the influence of the strain gradient, a very refined mesh is used near the crack tip, where the size of the elements is in the order of nanometers. An external applied load of  $K_I = 20\sigma_Y\sqrt{l}$  is assumed and the following material properties are adopted:  $\sigma_Y = 0.2\%E$ ,  $\nu = 0.3$ ,  $N = 0.2$

and  $l = 3.53 \mu\text{m}$ , where  $\sigma_Y$  is the initial yield stress and  $N$  is the strain hardening exponent. An isotropic power law material is adopted according to

$$\sigma = \sigma_Y \left( 1 + \frac{E \varepsilon^P}{\sigma_Y} \right)^N \quad (3.36)$$

The reference stress of (3.4) will correspond to  $\sigma_{ref} = \sigma_Y \left( \frac{E}{\sigma_Y} \right)^N$  and  $f(\varepsilon^P) = \left( \varepsilon^P + \frac{\sigma_Y}{E} \right)^N$ . Fig. 3.2 shows, in a double logarithm diagram, the normalized effective stress  $\sigma_e / \sigma_Y$  versus the normalized distance  $r/l$  ahead of the crack tip ( $\theta = 1.014^\circ$ ) for an external applied load of  $K_I = 20\sigma_Y\sqrt{l}$ .

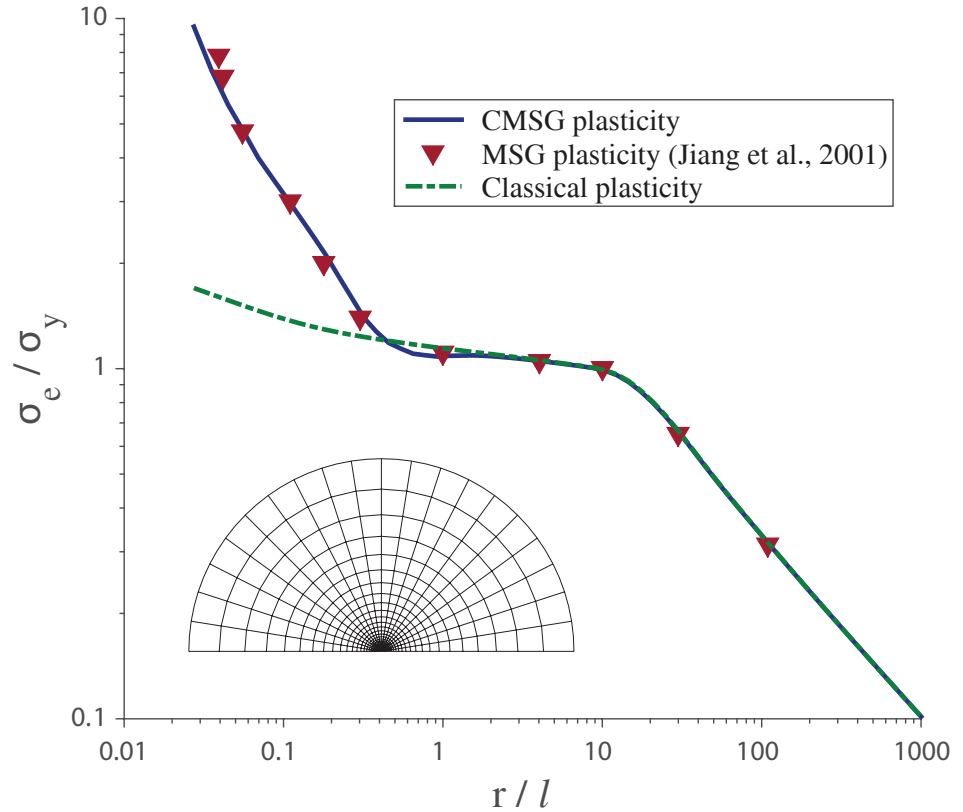


Figure 3.2: Effective stress distribution ahead of the crack-tip. Comparison between MSG plasticity predictions (symbols, taken from Jiang et al. [32]), CMSG plasticity (solid line) and conventional  $J_2$  plasticity (dashed line).

As shown in the figure, a very good agreement is obtained between the stress distributions obtained by means of the CMSG theory and MSG plasticity (taken from [32]), validating the present numerical implementation and confirming that higher order boundary conditions do not influence crack tip fields within its physical domain of validity ( $\approx 100 \text{ nm}$ ). Results prove the suitability of CMSG plasticity in the present study, allowing to develop a robust implicit numerical scheme (see [72]).

### 3.1.2 A novel X-FEM scheme

As outlined above, an appropriate characterization of gradient effects ahead of a crack requires the use of extremely refined meshes, with a characteristic element length of a few nanometers in the vicinity of the crack. The vast majority of fracture and damage studies under SGP theories (see, e.g., [28–30, 32, 72, 76]) have been conducted in the framework of the finite element method. Pan and Yuan [35, 77] used the element-free Galerkin method with the aim of avoiding the lack of convergence associated with FE schemes (especially as the element distortion becomes large or elements lose bearing capacity) at the expense of increasing the computational cost. In this subsection a novel numerical framework is proposed for crack tip assessment within MSG plasticity. The constitutive choice is motivated by the work by Shi et al. [73], who characterized the stress-dominated asymptotic field around a crack tip within MSG plasticity. The use of the Extended Finite Element Method (X-FEM) is therefore particularly appealing, as one can significantly alleviate the degree of mesh refinement by enriching the solution. A novel non-linear X-FEM scheme is therefore presented, which includes (i) gradient-enhanced asymptotic functions, (ii) linear and quadratic elements, (iii) a linear weighting function for the blending elements, (iv) an iterative solver for nonlinear systems and (v) an appropriate triangular integration scheme.

#### 3.1.2.1 Enriched solution

The approximation power of the FE method can be further enhanced by augmenting *suitable* functions to the finite element space; these functions represent the local nature of the solution. This can be achieved by means of the X-FEM, a numerical enrichment strategy within the framework of the Partition of Unity Method. The displacement approximation can be thus decomposed into a standard part and an enriched part,

$$u_i^h = \underbrace{\sum_{I \in \mathcal{N}^{fem}} N_i^I u_i^I}_{\text{Standard}} + \underbrace{\sum_{J \in \mathcal{N}^c} N_i^J H(\phi) a_i^J + \sum_{K \in \mathcal{N}^f} N_i^K \sum_{\alpha=1}^n F_\alpha(r, \theta) b_i^{K\alpha}}_{\text{Enriched}} \quad (3.37)$$

where  $\mathcal{N}^{fem}$  is the set of all nodes in the FE mesh,  $\mathcal{N}^c$  is the set of nodes whose shape function support is cut by the crack interior and  $\mathcal{N}^f$  is the set of nodes whose shape function support is cut by the crack tip.  $H(\phi)$  and  $F_\alpha(r, \theta)$  are the enrichment functions chosen to respectively capture the displacement jump across the crack surface and the singularity at the crack tip, with  $a_i^J$  and  $b_i^{K\alpha}$  being their as-

sociated degrees of freedom. Hence, the Heaviside jump enrichment function is defined as:

$$H(\phi) = \begin{cases} 1 & \text{for } \phi(x_i) > 0 \\ -1 & \text{for } \phi(x_i) < 0 \end{cases} \quad (3.38)$$

where  $\phi(x_i)$  is the signed distance function from the crack surface, given by,

$$\phi(x_i) = \min_{\bar{x}_i \in \Gamma_c} \|x_i - \bar{x}_i\| \text{sign}(n_i \cdot (x_i - \bar{x}_i)) \quad (3.39)$$

with  $n_i$  being the unit outward normal and  $\text{sign}()$  the sign function.

A set of functions with singular derivative near the crack that spans the near tip stress field is also defined. For example, in the case of linear elastic fracture mechanics, the following asymptotic displacement field is used:

$$F_\alpha(r, \theta) = r^{1/2} \left\{ \sin \frac{\theta}{2}, \cos \frac{\theta}{2}, \sin \frac{\theta}{2} \sin \theta, \cos \frac{\theta}{2} \sin \theta \right\} \quad (3.40)$$

where  $r$  is the distance from the crack tip and  $\theta$  represents the angular distribution. The linear elastic solution breaks down in the presence of plasticity, with the known HRR fields describing the nature of the dominant singularity instead. Elguedj et al. [78] enriched the shape function basis with the HRR plastic singularity, achieving accurate estimations of standard fracture parameters. Such approach is further extended in this work to incorporate the role of relevant microstructural features (namely, GNDs) in crack tip fields through MSG plasticity. Shi and co-workers [73] characterized the stress-dominated asymptotic field around a mode I crack tip in MSG plasticity by solving iteratively through Runge-Kutta a fifth order Ordinary Differential Equation. The numerical shooting method was employed to enforce two crack-face stress-traction free conditions and subsequently obtain the power of the stress singularity, roughly  $r^{-2/3}$ . The power of the stress singularity in MSG plasticity is therefore independent of the strain hardening exponent  $N$ . This is due to the fact that the strain gradient becomes more singular than the strain near the crack tip and dominates the contribution to the flow stress in (3.4). From a physical viewpoint, this indicates that the density of GNDs  $\rho_G$  in the vicinity of the crack tip is significantly larger than the density of SSDs  $\rho_S$ .

Consequently, crack tip fields can be divided in several domains, as depicted in Fig. 3.3. Far away from the crack tip deformation is elastic and the asymptotic stress field is governed by the linear elastic singularity. When the effective stress overcomes the initial yield stress  $\sigma_Y$ , plastic deformations occur and the stress field is characterized

by the Hutchinson, Rice and Rosengren (HRR) [79, 80] solution. As the distance to the crack tip decreases to the order of a few microns, large gradients of plastic strain promote dislocation hardening and the stress field is described by the asymptotic stress singularity of MSG plasticity.

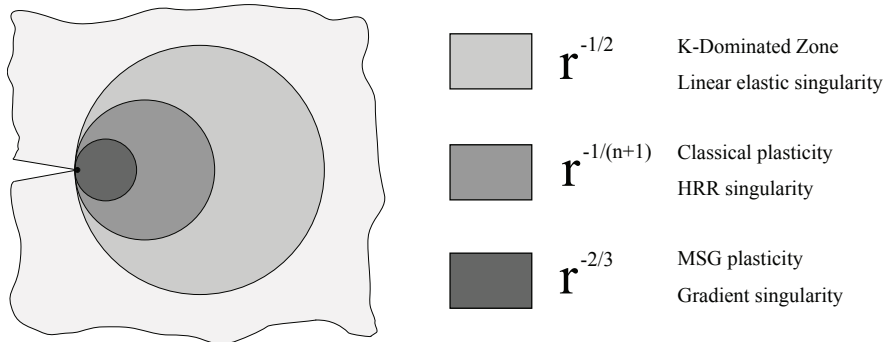


Figure 3.3: Schematic diagram of the different domains surrounding the crack tip. Three regions are identified as a function of asymptotic stress fields: the linear elastic solution, the HRR solution and the MSG plasticity solution.

A novel enrichment basis is therefore proposed, where the power of the stress singularity equals  $r^{-2/3}$ . As the angular functions play a negligible role in the overall representation of the asymptotic fields [81], the linear elastic fracture mechanics functions are employed. A direct consequence of the enrichment strategy adopted is the possibility of employing simpler meshes that do not need to conform to the crack geometry. In the present study, a level set representation [82] is used and the enrichment functions at any point of interest are computed using the finite element approximation of the level set functions.

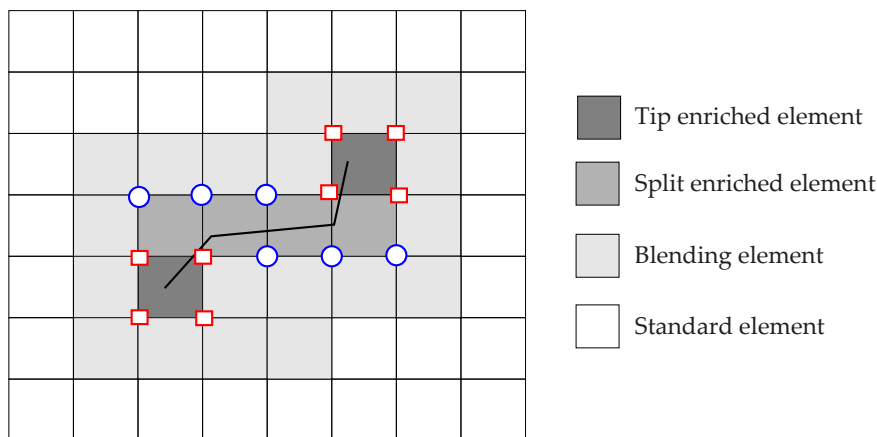


Figure 3.4: Typical X-FEM mesh with an arbitrary crack. Circled nodes are enriched with the discontinuous function while squared nodes are enriched with near-tip asymptotic fields.

Figure 3.4 shows a typical X-FEM mesh with an arbitrary crack. The enrichment zone is restricted to the vicinity of the crack tip. Elements can be classified into four categories: (a) standard elements; (b) tip enriched elements, (c) split enriched elements and (d) blending elements. The latter are elements at the interface of the standard and enriched elements where the partition of unity is not satisfied and oscillations in the results are observed. To overcome this pathological behavior, a linear weighting function is employed, as proposed by Fries [83]. Another commonly investigated problem associated with the XFEM is the numerical integration of singular and discontinuous integrands (c.f. Equations 3.38 - 3.40). One powerful and yet simple solution for the numerical integration is to partition the elements into triangles. Hence, such strategy is here adopted and the triangular quadrature rule is employed to integrate the terms in the stiffness matrix. Both *geometrical* (where a fixed area around the crack tip is enriched with singular functions) and *topological* (where only one layer of elements around the crack tip is enriched) enrichment approaches are considered.

An in-house code is developed in MATLAB where Newton-Raphson is employed as solution procedure for the non-linear problem. Stress contours are obtained by performing a Delaunay triangulation and interpolating linearly within the vertex of the triangles (integration points).

### 3.1.2.2 Verification

As shown in Fig. 3.5, a cracked plate of dimensions  $W = 35$  mm (width) and  $H = 100$  mm (height) subjected to uniaxial displacement is examined. Plane strain conditions are assumed and the horizontal displacement is restricted in the node located at  $x_1 = W$  and  $x_2 = H/2$  so as to avoid rigid body motion. The crack is horizontal and located in the middle of the specimen ( $H/2$ ) with the distance from the edge to the tip being 14 mm. The following material properties are adopted thorough the work:  $E = 260000$  MPa,  $\nu = 0.3$ ,  $\sigma_Y = 200$  MPa and  $N = 0.2$ , with isotropic hardening being defined by (3.36). A material length scale of  $l = 5$   $\mu\text{m}$  is considered, which would be a typical estimate for nickel [4] and corresponds to an intermediate value within the range of experimentally observed material length scales reported in the literature (see Table 1).

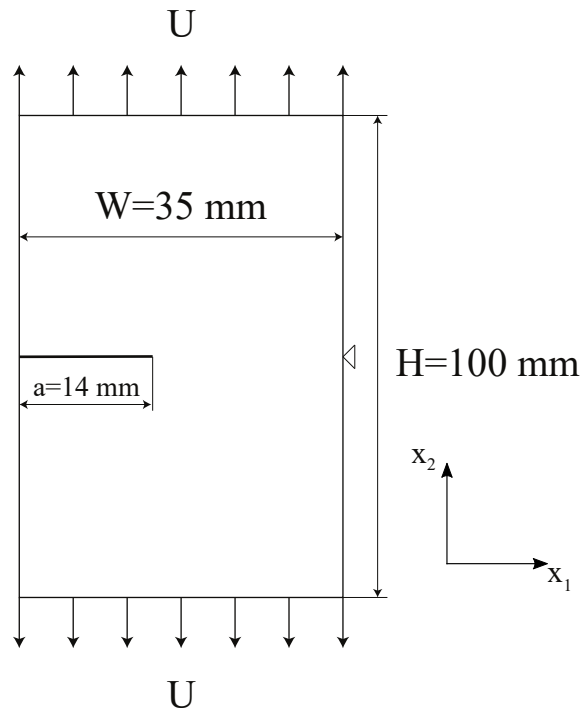


Figure 3.5: Single edge cracked plate: dimensions and boundary conditions.

Fig. 3.6 shows the results obtained by means of the standard FE method for different mesh densities. The legend shows the number of degrees of freedom (DOFs) intrinsic to each mesh, along with the characteristic length of the smallest element in the vicinity of the crack. Quadratic elements with reduced integration have been employed in all cases. The opening stress distribution  $\sigma_{22}$  ahead of the crack tip is shown normalized by the initial yield stress while the distance to the crack tip is plotted in logarithmic scale and normalized by the length scale parameter. Results have been obtained for an applied displacement of  $U = 0.0011 \text{ mm}$ . The prediction obtained for conventional plasticity is also shown in a fine black line and one can easily see that the strain gradient dominated zone is in all cases within  $r/l < 0.1$  (i.e.,  $0.5 \text{ }\mu\text{m}$ ) for the particular problem, material properties and loading conditions considered.

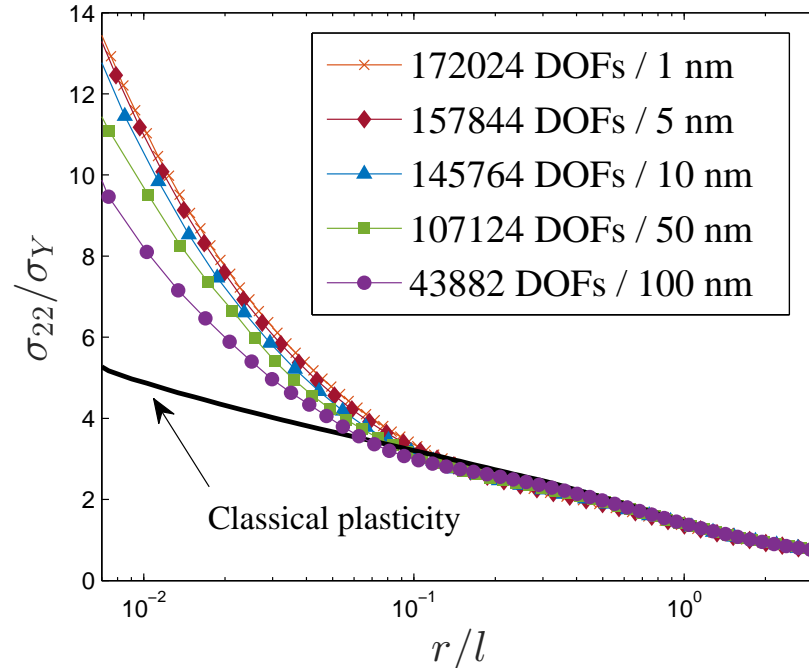


Figure 3.6: Normalized opening stress distribution ahead of the crack tip for different mesh densities, identified as a function of the total number of degrees of freedom (DOFs) and the characteristic length of the element at the crack tip. The figure shows results along the extended crack plane with the normalized distance to the crack tip  $r/l$  in log scale.

Fig. 3.6 reveals that numerical convergence has been achieved for a mesh with 157844 DOFs and a characteristic length of the smallest element of 5 nm, as further refinement in the crack tip region leads to almost identical results. This will be considered as the reference FE solution. A representative illustration of the mesh employed is shown in Fig. 3.7, where only half of the model is shown, taking advantage of symmetry. As it can be seen in the figure, special care is taken so as to keep an element ratio of 1 close to the crack tip while the mesh gets gradually coarser as we move away from the crack. The use of such small elements is not only very computationally expensive but it also leads to convergence problems as the elements at the crack tip get distorted. Avoiding such level of mesh refinement could strongly benefit fracture and damage assessment within strain gradient plasticity.

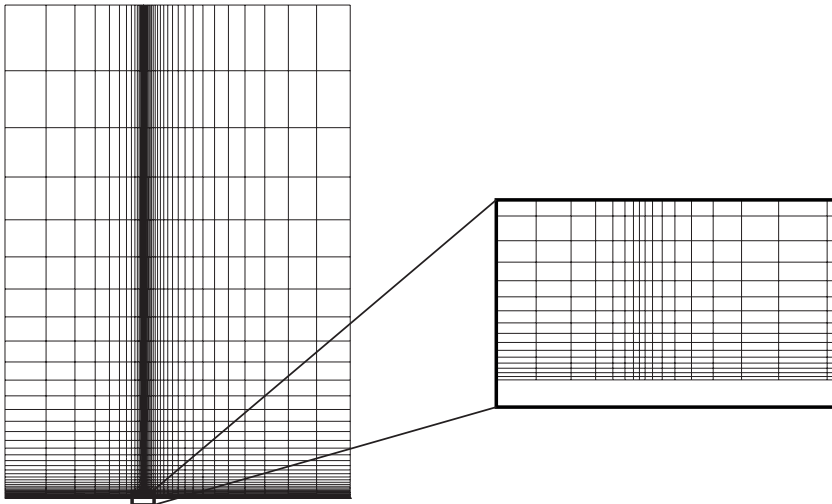


Figure 3.7: Representative finite element mesh, only the upper half of the model is shown due to symmetry.

The opening stress is subsequently computed in the cracked plate by means of the **X-FEM** framework described before. A much coarser mesh, relative to the conventional **FE** case, but with a similar uniform structure is employed, as depicted in Fig. 3.8. A tip element with a characteristic length of  $1 \mu\text{m}$  is adopted to ensure that the enriched region engulfs the gradient dominated zone.

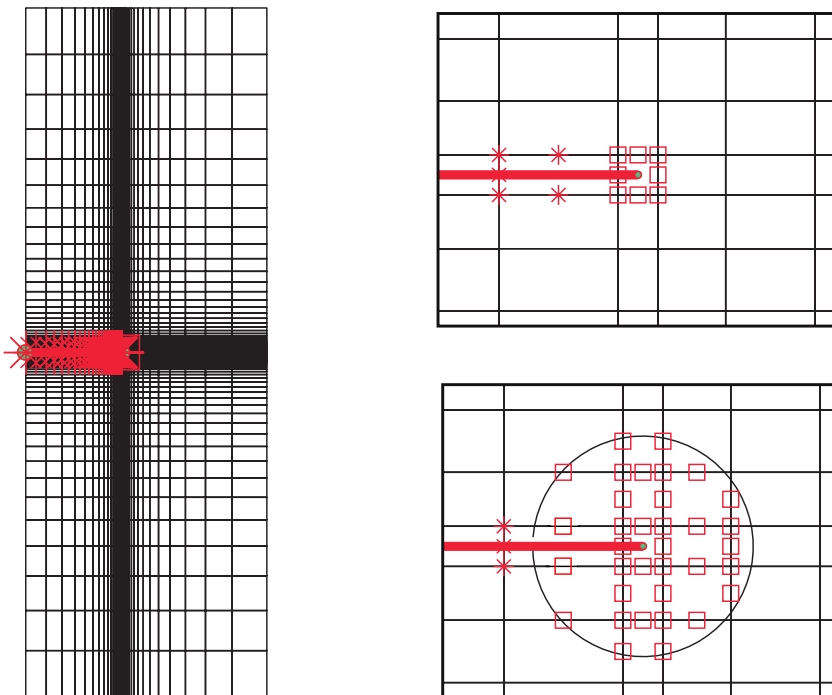


Figure 3.8: Mesh employed in the X-FEM calculations, schematic view and detail of the topological (top) and geometrical (bottom) enrichment regions.

Results obtained for both quadratic and linear elements are shown in Fig. 3.9. As in the conventional FE case, the normalized opening stress  $\sigma_{22}/\sigma_Y$  is plotted as a function of the normalized distance  $r/l$ , the latter being in logarithmic scale.

X-FEM predictions reveal a good agreement with the reference FE solution, despite the substantial differences in the number of degrees of freedom. Moreover, and unlike the conventional FE case, the influence of strain gradients can also be captured by means of linear quadrilateral elements. This enrichment-enabled capability allows the use of lower order displacement elements, minimizing computational efforts and maximizing user versatility. Further results have been consequently computed with linear elements.

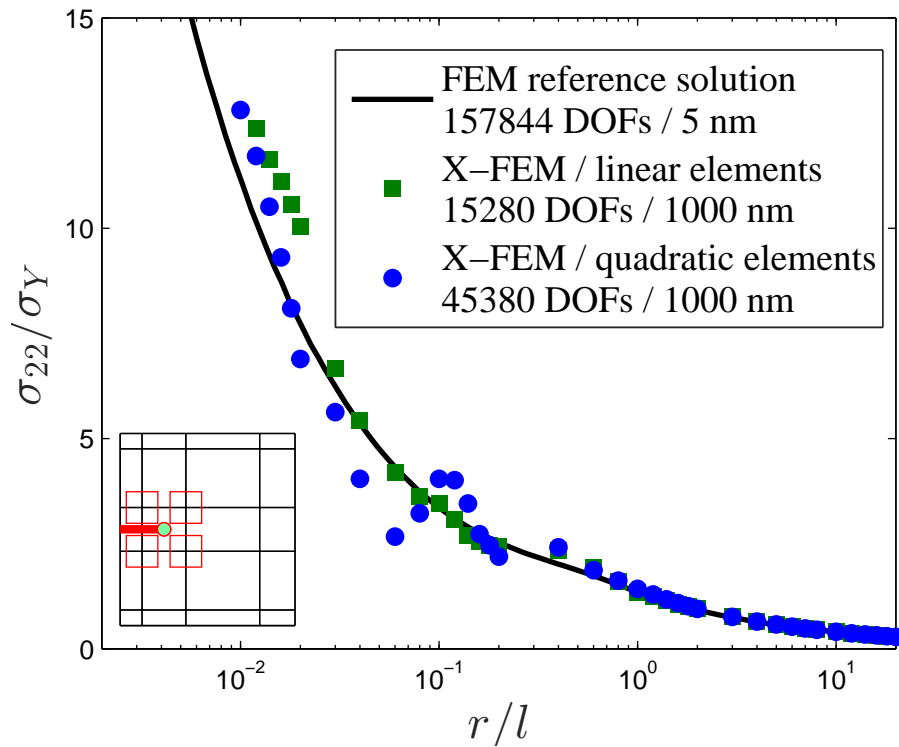


Figure 3.9: Normalized opening stress distribution ahead of the crack tip for topological enrichment, with both linear and quadratic elements and different mesh densities, identified as a function of the total number of degrees of freedom (DOFs) and the characteristic length of the element at the crack tip. The figure shows results along the extended crack plane with the normalized distance to the crack tip  $r/l$  in log scale.

The present gradient-enhanced X-FEM scheme thus shows very good accuracy for a characteristic element length that is two orders of magnitude larger than its standard FE counterpart. At the local level, small differences are observed in the blending elements, despite

the corrected X-FEM approximation adopted. Figure 3.10 shows the results obtained for a fixed geometrical enrichment radius and different mesh densities.

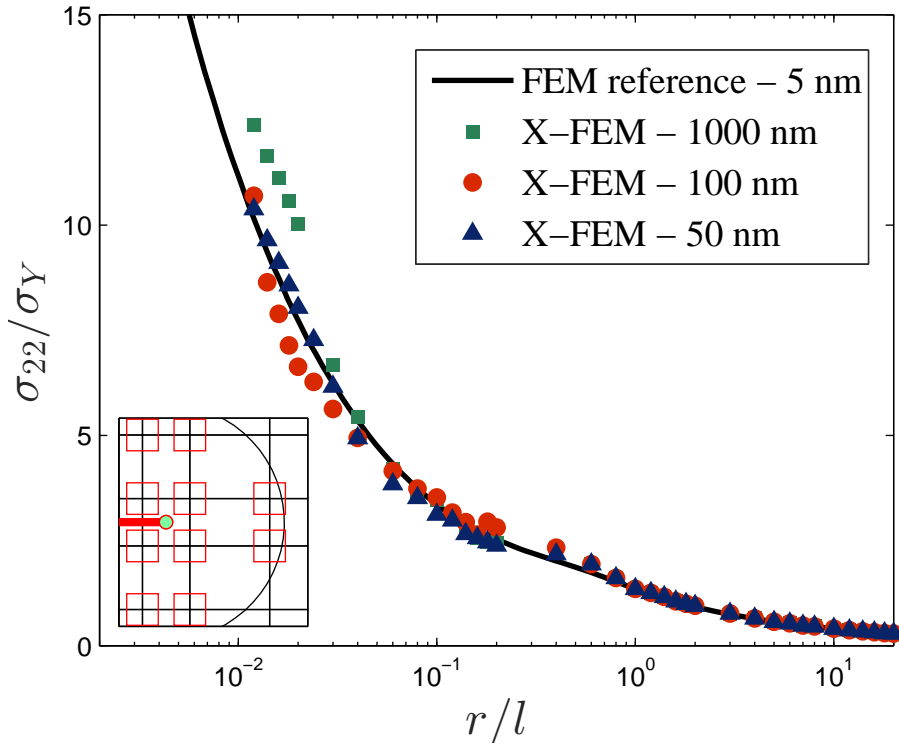


Figure 3.10: Normalized opening stress distribution ahead of the crack tip for geometrical enrichment with enrichment radius  $r_e = 0.5 \mu\text{m}$ , linear elements and different mesh densities, identified as a function of the characteristic length of the element at the crack tip. The figure shows results along the extended crack plane with the normalized distance to the crack tip  $r/l$  in log scale.

As in the topological case, a very promising agreement can be observed, with mesh densities being significantly smaller than the reference FE solution and computation times varying accordingly. A fixed enrichment radius of  $r_e = 0.5 \mu\text{m}$  is considered in all cases as the highest precision is achieved when the enriched area and the gradient dominated zone agree. Unlike pure linear elastic analyses, accounting for plastic deformations and the influence of GNDs implies having a crack tip region characterized by three different singular solutions (see Fig. 3.3). Ideally three classes of asymptotically-enriched nodes should be defined, but such an elaborated scheme is out of the scope of the present work. Hence, the size of the enriched domain must be selected with care to achieve convergence with coarser meshes. This limitation is also intrinsic to the seminal work by Elguedj et al. [78], where plasticity was confined to the HRR-enriched tip element. The size of the GND-dominated

region is nevertheless much less sensitive to material properties or the external load than the plastic zone, and can be properly chosen based on previous parametric studies [72].

Results reveal that the proposed **X-FEM** methodology largely outperforms the standard **FE** approach [84]. The present numerical scheme could therefore have important implications on the use of microstructurally-motivated models in large scale applications. The non-linear **X-FEM** code developed in MATLAB can be downloaded from [www.empaneda.com/codes](http://www.empaneda.com/codes).

### 3.2 PHENOMENOLOGICAL HIGHER ORDER SGP

The numerical framework developed for Fleck and Hutchinson's phenomenological **SGP** theory [13] is largely based on the work of Niordson and Hutchinson [51]. The higher order nature of the formulation entails several peculiarities in the numerical implementation. A special **FE** scheme is employed where plastic strains are treated as primary variables, higher order stresses are defined and additional boundary conditions are required.

For the sake of brevity, constitutive details of Fleck-Hutchinson (2001) formulation will not be given here. A comprehensive description can be found in Section 2.2 of Chapter 2 and in the original paper [13].

#### 3.2.1 Numerical method

A special kind of **FE** method is used where, in addition to the nodal displacement increments,  $\dot{U}^n$ , the nodal effective plastic strain increments,  $\dot{\varepsilon}_p^n$ , appear directly as unknowns. The displacement increments,  $\dot{u}_i$ , and the effective plastic strain increments,  $\dot{\varepsilon}_p$ , are interpolated within each element by means of the shape functions:

$$\dot{u}_i = \sum_{n=1}^{2k_u} N_i^n \dot{U}^n, \quad \dot{\varepsilon}_p = \sum_{n=1}^{k_p} M^n \dot{\varepsilon}_p^n \quad (3.41)$$

where  $k_u$  and  $k_p$  are the number of nodes used for the displacement and effective plastic strain interpolations, respectively. The components  $N_i^n$  ( $i = 1, 2; n = 1, \dots, 2k_u$ ) form the shape function matrix which, by multiplication with the array  $\dot{U}^n$  ( $n = 1, \dots, 2k_u$ ), gives the displacement field. Similarly, the equivalent plastic strain field is determined from the shape function matrix  $M^n$  and the array of nodal effective plastic strain increments  $\dot{\varepsilon}_p^n$ . Accordingly, the total strain in-

crements  $\hat{\epsilon}_{ij}$  and the incremental value of the gradient of the effective plastic strain  $\hat{\epsilon}_{p,i}$  are related to the nodal quantities by

$$\hat{\epsilon}_{ij} = \sum_{n=1}^{2k_u} B_{ij}^n \dot{U}^n, \quad \hat{\epsilon}_{p,i} = \sum_{n=1}^{k_p} M_{,i}^n \hat{\epsilon}_p^n \quad (3.42)$$

with  $B_{ij}^n = \frac{1}{2} (N_{i,j}^n + N_{j,i}^n)$  being the conventional strain-displacement matrix. By introducing the FE interpolation of the displacement and the effective plastic strain fields, and their appropriate derivatives, in the principle of virtual work, the following discretized system of equations is obtained:

$$\begin{bmatrix} \mathbf{K}_e & \mathbf{K}_{ep} \\ \mathbf{K}_{ep}^T & \mathbf{K}_p \end{bmatrix} \begin{bmatrix} \dot{U} \\ \hat{\epsilon}^p \end{bmatrix} = \begin{bmatrix} \dot{\mathbf{F}}_1 \\ \dot{\mathbf{F}}_2 \end{bmatrix} \quad (3.43)$$

Here,  $\mathbf{K}_e$  is the elastic stiffness matrix,

$$\mathbf{K}_e^{n,m} = \int_V (B_{ij}^n C_{ijkl} B_{kl}^m) dV \quad (3.44)$$

$\mathbf{K}_{ep}$  is a coupling matrix of dimension force

$$\mathbf{K}_{ep}^{n,m} = - \int_V (B_{ij}^n C_{ijkl} m_{kl} M^m) dV \quad (3.45)$$

and  $\mathbf{K}_p$  is the plastic resistance, a matrix of dimension energy

$$\mathbf{K}_p^{n,m} = \int_V \left( m_{ij} C_{ijkl} m_{kl} M^m M^n + h \left( M^m M^n + A_{ij} M_{,j}^m M_{,i}^n + \frac{1}{2} B_i \left( M_{,i}^m M^n + M^m M_{,i}^n \right) + C M^m M^n \right) \right) dV \quad (3.46)$$

with  $C_{ijkl}$  being the elastic stiffness,  $h$  the hardening coefficient, and  $A_{ij}$ ,  $B_i$  and  $C$  are coefficients that depend on the material length-scales  $l_i$  and the current stress state of the material (see Section 2.2 of Chapter 2 and [13]). The right-hand side of Eq. (3.43) is composed of the conventional external incremental force vector

$$\dot{\mathbf{F}}_1^n = \int_S \bar{T}_i N_i^n dS \quad (3.47)$$

and the incremental higher order force vector

$$\dot{\mathbf{F}}_2^n = \int_S \dot{t} M^n dS \quad (3.48)$$

In the elastic regime the plastic strain contribution is disabled by setting  $\mathbf{K}_{ep} = 0$  and the weight of  $\mathbf{K}_p$  is minimized by multiplying it by a small factor (e.g.  $10^{-8}$ ), preserving the non-singular nature of the global system. The latter numerical feature eliminates any

significant contribution to the solution of the nodal plastic strain increments on the current elastic-plastic boundary. This lack of constraint of plastic flow at the internal boundary can be physically interpreted as allowing dislocations to pass through it, as is the case in conventional plasticity (a detailed discussion can be found in [51]).

Based on a forward Euler scheme, when nodal displacement and effective plastic strain increments have been determined, the updated strains,  $\varepsilon_{ij}$ , stresses,  $\sigma_{ij}$ , higher order stresses,  $\zeta_i$ , and  $Q$  are computed at each integration point. A time increment sensitivity analysis is conducted to ensure that the numerical solution does not drift away from equilibrium.

### 3.2.2 Verification

#### 3.2.2.1 Infinitesimal deformation framework

Within a small strains scheme, the present numerical implementation is verified against the crack tip assessment results of Komaragiri et al. [28]. As in the previous section (see subsection 3.1.1.4), a remote  $K_I$  load is imposed by what is usually referred to as boundary layer formulation through enforcing displacements in the nodes located in the outer boundary. Following [28], a power law hardening relation between the stress  $\sigma$  and the gradient-enhanced effective plastic strain  $E^P$  of the type

$$\sigma = \sigma_Y \left( \frac{EE^P}{\sigma_Y} + 1 \right)^N \quad (3.49)$$

is adopted, with  $E$  being the Young's modulus,  $\sigma_Y$  the yield stress and  $n$  the strain hardening exponent. Plane strain conditions are assumed, with a Poisson ratio  $\nu = 0.3$  and a strain hardening exponent of  $N = 0.2$ . In order to compare with [28], the hydrostatic stress  $\sigma_H$  is computed ahead of the crack tip within the infinitesimal deformation theory for an external load of  $K_I = 150\sigma_Y\sqrt{l_1}$ .

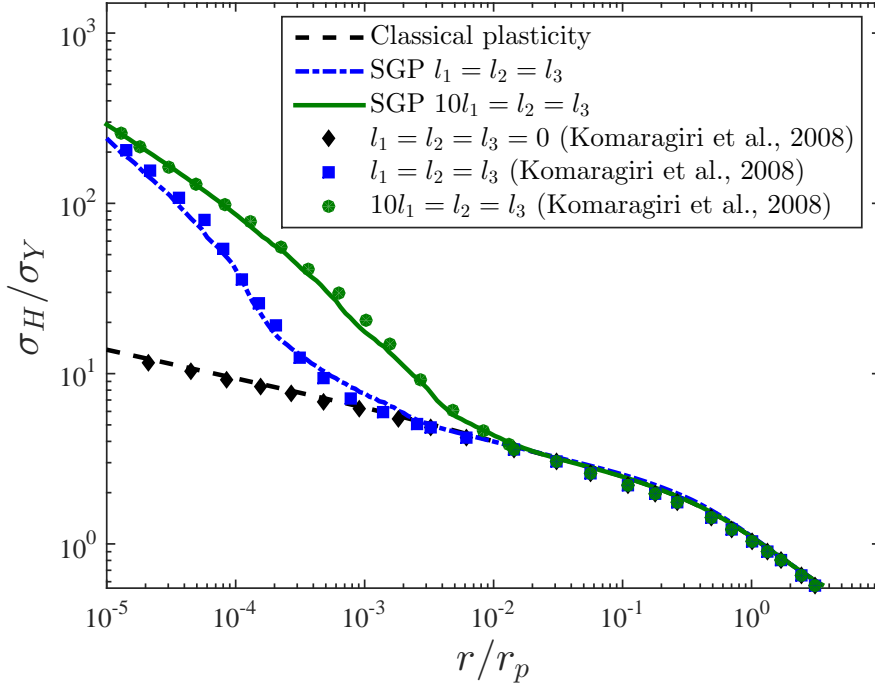


Figure 3.11: Hydrostatic stress distribution ahead of the crack-tip. Comparison of the numerical results of the present implementation (lines) with the predictions of Komaragiri et al. [28] (symbols) for different combinations of the length parameters.

Results obtained for different combinations of the length parameters are shown in Fig. 3.11, along with the digitalized results from Komaragiri et al. [28]. The distance to the crack tip  $r$  is normalized by the Irwin-type small scale yielding estimation of the plastic zone size

$$r_p = \frac{1}{3\pi} \left( \frac{K_I}{\sigma_Y} \right)^2 \quad (3.50)$$

A very good quantitative and qualitative agreement is observed, validating the present small strain numerical implementation.

### 3.2.2.2 Finite deformation framework

The numerical implementation of the finite strains generalization of Fleck-Hutchinson (2001) theory [13] is validated by establishing a comparison with the results obtained by Mikkelsen and Goutianos [30]. Within a mode I crack, Mikkelsen and Goutianos [30] investigated the relation between the plastic zone size  $r_p$  and the material length scales  $l = l_1 = l_2 = l_3$ , defining the interval where the ratio  $l/r_p$  leads to a solution within the elastic and conventional elasto-plastic bounds.

As in [30], the normalized opening stress  $\sigma_{\theta\theta}/\sigma_Y$  is obtained along the symmetry line in front of a blunted crack tip. A remote mode I load  $K_I$  is imposed by means of a boundary layer formulation and a very refined mesh is employed, with approximately 8000 quadrilateral quadratic plane strain elements. The size of the plastic zone is estimated following Irwin's approach (3.50) and the initial blunting radius is defined as  $r_{tip}/r_p = 0.05$ . An isotropic homogeneous material with  $\sigma_Y/E = 0.01$ ,  $\nu = 0.3$  and  $N = 0.2$  is studied, where a standard isotropic hardening power law is used with the hardening modulus  $h$  and the tangent modulus  $E_t$ ,

$$\frac{1}{h} = \frac{1}{E_t} - \frac{1}{E}, \quad E_t = \frac{E}{n} \left( \frac{E E P}{\sigma_Y} + 1 \right)^{N-1} \quad (3.51)$$

Results obtained by means of the present numerical implementation (lines) and those by Mikkelsen and Goutianos [30] (symbols) are shown in Fig. 3.12, with a very good agreement being attained.

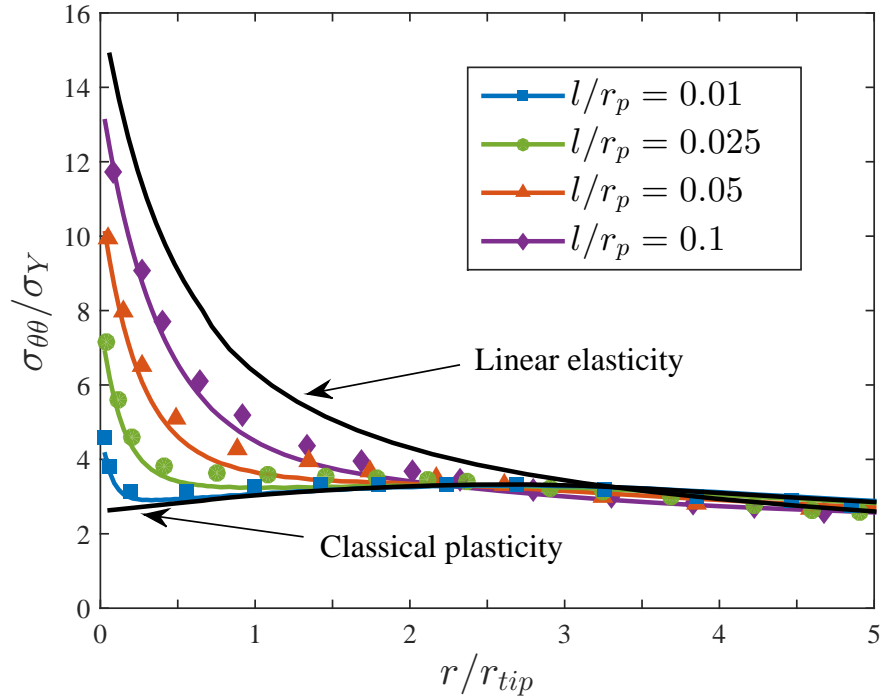


Figure 3.12: Opening stress distribution ahead of the crack-tip. Comparison of the numerical results of the present implementation (lines) with the predictions of Mikkelsen and Goutianos [30] (symbols) for different combinations of  $l/r_p$ , with  $l = l_1 = l_2 = l_3$ .

### 3.3 NUMERICAL MODELING OF ENERGETIC AND DISSIPATIVE SIZE EFFECTS

The class of **SGP** theories put forward by Gudmundson [6] and Gurtin and Anand [16] is numerically implemented following the

work by Nielsen and Niordson [85, 86]. As described in detail in Section 2.3, the formulation incorporates both energetic (or recoverable) and dissipative (or unrecoverable) higher order terms. The present numerical implementation builds upon the mathematical basis established by Fleck and Willis [65, 87].

A viscoplastic formulation is adopted with the aim of circumventing complications in the corresponding time-independent model associated with identifying active plastic zones (by, for instance, using image analysis, as proposed by Nielsen and Niordson [85, 86]). Within this framework, plastic dissipation is characterized through a visco-plastic potential

$$\mathcal{V}(\dot{E}^P, E^P) = \int_0^{\dot{E}^P} \Sigma(e, E^P) de \quad (3.52)$$

with  $\dot{E}^P$  denoting the gradient enhanced phenomenological effective plastic flow rate and  $\Sigma(\dot{E}^P, E^P)$  the effective stress, work conjugate to  $\dot{E}^P$  (see Section 2.3). The viscoplastic hardening rule is given by

$$\Sigma(\dot{E}^P, E^P) = \sigma_F(E^P) \left( \frac{\dot{E}^P}{\dot{\epsilon}_0} \right)^m \quad (3.53)$$

Here,  $m$  is the rate sensitivity exponent,  $\sigma_F(E^P)$  the current flow stress according to the hardening rule and  $\dot{\epsilon}_0$  the reference strain rate.

### 3.3.1 Minimum Principles

As described in detail by Fleck and Willis [65, 87], if the stresses and strains in the current state are known, the plastic strain rate field  $\dot{\epsilon}_{ij}^P$  in the subsequent increment satisfies the following minimum statement (Minimum Principle I):

$$\mathcal{H} = \inf_{\dot{\epsilon}_{ij}^P} \int_V \left( \mathcal{V}(E^P, \dot{E}^P) + \tau_{ijk} \dot{\epsilon}_{ij,k}^P - \sigma'_{ij} \dot{\epsilon}_{ij}^P \right) dV - \int_S t_{ij} \dot{\epsilon}_{ij}^P dS \quad (3.54)$$

where, as described in Section 2.3,  $t_{ij}$  are the higher order tractions and  $\tau_{ijk}$  is the higher order stresses, which decomposes into an energetic part,  $\tau_{ijk}^E$ , and a dissipative part,  $\tau_{ijk}^D$ .

If  $\dot{\epsilon}_{ij}^P$  is known from Minimum Principle I (3.54), the incremental solution for the displacement field  $\dot{u}_i$  can be determined by making use of Minimum Principle II: [87]

$$\mathcal{J}(\dot{u}_i) = \frac{1}{2} \int_V C_{ijkl} \left( \dot{\epsilon}_{ij} - \dot{\epsilon}_{ij}^P \right) \left( \dot{\epsilon}_{kl} - \dot{\epsilon}_{kl}^P \right) dV - \int_S \bar{T}_i \dot{u}_i dS \quad (3.55)$$

Here,  $C_{ijkl}$  denotes the elastic stiffness and  $\bar{T}_i$  the conventional tractions.

### 3.3.2 Numerical implementation

In accordance with the theoretical framework (see Section 2.3) plastic strains are employed - in addition to displacements - as nodal degrees of freedom.  $C_0$ -continuity finite elements can be adopted as the resulting differential equations are of second order. Thus, the following FE interpolation is used,

$$u_i = \sum_{n=1}^{N_{II}} N_i^n \dot{U}^n \quad (3.56)$$

$$\dot{\varepsilon}_{ij}^p = \sum_{n=1}^{N_I} M_{ij}^n \dot{\varepsilon}_p^n \quad (3.57)$$

The number of degrees of freedom (n) are denoted by  $N_{II}$  and  $N_I$ . The nodal values of the plastic strain components  $\dot{\varepsilon}_p^n$  are interpolated by means of shape functions one order lower than those employed for the nodal displacements  $\dot{U}^n$ , giving plastic and total strain fields the same degree of interpolation. Hence, quadratic shape functions  $N_i^n$  are used for the displacement field interpolation while linear shape functions  $M_{ij}^n$  are employed in the interpolation of the plastic strain field.

Focusing first on Minimum Principle I (3.54), stationarity of the functional ( $\delta \mathcal{H} = 0$ ) results in the following variational statement

$$\begin{aligned} & \int_V \left( q_{ij} \delta \dot{\varepsilon}_{ij}^p + \tau_{ijk}^D \delta \dot{\varepsilon}_{ij,k}^p \right) dV = \\ & \int_V \left( \sigma'_{ij} \delta \dot{\varepsilon}_{ij}^p - \tau_{ijk}^E \delta \dot{\varepsilon}_{ij,k}^p \right) dV + \int_S t_{ij} \delta \dot{\varepsilon}_{ij}^p dS \end{aligned} \quad (3.58)$$

That corresponds to the microscopic virtual power relation, on which the FE discretization is based. As setting to zero the first variation of the functional  $\mathcal{H}$  with respect to  $\dot{\varepsilon}_{ij}^p$  leads to the balance field equation (2.40) and the corresponding natural boundary conditions, proof of Minimum Principle I is given [87]. By introducing the FE interpolation, among the constitutive equations (Section 2.3), in the microscopic virtual work Eq. (3.58), that it must hold for all admissible variations, the discretized system of equations is obtained:

$$\begin{aligned} & \dot{\varepsilon}_p^n \left( \int_V \frac{\Sigma}{\bar{E}^p} \left( \frac{2}{3} \dot{\varepsilon}_{ij}^p M_{ij}^n M_{ij}^m + (L)^2 \dot{\varepsilon}_{ij,k}^p M_{ij,k}^n M_{ij,k}^m \right) dV \right) \\ & = \int_V \left( \sigma'_{ij} M_{ij}^n - \tau_{ijk}^E M_{ij,k}^n \right) dV + \int_S t_{ij} M_{ij}^n dS \end{aligned} \quad (3.59)$$

In a similar manner, a weak form suitable for numerical implementation can be obtained from the stationarity of the *macroscopic* functional (3.55),

$$\int_V C_{ijkl} \dot{\varepsilon}_{kl} \delta \dot{\varepsilon}_{ij} dV = \int_V C_{ijkl} \dot{\varepsilon}_{kl}^p \delta \dot{\varepsilon}_{ij} dV + \int_S \dot{T}_i \delta u_i dS \quad (3.60)$$

By requiring the variational statement to hold for any admissible field and accounting for the standard **FE** interpolation of the displacements and the strains, the *macroscopic* global system of equations is readily obtained

$$\begin{aligned} \dot{U}^n \left( \int_V B_{ij}^{mT} C_{ijkl} B_{kl}^n dV \right) = \\ \int_V B_{ij}^{mT} C_{ijkl} \dot{\varepsilon}_{kl}^p dV + \int_S \dot{T}_i N_i^m \end{aligned} \quad (3.61)$$

The solution procedure is described in Fig. 3.13. First, the incremental solution for the displacement and stress fields are obtained from Minimum Principle II for a given plastic strain field (in the first increment  $\varepsilon_{ij}^p = 0$  is assumed). Subsequently, the plastic strain rate field is obtained from Minimum Principle I by solving iteratively (3.59) until the relative norm of the change in the solution vector is below  $10^{-8}$ . The effective stress  $\Sigma$ , the microstress  $q_{ij}$  and the dissipative higher order stress  $\tau_{ijk}^D$  are computed in each iteration. Once convergence has been achieved, the current solution of the plastic strain field  $\varepsilon_{ij}^p$ , the gradient-enhanced plastic strain rate  $E^P$  and the energetic higher order stress  $\tau_{ijk}^E$  are updated. The numerical procedure is therefore staggered, unlike other **FE** schemes (e.g., Section 3.2), where the solution to all degrees of freedom is obtained at the same time (monolithic).

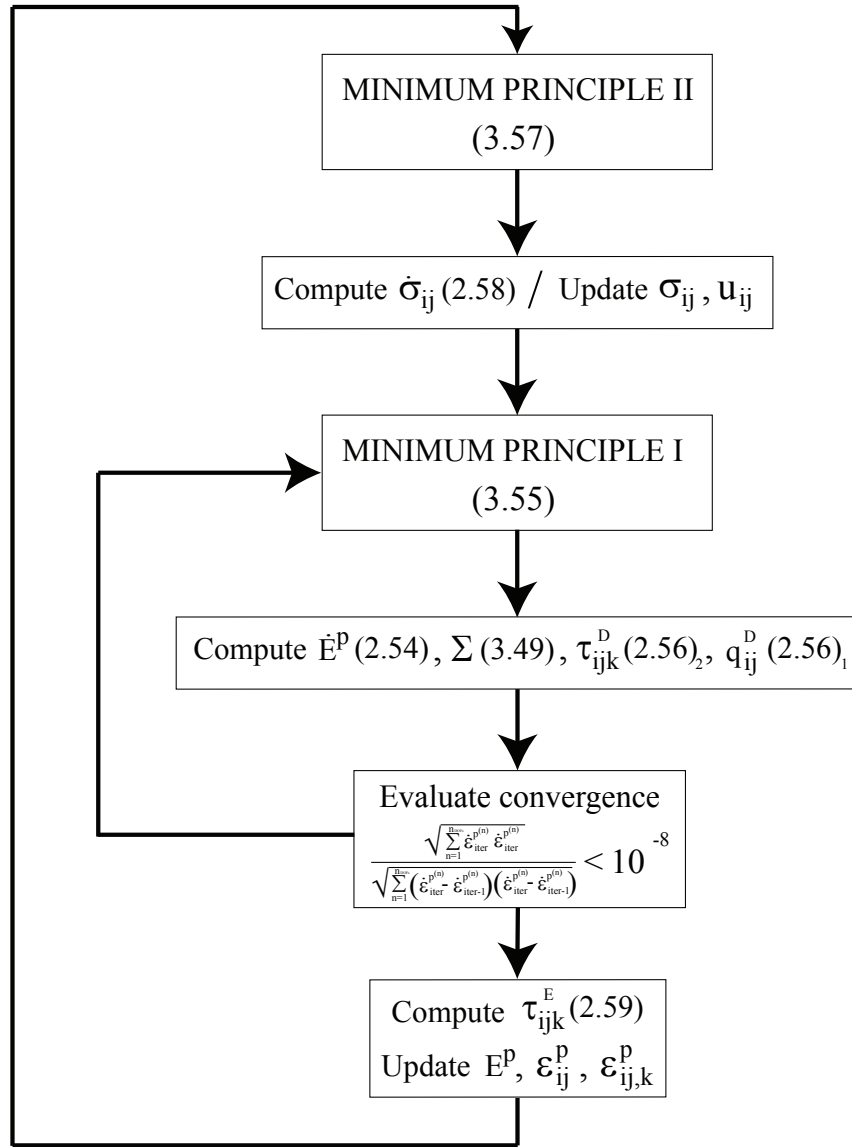


Figure 3.13: Outline of the staggered numerical procedure

General FE implementations of viscoplastic dissipative SGP based on the principle of virtual work (e.g., [88, 89]) solve for the time derivative of the plastic rate field. The main advantage of employing the minimum principle is that the plastic strain rate field is directly obtained from (3.59) in the context of dissipative gradient effects. This makes the numerical scheme more robust, enabling to accurately reproduce rate independent behavior by choosing an appropriately small rate sensitivity exponent. Despite adopting a Forward Euler scheme iterations are still needed to compute  $\dot{\epsilon}_{ij}^p$  since (3.59) is not a linear equation: the term  $\Sigma/\dot{E}^p$  depends on the plastic strain rate field. A time increment sensitivity analysis is conducted in all computations to ensure that the numerical solution does not drift away from the equilibrium configuration.

### 3.3.3 Verification

The numerical implementation is validated by comparing with the results of Nielsen and Niordson [85] for tensile loading of a clamped plate and Idiart et al. [90] for bending of thin foils. The former have been obtained by means of the rate-dependent formulation adopted as basis for the present implementation while numerical minimization procedures have been employed in the latter.

#### 3.3.3.1 Tensile loading of a clamped slab

Following [85], the behavior of an homogeneous finite slab clamped between rigid platens and subjected to tensile loading is examined. A square slab is considered ( $h = w$ ) and all the components of the displacement field are constrained at  $x_2 = h$  and  $x_2 = 0$  (see Fig. 3.14). A vertical displacement rate of  $\dot{\Delta} = h\dot{\epsilon}_0/10$  is imposed in the upper edge ( $x_2 = h$ ).

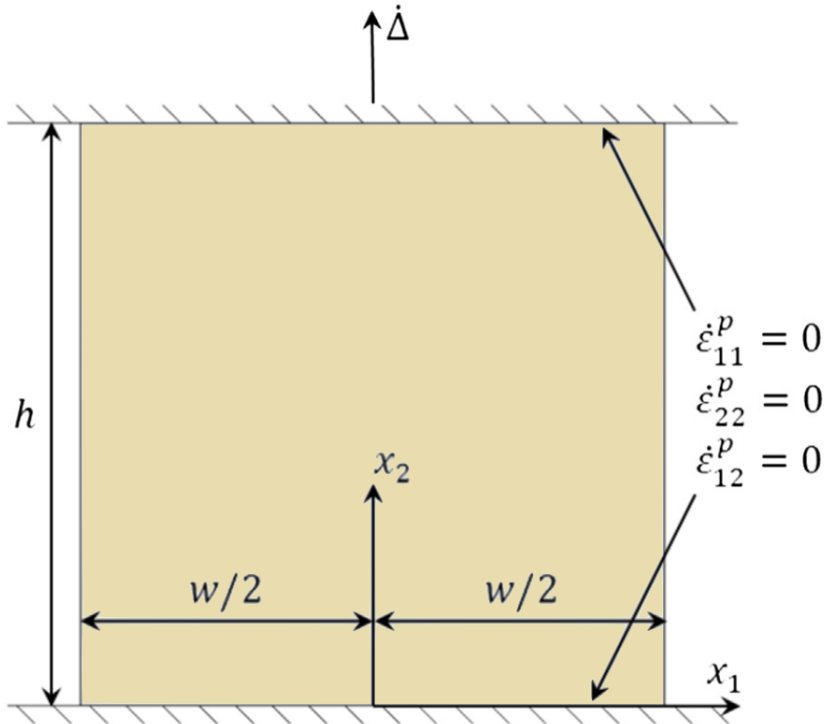


Figure 3.14: Geometry and boundary conditions for a finite slab of homogeneous material constrained between rigid platens. Adapted from [85].

An isotropic hardening law of the type,

$$\sigma_F(E^P) = \sigma_Y \left( 1 + \frac{E^P}{\sigma_Y/E} \right)^N \quad (3.62)$$

is adopted and, as in [85], the following material properties have been assumed:  $\sigma_Y/E = 0.001$ ,  $\nu = 0.3$ ,  $N = 0.1$  and  $\dot{\epsilon}_0 = 0.001$ .

A uniform mesh of 400 quadrilateral finite elements is employed. The results obtained by means of the present numerical implementation, along with those reported in [85], are shown in Fig. 3.15. Different values of length scale parameters and the rate sensitivity exponent have been considered. A very good agreement with the numerical results by Nielsen and Niordson [85] is observed in all cases.

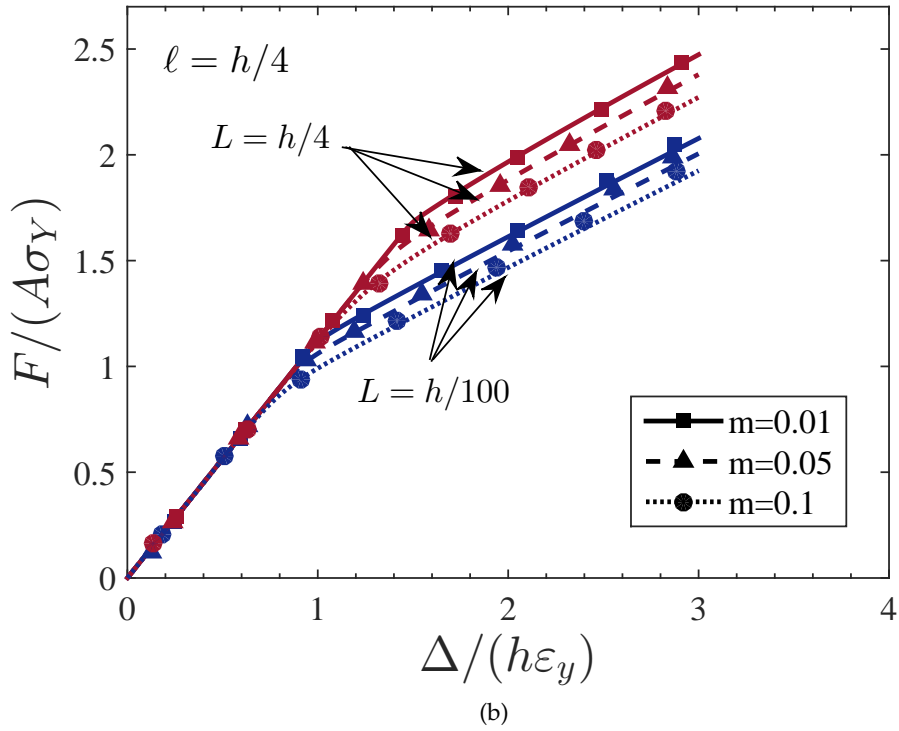
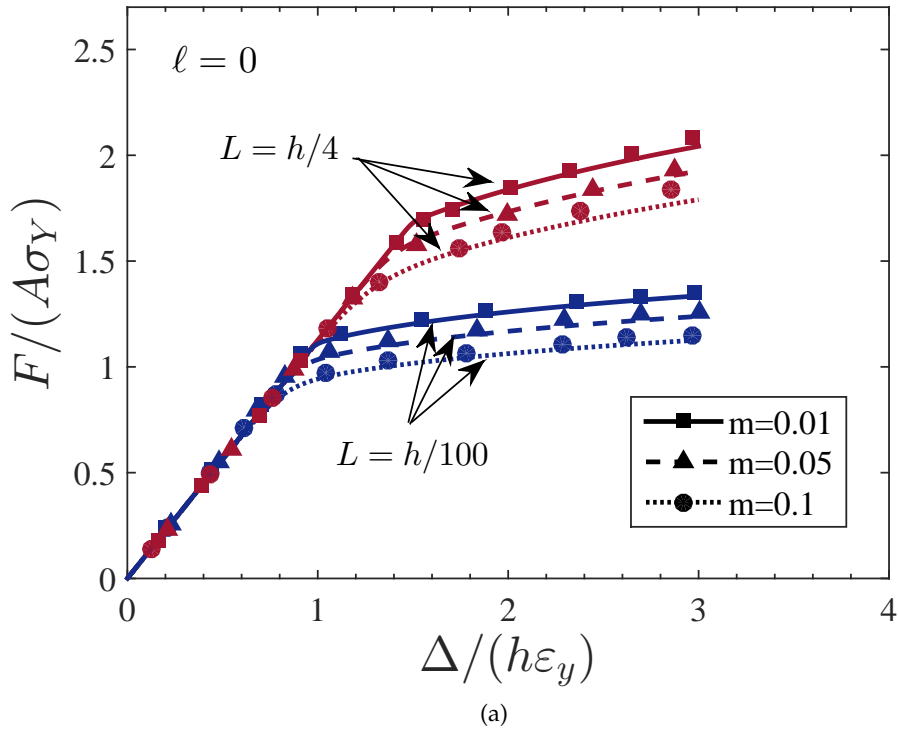


Figure 3.15: Material response curves for a clamped slab subjected to tensile loading. Numerical results from the present numerical implementation (lines) and Nielsen and Niordson [85] (symbols) for (a)  $\ell = 0$  and (b)  $\ell = h/4$  and different values of  $L$  and the rate sensitivity exponent  $m$ . Other parameters:  $A = wt$  and  $\varepsilon_y = \sigma_Y/E$ .

### 3.3.3.2 Microbending

As in [90], a foil of thickness  $2H$  and length  $2W$  subjected to bending is analyzed. As depicted in Fig. 3.16, illustrating the conventional boundary conditions, the longitudinal displacement component is prescribed at the foil ends according to

$$u_1 = x_2 x_1 \kappa \quad \text{at} \quad \pm W \quad (3.63)$$

where  $\kappa$  is the applied curvature. The higher order boundary conditions are microfree on the entire boundary, meaning that dislocations are free to exit the body.

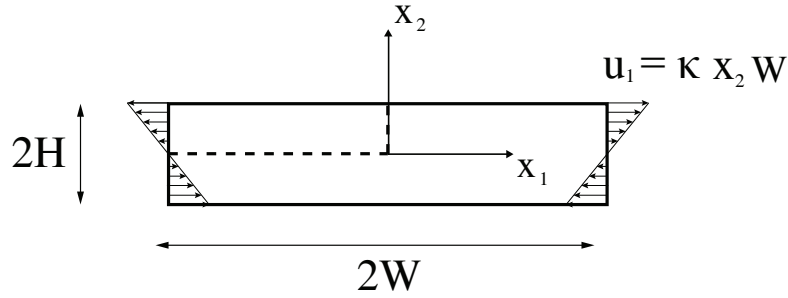


Figure 3.16: Bending of a thin foil: boundary conditions on the undeformed configuration

As the problem is essentially one-dimensional, the foil is modeled using a single column of 80 elements. Following the work by Idiart and co-workers [90] a perfectly plastic behavior is assumed with  $E = 1000\sigma_Y$ ,  $\nu = 0.3$ ,  $m = 0.2$ ,  $\dot{\epsilon}_0 = 0.001$  and  $\ell = 0$ . Different values of  $L$  will be considered to examine the role of the dissipative length scale. The foil is loaded at a rate of curvature  $\dot{\kappa}_0 = (\sqrt{3}\dot{\epsilon}_0/2H)$ , such that, in conventional bending, the most stretched material points would be loaded at a conventional effective plastic strain rate equal to  $\dot{\epsilon}_0$  when elastic strain increments vanish. Fig. 3.17 shows the normalized distribution of the axial stress along the foil thickness at a curvature level of  $(2H\kappa/\sqrt{3}) = 0.05$ . The predictions of the present numerical scheme (lines) reveal a good agreement with the results by Idiart et al. [90] (symbols).

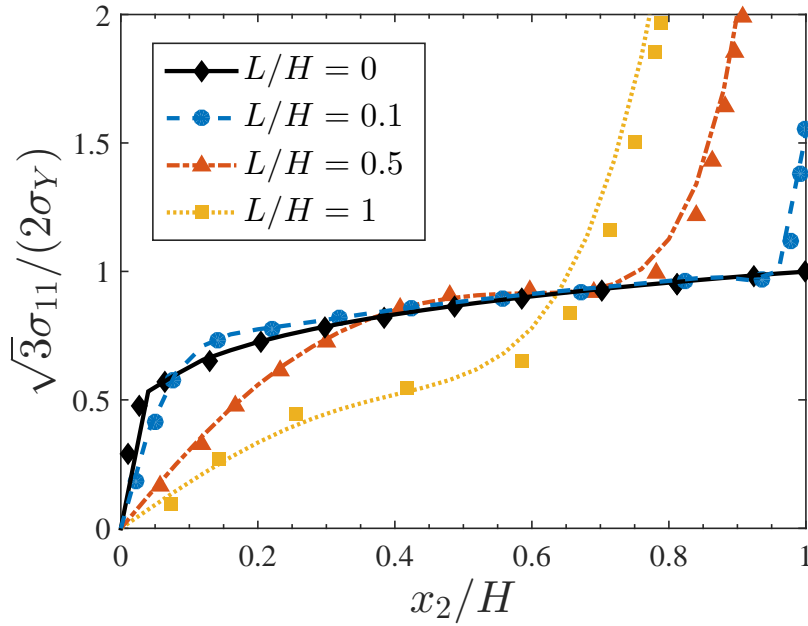


Figure 3.17: Distribution of axial Cauchy stress at  $(2H\kappa/\sqrt{3}) = 0.05$  obtained from the present numerical implementation (lines) and Idiart et al. [90] (symbols) for various values of  $L$ .

### 3.4 A FINITE ELEMENT BASIS FOR DGP

Despite the superior modeling capability of **DGP** with respect to **SGP**, the literature is scarce on the development of a general purpose **FE** framework for gradient plasticity theories accounting for the dissipation due to the plastic spin. Particularly, the use of higher-order dissipative terms - associated with strengthening mechanisms - is generally avoided due to the related computational complexities. This is the case of the very recent **FE** implementation of Poh and Peerlings [62] and the earlier work by Ostien and Garikipati [91], who implemented Gurtin (2004) [15] theory within a Discontinuous Galerkin framework. Energetic and dissipative contributions are both accounted for in the recent *ad hoc* **FE** formulation for the torsion problem by Bardella and Panteghini [59], also showing that, contrary to higher-order **SGP** theories, Gurtin (2004) **DGP** can predict some energetic strengthening even with a quadratic defect energy.

A general purpose **FE** framework for **DGP** is developed on the basis of an extension of the minimum principles proposed by Fleck and Willis [87]. The numerical scheme includes both energetic and dissipative higher order stresses and has been used to investigate several boundary value problems of particular interest for micron-scale metal plasticity (see Martínez-Pañeda et al. [60]).

### 3.4.1 Minimum Principles

A rate-dependent formulation is adopted since, otherwise, tracking the interaction and evolution of plastic zones may be complicated by, for instance, requiring image analysis, as proposed by Nielsen and Niordson [85, 86]. However, rate-independent behavior can also be accurately reproduced within the present FE framework by choosing an appropriately small rate sensitivity, as shown later in the validation example. As in section 3.3, the plastic dissipation is therefore accounted for through a visco-plastic potential

$$\mathcal{V}(\dot{\mathbf{E}}^P, \mathbf{E}^P) = \int_0^{\dot{\mathbf{E}}^P} \Sigma(e, \mathbf{E}^P) de \quad (3.64)$$

where  $\dot{\mathbf{E}}^P$  is the gradient enhanced phenomenological effective plastic flow rate and  $\Sigma(\dot{\mathbf{E}}^P, \mathbf{E}^P)$  is the flow resistance, work conjugate to  $\dot{\mathbf{E}}^P$  (see Section 2.4). In this work the following viscoplastic potential is adopted

$$\mathcal{V}(\dot{\mathbf{E}}^P, \mathbf{E}^P) = \frac{\sigma_F(\mathbf{E}^P) \dot{\epsilon}_0}{m+1} \left( \frac{\dot{\mathbf{E}}^P}{\dot{\epsilon}_0} \right)^{m+1} \quad (3.65)$$

and accordingly

$$\Sigma(\dot{\mathbf{E}}^P, \mathbf{E}^P) = \frac{\partial \mathcal{V}(\dot{\mathbf{E}}^P, \mathbf{E}^P)}{\partial \dot{\mathbf{E}}^P} = \sigma_F(\mathbf{E}^P) \left( \frac{\dot{\mathbf{E}}^P}{\dot{\epsilon}_0} \right)^m \quad (3.66)$$

with  $m$  denoting the rate sensitivity exponent,  $\sigma_F(\mathbf{E}^P)$  the current flow stress according to the hardening rule and  $\dot{\epsilon}_0$  the reference strain rate.

Hence, it is possible to define a *microscopic* minimum principle, given by the stationarity of the following functional

$$\mathcal{H}(\dot{\gamma}_{ij}^P) = \int_V \left( \mathcal{V}(\dot{\mathbf{E}}^P, \mathbf{E}^P) + \zeta_{ij} \dot{\alpha}_{ij} - \sigma_{ij} \dot{\epsilon}_{ij}^P \right) dV \quad (3.67)$$

such that, for a given stress state, the plastic distortion field  $\dot{\gamma}_{ij}^P$  can be obtained. Here, as described in Section 2.4 of Chapter 2,  $\sigma_{ij}$  denotes the Cauchy stress,  $\dot{\epsilon}_{ij}^P$  the plastic strains tensor,  $\zeta_{ij}$  the defect stress and  $\dot{\alpha}_{ij}$  Nye's tensor. The incremental solution for the displacements  $\dot{u}_i$  can be obtained, for a given plastic distortion field, by minimizing the following functional (*macroscopic* minimum principle):

$$\mathcal{J}(\dot{u}_i) = \frac{1}{2} \int_V C_{ijkl} \left( \dot{\epsilon}_{ij} - \dot{\epsilon}_{ij}^P \right) \left( \dot{\epsilon}_{kl} - \dot{\epsilon}_{kl}^P \right) dV - \int_S \dot{T}_i \dot{u}_i dS \quad (3.68)$$

where  $C_{ijkl}$  is the elastic stiffness and  $\dot{T}_i$  are the conventional tractions.

### 3.4.2 Numerical formulation and solution procedure

The numerical framework proposed leans on the novel mathematical principles (3.67) and (3.68). A special FE formulation is employed, where the plastic distortion components are treated as variables placing them on a footing similar to the displacements. Consequently, the following discretization is adopted

$$\dot{u}_i = \sum_{n=1}^{N_{II}} N_i^n \dot{U}^n \quad (3.69)$$

$$\dot{\gamma}_{ij}^p = \sum_{n=1}^{N_I} M_{ij}^n \dot{\gamma}_p^n \quad (3.70)$$

where  $n$  indicates the corresponding degree of freedom. Quadratic shape functions are used for the displacement field interpolation while linear shape functions are employed in the interpolation of the plastic distortion field. Here,  $\dot{U}^n$  and  $\dot{\gamma}_p^n$  refer to the nodal values of the unknown rate variables.

The weak form of the higher order balance equations corresponds to the stationarity of the *microscopic* functional (3.67)

$$\begin{aligned} & \int_V \left( q_{ij} \delta \dot{\epsilon}_{ij}^p + \omega_{ij} \delta \dot{\vartheta}_{ij}^p + \tau_{ijk} \delta \dot{\epsilon}_{ij,k}^p \right) dV \\ & = \int_V \left( \sigma'_{ij} \dot{\epsilon}_{ij}^p - \zeta_{ij} \delta \dot{\alpha}_{ij} \right) dV \end{aligned} \quad (3.71)$$

where the constitutive relations respectively relating the plastic strain gradients  $\dot{\epsilon}_{ij,k}^p$ , the plastic strains  $\dot{\epsilon}_{ij}^p$  and the plastic rotations  $\dot{\vartheta}_{ij}^p$  with the symmetric  $q_{ij}$  and skew-symmetric parts  $\omega_{ij}$  of the micro-stress  $S_{ij}$  and the higher order stress tensor  $\tau_{ijk}$ , have been accounted for (see Section 2.4 of Chapter 2). The discretized system of equations can be readily obtained by requiring the variational statement to hold for any admissible field and by considering again the aforementioned constitutive relations

$$\begin{aligned} & \dot{\gamma}_p^n \left( \int_V \frac{\Sigma}{\dot{\epsilon}_p} \left( \frac{2}{3} [\text{sym } M]_{ij}^n [\text{sym } M]_{ij}^m \right. \right. \\ & \quad \left. \left. + \chi [\text{skw } M]_{ij}^n [\text{skw } M]_{ij}^m + \frac{2}{3} L^2 [\text{sym } M]_{ij,k}^n [\text{sym } M]_{ij,k}^m \right) dV \right) \\ & = \int_V \left( \sigma'_{ij} [\text{sym } M]_{ij}^n - \tau_{ijk} [\text{curl } M]_{ij}^n \right) dV \end{aligned} \quad (3.72)$$

where  $\chi$  is the material parameter governing the dissipation due to the plastic spin and  $L$  is the dissipative length scale. Here the operators  $[\text{sym } M]_{ij}^n$ ,  $[\text{skw } M]_{ij}^n$ ,  $[\text{sym } M]_{ij,k}^n$  and  $[\text{curl } M]_{ij}^n$  contain the shape functions that deliver the discretizations of  $\dot{\epsilon}_{ij}^p$ ,  $\dot{\vartheta}_{ij}^p$ ,  $\dot{\epsilon}_{ij,k}^p$  and  $\dot{\alpha}_{ij}$ , respectively, from the nodal values of the plastic distortion  $\dot{\gamma}_p^n$ .

Such that, for a given node  $i$  and within a plastic strain setup, the relevant components of the plastic strain  $[\varepsilon_{11}^p{}^i, \varepsilon_{22}^p{}^i, \varepsilon_{12}^p{}^i, \varepsilon_{21}^p{}^i, \varepsilon_{33}^p{}^i]^T$ , the plastic spin  $[\vartheta_{12}^i, \vartheta_{21}^i]^T$ , the gradient of the plastic strain  $[\varepsilon_{11,1}^p{}^i, \varepsilon_{11,2}^p{}^i, \varepsilon_{22,1}^p{}^i, \varepsilon_{22,2}^p{}^i, \varepsilon_{12,1}^p{}^i, \varepsilon_{12,2}^p{}^i, \varepsilon_{21,1}^p{}^i, \varepsilon_{21,2}^p{}^i, \varepsilon_{33,1}^p{}^i, \varepsilon_{33,2}^p{}^i]^T$  and the Nye tensor  $[\alpha_{13}^i, \alpha_{23}^i, \alpha_{31}^i, \alpha_{32}^i]^T$  are obtained from the nodal plastic distortion components  $[\gamma_{11}^i, \gamma_{22}^i, \gamma_{12}^i, \gamma_{21}^i]^T$  by means of the following matrices:

$$[\text{sym } M]_{ij}^i = \begin{bmatrix} N_i & 0 & 0 & 0 \\ 0 & N_i & 0 & 0 \\ 0 & 0 & \frac{1}{2}N_i & \frac{1}{2}N_i \\ 0 & 0 & \frac{1}{2}N_i & \frac{1}{2}N_i \\ -N_i & -N_i & 0 & 0 \end{bmatrix} \quad (3.73)$$

$$[\text{skw } M]_{ij}^i = \begin{bmatrix} 0 & 0 & \frac{1}{2}N_i & -\frac{1}{2}N_i \\ 0 & 0 & -\frac{1}{2}N_i & \frac{1}{2}N_i \end{bmatrix} \quad (3.74)$$

$$[\text{sym } M]_{ij,k}^i = \begin{bmatrix} \frac{\partial N_i}{\partial x} & 0 & 0 & 0 \\ \frac{\partial N_i}{\partial y} & 0 & 0 & 0 \\ 0 & \frac{\partial N_i}{\partial x} & 0 & 0 \\ 0 & \frac{\partial N_i}{\partial y} & 0 & 0 \\ 0 & 0 & \frac{1}{2} \frac{\partial N_i}{\partial x} & \frac{1}{2} \frac{\partial N_i}{\partial x} \\ 0 & 0 & \frac{1}{2} \frac{\partial N_i}{\partial y} & \frac{1}{2} \frac{\partial N_i}{\partial y} \\ 0 & 0 & \frac{1}{2} \frac{\partial N_i}{\partial x} & \frac{1}{2} \frac{\partial N_i}{\partial x} \\ 0 & 0 & \frac{1}{2} \frac{\partial N_i}{\partial y} & \frac{1}{2} \frac{\partial N_i}{\partial y} \\ -\frac{\partial N_i}{\partial x} & -\frac{\partial N_i}{\partial x} & 0 & 0 \\ -\frac{\partial N_i}{\partial y} & -\frac{\partial N_i}{\partial y} & 0 & 0 \end{bmatrix} \quad (3.75)$$

$$[\text{curl } M]_{ij}^i = \begin{bmatrix} -\frac{\partial N_i}{\partial y} & 0 & \frac{\partial N_i}{\partial x} & 0 \\ 0 & \frac{\partial N_i}{\partial x} & 0 & -\frac{\partial N_i}{\partial y} \\ -\frac{\partial N_i}{\partial y} & -\frac{\partial N_i}{\partial y} & 0 & 0 \\ \frac{\partial N_i}{\partial x} & -\frac{\partial N_i}{\partial x} & 0 & 0 \end{bmatrix} \quad (3.76)$$

Following Niordson and Hutchinson [92], based on the known energetic stresses  $\sigma_{ij}$  and  $\zeta_{ij}$  for the current state, the incremental plastic distortion field is determined from the *microscopic* minimum principle (3.67) by solving the global system of equations (3.72). And

for a known plastic distortion rate field  $\dot{\gamma}_{ij}^p$ , the incremental solution for the displacement field is determined from the macroscopic minimum principle (3.68), as detailed in Section 3.3. In the present incremental procedure a Forward Euler time integration scheme is adopted and an iterative algorithm is implemented so as to ensure convergence in the computation of the plastic distortion rate field.

### 3.4.3 Verification

In order to validate the present numerical model, the simple shear of a constrained strip is analyzed so as to compare the results with those obtained by Bardella [61] from the minimization of the Total Complementary Energy functional in the deformation theory context. As in [61], a long strip of height  $H$  free from body forces is considered, with isotropic behavior and sheared between two bodies in which dislocations cannot penetrate. Hence, the displacement is fully constrained in the lower strip surface,  $u_1(x_2 = 0) = u_2(x_2 = 0) = 0$ , while the upper strip surface is subjected to uniform horizontal displacement  $u_1(x_2 = H) = \Gamma H$  with  $u_2(x_2 = H) = 0$ . Here,  $\Gamma$  is referred to as the applied strain, whose rate is assumed to be equal to the adopted reference strain rate ( $\dot{\Gamma} = \dot{\varepsilon}_0$ ). Since dislocations pile-up when they reach the strip lower and upper surfaces, the plastic distortion must be zero at  $x_2 = 0$  and  $x_2 = H$ . The problem is essentially one-dimensional, so that the strip, unbounded along both the shearing direction  $x_1$  and the  $x_3$  direction, is modeled using a single column of 80 plane strain quadrilateral elements along the strip height ( $H$ ) with appropriate boundary conditions at the sides of the column ( $u_2 = \gamma_{11} = \gamma_{22} = 0 \ \forall x_2$ ).

As in [61], the following hardening law is used:

$$\sigma_F(E^p) = \sigma_Y \left( \frac{E^p}{\varepsilon_0} \right)^N \quad (3.77)$$

and the following material properties are assumed:  $\mu = 26.3$  GPa,  $\varepsilon_0 = 0.02$ ,  $\sigma_Y = 200$  MPa, and  $N = 0.2$ . Within the rate-dependent framework adopted, a reference strain rate of  $\dot{\varepsilon}_0 = 0.02 \text{ s}^{-1}$  is employed and the effect of the viscoplastic exponent  $m$  is studied in order to approach rate-independent behavior.

Fig. 3.18 shows the numerical results obtained for different combinations of the material parameter governing the dissipation due to the plastic spin,  $\chi$ , and the energetic and dissipative length scales, in terms of the ratios  $H/\ell$  and  $H/L$ , respectively. Discrete symbols represent the results obtained by Bardella [61] while solid lines ( $m = 0.05$ ), dashed lines ( $m = 0.1$ ), and dotted lines ( $m = 0.2$ ) show the results of the present FE implementation.

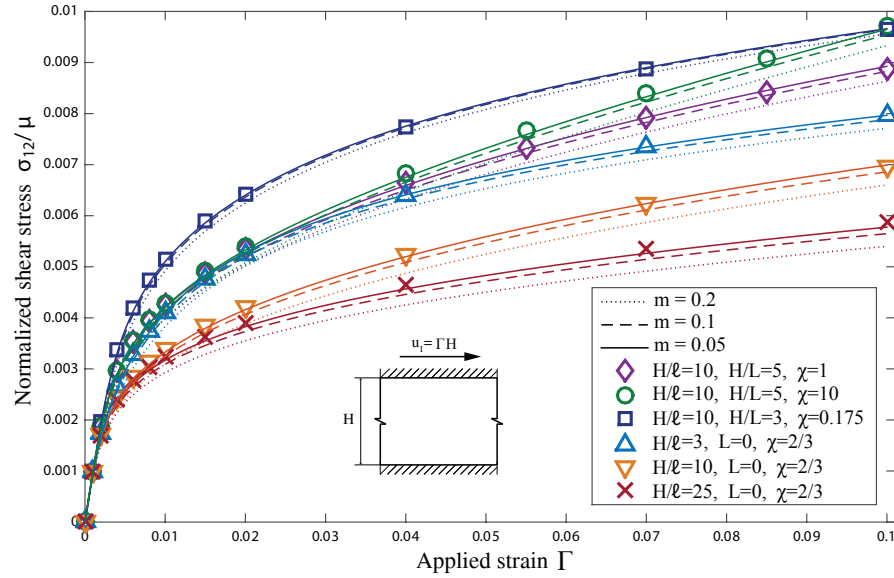


Figure 3.18: Simple shear of a constrained strip. Comparison of the numerical results of the present model (lines) with the predictions of Bardella [61] (symbols) for different values of  $H/\ell$ ,  $H/L$ , and  $\chi$ . Other material parameters are  $\sigma_Y = 200$  MPa,  $\varepsilon_0 = 0.02$ ,  $N = 0.2$ ,  $\mu = 26.3$  GPa, and  $\dot{\varepsilon}_0 = 0.02$  s<sup>-1</sup>.

As it can be seen in Fig. 3.18, the FE framework reproduces the results of Bardella [61] with a very good qualitative and quantitative agreement. Since the solution procedure presented in this paper rests on a rate-dependent approach, a very small amount of viscoplastic gradient effects have been included by choosing  $L/H = 0.01$  for the cases involving exclusively energetic gradient contributions ( $L = 0$ ) in [61]. This facilitates convergence of the proposed FE implementation and has a negligible effect on the mechanical response.

Part II

RESULTS



## MECHANISM-BASED CRACK TIP CHARACTERIZATION

---

### 4.1 INTRODUCTION

Motivation for exploring the effect of plastic strain gradients on crack tip tractions derives from deficiencies based on conventional plasticity theory concerning the maximum stress levels attained ahead of a growing crack surrounded by a plastic zone [27]. Conventional plasticity predicts a maximum normal stress ahead of the crack tip of about 2.6 times the initial yield stress for a mode I crack in a perfectly plastic material. Strain hardening gives rise to higher stresses but maximum values never exceed 4-5 times the yield stress for relevant values of the strain hardening exponent. Consequently, fracture occurring by cleavage or decohesion at the atomic scale in the presence of significant plastic flow (as observed experimentally by Elssner et al. [25] and Korn et al. [26]) remains a paradox, as atomic separation requires traction levels on the order of the theoretical lattice strength. As pointed out by Hutchinson [93], attempts to link macroscopic cracking to atomistic fracture are frustrated by the inability of classic continuum theories to model behavior adequately at the small scales involved in crack tip deformation [32]. SGP theories have the potential to bridge the gap between atomistic fracture and macroscopic cracking and several SGP formulations have been employed to characterize crack tip fields (see, e.g., [27, 28, 31–34]). However, the vast majority of studies have been conducted in the framework of the infinitesimal deformation theory, and although large deformations occur in the vicinity of the crack, little work has been done to investigate crack tip fields under SGP accounting for finite strains. Hwang et al. [71] developed a finite deformation framework for the MSG plasticity theory but they were unable to reach strain levels higher than 10% near the crack tip due to convergence problems. Pan and Yuan [35] used the element-free Galerkin method to characterize crack tip fields through a lower order gradient plasticity (LGP) model [94]. From a phenomenological perspective, Tvergaard and Niordson [29] analyzed the influence of strain gradients at a crack tip interacting with a number of voids while Mikkelsen and Goutianos [30] determined the range of material length scales where a full strain gradient dependent plasticity simulation is necessary.

Moreover, identifying and quantifying the relation between material parameters and the physical length over which gradient effects prominently enhance crack tip stresses is essential in rating their influence on crack-growth mechanisms, and for rationally applying [SGP](#) theories to predict damage and fracture. This has been done recently by Komaragiri et al. [28] for the phenomenological [SGP](#) theory of Fleck and Hutchinson [13] within a small strain framework. But, as the strain gradient contributes to the work hardening of the material, lowering crack tip blunting and significantly altering the stress distribution, it is imperative to quantify the distance ahead of the crack tip influenced by the plastic size effect accounting for finite strains.

This chapter is therefore devoted to numerically assess the influence of plastic strain gradients on the fracture process of metallic materials in the framework of small and large deformations through a mechanism-based [SGP](#) approach. An extensive parametric study is conducted and differences in the stress distributions ahead of the crack tip, relative to conventional plasticity, are quantified. Implications of the results on fracture and damage modeling are thoroughly discussed.

#### 4.2 CRACK TIP FIELDS WITH INFINITESIMAL STRAINS

Crack tip fields are evaluated in the framework of the finite element method by means of a boundary layer formulation, where the crack region is contained by a circular zone and a mode-I load is applied at the remote circular boundary through a prescribed displacement:

$$u(r, \theta) = K_I \frac{1 + \nu}{E} \sqrt{\frac{r}{2\pi}} \cos\left(\frac{\theta}{2}\right) (3 - 4\nu - \cos\theta) \quad (4.1)$$

$$v(r, \theta) = K_I \frac{1 + \nu}{E} \sqrt{\frac{r}{2\pi}} \sin\left(\frac{\theta}{2}\right) (3 - 4\nu - \cos\theta) \quad (4.2)$$

$u$  and  $v$  being the horizontal and vertical components of the displacement boundary condition, respectively;  $r$  and  $\theta$  the radial and angular coordinates of a polar coordinate system centered at the crack tip,  $E$  and  $\nu$  the elastic properties of the material, and  $K_I$  the stress intensity factor that quantifies the remote applied load.

The [CMMSG](#) theory will be employed to characterize crack tip fields accounting for the role of [GNDs](#) from a mechanism-based perspective. The material model is implemented in the commercial finite element package ABAQUS via its user-material subroutine UMAT. Since higher-order boundary conditions are not involved, the governing equations of the [CMMSG](#) theory are essentially the same as those in conventional plasticity. The plastic strain gradient is obtained

by numerical differentiation within the element: the plastic strain increment is interpolated through its values at the Gauss integration points in the isoparametric space and afterwards the increment in the plastic strain gradient is calculated by differentiation of the shape function. Another possible implementation scheme lies in using  $C^0$  finite elements incorporating the effect of the strain gradient as an extension of the classic FE formulation [95, 96].

Plane strain conditions are assumed and only the upper half of the circular domain is modeled because of symmetry. An outer radius of  $R=42$  mm is defined and the entire specimen is discretized using 1580 eight-noded quadrilateral plane-strain elements with reduced integration (CPE8R). As seen in Fig. 4.1, to accurately characterize the strain-gradient effect, a very fine mesh is used near the crack tip, where the length of the smallest element is approximately 10 nm.

To compare and validate the numerical implementation, the same material properties as those considered by Qu et al. [33] have been adopted. Thus, if the stress-strain relation in uniaxial tension can be written as:

$$\sigma = \sigma_{ref} f(\varepsilon^P) = \sigma_Y \left( \frac{E}{\sigma_Y} \right)^N \left( \varepsilon^P + \frac{\sigma_Y}{E} \right)^N \quad (4.3)$$

where  $\sigma_Y$  is the initial yield stress and  $N$  is the strain hardening exponent.  $\sigma_{ref} = \sigma_Y (E/\sigma_Y)^N$  is the assumed reference stress, and  $f(\varepsilon^P) = (\varepsilon^P + (\sigma_Y/E))^N$ ; the material parameters being  $\sigma_Y = 0.2\%$  of  $E$ ,  $\nu = 0.3$ ,  $N = 0.2$ ,  $m = 20$ ,  $b = 0.255$  nm, and  $\alpha = 0.5$ , which gives an intrinsic material length of  $l = 3.53$   $\mu\text{m}$  according to (2.10). Results are post-processed by means of *Abaqus2Matlab*, a novel piece of software that links the well-known FE package ABAQUS with MATLAB, the most comprehensive program for mathematical analysis [97].

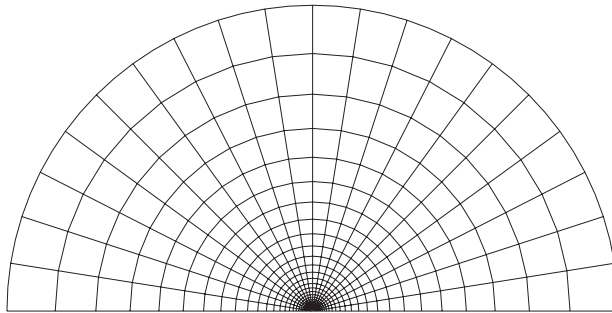


Figure 4.1: Finite element mesh for the boundary layer formulation

Fig. 4.2 shows the hoop stress  $\sigma_{\theta\theta}$  distribution ahead of the crack tip ( $\theta = 0^\circ$ ) under a remote load of  $K_I = 17.3\sigma_Y\sqrt{l}$  for both CMSG and classic plasticity theories;  $\sigma_{\theta\theta}$  is normalized with the material yield stress and the distance to the crack tip  $r$  ranges from 0.1  $\mu\text{m}$ ,

the lower limit of CMSG plasticity, to 100  $\mu\text{m}$ . As depicted in Fig. 4.2, the stress-field predicted by the CMSG theory agrees with the estimations of Hutchinson, Rice, and Rosengren (HRR) [79, 80] away from the crack tip, but becomes much larger within 1  $\mu\text{m}$  distance from it. Indeed, the stress level in the CMSG theory at  $r = 0.1 \mu\text{m}$  is equal to  $12\sigma_Y$ , which is high enough to trigger cleavage fracture as discussed in [33]. Results agree with those obtained by Qu et al. [33] and Jiang et al. [32] for the CMSG and MSG theories, respectively, proving that higher-order boundary conditions do not influence crack tip fields within its physical domain and thus validating the present numerical implementation.

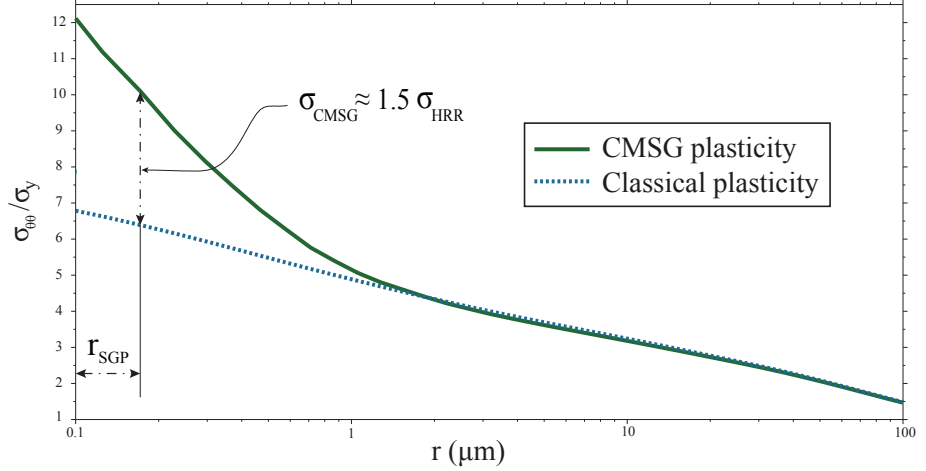


Figure 4.2:  $\sigma_{\theta\theta}$  distribution ahead of the crack tip for both CMSG and classic plasticity theories in small strains,  $r$  being the distance to the crack tip in log scale for  $K_I = 17.3\sigma_Y\sqrt{l}$ ,  $\sigma_Y = 0.2\%$  of  $E$ ,  $\nu = 0.3$ ,  $N = 0.2$  and  $l = 3.53 \mu\text{m}$

A parametric study covering several material properties, applied loads, and constraint conditions is conducted as a function of physical inputs to determine the influence of the strain gradient on crack tip fields. As shown in Fig. 4.2, with the aim of quantifying the size of the region that is affected by the plastic size effect, the distance over which the stress is significantly higher than that predicted by conventional plasticity ( $\sigma_{\text{CMSG}} > 1.5\sigma_{\text{HRR}}$ ) is defined by  $r_{\text{SGP}}$ . Differences between the stress field obtained at a given point in the crack tip region, for the CMSG theory ( $\sigma_{\text{CMSG}}$ ), and the HRR field ( $\sigma_{\text{HRR}}$ ) will depend on the following dimensionless terms:

$$\frac{\sigma_{\text{CMSG}}}{\sigma_{\text{HRR}}} = f\left(\frac{\sigma_Y}{E}, N, \nu, \frac{l}{R}, \frac{K_I}{\sigma_Y\sqrt{l}}\right) \quad (4.4)$$

The material properties considered in Fig. 4.2 are taken as reference values and its corresponding variables are denoted with an asterisk to avoid confusion. Moreover, to quantify the plastic size effect under different crack tip constraint conditions, the stress-fields are evalua-

ted through a modified boundary layer (MBL) formulation where the remote boundary is also dependent on the elastic T-stress [98]:

$$u(r, \theta) = K_I \frac{1+\nu}{E} \sqrt{\frac{r}{2\pi}} \cos\left(\frac{\theta}{2}\right) (3-4\nu - \cos\theta) + T \left(\frac{1-\nu^2}{E}\right) R \cos\theta \quad (4.5)$$

$$v(r, \theta) = K_I \frac{1+\nu}{E} \sqrt{\frac{r}{2\pi}} \sin\left(\frac{\theta}{2}\right) (3-4\nu - \cos\theta) - T \left(\frac{\nu(1+\nu)}{E}\right) R \sin\theta \quad (4.6)$$

Fig. 4.3a shows the size of the domain influenced by the strain gradient plotted as a function of the applied load for the same configuration and material properties as above with  $r_{SGP}$  normalized to the reference length scale  $l^*$  and the normalized applied stress intensity factor going from  $K_I = 30\sigma_Y^* \sqrt{l^*}$  to  $K_I = 300\sigma_Y^* \sqrt{l^*}$ . The trend described by  $r_{SGP}$  could be justified by the influence of geometrically necessary dislocations on plastic resistance. Since, as shown in (2.9) and (3.3), the plastic strain gradient  $\eta^p$  is an internal variable of the constitutive equation of the CMSG theory which acts to increase the tangent modulus, hence reducing the plastic strain rate. Therefore, the plastic size effect leads to additional hardening, which causes an increase of the stress level that is enhanced as the applied load increases. Maintaining small-scale yielding (SSY) conditions, three load levels are considered in the analysis of subsequent parameters:  $K_I = 0.12\sigma_Y^* \sqrt{R}$ ,  $K_I = 0.6\sigma_Y^* \sqrt{R}$  and  $K_I = 1.2\sigma_Y^* \sqrt{R}$ .

Fig. 4.3b shows the plots for the normalized relation between  $r_{SGP}$  and the material elastic properties for different values of the yield stress  $\sigma_Y$ . The results show that as the value of the yield stress increases, the length of the domain where crack tip fields are influenced by the size effect decreases. This is due to the fact that a higher value of  $\sigma_Y$  causes a reduction in plastic deformation, hence downsizing the interval in which the strain gradient influences the tangent modulus. Note also that while an increase in the value of  $\sigma_Y$  translates into a higher  $\sigma_{flow}$  in conventional plasticity, the magnitude of the term accounting for the strain-gradient effect in (2.9) is independent of the material yield stress since the intrinsic material length  $l$  (2.10) also depends on  $\sigma_Y$ .

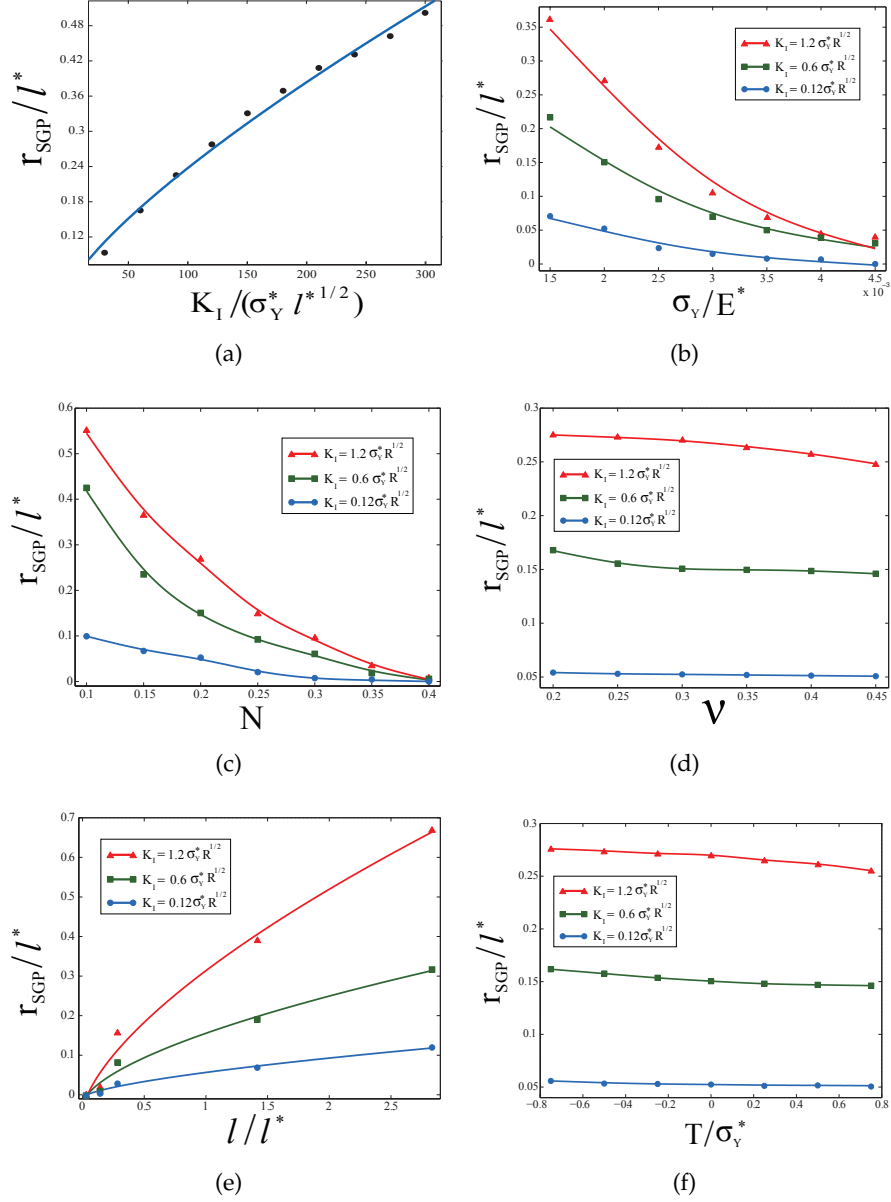


Figure 4.3: Distance ahead of the crack tip where the strain gradient significantly influences the stress distribution in small strains as a function of (a) applied load  $K_I$ , (b) yield stress  $\sigma_Y$ , (c) strain hardening exponent  $N$ , (d) Poisson's ratio  $\nu$ , (e) intrinsic material length  $l$  and (f) T-stress.

Fig. 4.3c illustrates the normalized distance over which the strain gradient significantly influences the stress distribution as a function of the strain hardening exponent  $N$ , with  $N$  values varying between 0.1 and 0.4. As seen in Fig. 4.3c, the higher the work hardening degree of the material the lower the extension of the influence of the plastic size effect on crack tip fields. Since, as shown by Shi et al. [73] for the MSG theory, and unlike the HRR field, the power of stress-singularity in CMSG plasticity is independent of  $N$ . This is

because the strain gradient becomes more singular than the strain near the crack tip, and it dominates the contribution to the flow stress in (2.9), implying that the density of geometrically necessary dislocations  $\rho_G$  around the crack tip is significantly larger than the density of statistically stored dislocations  $\rho_S$ .

Fig. 4.3d shows the variation of the normalized magnitude of the domain influenced by the size effect for different values of the Poisson's ratio  $\nu$  (0.2-0.45). The results show that an increase in the Poisson's ratio leads to a reduction in the extension of the differences caused by the plastic size effect. This is a result of the Poisson's ratio influence on plastic deformation and its weight on the intrinsic material length (2.10).

In Fig. 4.3e the normalized distance ahead of the crack tip where the strain gradient influences the stress distribution is plotted as a function of the intrinsic material length  $l$ . A range of values for  $l$  of 0.1-100  $\mu\text{m}$  is considered, since the scale at which the plastic size effect is observed is on the order of microns [39], and corresponds to the range of values that  $l$  can take according to (2.10) for material properties common to metals. As expected, higher values of  $l$  also result in higher values of  $r_{SGP}$  since the influence of the term associated with the strain gradient inside the square root in (2.9) increases.

Fig. 4.3f shows the variation of the normalized size of the domain influenced by the strain gradient for different constraint situations. As observed,  $r_{SGP}$  decreases as the constraint level increases because of the plastic-zone size dependence on the elastic T-stress [99]. However, the length of the domain where crack tip fields are influenced by the size effect shows very low sensitivity to different crack tip constraint conditions since changes on the T-stress value entail the same effect in both CMSG and HRR fields: negative T-stresses lead to a significant downward shift in the stress fields whereas positive values of T slightly increase the stress level near the crack.

### 4.3 CRACK TIP FIELDS WITH FINITE STRAINS

Stress distributions in the vicinity of the crack are obtained in the framework of the finite deformation theory. Rigid body rotations for the strains and stresses are conducted by the Hughes and Winget [100] algorithm and the strain gradient is obtained from the deformed configuration since the infinitesimal displacement assumption is no longer valid.

The initial configuration and the background mesh of the boundary layer formulation are shown in Fig. 4.4. A very fine mesh of 6134

CPE8R elements is used to obtain accurate results. As seen in Fig. 4.5, the hoop stress  $\sigma_{\theta\theta}$  distribution ahead of the crack line is obtained for both the CMSG and classic plasticity theories for the same material properties and loading conditions as in Fig. 4.2.

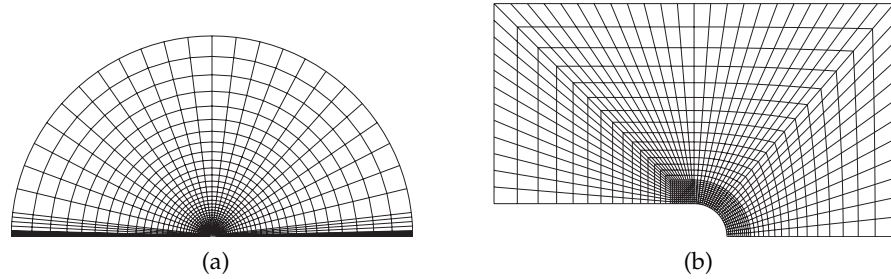


Figure 4.4: Finite element mesh for the boundary layer formulation under large deformations: (a) complete model and (b) vicinity of the crack

In classic plasticity large strains at the crack tip cause the crack to blunt, which reduces the stress triaxiality locally. However, because of the strain gradient contribution to the work hardening of the material, this behavior is not appreciated when the plastic size effect is considered. As proved by McMeeking [101], in conventional plasticity the crack opening stress reaches a peak at approximately the same distance from the crack tip as the onset of the asymptotic behavior of the plastic strain distribution. Therefore, as seen in Fig. 4.5, the strain gradient influences the stress distribution of the CMSG theory at approximately the same distance where a maximum of  $\sigma_{\theta\theta}$  is obtained in conventional plasticity, significantly increasing the differences between the stress distributions of the SGP and classic plasticity theories; the magnitude of the distance where these differences occur,  $r_{SGP}$ , is one order of magnitude higher than that presented in Fig. 4.2.

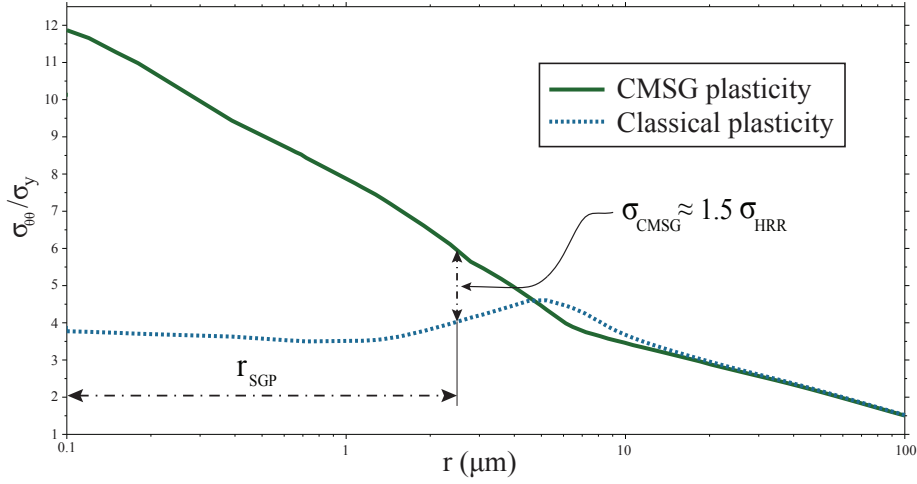


Figure 4.5:  $\sigma_{\theta\theta}$  distribution ahead of the crack tip for both CMSG and classic plasticity theories in large deformations,  $r$  being the distance to the crack tip in log scale for  $K_I = 17.3\sigma_Y\sqrt{l}$ ,  $\sigma_Y = 0.2\%$  of  $E$ ,  $\nu = 0.3$ ,  $N = 0.2$ , and  $l = 3.53 \mu\text{m}$

To quantify the domain of influence of the strain gradient under large deformations, a parametric study is conducted. Furthermore, with the aim of establishing a comparison, results are obtained in the framework of the infinitesimal deformation theory; mimicking material properties and loading conditions. The variation of the normalized distance over which the strain gradient significantly influences the stress distribution - as a function of material properties, constraint conditions, and the applied load - is plotted in Fig. 4.6. Following the work by McMeeking [101], a relation between the crack tip and outer radii ( $R/r = 10^5$ ) is considered and a sufficiently higher upper bound for the load range ( $K_I = 1.2\sigma_Y^*\sqrt{R}$ ) is chosen to ensure a final blunting five times larger than the initial radius. Since the same range of values used for each parameter in section 3 is also considered in this case, results obtained can be compared with those shown in Fig. 4.4.

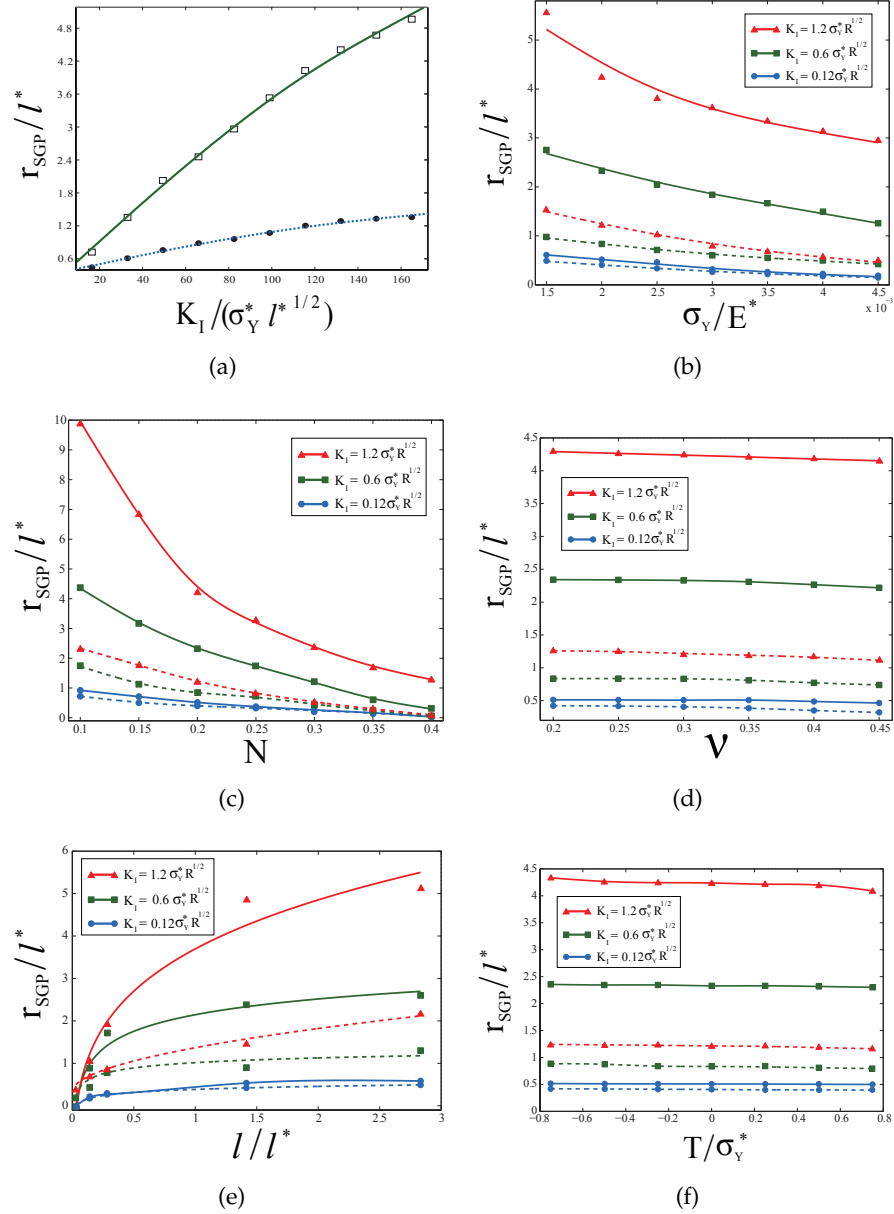


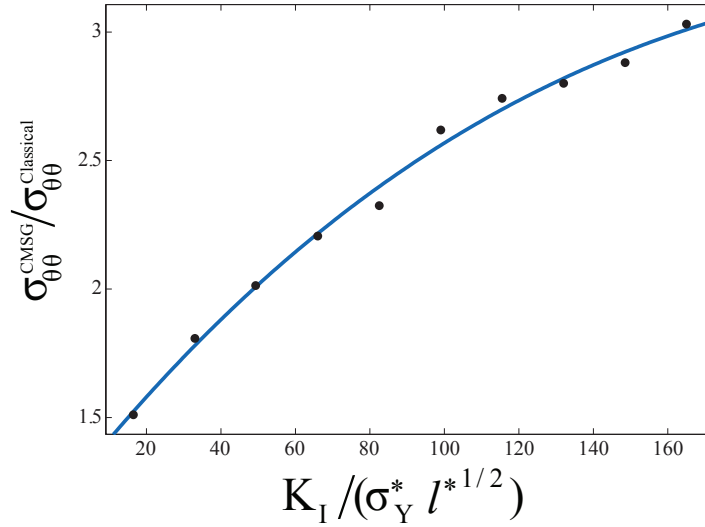
Figure 4.6: Distance ahead of the crack tip where the strain gradient significantly influences the stress distribution under small (dashed lines) and large (solid lines) strains as a function of (a) applied load  $K_I$ , (b) yield stress  $\sigma_Y$ , (c) strain hardening exponent  $N$ , (d) Poisson's ratio  $\nu$ , (e) intrinsic material length  $l$ , and (f) T-stress. The material properties considered in Fig. 4.2 are considered as the reference values (\*).

The trends shown in Fig. 4.6 for both large (solid lines) and small (dashed lines) strains are the same as those obtained for the parametric analysis in section 4.2. However, significantly higher values of  $r_{SGP}$  are obtained in all cases when large deformations are considered. These results reveal that even in the case of a very small load ( $K_I = 0.12\sigma_Y^*\sqrt{R}$ ), accounting for large strains brings a relatively

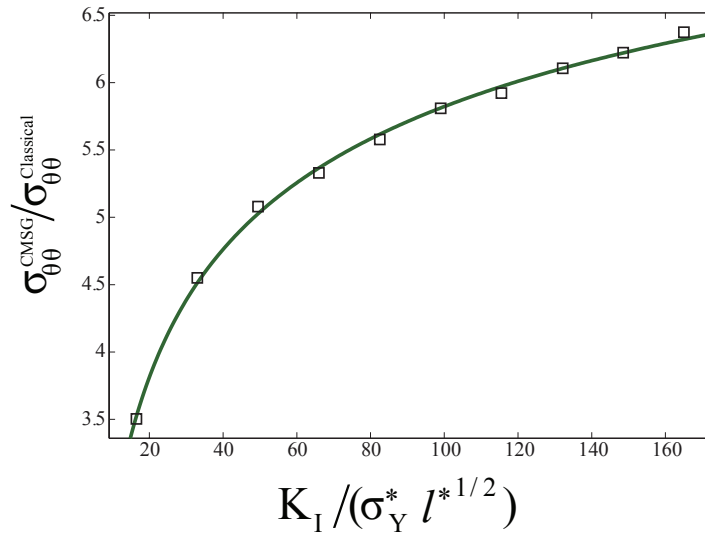
meaningful influence of the strain gradient. These differences with respect to the predictions that could be expected from the classic plasticity theory are much higher for load levels relevant to fracture and damage in metals ( $K_I = 0.6\sigma_Y^*\sqrt{R}$  and  $K_I = 1.2\sigma_Y^*\sqrt{R}$ ). Moreover, the results show a high sensitivity of the plastic size effect to the material properties and the applied load, so that a parametric study within the finite deformation theory is essential to rationally assess the need to incorporate an intrinsic material length in the continuum analysis.

#### 4.4 DISCUSSION

The parametric study shows that higher values of the applied load and the intrinsic material length increase the influence of the strain gradients on crack tip fields, whereas the opposite is true for the yield stress, the strain hardening exponent and the Poisson's ratio, being  $r_{SGP}$  less sensitive to the latter parameter. Results concerning the yield stress are especially relevant since the hydrostatic stress follows the same trends. Therefore, the plastic size effect could strongly influence the process of hydrogen embrittlement, which severely degrades the fracture resistance of high strength steels. This is due to the central role that the stress field close to the crack tip plays on both hydrogen concentration and interface decohesion [102]. Also, while results obtained within the infinitesimal deformation theory show that the effect of plastic strain gradient is negligible for higher values of  $\sigma_Y$ , which are common to high strength metallic alloys, strong differences arise between the stress fields of SGP and conventional plasticity theories when large strains are considered. This demonstrates the need to include the plastic size effect in the modelization of hydrogen-assisted cracking in metals. It is important to note that hydrogen-assisted damage occurs very close to the crack tip, the critical distance being lower than  $1 \mu\text{m}$  (see e.g. [36]) where the magnitude of stress elevation due to the influence of the strain gradient is significant. The ratio between CMSG and classic plasticity opening stress predictions is plotted in Fig. 4.7, where it can also be noticed that much higher values are obtained when large strains are considered.



(a)



(b)

Figure 4.7: Ratio between the  $\sigma_{\theta\theta}$  predictions of CMSG and classic plasticity at  $r = 0.1\mu\text{m}$  ahead of the crack tip ( $\theta = 0$ ) as a function of the applied load for (a) small strains and sharp crack and (b) large strains and blunted crack. The material properties are the same as those in Fig. 4.2

Previous works established that the domain where SGP effects can significantly elevate stresses over the HRR result for small strains was confined to distances less than  $10\ \mu\text{m}$  from the crack tip [28]. However, results shown in section 4.3 reveal that, when finite strains are considered, stress elevations persist to distances that could be one order of magnitude higher than those obtained within the infinitesimal deformation theory. This could have important implications on fracture and damage modeling of metals since the area where the strain gradient would significantly alter the crack

tip fields could span several voids ahead of the crack, and therefore influence various damage mechanisms that are characteristic of ductile fracture. Thus, results obtained from this work reveal that in the presence of a crack, near-tip stress elevation predicted by *SGP* theories could significantly influence the probability of cleavage fracture in ductile-to-brittle transition analyses [103], the prediction of stress-controlled nucleation of voids at large inclusions [104], the value of the parameters intrinsic to micromechanical failure models [105, 106] when fitted through a top-down approach, or the onset of damage in stress-related coalescence criteria [107]. This is unlike previous studies on cleavage fracture and void growth, which did not consider the influence of the plastic strain gradient in modelization.

Results concerning the *MBL* formulation (Figs. 4.3f and 4.6f) reveal that the aforementioned influence of the strain gradient on crack tip fields remains under different constraint conditions since the size of the domain where significant differences between the stress fields of the *SGP* and the conventional plasticity theories arise is almost insensitive to changes in the T-stress value.

#### 4.5 CONCLUSIONS

In this chapter, the influence of *MSG* plasticity on the fracture process of metallic materials has been numerically analyzed for both small and large deformations. The extensive parametric study conducted relates material properties, constraint scenarios, and applied loads with the physical distance ahead of the crack tip where the strain gradient significantly influences the stress distribution, thus identifying the conditions where the plastic size effect should be included in crack tip damage modeling.

Moreover, accounting for large strains and finite geometry changes in the numerical model reveals a meaningful increase in the domain influenced by the size effect, which may indicate the need to take into consideration the influence of the plastic strain gradient in the modeling of damage mechanisms, which has not been considered so far in the literature.



## ON FRACTURE IN FINITE STRAIN GRADIENT PLASTICITY

---

### 5.1 INTRODUCTION

Predictive modeling of fracture and damage requires an appropriate characterization of crack tip deformation. *SGP* theories provide a more accurate description than conventional continuum theories by incorporating certain microstructural features (*GNDs*) into the modeling. However, uncertainties remain and the complexities associated with experimental measurements within micrometers to the crack hinder model verification. A number of *SGP* formulations exist and the impact in crack tip characterization of the different constitutive prescriptions proposed must be examined. Moreover, as shown in Chapter 4, a quantitative estimation of the differences with conventional theories requires to incorporate finite strains and rotations into the modeling.

Isotropic *SGP* formulations can be classified according to different criteria, one distinguishing between phenomenological theories (e.g, [11, 13]) and microstructurally/mechanism-based ones [12, 14]<sup>1</sup>. These two main classes of *SGP* formulations are employed to thoroughly evaluate crack tip fields with the aim of gaining insight into the role of the increased dislocation density associated with large gradients in plastic strain near the crack. Differences between phenomenological and mechanism-based *SGP* models are examined and their physical implications discussed.

From a mechanism-based perspective, the lower order *CMSG* theory is employed as it allows for a very robust finite strain numerical implementation (see [72] and Chapter 4). As discussed thoroughly in [33, 73] and proven in Section 3.1.1.4, higher order boundary conditions have essentially no effect on the stress distribution at a distance of more than 10 nm away from the crack tip in *MSG* plasticity, well below the lower limit of physical validity of these theories. Results shown are therefore independent of the order of the formulation and the conclusions from the present comparative study apply to both Gao et al. [12] and Huang et al. [14] models. Consequently, following a common procedure in the literature (see, e.g., [95]), all

---

<sup>1</sup> Although *MSG* plasticity is built from Taylor's dislocation model, all the *SGP* theories considered in the present work are phenomenological in that they employ isotropic measures of the plastic strain and its gradient.

the results obtained from the [CMSE](#) theory are henceforth labeled as [MSG](#) plasticity. The constitutive and numerical frameworks employed are described in detail in Chapter 4 and Sections 2.1 and 3.1.

On the other hand, the higher order [SGP](#) theory proposed by Fleck and Hutchinson [13] is considered to model size effects in metal plasticity from a phenomenological perspective. The numerical implementation follows the methodology described in Section 3.2, with the large strains version being largely based on the finite strain generalization proposed by Niordson and Redanz [49] (see Section 2.2).

## 5.2 NUMERICAL RESULTS

### 5.2.1 *Infinitesimal deformation theory*

Crack tip fields are first assessed within the framework of the infinitesimal deformation theory with the aim of introducing the comparative study between theories. Two dimensional plane strain crack tip fields are evaluated by means of a boundary layer formulation, where the crack region is contained by a circular zone and the Mode I load  $K_I$  is applied at the remote circular boundary through prescribed horizontal  $v$  and vertical  $v$  displacements according to (4.1) and (4.2), respectively, as described in Chapter 4. Plane strain conditions are assumed and only the upper half of the circular domain is modeled due to symmetry. Different mesh densities were used to study convergence behavior, and it was found that 1600 eight-noded quadrilateral elements with reduced integration were sufficient to achieve mesh-independent results. As in Chapter 4, a very refined mesh is used near the crack tip with the aim of accurately characterizing the influence of the strain gradient, being the size of the elements on the order of nanometers. Unless otherwise stated, the following set of non-dimensional material parameters is considered in the present work

$$N = 0.2, \quad \frac{\sigma_Y}{E} = 0.2\%, \quad \nu = 0.3 \quad (5.1)$$

where  $\sigma_Y$  is the initial yield stress,  $E$  is Young's modulus,  $\nu$  is the Poisson ratio of the material and  $N$  is the strain hardening exponent. An isotropic power law material is adopted according to

$$\sigma = \sigma_Y \left( 1 + \frac{E \varepsilon^P}{\sigma_Y} \right)^N \quad (5.2)$$

In the phenomenological approach, the hardening curve is evaluated at  $E^P$  (the gradient-enhanced effective plastic strain rate in Fleck-Hutchinson theory) instead of  $\varepsilon^P$  as discussed in [13]. The reference stress of (2.8) will correspond to  $\sigma_{ref} = \sigma_Y \left( \frac{E}{\sigma_Y} \right)^N$  and

$f(\varepsilon^P) = (\varepsilon^P + \frac{\sigma_Y}{E})^N$ . Fig. 5.1 shows the opening stress distributions  $\sigma_{\theta\theta}$  ahead of the crack tip ( $\theta = 0^\circ$ ) obtained from classic plasticity, phenomenological SGP (both single length and multiple length parameter theories) and MSG plasticity. The stress values are normalized by the material yield stress while the horizontal axis is left unchanged, due to the central role that the magnitude of the domain ahead of the crack tip influenced by strain gradients plays on damage modeling. In the present study, a material length scale of  $l = 5 \mu\text{m}$  has been considered. This would be a typical estimate for nickel [4] and corresponds to an intermediate value within the range of experimentally observed material length scales reported in the literature (1-10  $\mu\text{m}$ , see Table 1).

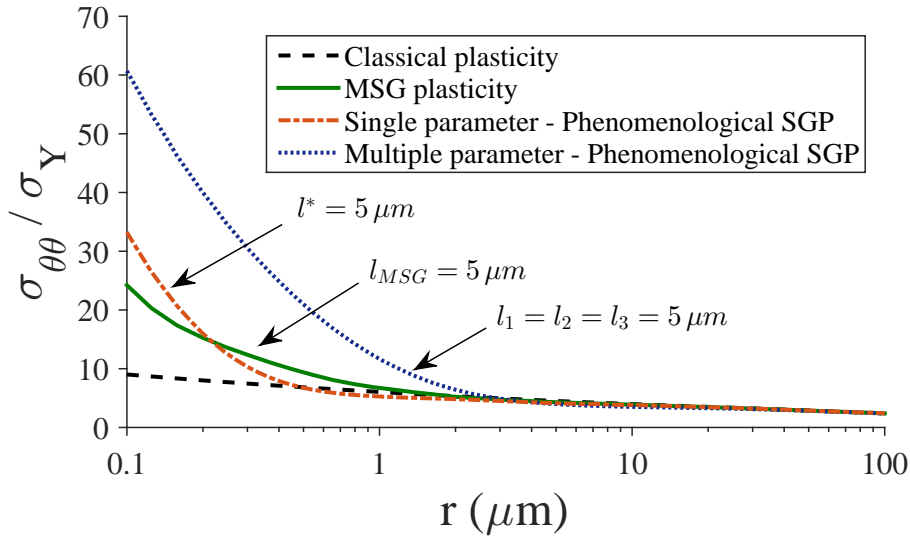


Figure 5.1: Small strain predictions of  $\sigma_{\theta\theta}$  ahead of the crack tip for classic plasticity and both mechanism-based and phenomenological SGP approaches. The figure shows results along the extended crack plane with the distance to the crack tip  $r$  in log scale for  $K_I = 25\sigma_Y\sqrt{l}$ ,  $\sigma_Y = 0.2\%E$ ,  $\nu = 0.3$ ,  $N = 0.2$  and material length scales of  $l^* = l_1 = l_2 = l_3 = l_{MSG} = 5 \mu\text{m}$

Results show that SGP stress predictions agree with classic plasticity away from the crack tip but become much larger within tens of microns from it. Fig. 5.1 reveals significant quantitative differences among theories for the same reference value of the material length scale. Within the phenomenological approach, the single length scale theory predicts much smaller size effects than the multiple parameter theory when all individual length scales  $l_i$  are set equal to  $l^*$ , as previously reported by Komaragiri et al. [28]. Furthermore, it is seen that the stress level attained near the crack tip from the phenomenological approach is much higher than MSG plasticity predictions, especially in the case of the multiple length scale theory. However,

the distance ahead of the crack tip where the stress distribution deviates from classic plasticity predictions is quite similar for the cases of MSG plasticity and the single parameter phenomenological theory, while a significantly larger size of the domain influenced by strain gradients is observed when the multiple length parameter theory is adopted.

### 5.2.2 *Finite deformation theory*

Since large strains take place in the vicinity of the crack, crack tip fields should be evaluated within the framework of the finite deformation theory in order to assess the influence of strain gradients in damage and fracture modeling. Moreover, the results shown in Chapter 4 (see also [72]) reveal a meaningful increase in the domain influenced by the plastic size effect when large strains are taken into account, as a consequence of the influence of strain gradients on the work hardening of the material. Following [101], a ratio between the radii of the outer boundary and the crack tip of  $R/r = 10^5$  is considered and, as in the small strain case, different mesh densities were evaluated in order to compute accurate results. As in Section 4.3, a very refined mesh is employed, where around 6200 eight-noded quadrilateral elements with reduced integration are generally used to achieve convergence.

Fig. 5.2 plots the normalized opening stress distribution under the same conditions as fig. 5.1 where, as in the small strains case, the distance to the crack tip  $r$  is shown in logarithmic scale. Results obtained with classic plasticity reproduce the well known behavior revealed by McMeeking [101], namely that large strains at the crack tip cause the crack to blunt, reducing the stress triaxiality locally. However, when size effects are included in the modeling, strain gradients increase the resistance to plastic deformation, lowering crack tip blunting and consequently, suppressing the local stress reduction. As it can be seen in the figure, a monotonic stress increase is still observed in SGP predictions and therefore the distance ahead of the crack tip where strain gradients severely influence the stress distributions increases significantly when compared to the small strain results.

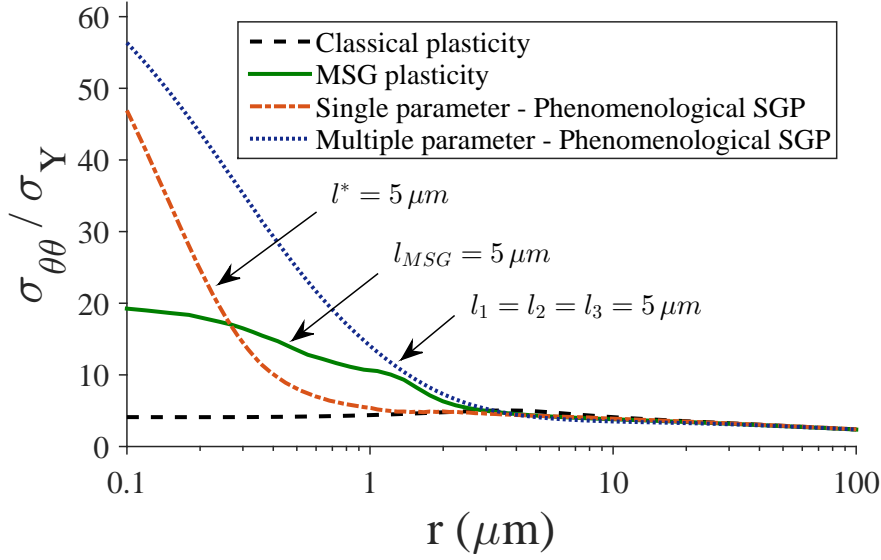


Figure 5.2: Finite deformation results for  $\sigma_{\theta\theta}$  ahead of the crack tip for classic plasticity and both mechanism-based and phenomenological SGP approaches. The figure shows results along the extended crack plane with the distance to the crack tip  $r$  in log scale for  $K_I = 25\sigma_Y\sqrt{l}$ ,  $\sigma_Y = 0.2\%E$ ,  $\nu = 0.3$ ,  $N = 0.2$  and material length scales of  $l^* = l_1 = l_2 = l_3 = l_{MSG} = 5 \mu m$ .

As in the small strain case, results shown in fig. 5.2 also reveal significant quantitative differences among SGP theories for the same reference material length scale. As in fig. 5.1, the single length parameter phenomenological theory predicts a smaller influence of GNDs when compared to the multiple parameter version, although the magnitude of stress elevation computed close to the crack tip from both theories is much closer when finite strains are taken into account. Both single and multiple length scale phenomenological theories predict much higher stress levels at the crack tip than MSG plasticity. However, the domain ahead of the crack tip where size effects alter the stress distribution in MSG plasticity is significantly greater in finite strains, close to the predictions obtained from the Fleck-Hutchinson multiple length parameter theory for the load level considered.

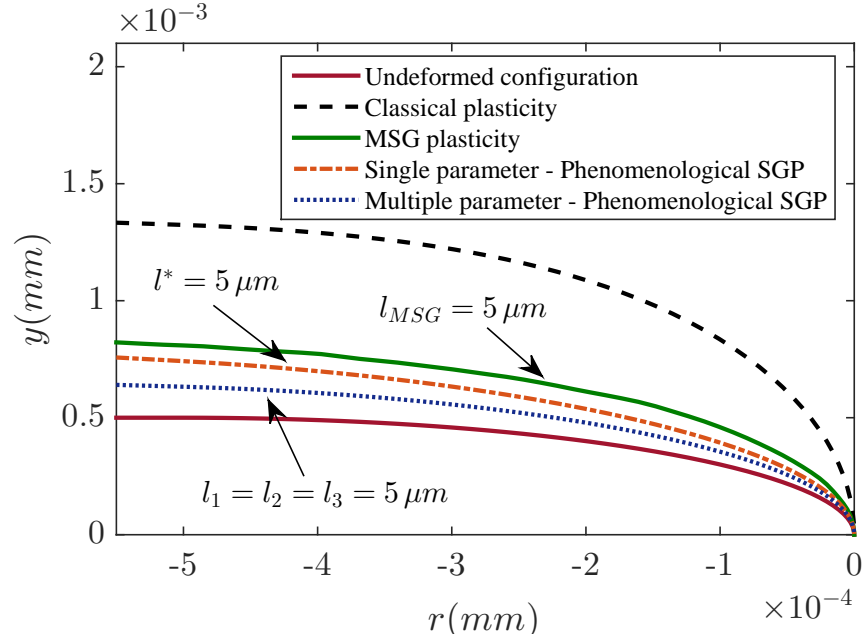


Figure 5.3: Initial and final crack tip blunting predicted by classic plasticity and both mechanism-based and phenomenological SGP approaches for  $K_I = 25\sigma_Y\sqrt{l}$ ,  $\sigma_Y = 0.2\%E$ ,  $\nu = 0.3$ ,  $N = 0.2$  and material length scales of  $l^* = l_1 = l_2 = l_3 = l_{MSG} = 5 \mu m$ .

Unlike classic plasticity, for all SGP stress distributions the maximum level of stress is achieved at the crack tip as a consequence of local hardening promoted by GNDs. Fig. 5.3 shows the degree of crack tip blunting under the same conditions as fig. 5.2 where it can be readily seen that blunting of the initial crack tip radius decreases significantly when size effects are included in the modeling. As the influence of strain gradients on crack tip fields persists all the way to the crack tip, essential differences arise when comparing with classic plasticity predictions in the blunting dominated zone. Hence, the magnitude of macroscopic stress elevation is much higher than that reported by previous studies, conducted within the infinitesimal deformation theory.

Figs. 5.4 and 5.5 quantify the differences from classic plasticity predictions as a function of (a) the external load and (b) the material length scale. Both the magnitude of stress elevation close to the crack tip and the physical length over which gradient effects significantly enhance crack tip stresses are evaluated. Figs. 5.4 and 5.5 show, respectively, the variation of the ratio of stress elevation  $\sigma_{SGP}/\sigma_{Classical}$  at  $r = 0.1 \mu m$  and  $r_{SGP}$ , the size of the domain ahead of the crack tip where the stress distribution significantly deviates from classic plasticity predictions ( $\sigma_{SGP} > 2\sigma_{Classical}$ ). In Fig. 5.4 stresses are sampled at  $r = 0.1 \mu m$  as it is considered the lower limit of physical validity of continuum SGP theories, while being suf-

ficiently close to the crack tip to provide representative results of interest for the modeling of several damage mechanisms. In both phenomenological and mechanism-based approaches the magnitude of stress elevation and the domain of influence of strain gradients monotonically increase with the external load and the value of the reference length scale parameter. For the higher load level considered the opening stress value at the crack tip is 15-25 times the estimation of classic plasticity, depending on the [SGP](#) theory considered, while the distance ahead of the crack where strain gradients significantly alter stress distributions spans several micrometers. One should note that a wide range of load levels of interest for damage modeling has been considered, with the largest load level roughly  $K_I \approx 100 \text{ MPa}\sqrt{\text{m}}$  for a typical steel of  $\sigma_Y = 400 \text{ MPa}$  and  $E = 200000 \text{ MPa}$ . Both the domain influenced by strain gradients and the ratio of stress elevation at the crack tip show sensitivity to the length scale parameter, especially for lower values of  $l$ . In fact, for high values of  $l$  both [MSG](#) plasticity and the phenomenological multiple length parameter theory predict an [SGP](#) influenced region bigger than the blunting dominated zone. Thus, for some particular combinations of  $l$ , applied load and material properties, the physical length over which strain gradients meaningfully enhance crack tip stresses spans several tens of micrometers. This may have important implications on fracture and damage modeling of metals since the critical distance of many damage mechanisms fall within this range.

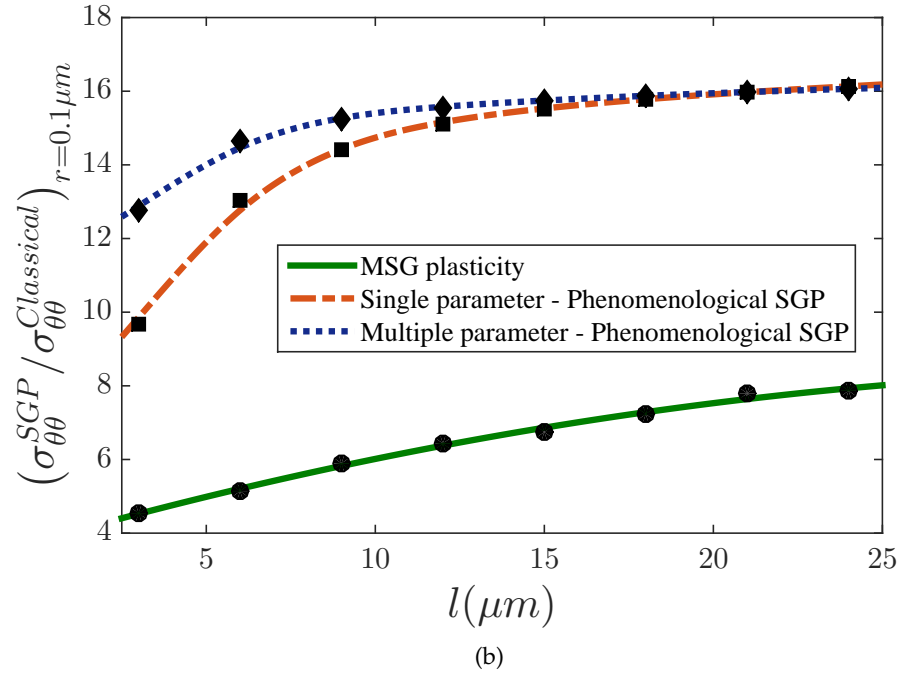
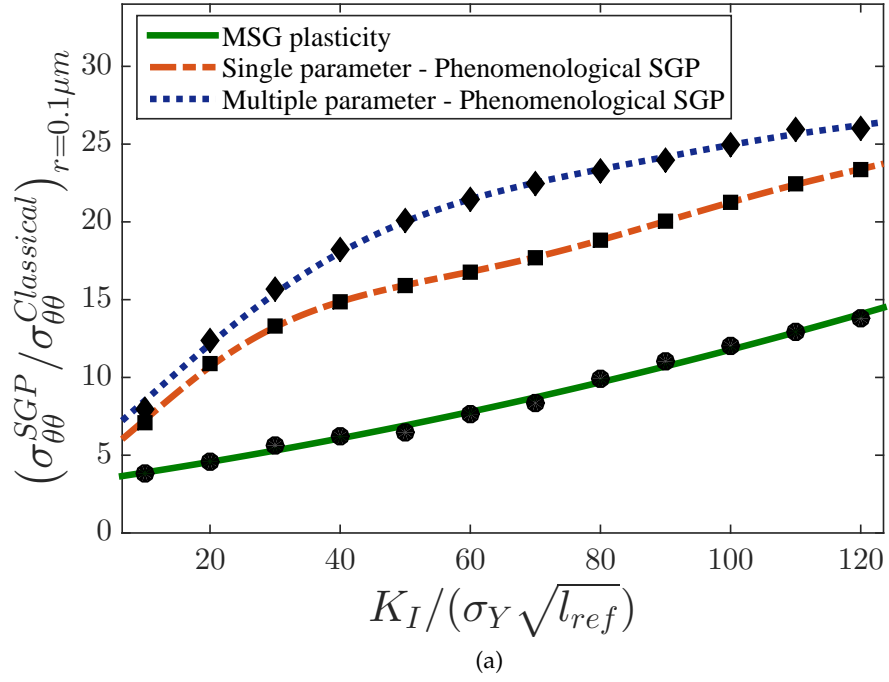
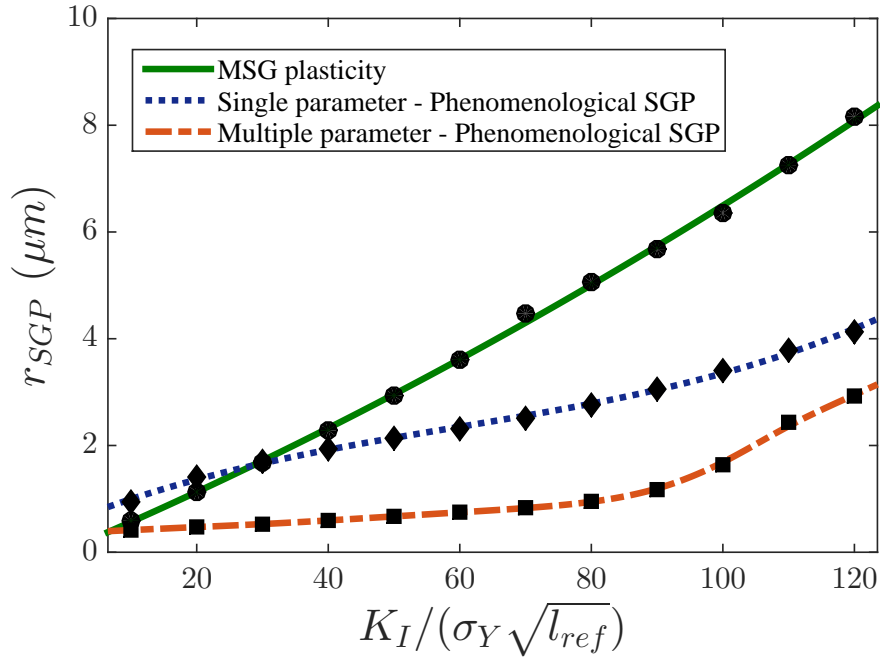
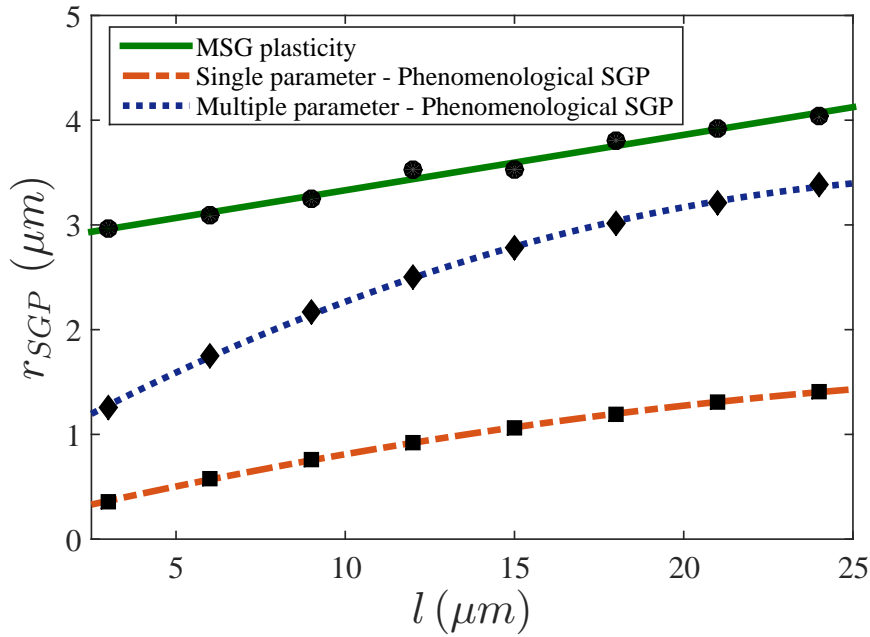


Figure 5.4: Ratio of stress elevation promoted by strain gradients at  $r = 0.1 \mu\text{m}$  ahead of the crack tip ( $\theta = 0^\circ$ ) as a function of (a) applied load  $K_I$  and (b) material length scale  $l$ , for  $\sigma_Y = 0.2\%E$ ,  $\nu = 0.3$  and  $N = 0.2$ . The length parameters in (a) are  $l^* = l_1 = l_2 = l_3 = l_{MSG} = 5 \mu\text{m}$  while the reference applied load in (b) is  $K_I = 25\sigma_Y\sqrt{l_{ref}}$  (with  $l_{ref} = 5 \mu\text{m}$ )



(a)



(b)

Figure 5.5: Distance ahead of the crack tip where the strain gradients significantly influence the stress distribution  $r_{SGP}$  as a function of (a) applied load  $K_I$  and (b) material length scale  $l$ , for  $\sigma_Y = 0.2\%E$ ,  $\nu = 0.3$  and  $N = 0.2$ . The length parameters in (a) are  $l^* = l_1 = l_2 = l_3 = l_{MSG} = 5 \mu m$  while the reference applied load in (b) is  $K_I = 25\sigma_Y\sqrt{l_{ref}}$  (with  $l_{ref} = 5 \mu m$ )

Moreover, damage modeling at the continuum level has been generally based on a distinct feature of classic plasticity: the peak stress ahead of the crack tip changes its position with the load but does not change its value. This is not the case when accounting for strain gradient effects in the constitutive modeling, as shown in fig. 5.6, where the normalized opening stress distribution  $\sigma_{\theta\theta}/\sigma_Y$  ahead of the crack tip is shown in a double logarithmic plot for different values of the crack tip load.

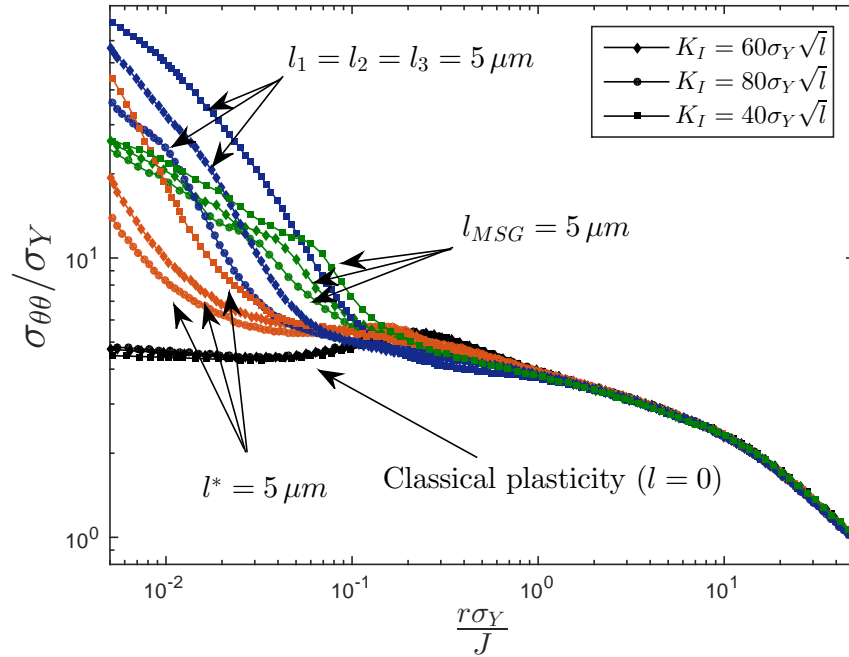


Figure 5.6: Double logarithm plot of the normalized opening stress distribution  $\sigma_{\theta\theta}/\sigma_Y$  ahead of the crack tip for classic plasticity and both mechanism-based and phenomenological **SGP** approaches, being the distance to the crack tip normalized by the external load  $r\sigma_Y/J$  for  $\sigma_Y = 0.2\%E$ ,  $\nu = 0.3$ ,  $N = 0.2$  and material length scales of  $l^* = l_1 = l_2 = l_3 = l_{MSG} = 5 \mu m$ . Finite deformation theory

The distance to the crack tip has been normalized by the external load  $r\sigma_Y/J$ , with  $J$  denoting the J-integral, that is related to the applied load by  $J = (1 - \nu^2) K_I^2/E$ . The figure reveals that the influence of **GNDs** persists all the way to the crack tip, even for very large amounts of crack tip blunting. Unlike classic plasticity (represented by the black curves), crack tip fields obtained from **SGP** theories cannot be scaled by the load and the maximum stress level increases with the external load.

The present results highlight the need to account for the influence of strain gradients in the modelization of several damage me-

chanisms. The extent ahead of the crack tip where strain gradients play an important role suggests that gradient enhanced simulations may be relevant for continuum modeling of cleavage fracture [108], ductile-to-brittle assessment [103], fatigue crack closure [109] and ductile damage [104, 105, 110]. Furthermore, accounting for the influence of GNDs in the vicinity of the crack may be particularly relevant in the modelization of hydrogen assisted cracking, due to the essential role that the hydrostatic stress has on both interface decohesion and hydrogen diffusion in relation to the fracture process zone (see [36]).

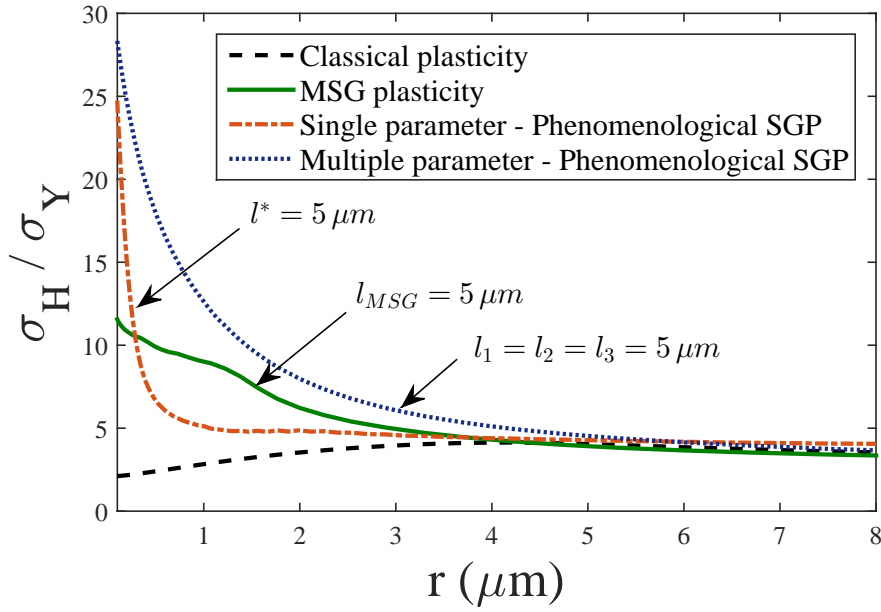


Figure 5.7: Finite deformation theory results for  $\sigma_H$  ahead of the crack tip for classic plasticity and both mechanism-based and phenomenological SGP approaches. The distance to the crack tip is denoted  $r$  and the parameters of the problem are  $K_I = 25\sigma_Y\sqrt{l}$ ,  $\sigma_Y = 0.2\%E$ ,  $\nu = 0.3$ ,  $N = 0.2$  and material length scales of  $l^* = l_1 = l_2 = l_3 = l_{MSG} = 5 \mu\text{m}$ .

Fig. 5.7 shows the hydrostatic stress distribution ahead of the crack tip under the same conditions as fig. 5.2. Results reveal that  $\sigma_H$  shows broadly identical trends as the opening stress. The conventional plasticity solution agrees with SGP predictions far from the crack tip but significant differences arise within several micrometers of the crack tip as the stress level decreases in the blunting dominated zone for conventional plasticity. The high level of crack tip surface hydrogen measured in high-strength steels suggests that damage takes place within  $1 \mu\text{m}$  of the crack surface (see [36, 111]). The stress level attained at  $r = 1 \mu\text{m}$  from MSG plasticity and single and multiple length parameter phenomenological theories is, respectively,  $\approx 3.5$ , 2 and 5 times the prediction of classic plasticity. Since results

have been obtained for a load level ( $\approx 20 \text{ MPa}\sqrt{\text{m}}$  for a typical steel) that could be considered a lower bound for damage modeling (see e.g. [112]), accounting for the influence of GNDs close to the crack tip appears to be imperative in hydrogen embrittlement models.

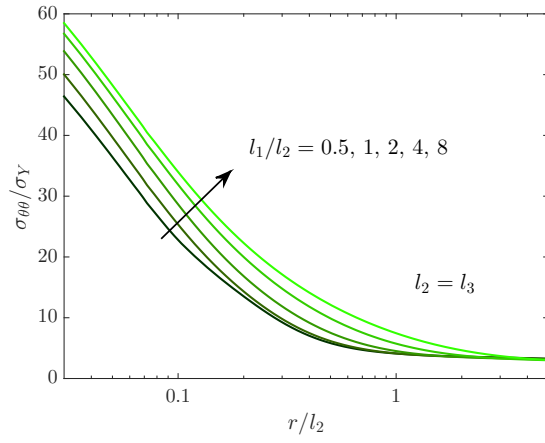
However, the quantitative differences observed among SGP theories hinder gradient enhanced modeling. Both opening (figs. 5.2, 5.3 and 5.6) and hydrostatic stress distributions (fig. 5.7) reveal substantial dissimilarities under the same reference length parameter. A qualitative agreement is found when examining the influence of the external load and the material length scale parameter for both phenomenological and mechanism-based SGP theories (figs. 5.4 and 5.5), although relevant quantitative differences are appreciated. A much higher value of  $l$  is needed in MSG plasticity to reach the crack tip stress predicted by means of both versions of Fleck-Hutchinson theory (fig. 5.4b) while the opposite is true when examining the distance ahead of the crack tip where the stress distribution deviates from conventional plasticity predictions (fig. 5.5b). Under the same conditions as fig. 5.3 a close degree of crack tip blunting is obtained by means of the following relation:

$$l_1 = l_2 = l_3 \approx \frac{1}{5}l_{\text{MSG}} \approx \frac{1}{2.5}l^* \quad (5.3)$$

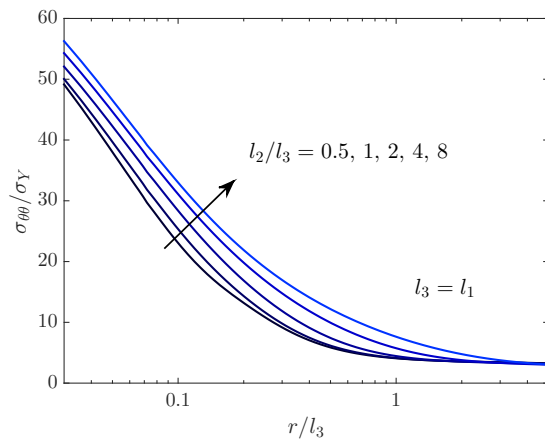
Using a cohesive zone model, Wei et al. [113] established that the relation between the steady-state fracture toughness and the separation strength obtained from MSG plasticity and from an earlier version of the Fleck-Hutchinson theory [11, 27] agrees if one considers the following approximate relation for the length scale parameter:

$$l_{\text{MSG}} \approx (4 - 5)l_{\text{SG}} \quad (5.4)$$

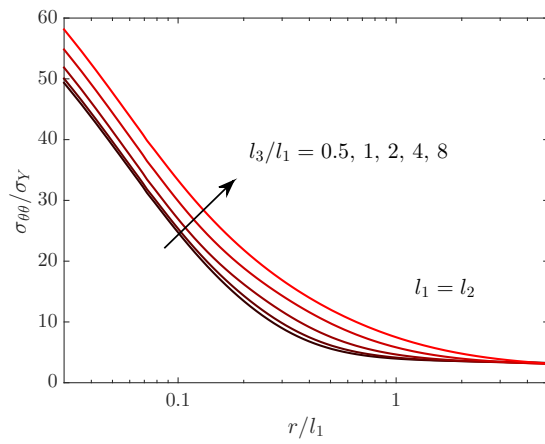
Here,  $l_{\text{MSG}}$  and  $l_{\text{SG}}$  are the material length scales of the MSG theory and the Fleck and Hutchinson (1997) [11] phenomenological theory, respectively. This correlation is similar to the one elucidated by means of crack tip blunting in the present work. However, since the material length scale has to be determined from micro-tests, it is still uncertain if the experimentally obtained value of  $l$  for MSG plasticity will be 4 – 5 times its counterpart in Fleck-Hutchinson theory. In fact, similar values of  $l$  have been obtained for polycrystalline copper from both approaches [1, 3] and therefore further research is needed to provide an accurate quantitative assessment of the influence of GNDs at the crack tip. With the aim of gaining insight into the role of individual length scales in the phenomenological three parameter theory, crack tip stress distributions are obtained for various combinations of the length scale parameters. In fig. 5.8 the influence of each of the parameters is examined by varying its value and keeping fixed the remaining two length scales.



(a)

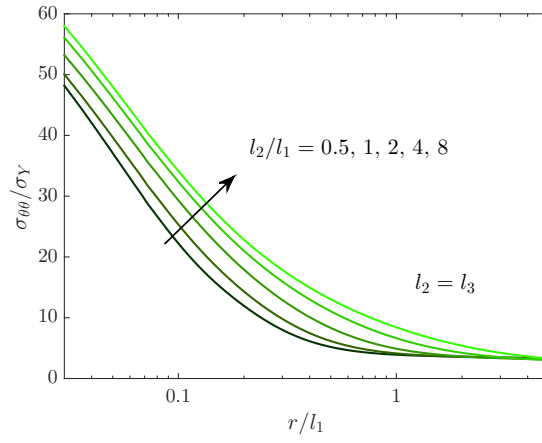


(b)

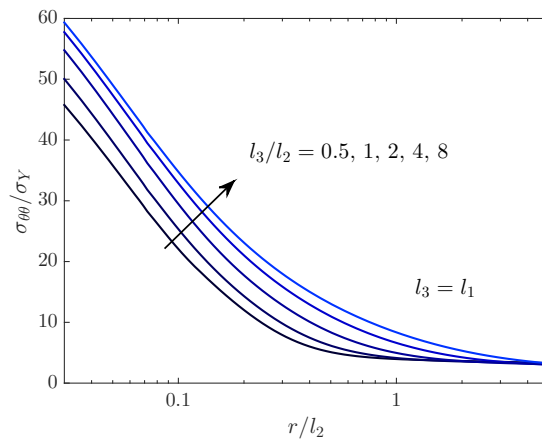


(c)

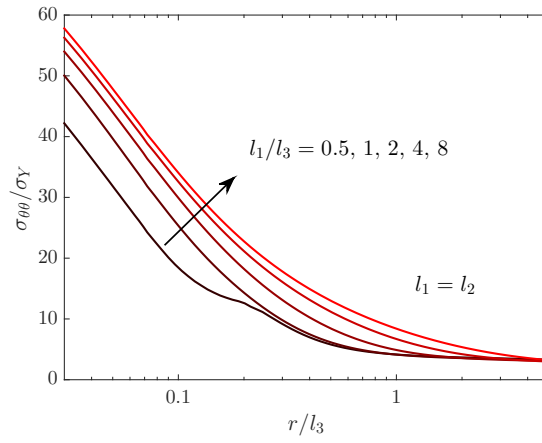
Figure 5.8: Opening stress distributions from the phenomenological multiple parameter theory for (a) fixed  $l_2$  and  $l_3$  ( $l_2 = l_3$ ) and varying  $l_1$ , (b) fixed  $l_1$  and  $l_3$  ( $l_3 = l_1$ ) and varying  $l_2$  and (c) fixed  $l_1$  and  $l_2$  ( $l_1 = l_2$ ) and varying  $l_3$ . For  $\sigma_Y = 0.2\%E$ ,  $\nu = 0.3$ ,  $N = 0.2$  and  $K_I = 25\sigma_Y\sqrt{l}$ .



(a)



(b)



(c)

Figure 5.9: Opening stress distributions from the phenomenological multiple parameter theory for (a) fixed  $l_1$  and varying  $l_2$  and  $l_3$  ( $l_2 = l_3$ ), (b) fixed  $l_2$  and varying  $l_1$  and  $l_3$  ( $l_1 = l_3$ ), and (c) fixed  $l_3$  and varying  $l_1$  and  $l_2$  ( $l_1 = l_2$ ). For  $\sigma_Y = 0.2\%E$ ,  $\nu = 0.3$ ,  $N = 0.2$  and  $K_I = 25\sigma_Y\sqrt{l}$ .

From the spread of the curves it is seen that the degree of stress elevation is more sensitive to the first parameter  $l_1$  (fig. 5.8a), while  $l_2$  (fig. 5.8b) and  $l_3$  (fig. 5.8c) play a less relevant role (with  $\sigma_{\theta\theta}/\sigma_Y$  ranging from 46 to 58.5 at, e.g.,  $r/l = 0.03$  versus 49 to 56 and 49.5 to 58, respectively). This behavior may be better appreciated in fig. 5.9, where one parameter is fixed and other two parameters are equally varied. Thus, fig. 5.9a shows the stress distributions obtained when  $l_1$  is kept constant. The comparison with figs. 5.9b (constant  $l_2$ ) and 5.9c (constant  $l_3$ ) immediately reveals smaller changes in the results when  $l_1$  is fixed. Varying  $l_2$  or  $l_3$  has a similar influence on the results.

The slightly higher relevance of  $l_1$ , the predominant material length in the presence of stretch gradients, supports previous findings by Komaragiri et al. [28] within the sharp crack problem. This further implies that the combination of length scales that characterizes the influence of strain gradients ahead of the crack must be obtained from indentation testing, where the dominating effect of  $l_1$  is also seen (see [114]).

### 5.3 CONCLUSIONS

Large gradients of plastic strain close to the crack tip must undoubtedly lead to additional hardening and very high crack tip stresses that classic plasticity is unable to predict. The experimental observation of cleavage fracture in the presence of significant plastic flow and the experimentally assessed domain where hydrogen cracking nucleates support the concept of an increased dislocation density due to GNDs in the vicinity of the crack.

In this work a general framework for damage and fracture assessment including the effect of strain gradients is provided. The numerical scheme of the two main approaches within continuum strain gradient plasticity modeling is developed so as to account for large strains and rotations and differences among theories are revealed and discussed. The following aspects must be highlighted:

- Due to the contribution of strain gradients to the work hardening of the material, crack tip blunting is largely reduced and the stress reduction intrinsic to conventional plasticity avoided. This significantly increases the differences with classic plasticity solutions reported in the literature within the infinitesimal deformation framework.
- The physical length ahead of the crack where SGP predictions deviate from the estimations of classic plasticity can span several tens of  $\mu\text{m}$ , embracing the critical distance of many damage mechanisms.

The magnitude of stress elevation close to the crack tip suggests that accounting for the effect of GNDs in the modelization can be particularly relevant in hydrogen assisted cracking, where damage takes place within  $1 \mu\text{m}$  to the crack tip.

- Results reveal significant quantitative differences among SGP theories for the same material length scale ( $l_1 = l_2 = l_3 = l_{MSG} = l^*$ ). Within the phenomenological approach, the single length parameter version predicts much smaller size effects than its multiple length parameter counterpart. Estimations from MSG plasticity lead to lower crack tip stresses but a larger gradient dominated zone, relative to the phenomenological predictions. Further research and experimental data are needed to gain insight into the existing correlation between the length scales inferred from each theory.

- A dominant effect of the first invariant of the strain gradient tensor is observed in the multiple length parameter version of the phenomenological SGP theory. Since  $l_1$  also plays an important role in indentation testing, results indicate that the constitutive length parameters that govern the influence of strain gradients in mode I fracture problems should be inferred from nanoindentation.

## THE ROLE OF ENERGETIC AND DISSIPATIVE LENGTH PARAMETERS

---

### 6.1 INTRODUCTION

Introduced by Gudmundson [6] (see also the works by Gurtin [15] and Gurtin and Anand [16]) to ensure positive plastic dissipation, energetic (or recoverable) and dissipative (or unrecoverable) gradient contributions are a common feature among the vast majority of the most recent *SGP* formulations. The degree to which size effects are mainly energetic or dissipative remains an open issue [65]. On the one hand, *GNDs* may be understood to translate into an increase in free energy of the solid [115]. On the other hand, experiments suggest that the core energy of dislocations stored during plastic deformation is much smaller than the plastic work dissipated in dislocation motion, such that *GNDs* movement in the lattice may contribute more to plastic dissipation [65].

Several authors have numerically shown that higher order recoverable stresses lead to higher material hardening while their unrecoverable counterparts increase the yield strength [61, 88, 89, 116]. This different qualitative response with diminishing size is also observed experimentally. Thus, several micro-tests, such as the torsion experiments by Fleck et al. [3] or the nano-indentation tests by Swadener et al. [117] reveal a significant increase in the yield strength; while mainly additional hardening is observed in other works (see, e.g., [4, 118]). And some experiments - such as the micro-bending tests by Haque and Saif [41] - even show a combination of strengthening and hardening. The influence of *GNDs* can be therefore accurately modeled by fitting the different length scale parameters to particular experiments and several authors have been able to phenomenologically capture the observed size effects (see, e.g., [59, 119]). However, the role of energetic and dissipative gradient effects on fracture assessment remains to be investigated.

In this chapter the influence of recoverable and unrecoverable gradient contributions will be assessed by means of two different classes of *SGP* formulations: a Gudmundson's [6] type theory (see Section 2.3) and Gurtin's [15] *DGP* (see Section 2.4). Crack tip fields and crack growth resistance are examined within a small strain formulation by means of the numerical framework described in Chapter 3. The ef-

fect of varying the dissipative  $L$  and energetic  $\ell$  length parameters is thoroughly analyzed and the physical implications discussed.

## 6.2 STATIONARY CRACK TIP FIELDS

As in previous studies (see Chapters 4 and 5) crack tip fields are computed by means of boundary layer formulation, where a remote mode I load is imposed by prescribing the displacements of the outer boundary. Due to symmetry only half of the model is examined and a very refined mesh is employed to accurately capture the influence of strain gradients close to the crack tip. As depicted in Fig. 6.1 a FE mesh of 11392 quadrilateral elements is employed, where the characteristic element length in the vicinity of the crack is of a few nanometers.

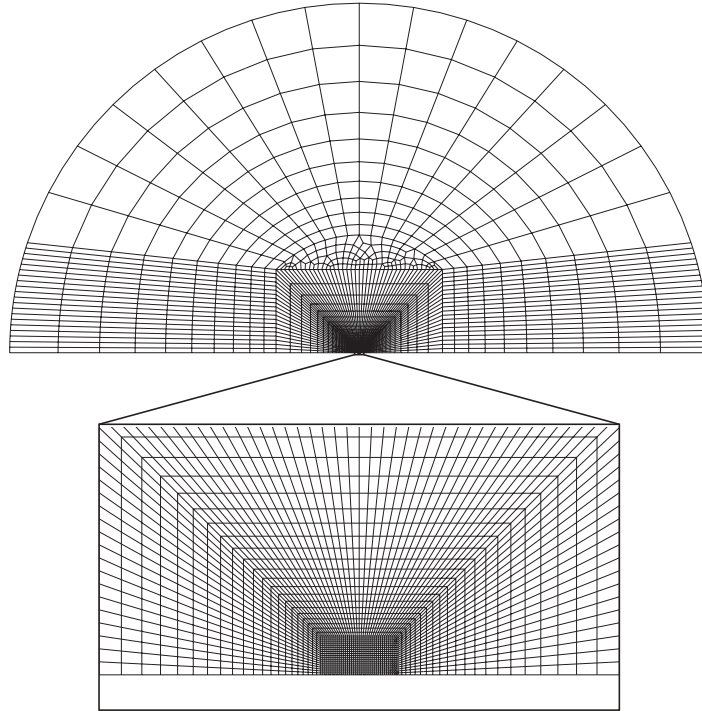


Figure 6.1: General and detailed representation of the FE mesh employed for the boundary layer model.

A standard isotropic hardening response is assumed, where the flow stress is given by

$$\sigma_F(E^P) = \sigma_Y \left( 1 + \frac{E E^P}{\sigma_Y} \right)^N \quad (6.1)$$

and the following material properties are adopted:  $\sigma_Y = 0.2\%E$ ,  $\nu = 0.3$ ,  $m = 0.1$ ,  $\dot{\epsilon}_0 = 0.02$  and  $N = 0.2$ . Stationary crack tip fields are first computed for the SGP formulation described in Section 2.3. Results obtained for different combinations of the energetic  $\ell$  and dissipative  $L$  length scale parameters are shown in Fig. 6.2.

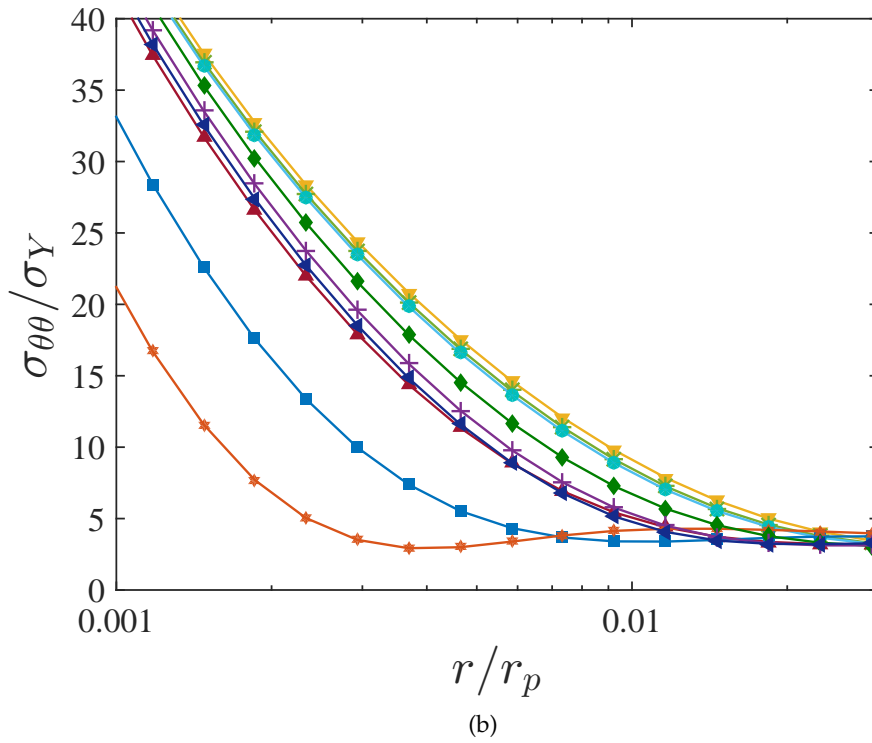
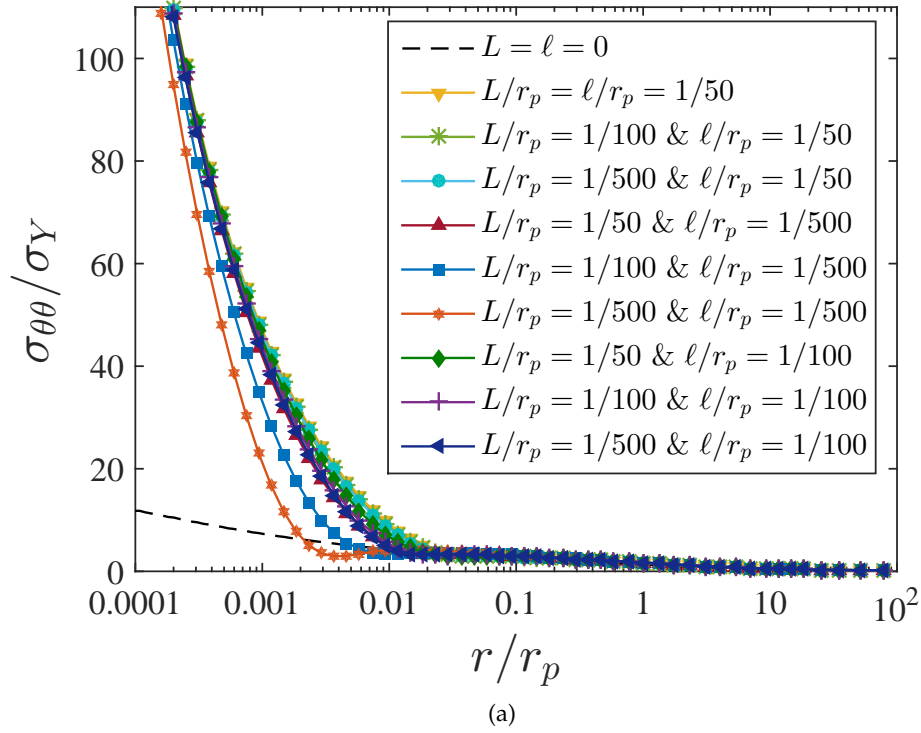


Figure 6.2: Normalized opening stress distribution ahead of the crack tip for different values of the energetic  $\ell$  and dissipative  $L$  length scales. The figures show results along the extended crack plane with the normalized distance to the crack tip in log scale for  $K_I = 28 \text{ MPa}\sqrt{\text{m}}$ ,  $\sigma_Y = 0.2\%E$ ,  $\nu = 0.3$ ,  $m = 0.1$ ,  $\varepsilon_0 = 0.02$  and  $N = 0.2$ .

The figure shows the normalized opening stress distribution  $\sigma_{\theta\theta}/\sigma_Y$  ahead of the crack tip ( $\theta = 0^\circ$ ) with the distance to the crack normalized by the Irwin-type small scale yielding estimation of the plastic zone size

$$r_p = \frac{1}{3\pi} \left( \frac{K_I}{\sigma_Y} \right)^2 \quad (6.2)$$

where  $K_I$  is the remote stress intensity factor, quantifying the external load. Results reveal that the different length scales do not influence the qualitative response ahead of a stationary crack: the stress predictions agree with those of conventional plasticity ( $L = \ell = 0$ ) far from the crack tip but are significantly higher as  $r$  goes towards 0. Quantitative differences for the different combinations of  $\ell$  and  $L$  can be observed by expanding the region of interest (Fig. 6.2b): the larger the weight of  $\ell$ , the higher the stress level. The differences between  $L$  and  $\ell$  further increase with the load, as shown in Fig. 6.3, where  $r_p^*$  corresponds to Irwin's plastic zone size estimation for the highest external load considered ( $K_I = 9 \text{ MPa}\sqrt{\text{m}}$ ). The response is almost identical for lower load values, but noticeable differences can be observed for load levels of interest from the structural integrity perspective.

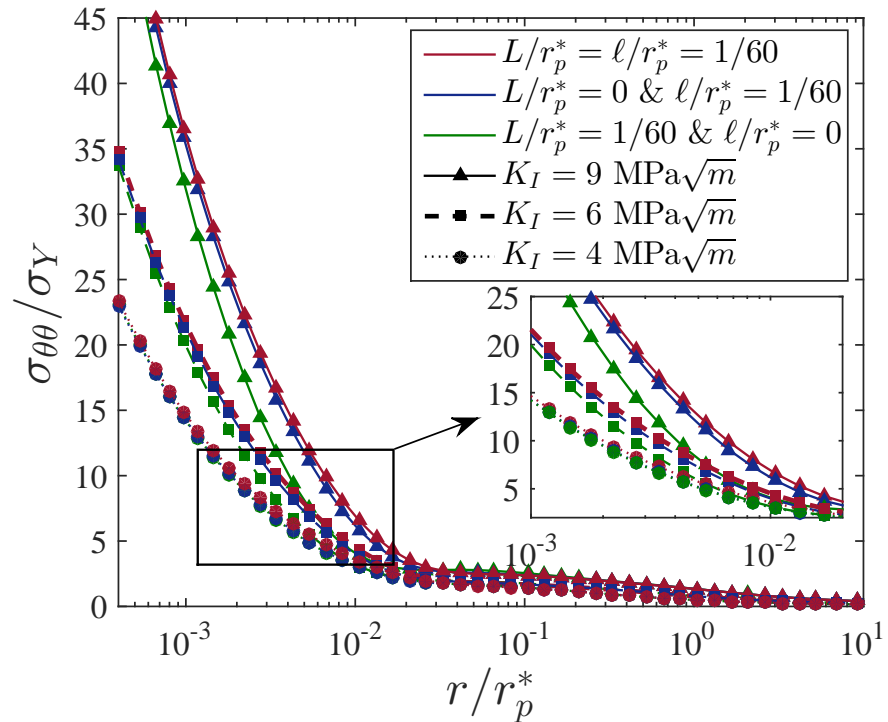


Figure 6.3: Normalized opening stress distribution ahead of the crack tip for different values of the energetic  $\ell$  and dissipative  $L$  length scales and different applied loads. The figure shows results along the extended crack plane with the normalized distance to the crack tip in log scale for  $\sigma_Y = 0.2\%E$ ,  $\nu = 0.3$  and  $N = 0.2$ .

The interpretation of the results is nevertheless complex. Due to the relatively low values of the applied load considered, highly proportional loading conditions are expected. Hence, differences observed for different combinations of  $L$  and  $\ell$  may be due to a number of reasons. On one side, the rate dependent parameters will most probably play a role, as the higher order dissipative stresses  $\tau_{ijk}^D$  are directly dependent on the effective stress  $\Sigma$ . On the other side, the size of the gradient dominated region may also influence the results. Danas et al. [120] analytically estimated - for the case of a beam under pure bending - that the dissipative contribution outweighs the energetic counterpart from a certain size of the plastic domain.

Crack tip fields are computed for the same conventional material properties by means of Gurtin [15] formulation, where the plastic spin is constitutively accounted for and the contribution of GNDs in the free energy is quantified by means of Nye's tensor [63]. As shown by Bardella [61] and Martínez-Pañeda et al. [60],  $\chi$ , the parameter governing the dissipation due to the plastic spin, weights the contributions of the shear components of the plastic spin  $\vartheta_{12}^p$  and the plastic strain  $\varepsilon_{12}^p$ .  $\chi = 2/3$  makes the effective plastic flow rate (2.76) equal to the norm of the plastic distortion in the absence of dissipative higher-order terms, while  $\chi \rightarrow \infty$  reproduces the conditions of Gurtin and Anand theory [16] (that is, irrotational plastic flow). Hence, aiming to ease the comparison between theories, results are shown in Fig. 6.4 for a very high value of  $\chi$ . The figure shows opening stress fields for different combinations of  $L$  and  $\ell$  and different values of the external load.

Fig. 6.4 reveals a dominant contribution of  $L$  to crack tip fields, the opposite trend to that depicted in Figs. 6.2 and 6.3. Differences must be related to the constitutive prescription of the defect energy. Thus, while DGP involves Nye's tensor as primal higher order kinematic variable (2.74), in Gudmundson's proposal the dissipative higher order stresses are directly related to the components of the plastic strain gradient (2.59). One should note that a quadratic form of the defect energy has been assumed in both cases; a greater impact is expected for less-than-quadratic forms that have proven to provide a closer description to certain micron-scale experiments (see, e.g., [59, 121]). The differences with the previous case are further augmented by the fact that - following [61] - the dissipative gradient contribution in the effective plastic flow rate (2.76) is weighted by  $2/3$ , unlike Gudmundson's formulation, see (2.54).

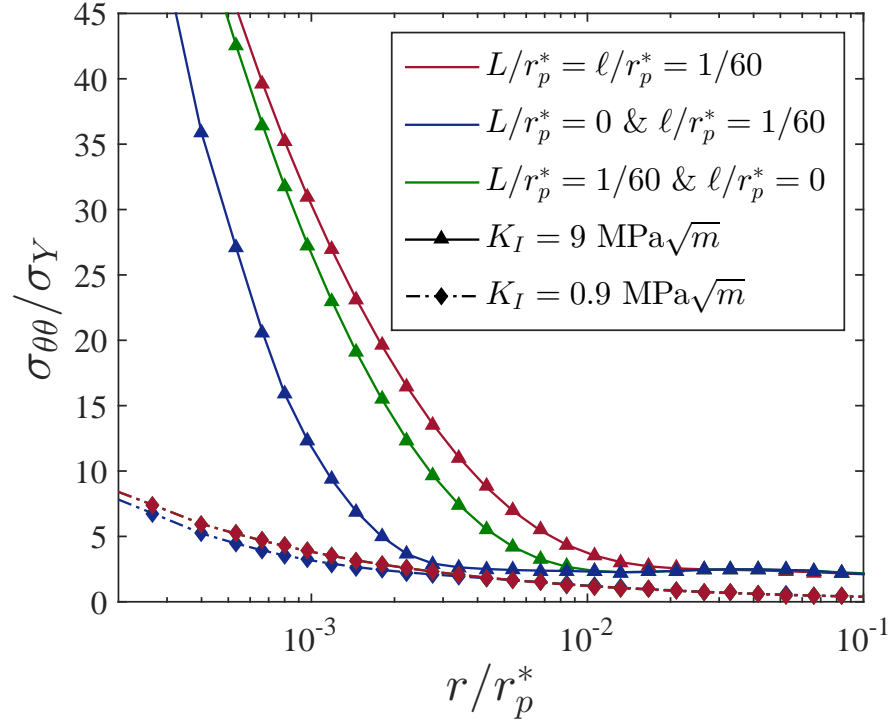


Figure 6.4: Normalized opening stress distribution predicted by DGP ahead of the crack tip for different values of the energetic  $\ell$  and dissipative  $L$  length scales and different applied loads. The figure shows results along the extended crack plane with the normalized distance to the crack tip in log scale for  $\sigma_Y = 0.2\%E$ ,  $\nu = 0.3$  and  $N = 0.2$ .

The influence of the parameter governing the dissipation due to the plastic spin is also examined. Opening stress distributions obtained for different values of  $\chi$  are shown in Fig. 6.5. Results show very little influence of the dissipation due to the plastic spin in the material response, as it may be expected for the mode I problem considered. The stress level increases with  $\chi$ , in accordance with the trends observed by Bardella [61] for the simple shear problem, where augmenting  $\chi$  leads to additional material hardening.

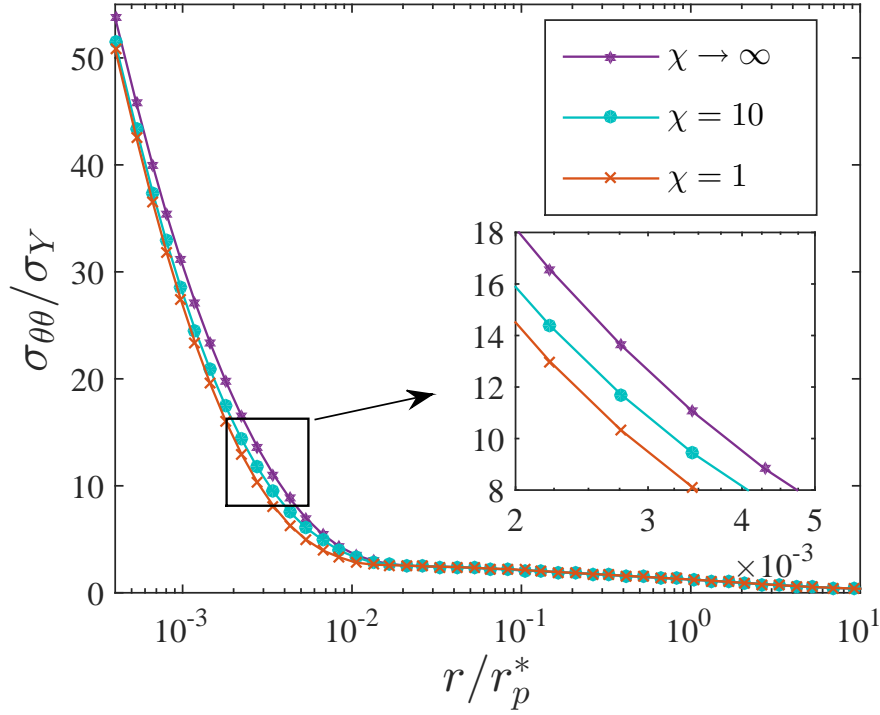


Figure 6.5: Normalized opening stress distribution ahead of the crack tip for different values of the parameter governing the dissipation due to the plastic spin  $\chi$ . The figure shows results along the extended crack plane with the normalized distance to the crack tip in log scale for  $\sigma_Y = 0.2\%E$ ,  $\nu = 0.3$ ,  $N = 0.2$  and  $L/r_p^* = \ell/r_p^* = 1/60$ .

### 6.3 STEADY-STATE CRACK GROWTH AND WORK OF FRACTURE

Inspired by the seminal work of Tvergaard and Hutchinson [122] crack growth initiation and subsequent resistance is examined for a solid characterized by Gudmundson's [6] SGP model (see Section 2.3). Crack growth in a single edge notched specimen (SENT) under uniaxial tension is analyzed by means of a cohesive zone formulation. The specimen configuration is depicted in Fig. 6.6, with a height-to-width ratio of  $H/W = 4$  and an initial edge crack of dimensions  $a_0/W = 0.1$ . Uniaxial tension is imposed by specifying a remote vertical displacement  $U$  at the upper edge  $x_2 = H$ . Plane strain conditions are assumed and due to symmetry only half of the specimen is modeled ( $0 \leq x_2 \leq H$ ). A perfectly plastic ( $N = 0$ ) rate dependent material is considered with  $\sigma_Y/E = 0.003$ ,  $m = 0.1$  and  $\varepsilon_0 = 0.25$ . The influence of the higher order gradient terms will be examined by varying the values of the energetic  $\ell$  and dissipative  $L$  length scale parameters.

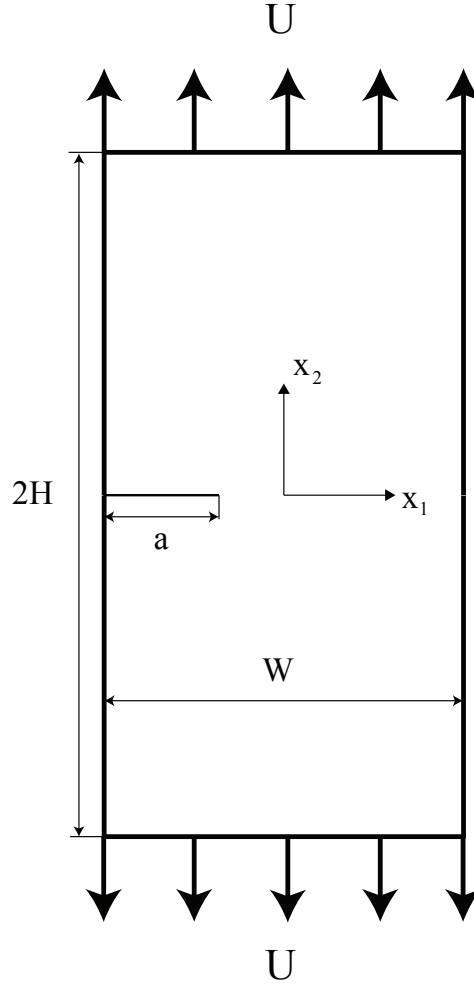


Figure 6.6: Schematic of the SENT specimen geometry and the applied boundary conditions.

The fracture process is modeled through the cohesive zone model by Xu and Needleman [123]. A cohesive surface is defined ahead of the crack whose properties are characterized by relations between the normal ( $T_n$ ) and tangential ( $T_t$ ) tractions across this surface and the corresponding displacement jumps ( $\Delta_n$  and  $\Delta_t$ , respectively). This relations are derived from a potential  $\phi$  as [123, 124]

$$T_i = -\frac{\partial \phi}{\partial \Delta_i} \quad (6.3)$$

with  $i = n, t$ ; and

$$\begin{aligned} \phi = & \phi_n + \phi_n \exp\left(-\frac{\Delta_n}{\delta_n}\right) \left\{ \left[1 - r + \frac{\Delta_n}{\delta_n}\right] \frac{1-q}{r-1} \right. \\ & \left. - \left[ q + \frac{(r-q)\Delta_n}{(r-1)\delta_n} \right] \exp\left(-\frac{\Delta_t^2}{\delta_t^2}\right) \right\} \end{aligned} \quad (6.4)$$

where  $\phi_n$  and  $\phi_t$  respectively denote the normal and tangential work of separation, which are given by

$$\phi_n = \exp(1)\sigma_{\max}\delta_n \quad (6.5)$$

$$\phi_t = \sqrt{\frac{\exp(1)}{2}}\tau_{\max}\delta_t \quad (6.6)$$

Here,  $\sigma_{\max}$  and  $\tau_{\max}$  indicate, respectively, the interface normal and tangential strengths, while  $\delta_n$  and  $\delta_t$  refer to the characteristic opening lengths for normal and tangential directions, respectively. The coupling between the latter is governed by  $q = \phi_t/\phi_n$  and  $r = \Delta_n^*/\delta_n$ , where  $\Delta_n^*$  is the value attained by the normal displacement jump after complete shear separation when  $T_n = 0$ . Accordingly, the expressions for the normal,

$$\begin{aligned} T_n = & \frac{\phi_n}{\delta_n} \exp\left(-\frac{\Delta_n}{\delta_n}\right) \left\{ \frac{\Delta_n}{\delta_n} \exp\left(-\frac{\Delta_t^2}{\delta_t^2}\right) \right. \\ & \left. + \frac{1-q}{r-1} \left[ 1 - \exp\left(-\frac{\Delta_t^2}{\delta_t^2}\right) \right] \left[ r - \frac{\Delta_n}{\delta_n} \right] \right\} \end{aligned} \quad (6.7)$$

and tangential tractions,

$$T_t = 2\frac{\phi_n}{\delta_t} \frac{\Delta_t}{\delta_t} \left\{ q + \left( \frac{r-q}{r-1} \right) \frac{\Delta_n}{\delta_n} \right\} \exp\left(-\frac{\Delta_n}{\delta_n}\right) \exp\left(-\frac{\Delta_t^2}{\delta_t^2}\right) \quad (6.8)$$

are readily obtained.

One of the most popular ways of numerically implementing a cohesive zone model is by employing what is usually referred to as *cohesive finite elements*. In the absence of higher order cohesive tractions (as required in the presence of a bimaterial interface, see [125]) the cohesive terms are exclusively related to the *macroscopic* stationary principle (Minimum Principle II), and consequently (3.60) reads,

$$\begin{aligned} \int_V C_{ijkl}\dot{\epsilon}_{kl}\delta\dot{\epsilon}_{ij}dV + \int_{S_0} \tilde{T}_i^c\delta\tilde{\Delta}_i dS = \\ \int_V C_{ijkl}\dot{\epsilon}_{kl}^p\delta\dot{\epsilon}_{ij}dV + \int_S \tilde{T}_i\delta\tilde{u}_i dS \end{aligned} \quad (6.9)$$

where  $S_0$  is the fracture surface,  $\tilde{T}_i^c$  is the cohesive traction along the fracture surface and  $\delta\tilde{\Delta}_i$  is the virtual separation, such that the second term of the left hand side is associated with the internal force of the cohesive surface elements. The local nodal displacement separation  $\tilde{\Delta}_n$  is related to the local nodal displacement  $\tilde{u}_n$  by

$$\tilde{\Delta}_n = L_{mn}\tilde{u}_n \quad (6.10)$$

where  $n$  denotes the corresponding degree of freedom and  $L_{mn}$  is a local displacement-separation relation matrix. The separation along

a cohesive surface element is interpolated from the nodal separation by means of shape functions,

$$\Delta_n = N_{nm} \tilde{\Delta}_m \quad (6.11)$$

and the global nodal displacement  $u_i$  is related to the local nodal displacement by means of a rotational matrix:

$$\tilde{u}_n = R_{mn} U^m \quad (6.12)$$

Such that combining the previous equations, the relationship between the local separation and the global nodal displacement is obtained,

$$\Delta_n = B_{nm}^c U^m \quad (6.13)$$

where  $B_{nm}^c$  is a global displacement-separation relation matrix:  $B_{nm}^c = N_{np} L_{pq} R_{qm}$ . Thus, accounting for the classic FE discretization in (6.9) and requiring the variational statement to hold for any admissible field, renders

$$\begin{aligned} \int_V C_{ijkl} \dot{\epsilon}_{kl} B_{ij}^n dV + \int_{S_0} \dot{T}_m^c B_{mn}^c dS = \\ \int_V C_{ijkl} \dot{\epsilon}_{kl}^p B_{ij}^n dV + \int_S \dot{T}_n N_{mn} dS \end{aligned} \quad (6.14)$$

where  $\dot{\epsilon}_{ij} = B_{ij}^n U^n$ , and  $T_m^c$  also depends on  $U^n$  through the traction-separation cohesive law. Hence,

$$T_n^c = \frac{\partial T_n^c}{\partial \Delta_m} \delta \Delta_m = \frac{\partial T_n^c}{\partial \Delta_m} B_{mn}^c U^m \quad (6.15)$$

and consequently,

$$\begin{aligned} \dot{U}^n \left( \int_V C_{ijkl} B_{kl}^m B_{ij}^n dV + \int_{S_0} (B_{np}^c)^T \frac{\partial T_p^c}{\partial \Delta_q} B_{qm}^c dS \right) = \\ \int_V C_{ijkl} \dot{\epsilon}_{kl}^p B_{ij}^n dV + \int_S \dot{T}_m N_{mn} dS \end{aligned} \quad (6.16)$$

where the components of the classic FE global system of equations can be readily identified. The stiffness matrix in the cohesive elements is therefore given by,

$$K_{nm}^{cohE} = \int_{S_0} (B_{np}^c)^T \frac{\partial T_p^c}{\partial \Delta_q} B_{qm}^c dS \quad (6.17)$$

with the element stiffness matrix being the gradient of the internal cohesive force vector  $K_{nm}^{cohE} = \partial f_m^{cohE} / \partial U^n$ , such that:

$$f_n^{cohE} = \int_{S_0} (B_{nm}^c)^T T_m^c dS \quad (6.18)$$

Quadratic cohesive elements with Gauss integration (following [126] a Newton-Cotes scheme is also adopted, but results show very little sensitivity) are implemented since quadratic shape functions are employed for the displacement interpolation in the standard continuum elements. A characteristic cohesive length is given by

$$l_c = \frac{\pi E \phi_n}{8 \sigma_{max}^2} \quad (6.19)$$

In order to ensure that the mesh adequately resolves the cohesive zone (so that results are mesh independent, see [127]) the characteristic element size close to the crack tip  $l_e$  satisfies  $l_e \leq l_c/20$ . Thus, a very refined mesh of approximately 50000 elements is employed, as shown in Fig. 6.7.

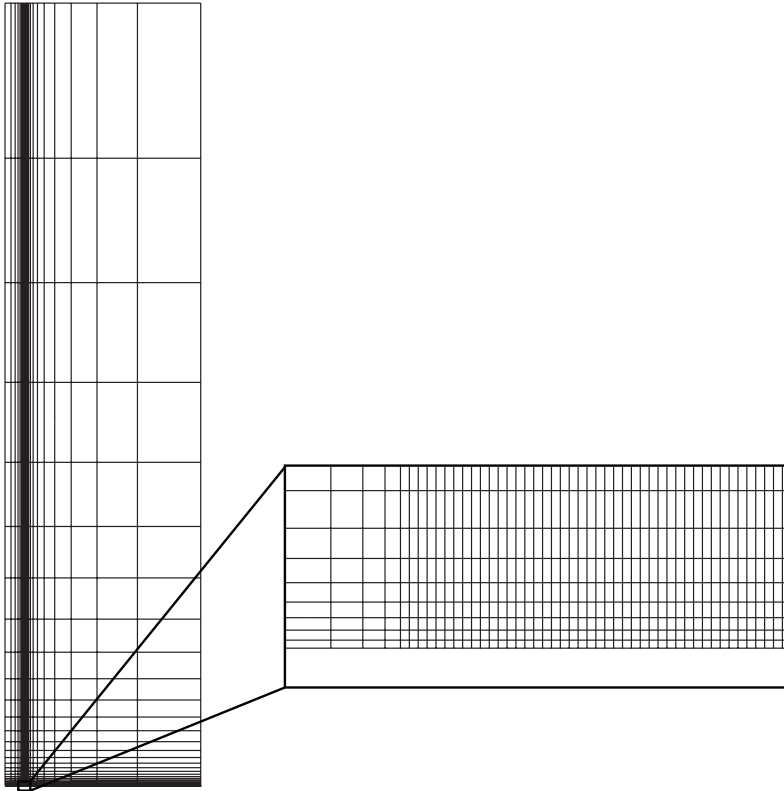


Figure 6.7: General and detailed representation of the FE mesh employed for the SENT specimen.

As in [122], the goal is to find a fundamental relation between the total work of fracture and the work of the fracture process, and elucidate the role of the energetic and dissipative gradient contributions on crack growth resistance. Following the notation of Tvergaard and Hutchinson [122] the work of separation per unit area will be denoted by  $\Gamma_0$ , which is equivalent to  $\phi_n$  in the mode-I crack problem under consideration. Hence, the work of fracture process is defined by the characteristic normal separation  $\delta_N$  and the maximum interface traction in the normal direction  $\sigma_{max}$ , as depicted in Fig. 6.8.

Based on Griffith criterion for elastic crack growth, a reference stress intensity factor  $K_0$  under plane strain conditions may be defined as

$$K_0 = \sqrt{\frac{E\Gamma_0}{(1-\nu^2)}} \quad (6.20)$$

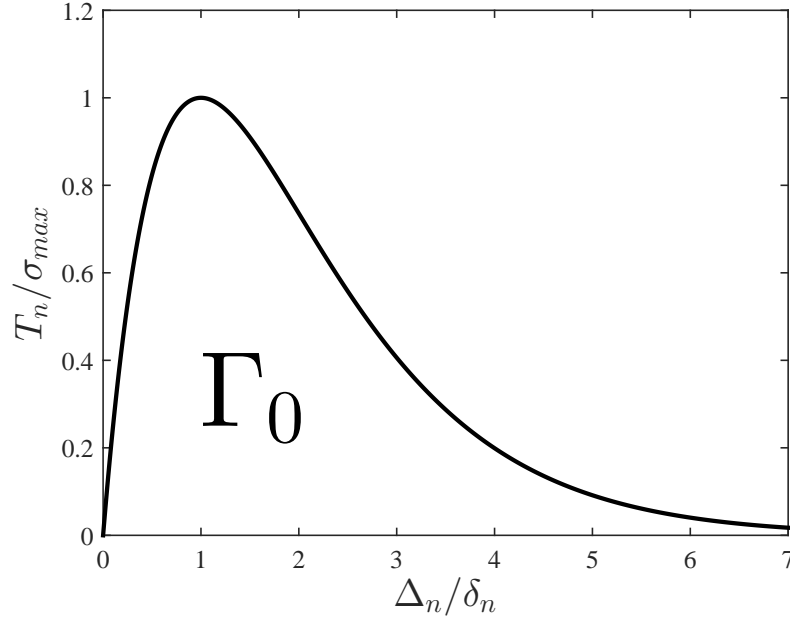


Figure 6.8: Traction-separation law employed in the cohesive zone model.

Numerical instabilities arise when modeling crack growth up to steady state toughness. The occurrence of snap-back in the load-displacement curve leads to severe convergence problems. In order to overcome these numerical difficulties the special mixed FE-Rayleigh-Ritz method proposed by Tvergaard [37] is employed to capture the global softening and unstable behavior (another control strategy is that proposed by Segurado and Llorca [128]). The solution of the linearized problem under consideration is therefore divided into three sub-problems, such that the load can be imposed by prescribing the crack opening displacement, a variable that increases monotonically during the whole loading history (see [129]). Hence, a crack tip opening displacement rate  $\dot{\delta}_T$  is imposed, such that a normalized crack tip opening displacement rate  $\bar{\delta} = \dot{\delta}_T / (\alpha_0 \dot{\epsilon}_0)$  is applied. The global displacement solution  $U_i$  to the edge cracked specimen under uniaxial traction is therefore obtained by solving

$$K_{ij} \dot{U}_j = F_i \quad (6.21)$$

through superposition. Here,  $K_{ij}$  is the global stiffness matrix - left hand side in (3.60) - and  $F_i$  corresponds to the first term of the right hand side in (3.60). As described in Fig. 6.9 the incremental solution

for a remote displacement  $U$  equals the weighted solution of three sub-problems,

$$\dot{U}_i = w_1 \dot{U}_i^{(1)} + w_2 \dot{U}_i^{(2)} + w_3 \dot{U}_i^{(3)} \quad (6.22)$$

With the nodal solution of each problem being computed by solving  $K_{ij} \dot{U}_i^{(m)} = F_i^{(m)}$ . The first sub-problem under consideration (Fig. 6.9b) involves imposing a unit velocity  $\dot{u}_2(x_1, H) = 1$  on the top edge with the displacement of the node at the crack tip constrained, such that  $\dot{u}_2(a_0, 0) = 0$  and  $F_i^{(1)} = 0$ . In the second sub-problem (Fig. 6.9c) an opening crack displacement of  $\dot{u}_2(a_0, 0) = \dot{\delta}_T$  is prescribed at the crack tip with  $\dot{u}_2(x_1, H) = 0$  on the boundary  $x_2 = H$  and  $F_i^{(2)} = 0$ . And in the third sub-problem both crack displacement  $\dot{u}_2(a_0, 0) = 0$  and remote displacement  $\dot{u}_2(x_1, H) = 0$  are constrained, with  $F_i^{(3)}$  being equal to the first term of the right hand side in (3.60).

In order to satisfy the constitutive relation  $w_3 = 1$  and since only the crack tip opening is imposed in the second sub-problem  $w_2 = 1$  [130]. The weight of the first sub-problem can be computed taking into account that the equilibrium of forces must be zero at the crack tip,

$$w_1 f_2^{T(1)} + w_2 f_2^{T(2)} + w_3 f_2^{T(3)} = 0 \quad (6.23)$$

with  $f_2^{T(2)}$  being the vertical nodal reaction force at the node located at the crack tip.

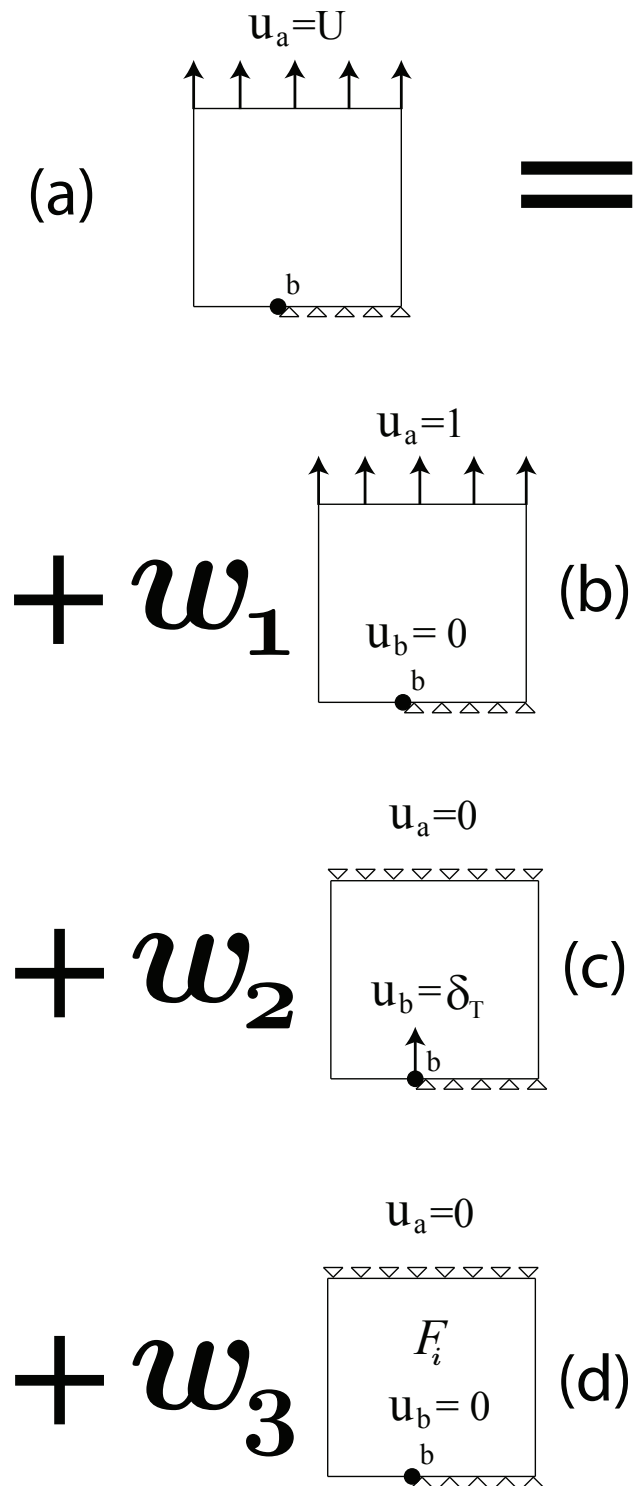


Figure 6.9: Outline of the mixed FE-Rayleigh-Ritz numerical methodology for a single edge notched specimen. Employing superposition the solution of the linearized problem (a) can be divided into three subproblems: (b) to (d).

Computed crack resistance curves are presented in Fig. 6.10 for different values of the energetic and dissipative length scales. The remote applied load  $K_R$  is obtained from

$$K_I = Y\sigma_R\sqrt{a} \quad (6.24)$$

where  $a$  is the current crack length,  $Y$  the calibration factor related to the configuration and  $\sigma_R$  is the vertical component of the remote stress on the boundary  $x_2 = H$ . The interface normal strength is defined as  $\sigma_{\max}/\sigma_Y = 6$  while the characteristic opening length in the normal direction is given by  $a_0/\delta_n = 2.5 \cdot 10^4$ . Following the criterion adopted by many authors, crack propagation is assumed when the normal separation  $\Delta_n$  is four times  $\delta_n$ .

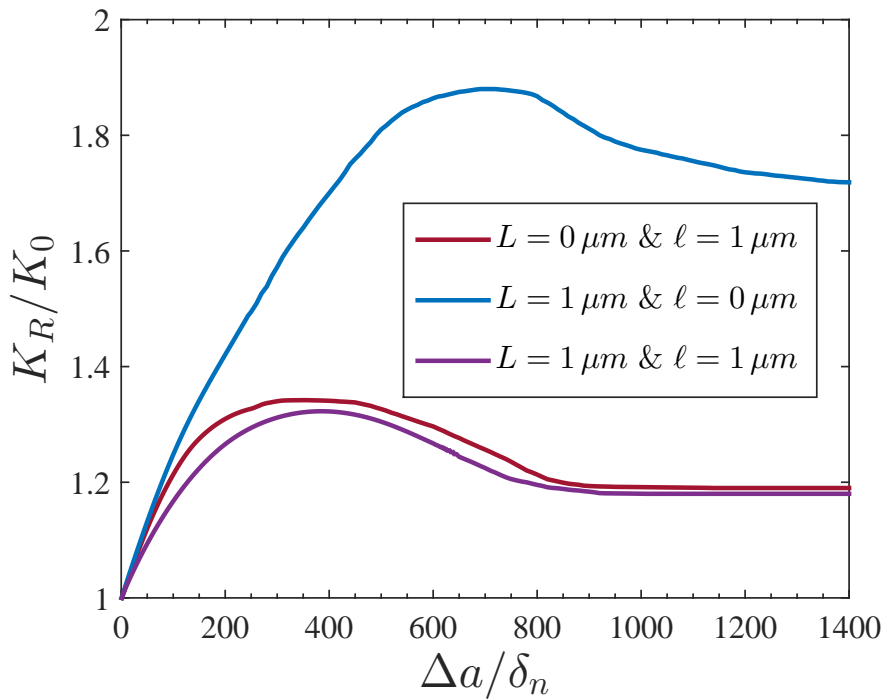


Figure 6.10: Crack growth resistance curves for different combinations of  $\ell$  and  $L$ . A perfectly plastic material ( $N = 0$ ) is considered with the following material properties:  $a_0/\delta_N = 2.5 \cdot 10^4$ ,  $\sigma_{\max}/\sigma_Y = 6$ ,  $m = 0.1$  and  $\varepsilon_0 = 0.25$ . The case  $L = 0$  is numerically approximated by setting  $L/\ell = 0.001$ .

Fig. 6.10 shows that, in all cases, crack initiation takes place at  $K^R = K_0$  (or equivalently  $G = \Gamma_0$ , being  $G$  the energy release rate). However, important differences arise when the crack propagates towards the steady state. Thus, results reveal that the energetic length scale  $\ell$  parameter significantly diminishes the steady state fracture toughness. As discussed by Tvergaard and Hutchinson [122], under steady state conditions it can be rigorously stated that the total energy release rate  $\Gamma_R^{SS}$  equals the work of the fracture process  $\Gamma_0$

plus an additional contribution that depends mostly on the bulk and interface properties; and which is mainly plastic dissipation together with a small amount of elastic energy locked in the crack wake. Consequently, the numerical results provide a precise partitioning of the total work of fracture into these two contributions when the crack is growing in steady state. Niordson and Legarth [89], in the framework of a cyclic plasticity study, have shown that  $L$  significantly increases the dissipation per load cycle while small differences are observed between the cases of pure energetic gradient effects ( $L \approx 0$ ) and combined energetic and dissipative gradient effects ( $\ell = L$ ). Hence, if higher order stresses are purely dissipative higher values of  $\Gamma_R^{SS}$  may be attained. However, as shown in [89], energetic and dissipative higher order contributions have a rather complicated effect on the dissipation during cyclic loading, with dissipation increasing for moderate values of  $L$  but decreasing for large values, as the response becomes closer to the elastic solution. Hence, a meticulous parametric study is needed to further assess the role of recoverable and unrecoverable gradient terms on steady state fracture toughness.

#### 6.4 CONCLUSIONS

The vast majority of advanced phenomenological *SGP* theories incorporates higher order energetic and dissipative terms to accommodate the strengthening effects (increased yield resistance and hardening) that are consistently being observed in a number of micron-scale experiments. *GNDs* could be associated with dissipative mechanisms, as the interaction between *GNDs* and *SSDs* may lead to dissipative jog formation; or they may they may originate from the blockage of grain boundaries, with the associated pile-up of dislocations giving rise to an energetic back-stress [131]. While the physical basis is not clear yet, energetic and dissipative length parameters have been successfully employed in phenomenological *SGP* models to capture the experimentally observed strengthening and hardening mechanisms.

In this work two different gradient plasticity models have been employed to assess the role of energetic and dissipative length parameters in fracture problems. The analysis of crack tip fields within a stationary crack reveals that both  $\ell$  and  $L$  lead to the same qualitative response, with their role weighted by the different constitutive prescriptions employed to account for the effect of *GNDs*. However, significant differences arise when crack growth resistance is modeled by means of a cohesive zone formulation: introducing energetic higher order terms translates into a severe reduction in the steady state fracture toughness. Hence, the material response after crack initiation is extremely sensitive to the identification of gradient contributions as

energetic or dissipative. Further research is needed to accurately characterize the physical behavior ahead of a propagating crack.



## HYDROGEN DIFFUSION TOWARDS THE FRACTURE PROCESS ZONE

---

### 7.1 INTRODUCTION

When exposed to hydrogen, high-strength alloys suffer from a loss of ductility and toughness leading to premature failure [132]. The atomistic mechanism for hydrogen embrittlement remains controversial with two major candidates being inferred from experiments: Hydrogen Enhanced Decohesion (HEDE) and Hydrogen Enhanced Localized Plasticity (HELP). Models adopting the hypothesis that interstitial hydrogen lowers the cohesive strength are able to capture the experimental trends depicted by high-strength steels in aqueous solutions and hydrogen-containing gaseous environments (see [36]). Several attractive hydrogen-sensitive cohesive zone formulations have been proposed within this HEDE framework (e.g., [133–136]); and accurate estimations of the threshold stress intensity  $K_{TH}$  and the stage II subcritical crack growth rate have been obtained by means of the Gerberich et al. [137] dislocation-based model [102, 112, 138]. However, uncertain adjustable parameters are a shortcoming of the models and it is necessary to better define conditions within 0.1–5  $\mu\text{m}$  of the crack tip, where dislocations, microstructure and chemistry dominate material behavior [139]. An accurate characterization of crack tip stresses appears fundamental as the hydrostatic stress dominates both lattice hydrogen concentration and interface decohesion.

The seminal paper by Sofronis and McMeeking [140] established the basis of hydrogen diffusion to the fracture process zone: lattice hydrogen concentration increases with distance from the crack tip, reaching its maximum at the peak site of the hydrostatic stress. The aforementioned hydrogen distribution follows the trend depicted by crack tip stresses in finite strain J2 plasticity and suggests that hydrogen trapped at microstructural sites plays a major role. However, classic continuum theories are unable to adequately characterize behavior at the small scales involved in crack tip deformation. Particularly, accounting for the influence of GNDs appears imperative, as the plastic zone adjacent to the crack tip is physically small and contains strong spatial gradients of deformation.

As a consequence of increasing interest in microtechnology, the role of GNDs associated with non-uniform plastic deformation has

been thoroughly investigated in a wide range of metallic materials. Thus, micro-test experiments such as bending [4], torsion [3] or nano-indentation [1] have shown that metals display a strong size effect, with smaller being stronger, when non-uniform plastic deformation is confined within a small volume. In parallel, a large theoretical (see, e.g., [9, 12, 13, 23]) and numerical (see, e.g., [19, 60, 61, 141]) literature has appeared seeking to model the experimentally observed increase in yield strength and material hardening with diminishing size. In order to do so, several continuum SGP theories have been developed through the years to incorporate length scale parameters in the constitutive equations. Gradient theories have been employed to provide a refined characterization of the stress distribution ahead of a crack and several authors have shown that GNDs close to the crack tip promote local strain hardening, leading to a much higher stress level as compared with classic plasticity predictions [27, 28, 31]. These studies have been extended to the finite deformation framework in Chapters 4 and 5, revealing a significant increase of the GND-dominated zone, as crack tip blunting is severely reduced due to the contribution of strain gradients to the work hardening of the material (see also [72, 76]). The aforementioned results show that SGP predictions deviate from conventional plasticity in a physical length that spans tens of  $\mu\text{m}$ , highlighting the need to account for GNDs in the modelization of many damage mechanisms. As an example, traction levels estimated by SGP have been employed to justify the experimental observation of cleavage fracture in the presence of significant plastic flow [25, 33].

Although several authors (see, e.g., [138, 142, 143]) have noted that GNDs may be of critical relevance in hydrogen assisted cracking, its influence in hydrogen transport has not been assessed. In the present work, crack tip hydrogen diffusion is examined within a large strain framework by means of strain gradient plasticity. Several cases of particular interest are addressed with the aim of gaining insight into the role of dislocations in the continuum modeling of hydrogen diffusion. Results obtained are compared to available experimental data and physical implications are thoroughly discussed.

## 7.2 NUMERICAL FRAMEWORK

Hydrogen diffusion to the crack tip is evaluated by means of a stress-diffusion finite element framework. A decoupled scheme is developed where a stress analysis is first conducted so as to compute the hydrostatic stress  $\sigma_H$  at a certain load level. The nodal average value of  $\sigma_H$  is then provided as initial condition in a subsequent diffusion study. Details of the finite strain SGP formulation employed in

the stress computations are given in sections 2.2 and 3.2, while the diffusion analysis is described below.

The diffusion problem, in a volume  $V$  of surface  $S$  and outward normal  $n_i$ , is derived from the requirement of mass conservation for the diffusing phase: (see, e.g., [140])

$$\frac{d}{dt} \int_V c \, dV + \int_S n_i J_i \, dS = 0 \quad (7.1)$$

Where  $d/dt$  is the time derivative,  $c$  is the mass concentration of the diffusing material and  $J_i$  is the flux of concentration of the diffusing phase. A normalized concentration is defined  $\phi = c/s$  denoting the relation between the mass concentration of the diffusing material  $c$  and its solubility in the base material  $s$ . Within this framework, stress-driven hydrogen diffusion to the crack tip is modeled by an extended form of Fick's law:

$$J_i = -sD\nabla(\phi - \kappa_p\sigma_H) \quad (7.2)$$

With  $D$  being the hydrogen diffusion coefficient and  $\kappa_p$  the pressure stress factor, which is defined by

$$\kappa_p = \frac{\bar{V}_H\phi}{R(T - T^z)} \quad (7.3)$$

Here,  $\bar{V}_H$  is the partial molar volume of hydrogen,  $T$  is the temperature (with  $T^z = 0\text{K}$  being its absolute zero value) and  $R$  is the universal gas constant. Time integration in the transient diffusion computations conducted is performed by means of the backward Euler method. Under steady-state conditions, the normalized concentration  $\phi$  is related to the hydrostatic stress  $\sigma_H$  by:

$$\phi = \phi_0 \exp\left(\frac{\bar{V}_H\sigma_H}{R(T - T^z)}\right) \quad (7.4)$$

With  $\phi_0$  being the normalized hydrogen concentration in the unstressed state.

### 7.3 FINITE ELEMENT RESULTS

The role of strain gradients in hydrogen diffusion is assessed by addressing several cases of particular interest. Thus, section 7.3.1 aims to model hydrogen transport towards a blunted crack tip in iron, following the pioneering work by Sofronis and McMeeking [140]. While, inspired by the work by Olden et al. [144], section 7.3.2 is devoted to the modeling of crack tip blunting and transient hydrogen diffusion on duplex stainless steel. And in section 7.3.3 the distribution of hydrogen ahead of a crack in X80 pipeline steel is examined and compared to the experimental results of Mao and Li [145].

### 7.3.1 Hydrogen transport in impure iron

In their pioneering work, Sofronis and McMeeking [140] established the basis for hydrogen transport ahead of the crack under large strains. The influence of GNDs is first examined by mimicking their conventional plasticity calculations. Crack tip fields are evaluated in the stress analysis by means of a boundary layer formulation. Hence, as described in Fig. 7.1, the crack region is contained by a circular zone and a remote Mode I load  $K_I$  is applied by prescribing the displacements of the nodes at the remote circular boundary:

$$u(r, \theta) = K_I \frac{1 + \nu}{E} \sqrt{\frac{r}{2\pi}} \cos\left(\frac{\theta}{2}\right) (3 - 4\nu - \cos\theta) \quad (7.5)$$

$$v(r, \theta) = K_I \frac{1 + \nu}{E} \sqrt{\frac{r}{2\pi}} \sin\left(\frac{\theta}{2}\right) (3 - 4\nu - \cos\theta) \quad (7.6)$$

Here,  $u$  and  $v$  are the horizontal and vertical components of the displacement boundary condition,  $r$  and  $\theta$  the radial and angular coordinates in a polar coordinate system centered at the crack tip, and  $K_I$  is the applied stress intensity factor, which quantifies the remote load. Following [101, 140], a ratio between the radii of the outer boundary and the blunted crack tip of  $R/r_0 = 10^5$  is adopted. Plane strain and small scale yielding conditions are assumed and only the upper half of the circular domain is modeled due to symmetry. After a thorough sensitivity study, a mesh of 6200 eight-noded quadrilateral elements with reduced integration is employed in both the diffusion and the stress analyses (see Chapter 4).

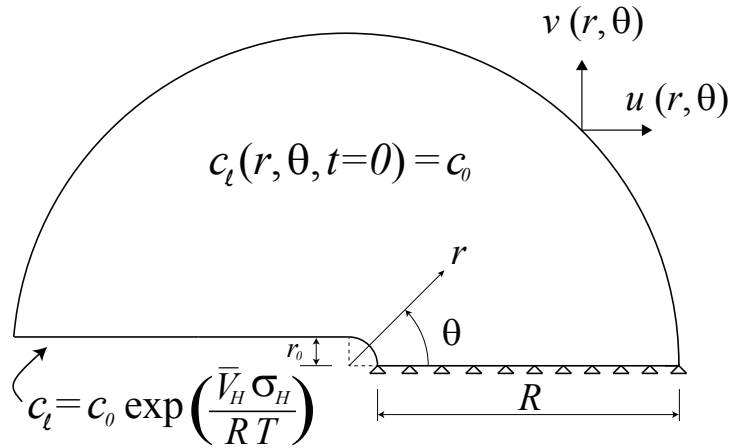


Figure 7.1: Description of the boundary and initial conditions for the stress and diffusion model employed for the impure iron case

Regarding the diffusion model, an initial bulk concentration  $c_0$  may be defined to avoid numerical oscillations (see [140]). The boundary concentration is prescribed in the crack flank as a function of the initial concentration and the hydrostatic stress (see Eq. (7.4))

and Fig. 7.1). The boundary conditions adopted accurately capture the diffusion of hydrogen to the fracture process zone under both internal and environmental assisted hydrogen cracking. Other combinations of hydrogen flux boundary conditions have been considered but, as already noted by Sofronis and McMeeking [140], the sensitivity of the hydrogen distribution ahead of the crack tip is negligible. The boundary conditions employed significantly alleviate convergence problems derived from the existing steep concentration gradients and follow the concept of prescribing a constant lattice chemical potential rather than a constant lattice hydrogen concentration, as introduced by Di Leo and Anand [146]. Unlike the gradient-enhanced stress computations, the diffusion study can be easily performed in commercial FE packages as it does not require a special formulation. In the case of the well-known FE code ABAQUS, the outcome of the stress analysis (averaged nodal values of  $\sigma_H$ ) can be read from a file and subsequently introduced as input in the diffusion study by means of a UPPRESS subroutine. A constant lattice chemical potential can be prescribed by reading the same file within a DISP subroutine.

Results are obtained for impure iron, with its uniaxial stress-strain law being characterized by (see [140])

$$\left(\frac{\sigma}{\sigma_Y}\right)^{1/N} = \frac{\sigma}{\sigma_Y} + \frac{3\mu}{\sigma_Y}\varepsilon^P \quad (7.7)$$

Where the strain hardening exponent, the yield stress and the shear modulus are given by  $N = 0.2$ ,  $\sigma_Y = 250$  MPa and  $\mu = 79.6$  GPa ( $E = 207$  GPa and  $\nu = 0.3$ ), respectively. A material length scale of  $l_1 = l_2 = l_3 = 5$   $\mu\text{m}$  is adopted in the gradient-enhanced computations. This would be a typical estimate for nickel (see [4]) and corresponds to an intermediate value within the range of experimentally fitted length scales reported in the literature (see Table 1). The hydrostatic stress distribution obtained for an external load of  $K_I = 89.7$  MPa $\sqrt{\text{m}}$  is shown in Fig. 7.2. The stress values are normalized by  $\sigma_Y$  while the distance to the crack tip  $r$  is left unchanged, with the aim of assessing the physical length where strain gradients are particularly relevant.

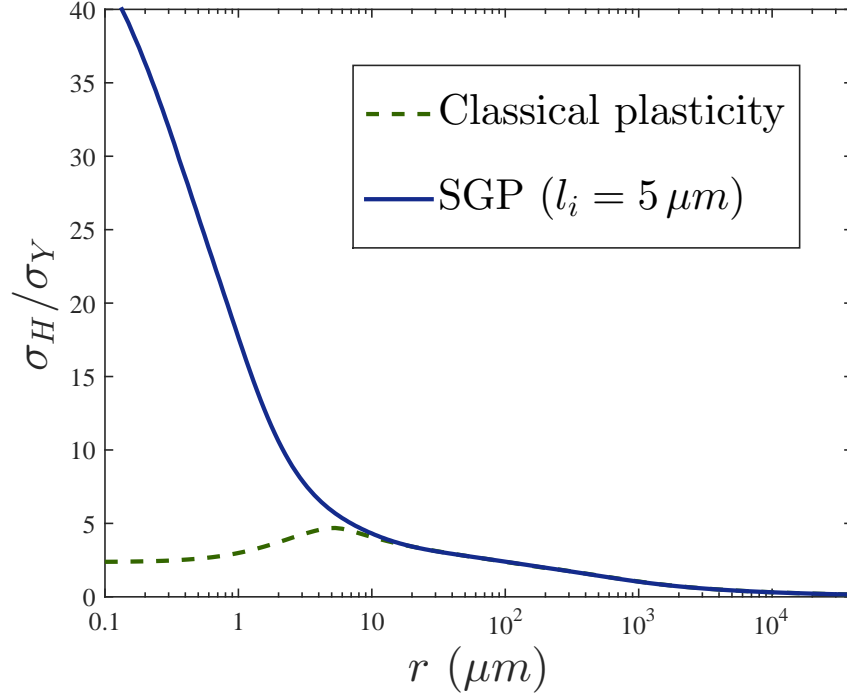


Figure 7.2: Normalized hydrostatic stress distribution ahead of the crack tip in impure iron for an external load of  $K_I = 89.7 \text{ MPa}\sqrt{\text{m}}$  from SGP (with  $l_i = 5 \mu\text{m}$ ) and conventional plasticity. The figure shows results along the extended crack plane with the distance to the crack tip in log scale.

Classic plasticity predictions reproduce the well known behavior revealed by McMeeking [101]:  $\sigma_H$  increases for decreasing values of  $r$  until the stresses become influenced by crack blunting. As large strains cause the crack to blunt, the stress triaxiality is reduced locally, with  $\sigma_H$  reaching a peak at - in the present case study -  $r \approx 6 \mu\text{m}$ . However, a monotonic increase of the stress level is observed when the influence of strain gradients is accounted for. SGP predictions agree with J2 plasticity far from the crack tip but significant differences arise in the vicinity of the crack, as the density of GNDs increases. Local stress reduction does not take place in SGP due to the contribution of strain gradients to the work hardening of the material [72, 76]. The influence on hydrogen diffusion of the macroscopic stress elevation attained due to gradient-enhanced hardening is examined in Fig. 7.3.

Fig. 7.3 shows the results obtained in the subsequent diffusion study of hydrogen transport in impure iron. Following [140], the lattice diffusion constant is given by  $D = 1.27 \cdot 10^{-8} \text{ m}^2\text{s}^{-1}$  and the initial concentration of hydrogen in the bulk is  $c_0 = 2.084 \cdot 10^{21} \text{ atoms per m}^3$ . As in [140, 146], the distribution of lattice hydrogen concentration  $c_\ell$  ahead of the crack tip is computed after 1419 hours.

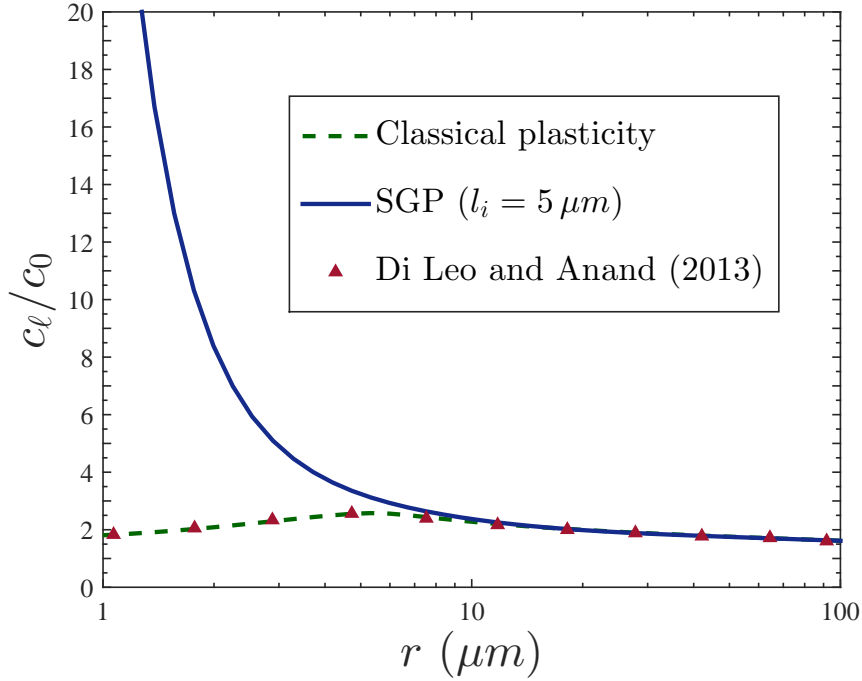


Figure 7.3: Normalized concentration of lattice hydrogen ahead of the crack tip in impure iron for SGP (with  $l_i = 5 \mu\text{m}$ ) and conventional plasticity. The figure shows results along the extended crack plane after 1419 hours, with the distance to the crack tip in log scale.

As discussed in [146], after 500 hours the change in concentration rate is negligible, such that  $t = 1419 \text{ h}$  is well beyond the time at which steady-state conditions are first reached. By prescribing a constant lattice chemical potential - as opposed to a constant lattice hydrogen concentration - numerical predictions are able to match the steady-state profile predicted by Eq. (7.4).

As in Di Leo and Anand [146], the distribution of lattice hydrogen estimated by means of conventional plasticity reaches a peak at  $c_l/c_0 \approx 2.7$  and then decreases as the crack tip is approached. On the contrary, in accordance with the trend depicted by  $\sigma_H$ , when strain gradients are accounted for the hydrogen concentration increases monotonically as  $r$  decreases. Consequently, significant differences arise between the predictions of conventional and gradient-enhanced plasticity formulations, with the latter estimating high levels of lattice hydrogen close to the crack surface. Results reveal that GNDs, absent in conventional plasticity predictions, play a very relevant role in hydrogen diffusion ahead of a crack tip.

### 7.3.2 *Crack tip blunting and hydrogen distribution in duplex stainless steel*

Despite its wide use in sub-sea applications, duplex stainless steels are sensitive to environmentally assisted hydrogen cracking at low corrosion protection potentials [147]. The role of plastic strain gradients on the onset of damage in 25%Cr duplex stainless steel is assessed by estimating the distribution of lattice hydrogen in the experiments carried out by Olden et al. [144]. Hence, single edge notched tensile (SENT) specimens under constant load and cathodic protection are examined. Due to symmetry, only half of the SENT specimen is modeled, as depicted in Fig. 7.4a. A mesh of approximately 4000 quadratic quadrilateral plane strain elements is employed, with an element size of a few nanometers in the vicinity of the 2 mm fatigued pre-crack. The material behavior is characterized by fitting the stress-strain tensile test data shown in Fig. 7.4b, and the load is applied by imposing an applied stress  $\sigma_a$  on the right edge of the specimen.

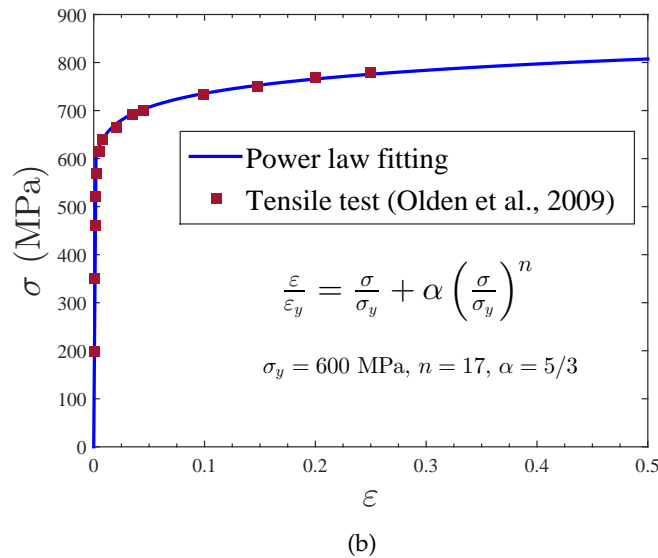
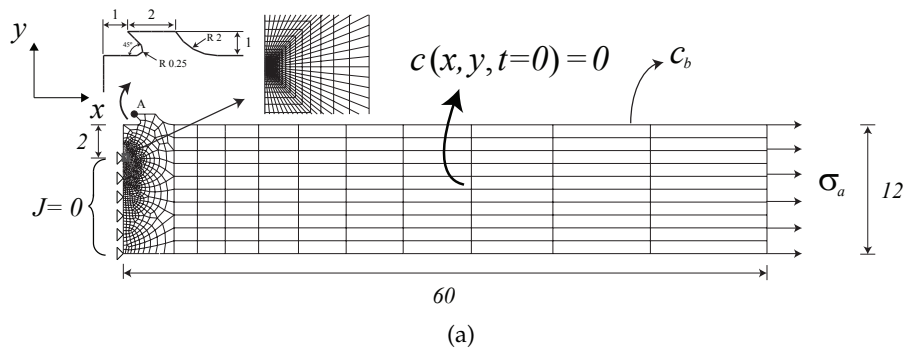


Figure 7.4: Finite element model for the duplex stainless steel study: (a) Mesh, geometry and boundary conditions, with all dimensions in mm and (b) Stress-strain curve

The stress analysis leads to the qualitative output depicted in Section 7.3.1: a monotonic increase of the hydrostatic stress is observed when strain gradients are accounted for. As outlined before, the stress triaxiality reduction near the crack tip intrinsic to classic plasticity is not observed in SGP theories due to the contribution of the strain gradients to the work hardening of the material. Namely, enhanced dislocation hardening significantly lowers crack tip blunting with respect to conventional plasticity predictions (see [76]). Fig. 7.5 shows the crack mouth opening displacement (CMOD, measured at point A in Fig. 7.4a) computed for several load levels from both classic plasticity and SGP. Computations are performed for three values of the intrinsic material length  $l_i$  with the aim of assessing the role of the parameter(s) governing the influence of the GNDs density. The experimentally measured data of Olden et al. [144] is also included.

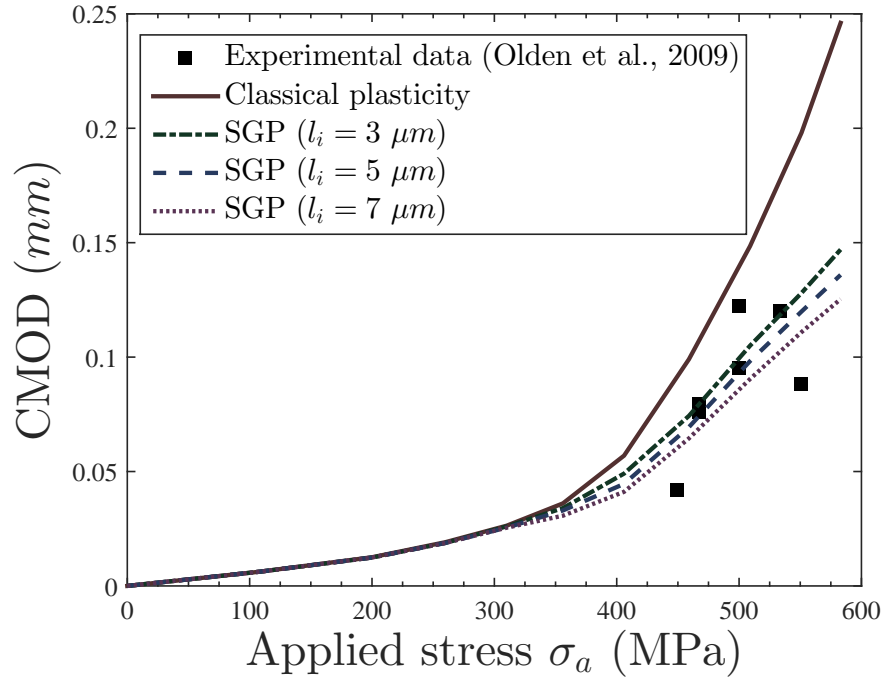


Figure 7.5: Experimental and numerical predictions for the crack mouth opening displacement in duplex stainless steel.

As shown in Fig. 7.5, crack blunting is significantly reduced when GNDs are accounted for, with the differences with classic plasticity increasing with the load. Results also show little influence of the material length scale  $l_i$ , despite varying its value over the range of experimentally reported values. Moreover, SGP predictions seem to provide a better fit with the experiments of Olden et al. [144].

For the subsequent diffusion study two different load levels have been considered, which correspond to net section stresses of 480 and 600 MPa or, equivalently, 80-100 % of the material yield strength (typical service stress levels for sub-sea pipelines are in the range of 60-80% of the yield stress). Following Olden et al. [144], a surface hydrogen concentration of 1 ppm is assumed, which corresponds to the conditions of the experimental setup (3% NaCl solution, artificial sea water at 4°C and an applied cathodic potential of -1050 mV<sub>SCE</sub>). A transient study is conducted with the aim of assessing crack tip hydrogen concentration after 200 h. of exposure. The diffusion coefficient is estimated to be  $3.7 \cdot 10^{-12} \text{ m}^2/\text{s}$  (see [144]). Boundary conditions are depicted in Fig. 7.4a with a constant lattice hydrogen concentration being prescribed, unlike the previous case study. Since GNDs lead to steep concentration gradients and a surface hydrogen concentration is imposed at the crack flanks, numerical convergence (with a negligible effect in the results for  $r > 0.1 \mu\text{m}$ ) can be significantly improved by isolating (i.e.,  $J = 0$ ) the node at the crack tip. Results are shown

in Fig. 7.6, where the SGP estimations have been computed for the intermediate value of the material length parameter ( $l_i = 5 \mu\text{m}$ ).

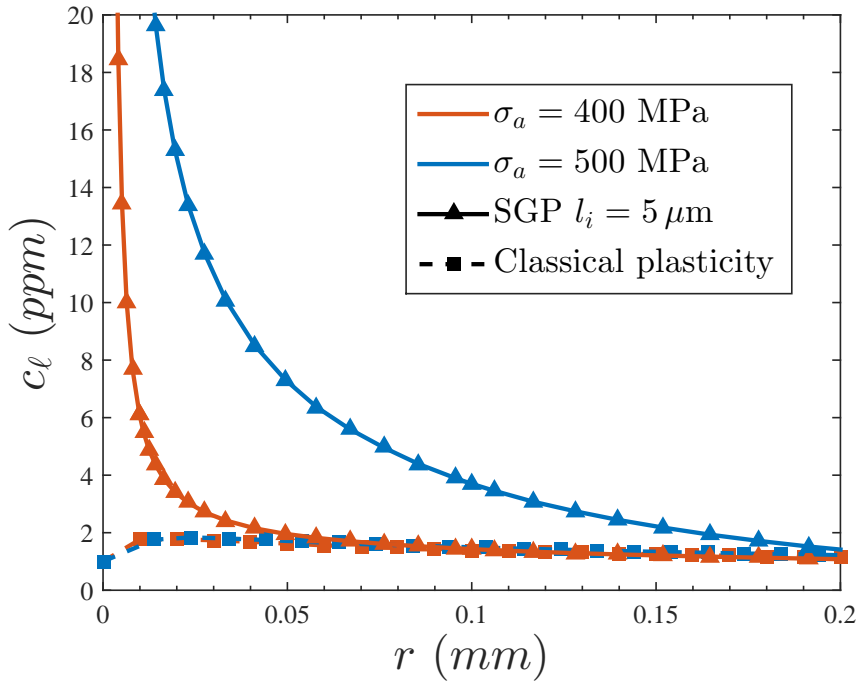


Figure 7.6: Concentration of lattice hydrogen ahead of the crack tip in duplex stainless steel for SGP (with  $l_i = 5 \mu\text{m}$ ) and conventional plasticity. The figure shows results along the extended crack plane for different applied stresses  $\sigma_a$  after 200 h.

Results reveal a major influence of GNDs over physically meaningful distances, with the lattice hydrogen concentration predicted by means of SGP significantly increasing within 0.05-0.1 mm to the crack tip. Classic plasticity predictions, in agreement with the computations of Olden et al. [144], show little sensitivity to the external load. This is not the case if strain gradients are accounted for, as the lattice hydrogen level increases with the applied stress.

### 7.3.3 Crack tip hydrogen concentration in X80 pipeline steel

There is a strong consensus that large gradients of plastic strain close to the crack tip promote additional hardening and very high crack tip stresses that classic plasticity is unable to capture. This must undoubtedly lead to high concentration of lattice hydrogen close to the crack surface. However, an experimental quantitative assessment is complicated as differences are located within a physical length on the order of micrometers. Secondary ion mass spectrometry (SIMS) seems to be one of the few techniques able to accurately measure hydrogen concentration profiles at such scales. By

means of SIMS, Mao and Li [145] were able to measure the hydrogen distribution around a crack tip in X80 pipeline steel. In their experimental work, compact tension specimens were first loaded in the absence of hydrogen and then immersed in NS-4 solution at free potential for 72 h (typical test solution for coating disbondment in Canadian pipelines, more details in [145]). Their experimental set-up is modeled with the aim of gaining quantitative insight into the role of GNDs in crack tip hydrogen diffusion. As in section 7.3.1 the remote mode I load is imposed by means of a boundary layer formulation with three load levels being considered (see [145]):  $K_I = 84 \text{ MPa}\sqrt{\text{m}}$  ( $J = 32 \cdot 10^3 \text{ J/m}^2$ ),  $K_I = 150 \text{ MPa}\sqrt{\text{m}}$  ( $J = 102 \cdot 10^3 \text{ J/m}^2$ ) and  $K_I = 173 \text{ MPa}\sqrt{\text{m}}$  ( $J = 136 \cdot 10^3 \text{ J/m}^2$ ). The elastic parameters of X80 steel are  $E = 200 \text{ GPa}$  and  $\nu = 0.3$ . A yield stress of  $\sigma_Y = 600 \text{ MPa}$  is adopted and following [145] a hardening law of the type

$$\frac{\varepsilon}{\varepsilon_y} = \frac{\sigma}{\sigma_Y} + \alpha \left( \frac{\sigma}{\sigma_Y} \right)^n \quad (7.8)$$

is assumed, with  $\varepsilon_y$  being the yield strain ( $\sigma_Y/E$ ). The dimensionless constant  $\alpha$  and the strain hardening exponent  $n$  adopt the values of 0.01 and 6.6, respectively. A value of  $l_i = 3 \mu\text{m}$  is adopted within theSGP formulation. The choice is based on the good agreement observed with the CMOD measurements in 25%Cr duplex stainless steel for  $l_i = 5 \mu\text{m}$  and the fact that a higher degree of work hardening is generally associated with a lower value of  $l_i$  (see, e.g., the expression for  $l$  provided by MSG plasticity, [33, 72]). Fig. 7.7 shows the hydrostatic stress distribution computed ahead of the crack tip for both classic and strain gradient plasticity formulations.

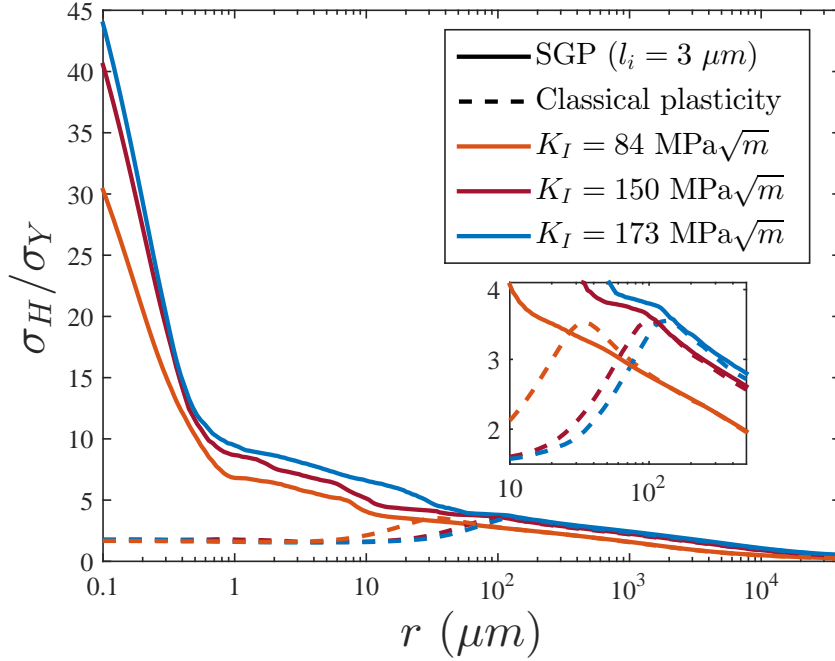


Figure 7.7: Normalized hydrostatic stress distribution ahead of the crack tip in X80 pipeline steel for SGP (with  $l_i = 5 \mu m$ ) and conventional plasticity. The figure shows results ahead of the crack tip for different load levels with the distance to the crack tip in log scale.

Results show that significantly higher stress levels are attained with the SGP formulation. The differences with respect to classic plasticity predictions are relevant in a domain that spans several tens of  $\mu m$ , embracing the critical distance of many damage mechanisms. Fig. 7.7 also shows a distinct feature of conventional plasticity: the value of the peak stress remains constant as the applied load increases, while its location moves away from the crack tip. This peculiarity of large strain J2 plasticity - on which many damage models are based - is not observed when GNDs are constitutively involved. On the contrary, the degree of stress elevation attained by means of SGP increases with the external load. Thereby, results reveal great differences between gradient and classic plasticity as the load increases, with  $\sigma_H$  in the former being more than 20 times the conventional prediction.

A subsequent diffusion study is conducted where, following [145], steady-state conditions are assumed. Mimicking the experimental setup a bulk initial concentration of  $c_\ell(t = 0) = 0$  is defined and a boundary concentration of  $c_\ell = c_0$  is imposed on crack flanks and outer radius. Convergence issues due to steep gradients can be alleviated by isolating a few nodes close to the crack tip, as in the previous case study. A lattice diffusion constant of  $D = 6.699 \cdot 10^{-11} \text{ m}^2\text{s}^{-1}$  is adopted, following the experimental measurements by Huang et al. [148]. The numerical results obtained after 72 h for both classic and gradient-enhanced formulations are shown in Fig. 7.8. The experi-

mental SIMS measurements performed by Mao and Li [145] are also included.

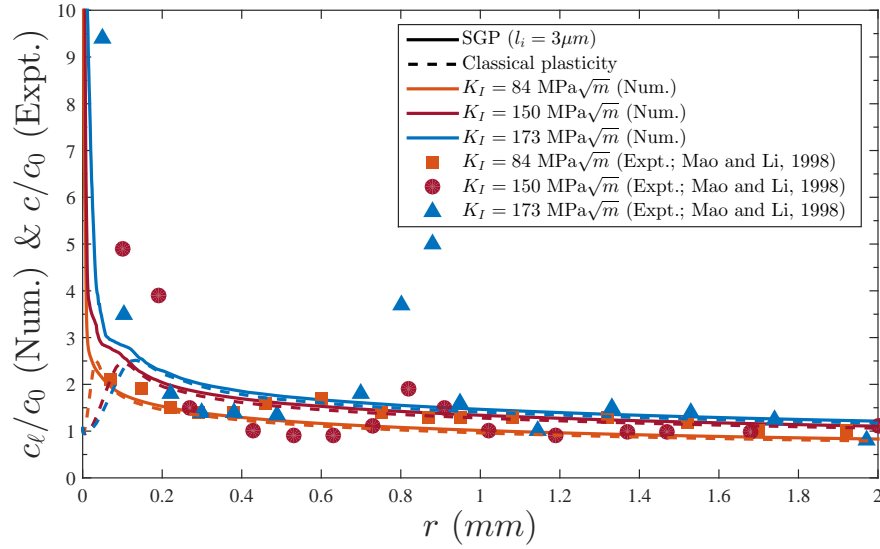


Figure 7.8: Experimental measurements and numerical predictions of, respectively, the diffusible and lattice hydrogen concentrations ahead of the crack tip in X80 pipeline steel after 72 h. The figure shows results along the extended crack plane for different load levels.

Fig. 7.8 reveals important differences between conventional and gradient-enhanced predictions, with very high values of lattice hydrogen being predicted in the vicinity of the crack if certain microstructural features (GNDs) are incorporated into the modeling. The same trends are observed for the experimental measurements of diffusible hydrogen  $c$  and SGP-based predictions of  $c_l$ ; namely, hydrogen concentration (i) increases with the external load and (ii) raises sharply within microns to the crack tip as  $r \rightarrow 0$ .

#### 7.4 THE ROLE OF HYDROGEN TRAPPING

Comprehensive modeling of hydrogen transport to the fracture process zone undoubtedly requires hydrogen trapping assessment. The role played by hydrogen reversibly trapped at dislocations is of particular interest for the present study. Thus, the dislocation density  $\rho$  is composed of the sum of the density  $\rho_S$  for statistically stored dislocations (SSDs) and the density  $\rho_G$  for geometrically necessary dislocations (GNDs), which are respectively associated with the macroscopic concepts of plastic strain  $\varepsilon_p$  and plastic strain gradient  $\varepsilon_{p,i}$ . The modeling of lattice hydrogen diffusion in an iron-based material (Fig. 7.3), duplex stainless steel (Fig. 7.6) and X-80 steel (Fig. 7.8) reveals significant quantitative and qualitative differences

between conventional plasticity and SGP based predictions. As GNDs do not contribute to plastic strains but to material work hardening by acting as obstacles to the motion of SSDs, incorporating their influence into the modeling leads to high levels of  $c_\ell$  in the vicinity of the crack, where a large density of GNDs is attained to accommodate lattice curvature due to non-uniform plastic deformation. SGP predictions suggest that a critical combination of hydrogen concentration and stress will be attained very close to the crack tip, favoring hydrogen-enhanced decohesion. From a HEDE-based perspective, Olden et al. [144] accurately predicted crack initiation by lowering the cohesive resistance as a function of the total hydrogen concentration  $c$ . A linear relation between  $\varepsilon_p$  and hydrogen trapped in microstructural defects was assumed in their study, leading to crack tip levels of reversibly-trapped hydrogen concentration  $c_t$  one order of magnitude higher than  $c_\ell$ . Accordingly, damage nucleation (represented by collapse of the first cohesive element) occurred at the crack tip surface and not at the local stress peak (given by the conventional  $\sigma_H$  distribution). Experimental measurements of high levels of surface hydrogen and critical distances of the order of micro-meters are understood, within a conventional plasticity setting, to be due to very high levels of reversibly-trapped hydrogen in the vicinity of the crack (a thorough analysis can be found in [149]). However, SGP-based estimations imply that the weight of  $c_\ell$  within the total hydrogen concentration close to the crack tip could be much larger than previously anticipated and may provide some physical background to recent experimental and theoretical studies [150] that estimate a predominant role of lattice hydrogen in failure strength degradation. Fig. 7.8 reveals little differences between the total diffusible and the lattice hydrogen concentrations, suggesting a lesser role of reversible trapped hydrogen.

Physically-consistent relations between: (i) the plastic strain gradients and  $\rho_G$ , (ii) the plastic strains and  $\rho_S$ , and (iii) the total dislocation density and  $c_t$ , need to be established to model the kinetics of dislocation trapping accounting for both GNDs and SSDs. Large strain gradients of plastic strain close to the crack tip lead to additional hardening and lower values of  $\varepsilon_p$  relative to conventional predictions. Fig. 7.9 shows the effective plastic strain distribution predicted by classic and gradient-enhanced plasticity models for an iron-based material under the same conditions as Fig. 7.2.

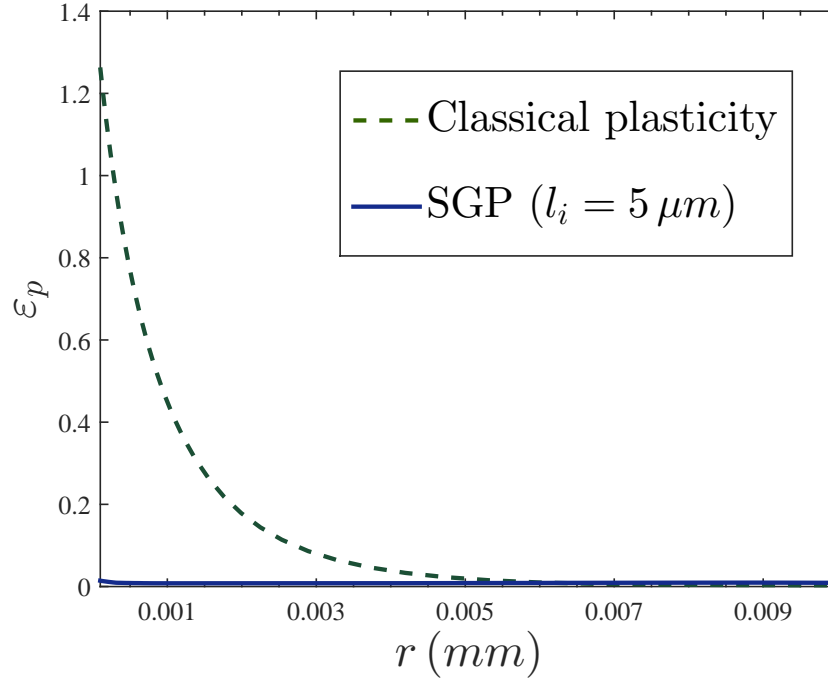


Figure 7.9: Equivalent plastic strain distribution ahead of the crack tip in an iron-based material for SGP (with  $l_i = 5 \mu\text{m}$ ) and conventional plasticity.

In consistency with the trends depicted by  $\sigma_H$  (see Fig. 7.2), results reveal a very strong influence of GNDs within microns to the crack. This necessarily implies that gradient effects lead to a much lower SSDs density with respect to conventional plasticity predictions. However, the same argument cannot be used for  $c_t$ ; as shown in [33, 151], SGP models predict large values of  $\rho$  in the vicinity of the crack, as  $\rho_G$  largely dominates the total dislocation density. Therefore, further research and critical experiments are needed to quantitatively elucidate the role of GNDs in hydrogen trapping and other embrittlement mechanisms.

## 7.5 CONCLUSIONS

The role of GNDs on crack tip hydrogen diffusion has been thoroughly investigated by means of SGP. The hydrostatic stress elevation and subsequent increase of hydrogen transport towards the crack tip associated with large gradients of plastic strain is examined in several metallic materials and differences with conventional plasticity quantified.

Results reveal a profound influence of the microstructure in several cases of particular interest from the engineering perspective.

Particularly, the following key points must be highlighted:

- **GNDs** near the crack tip promote local hardening and lead to very high stresses over meaningful physical distances. The differences with classic plasticity are further enhanced in a finite strains scheme due to the contribution of strain gradients to the work hardening of the material, significantly lowering crack blunting and avoiding the local stress reduction that is observed if **GNDs** are neglected. A good agreement with experimental observations of crack tip deformation is observed.

- Very high levels of crack tip lattice hydrogen concentration are attained as a consequence of the increased dislocation density associated with gradients of plastic strain. Unlike  $J_2$  plasticity-based predictions, the concentration of lattice hydrogen increases monotonically towards the crack tip.

- Results aim to provide insight into the embrittlement mechanisms that take place ahead of a crack. Thus, the richer description of crack tip fields provided by **SGP** suggests that lattice hydrogen may play a prominent role and decohesion could be readily triggered due to the high levels of stress and hydrogen concentration attained in the vicinity of the crack.



## 8.1 INTRODUCTION

Multi-scale model predictions of material properties are important for alloy and process development, material life-cycle optimization, and component performance prognosis [152]. Interdisciplinary advances in deformation processing [153], fatigue [154], stress corrosion cracking (SCC) [155], and hydrogen embrittlement [156] illustrate this cutting-edge approach. Internal hydrogen and hydrogen environment assisted cracking degrade high toughness alloys in fracture-critical aerospace, ship, energy, and ground transportation structures [142]. Moreover, hydrogen-stimulated damage is a primary mechanism for SCC of titanium, iron, nickel and aluminum-based alloys [36]. Models based on HEDE [157], interacting with HELP [158], predict trends in the subcritical crack growth rate properties of alloys stressed in environments that produce atomic hydrogen via chemical and electrochemical reactions on crack tip surfaces [36, 159]. However, improvements are required; local crack tip stress and dislocation configuration, as well as crack opening profile, are particularly important [160, 161].

Building on elastic stress intensity factor ( $K_I$ ) similitude for subcritical crack propagation [159], a diversity of Internal Hydrogen Assisted Cracking (IHAC) and Hydrogen Environment Assisted Cracking (HEAC) models [133, 149, 162–168], employ a crack tip stress field from classic continuum fracture mechanics [159, 169], including finite-strain blunting [101], to predict growth threshold ( $K_{TH}$ ) and rate ( $da/dt$ ) properties. Alternative modeling is based on dislocation shielding of elastic crack tip stresses [137, 170–172]. The difference between these two approaches centers on the magnitude and distribution of crack tip stresses, which define the location and severity of crack tip hydrogen-damage in the Fracture Process Zone (FPZ). Continuum plasticity modeling shows that the maximum opening-direction stress is 3-5 times alloy yield strength and located at 1-2 blunted crack tip opening displacements (of order 2 to 20  $\mu\text{m}$ ) ahead of the crack tip surface [101]. Dislocation-based models predict crack opening-direction stresses of 12-25 times yield strength and located much closer to the crack tip [137, 170]. This difference is important because HEDE defines cracking as the balance between local tensile stress and hydrogen-concentration-reduced interface strength [157] (or reduced-total work of fracture [163, 164]). Crack

tip hydrogen concentration increases exponentially with rising hydrostatic stress [173, 174], the crack tip stress gradient affects hydrogen diffusion [149, 168], and dislocation density impacts the hydrogen flux via reversible-hydrogen trapping [149]. Next generation hydrogen-cracking models require an improved-quantitative description of the crack tip stress field between the extremes represented by classic continuum plasticity and dislocation shielding.

Extensive research has focused on the *smaller is harder* behavior of metals [4, 12, 13, 59]. This size effect is attributed to GNDs, which accommodate lattice curvature due to non-uniform plastic deformation. Since classic plasticity lacks an intrinsic material length, SGP theories have been proposed to capture size effects. Isotropic SGP formulations are phenomenological (PSGP) [13] or microstructure-mechanism based (MSGP) [12, 14]. These theories bridge the gap between length-independent continuum plasticity and discrete dislocation modeling by linking statistically stored and geometrically necessary dislocation densities to the mesoscale plastic strain/strain gradient and strain hardening. Since the plastic zone is small and contains a large spatial gradient of high-strain deformation [101], it is imperative to account for GNDs in modeling crack tip stress and strain. Critically important for IHAC and HEAC, SGP modeling has consistently shown that increased GNDs density near the crack tip leads to: (a) higher local stresses, (b) a change in the crack tip stress distribution, and (c) reduced blunting; each compared to classic plasticity [28, 72, 76]. SGP must be quantitatively described and implemented in material-damage models [175], as recognized for cleavage accompanied by plasticity [26], interface fracture [176], layered-structure damage [177], ductile-microvoid fracture [107], fatigue [178], and hydrogen-enhanced cracking [36, 179].

Recent SGP advances are relevant to FE analysis of crack tip stress and strain. PSGP theory with the full complement of three-gradient terms predicts high stresses that persist to a 10-fold larger distance ahead of the sharp crack tip compared to predictions from a single-length formulation [28]. However, this FE analysis was based on infinitesimal strain [13, 28]. A large strain FE analysis of a blunting crack tip demonstrated that PSGP and MSGP formulations each predict elevated crack tip tensile stress and reduced crack tip opening compared to conventional plasticity [72, 76]. The distance over which this stress elevation persists is up to tens of micro-meters, sufficient to engulf the FPZ for HEAC [36], before merging with conventional predictions at larger distances within the plastic zone. While classic plasticity predicts a stress maximum located at 1-2 blunted openings in front of the crack tip [101, 169], large strain SGP-enhanced stresses are highest at the smallest distance (100 nm) ahead of the tip, which was

modeled by FE analysis, with no evidence of a stress maximum. Finally, SGP promotes stress elevation that depends on applied load, in sharp contrast to the  $K_I$  independence of maximum stress predicted by classic plasticity [101]. The crack tip stress distribution is affected by both the SGP model used and value(s) of the material length(s). Uncertainties remain regarding: (a) the constitutive prescription that best captures increased GNDs density associated with a plastic strain gradient [59], and (b) absolute values of material-dependent length(s) traced to test method (e.g., nano-indentation) and SGP-model analysis of such measurements [28, 76].

## 8.2 OBJECTIVE

The objective of this research is to assess and validate the coupling of large strain FE-SGP analysis of crack tip stress with HEDE-mechanism-based models that predict HEAC propagation threshold and kinetics properties. Specific aims are to: (1) improve the basis for HEAC models using SGP inputs and insights, (2) predict hydrogen-cracking properties with fewer model parameters, (3) contribute insight into the role of GNDs ahead of a crack tip, and (4) experimentally assess the proper continuum-SGP formulation of crack tip stresses.

Model assessment is based on detailed measurements of  $da/dt$  versus  $K_I$  reported for HEAC in a Ni-Cu superalloy [112, 180] and two ultra-high strength martensitic steels [102, 181], each stressed in a chloride solution. Electrochemistry measurements and modeling yielded crack tip H concentration versus applied potential ( $E_{APP}$ ) [112, 182], as well as trap-affected effective hydrogen diffusivity ( $D_{H-EFF}$ ) for each alloy [183–185]. The  $E_{APP}$  dependencies of  $K_{TH}$  and the hydrogen-diffusion limited Stage II crack growth rate ( $da/dt_{II}$ ) were originally modeled [102, 112, 180, 181] using crack tip stress from a continuum blunt-crack formulation [101]. This database and the HEDE-modeling approach are reanalyzed using crack tip stress distributions from new FE analyses that incorporate: (a) the finite strain framework for both PSGP and MSGP formulations [76], and (b) specific alloy-dependent properties and load levels that create H cracking.

## 8.3 EXPERIMENTAL PROCEDURE

Three high strength alloys were modeled, an austenitic Ni-Cu superalloy precipitation hardened by  $\gamma'$  ( $Ni_3(Al,Ti)$ ) and two martensitic ultra-high strength steels strengthened by  $(Cr,Mo)_2C$  precipitates. The heat treatment and microstructure of the superalloy, Monel K-500 (Ni-28.6Cu-2.89Al-0.45Ti-0.166C by wt pct), are described elsewhere [112, 183]: 0.2% offset yield strength ( $\sigma_{YS}$ ) is 773 MPa,

elastic modulus (E) is 183.9 GPa, and ultimate tensile strength ( $\sigma_{UTS}$ ) is 1169 MPa from tensile testing; Ramberg-Osgood flow constants from compression testing (to 2% total strain) are  $n = 20$ ,  $\alpha=0.39$ ,  $E = 185.7$  GPa and  $\sigma_0 = \sigma_{YS} = 773$  MPa; and plane strain fracture toughness ( $K_{IC}$ ) is 200 to 340  $\text{MPa}\sqrt{\text{m}}$ . The heat treatment and microstructure of two similar quenched and aged martensitic alloy steels, AerMet<sup>TM</sup>100 (Fe-13.4Co-11.1Ni-3.0Cr-1.2Mo-0.23C by wt pct) and Ferrium<sup>TM</sup>M54 (Fe-7.0Co-10.1Ni-1.0Cr-2.1Mo-1.3W-0.1V-0.30C by wt pct), are described elsewhere [102, 181, 184]. For AerMet<sup>TM</sup>100 and Ferrium<sup>TM</sup>M54, respectively,  $\sigma_{YS}$  is 1725 MPa and 1720 MPa and  $\sigma_{UTS}$  is 1965 MPa and 2020 MPa from tensile testing; Ramberg-Osgood constraints (compression to 2% total strain) are  $n=13$  and  $14$ ,  $\alpha = 1.0$ ,  $E=194$  and  $198$  GPa, and  $\sigma_c = \sigma_{YS} = 1985$  MPa and  $1951$  MPa; and  $K_{IC}$  is  $130$   $\text{MPa}\sqrt{\text{m}}$  and  $126$   $\text{MPa}\sqrt{\text{m}}$ .

The kinetics of HEAC were measured for Monel K-500, AerMet<sup>TM</sup>100, and Ferrium<sup>TM</sup>M54 using precracked fracture mechanics specimens stressed under slow-rising  $K_I$  while immersed in an aqueous solution of 0.6 M NaCl, as detailed elsewhere [102, 112, 156, 180, 181]. The  $da/dt$  versus  $K_I$  results for each alloy, characterized as a function of  $E_{APP}$ , are typical of HEAC in high strength alloys [36]. Two material properties characterize these data; specifically, the apparent  $K_{TH}$  for the onset of hydrogen crack propagation under slow-rising  $K_I$ , which rapidly accelerates in Stage I then transitions in Stage II to K-independent growth at a plateau level ( $da/dt_{II}$ ) due to chemical reaction or mass transport limitation. The measured  $E_{APP}$  dependencies of  $K_{TH}$  and  $da/dt_{II}$  (taken at a fixed  $K_I$  of 40 to 50  $\text{MPa}\sqrt{\text{m}}$  within Stage II) are used to assess HEAC models that incorporate either MSGP or PSGP.

## 8.4 MODELING PROCEDURE

### 8.4.1 Hydrogen assisted-cracking modeling

$K_{TH}$  is modeled following the approach by Gerberich et al. [170] that yielded:

$$K_{TH} = \frac{1}{\beta'} \exp \frac{(k_{IG} - \alpha C_{H\sigma})^2}{\alpha'' \sigma_{YS}} \quad (8.1)$$

The  $\beta'$  and  $\alpha''$  constants,  $0.2$   $(\text{MPa}\sqrt{\text{m}})^{-1}$  and  $0.0002$   $\text{MPa} \cdot \text{m}$ , respectively, are determined from numerical analysis of computer simulation results for an assumed configuration of dislocation shielding of the crack tip [137, 186], and  $C_{H\sigma}$  is defined below. The  $\alpha$  ( $\text{MPa}\sqrt{\text{m}}$  per atom fraction H) is a weighting factor, which governs hydrogen-lowering of the Griffith toughness ( $k_{IG}$ ,  $\text{MPa}\sqrt{\text{m}}$ ), or the reversible work of fracture related to surface energy ( $\gamma_S$ ) through

$k_{IG}^2 = 2\gamma_s E / (1 - \nu^2)$ . The  $\beta'$  and  $\alpha''$  capture the impact of plasticity (plastic work of fracture) on this  $\gamma_s$ -based description. For the cases investigated, hydrogen diffusion from the crack tip into the FPZ likely governs the Stage II  $da/dt_{II}$ , modeled as [102, 187, 188]:

$$\left(\frac{da}{dt}\right)_{II} = \frac{4D_{H-EFF}}{x_{crit}} \left[1 - \frac{C_{H\sigma-crit}}{C_{H\sigma}}\right]^2 \quad (8.2)$$

where  $x_{crit}$  is the critical distance ahead of the crack tip where hydrogen cracking nucleates leading to an increment of discontinuous crack advance.  $C_{H\sigma-crit}$  is the critical concentration of hydrogen necessary for hydrogen decohesion at  $x_{crit}$  and an inverse function of local tensile stress [157, 189].

$C_{H\sigma}$  is the crack tip  $\sigma_H$ -enhanced concentration of hydrogen in equilibrium with the crack tip overpotential for H production ( $\eta_H$ ). Since  $\sigma_H$  depends on distance ahead of the tip,  $C_{H\sigma}$  varies with location, and is evaluated at  $x_{crit}$  for use in (8.1) and (8.2).  $C_{H\sigma}$  is derived as follows. Diffusible hydrogen concentration,  $C_{H-Diff}$ , is the sum of the normal-interstitial-lattice hydrogen ( $C_L$ ) and reversibly trapped hydrogen ( $C_{RT}$ ) for a single trap site, with  $C_{RT}$  in local equilibrium with  $C_L$  and described using Fermi-Dirac statics [173].  $\sigma_H$  increases  $C_L$  to  $C_{L\sigma}$  due to lattice dilation [174], thus enhancing  $C_{RT}$  in equilibrium with  $C_{L\sigma}$  to yield  $C_{H\sigma}$  [112]:

$$C_{H\sigma} = \left[ C_L \frac{(1 - C_{L\sigma})}{(1 - C_L)} \exp\left(\frac{\sigma_H V_H}{RT}\right) \right] \left[ 1 + \frac{(1 - C_{RT})}{1 - C_L} \exp\left(\frac{E_B}{RT}\right) \right] \quad (8.3)$$

where  $V_H$  is the partial molar volume of hydrogen in the metal lattice,  $E_B$  is the binding energy of hydrogen to the dominant-reversible trap site adjacent to the crack path,  $T$  is temperature, and  $R$  is the gas constant. For hydrogen dissolved in the ultra-high strength steels and Ni superalloy in NaCl solution,  $C_L$  and  $C_{RT}$  are less than 0.001 atom fraction H, to justify that  $(1 - C_L)$  and  $(1 - C_{RT})$  equal 1.  $E_B$  for hydrogen in Monel K-500 and AerMet<sup>TM</sup>100 is 10 kJ/mol for H trapping at  $Ni_3(Al,Ti)$  or  $M_2C$ , respectively [183, 184]. Therefore the  $E_B$  term in (8.3) is much greater than 1 and:

$$C_{H\sigma} = \left[ (1 - C_{L\sigma}) \exp\left(\frac{\sigma_H V_H}{RT}\right) \right] \left[ C_L \exp\left(\frac{E_B}{RT}\right) \right] \quad (8.4)$$

The second-bracketed exponential term in (8.4) is  $C_{RT}$ , which essentially equals experimentally measurable  $C_{H-Diff}$  and is elevated by  $\sigma_H$  through the first-bracketed term. The  $(1 - C_{L\sigma})$  often equals 1 since  $C_L$  is less than 0.001 wppm and  $C_{L\sigma}$  is typically much less than 1.

The analysis in (8.1) to (8.4) is based on the assumption that HEAC is governed by the concentration of hydrogen produced at the stressed crack tip,  $C_{H\sigma}$ . Measurements of artificial crevice pH and potential, coupled with a geometric model that scales crevice behavior to a tight crack, yielded the following relationship between bold-surface applied potential,  $E_{APP}$ , and crack tip hydrogen solubility ( $C_{H-Diff}$ ) for Monel K-500 in aqueous chloride [112]

$$C_{H-Diff} \text{ (wppm)} = -52.5 - 68.7E_{APP} (V_{SCE}) \quad (8.5)$$

This result is relevant to  $K_{TH}$  and  $da/dt_{II}$ , specifically: (a)  $E_{APP}$  less than  $-0.575 V_{SCE}$ , below the open circuit potential (OCP, about  $-0.225 V_{SCE}$ ) and (b)  $10 < \xi < 60$  cm, where  $\xi$  is the ratio of crack length squared to the average of crack mouth and blunt-tip openings. For AerMet<sup>TM</sup>100 in 0.6M NaCl at  $E_{APP}$  below  $-0.750 V_{SCE}$ , the crack tip hydrogen solubility is [182]

$$C_{H-Diff} \text{ (wppm)} = 19.125E_{APP}^3 + 78.568E_{APP}^2 + 80.026E_{APP} + 24.560 (V_{SCE}) \quad (8.6)$$

for an HEAC-relevant  $\xi$  of 15 to 20 cm (increasing  $\xi$  from 10 cm to 1000 cm results in at most a 10% increase in  $C_{H-Diff}$ ). For  $E_{APP}$  between  $-0.750 V_{SCE}$  and  $-0.480 V_{SCE}$ , compared to the OCP of about  $-0.525 V_{SCE}$ , crack tip  $C_{H-Diff}$  is less certain [182]. For example,  $C_{H-Diff}$  increases from 1.7 wppm to 2.8 wppm as  $\xi$  rises from 10 cm to 1000 cm, with the latter typical of low  $K_I$  (10-20 MPa $\sqrt{m}$ ) and restricted crack opening compared to classic blunting [101]. Moreover, hydrogen solubility is reduced to nearly 0 with increasing crack surface passivation. Given these complications and limited electrochemical data, crack tip hydrogen solubility for the two steels is given by (8.6) as the lower bound for all  $E_{APP}$ . The upper bound is also given by (8.6) for  $E_{APP}$  less than  $-0.750 V_{SCE}$ , with the following relationship accurate for higher  $E_{APP}$  [182]

$$C_{H-Diff} \text{ (wppm)} = -739.24E_{APP}^5 - 3121.1E_{APP}^4 - 5147.1E_{APP}^3 - 4099.2E_{APP}^2 - 1563.8E_{APP} - 225.77V_{SCE} \quad (8.7)$$

The applied potential dependence of  $K_{TH}$  is predicted by relating  $E_{APP}$  to  $C_{H\sigma}$  using (8.5) for Monel K-500, or (8.6) and (8.7) for the steels in (8.4) with the relevant  $C_{H\sigma}$  from SGP FE analysis, then fitting the single-unknown parameter,  $\alpha$ , in (8.1) to  $K_{TH}$  measured for any  $E_{APP}$ . A similar procedure is employed to predict the  $E_{APP}$  dependence of  $da/dt_{II}$  using (8.2), with measured  $D_{H-Eff}$  [185] and independently determined  $x_{crit}$  [36, 188]. Critically,  $da/dt_{II}$  is predicted without adjustable parameters since  $C_{H\sigma}$  appears in (8.1) and (8.2). Equating (8.1) and (8.2) defines  $C_{H\sigma-crit}$  as a function of  $\alpha$

from  $K_{TH}$  modeling, plus a single-measured  $K_{TH}$  and  $da/dt_{II}$  at any  $E_{APP}$ :

$$C_{H\sigma-crit} = \frac{1}{\alpha} \left( k_{IG} - \sqrt{\alpha'' \sigma_{YS} \ln(K_{TH} \beta')} \right) \left[ 1 - \operatorname{erf} \left( \sqrt{\frac{\left(\frac{da}{dt}\right)_{II} x_{crit}}{4D_H}} \right) \right] \quad (8.8)$$

$C_{H\sigma-crit}$  from (8.8) and  $C_{H\sigma}$  from (8.4) must be evaluated at the same  $K_I$ ; however, any value can be used since  $C_{H\sigma-crit}/C_{H\sigma}$  is a constant independent of  $\sigma_H$  and the associated  $K_I$ .

#### 8.4.2 Strain gradient plasticity modeling

PSGP [13] and MSGP [14] models were incorporated in an FE analysis of crack tip stress, as detailed elsewhere [72, 76]. In the PSGP generalization of  $J_2$  flow theory [76], hardening due to the plastic strain gradient is incrementally captured through the generalized plastic strain rate ( $\dot{\epsilon}_p$ ), formulated as a function of the conventional plastic strain rate ( $\dot{\epsilon}_p$ ), three unique non-negative invariants ( $I_i$ ) of  $\dot{\epsilon}_{ij,k}^p$ , and three material lengths,  $l_i$ :

$$\dot{\epsilon}_p = \sqrt{\dot{\epsilon}_p^2 + l_1^2 I_1 + l_2^2 I_2 + l_3^2 I_3} \quad (8.9)$$

The MSGP formulation is based on the Taylor relationship between flow strength ( $\sigma_{flow}$ ) and dislocation density, given by the sum of statistically stored ( $\rho_S$ ) and geometrically necessary ( $\rho_G$ ) dislocation densities [12, 14]. The GNDs density is related to the effective plastic strain ( $\epsilon^p$ ) gradient ( $\eta^p$ ) through the Nye-factor ( $\bar{r}$ ) and Burger's vector ( $b$ ):

$$\rho_G = \bar{r} \frac{\eta^p}{b} \quad (8.10)$$

These MSGP relationships predict flow strength as a function of  $\epsilon^p$ ,  $\eta^p$ , a single length parameter ( $l$ ) and a reference stress ( $\sigma_{ref}$ ) determined from the material flow rule [12, 72]:

$$\sigma_{flow} = \sigma_{ref} \sqrt{f^2(\epsilon^p) + l \eta^p} \quad (8.11)$$

Since the Taylor dislocation model represents an average of dislocation activities, the MSGP theory is only applicable at a scale larger than the average dislocation spacing ( $r \geq 100$  nm).

The material length is a single or multiple coefficient(s), calculated to fit experimental measurements of a size dependent property (e.g., hardness) using a specific SGP theory. Various micro-tests

should be conducted to establish the  $l_i$  parameter(s); however, this determination is outside the scope of the present work. The observed range of  $l_i$  for metals is from 300 nm to 10  $\mu\text{m}$  (e.g., [4, 42, 43, 114]). Reference lengths ( $l = l_{ref}$  in MSGP and  $l_1 = l_2 = l_3 = l_{ref}$  in PSGP) of 5  $\mu\text{m}$  for Monel K-500 and 7  $\mu\text{m}$  for AerMet<sup>TM</sup><sub>100</sub> are adopted. The former is based on micro-bending experiments with pure nickel [4], while the choice for AerMet<sup>TM</sup><sub>100</sub> rests on nano-indentation tests with a moderate strength steel [43].

Crack tip stress analysis by boundary layer FE analysis, with PSGP and MSGP in the finite-strain framework, is detailed elsewhere (see [72, 76] and Chapters 4 and 5).  $K_I$  quantifies the applied load, assuming plane strain and small-scale yielding. A refined mesh is used near the tip, where the length of the smallest element is 5 nm. The cracked body is discretized by 6400 quadrilateral quadratic elements and the starting blunt-tip radius is  $10^5$ -times the outer radius of the field [101].

## 8.5 RESULTS

### 8.5.1 Monel K-500

The crack tip hydrostatic stress distribution is computed for several applied  $K_I$  in the range where HEAC occurred in Monel K-500. Figure 8.1 shows normalized  $\sigma_H/\sigma_Y$  versus distance from the crack tip,  $r$ , for three cases: MSGP (with  $l_{ref} = 5 \mu\text{m}$ ), PSGP (with  $l_1 = l_2 = l_3 = l_{ref} = 5 \mu\text{m}$ ), and classic von Mises plasticity. All finite-strain, blunt-crack predictions agree beyond the location of maximum stress in the conventional analysis, but significant differences arise closer to the crack tip. These findings are consistent with the SGP model results for a low strength-high work hardening alloy [76]. Specifically, for MSGP and PSGP compared to conventional plasticity: (1) crack tip stresses are substantially elevated, (2) a stress maximum is not evident, and (3) the stress distribution rises with increasing  $K_I$ . For the length(s) used,  $\sigma_H$  from the 3-parameter PSGP model is substantially higher than that predicted for MSGP. For each model, the maximum distance of 2.5 to 12  $\mu\text{m}$  ahead of the crack tip where GNDs significantly influence the stress distribution suggests that SGP plays an important role in HEAC.

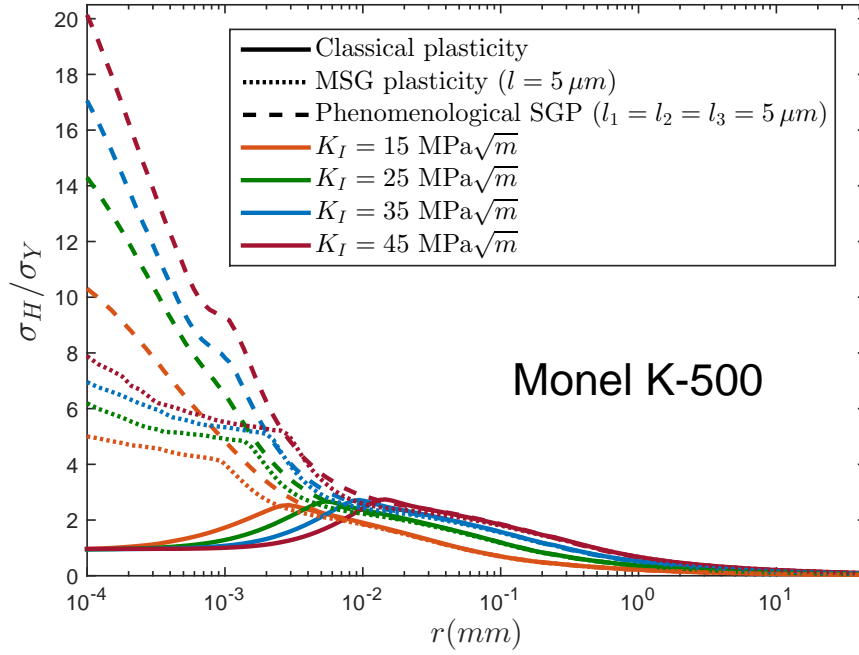
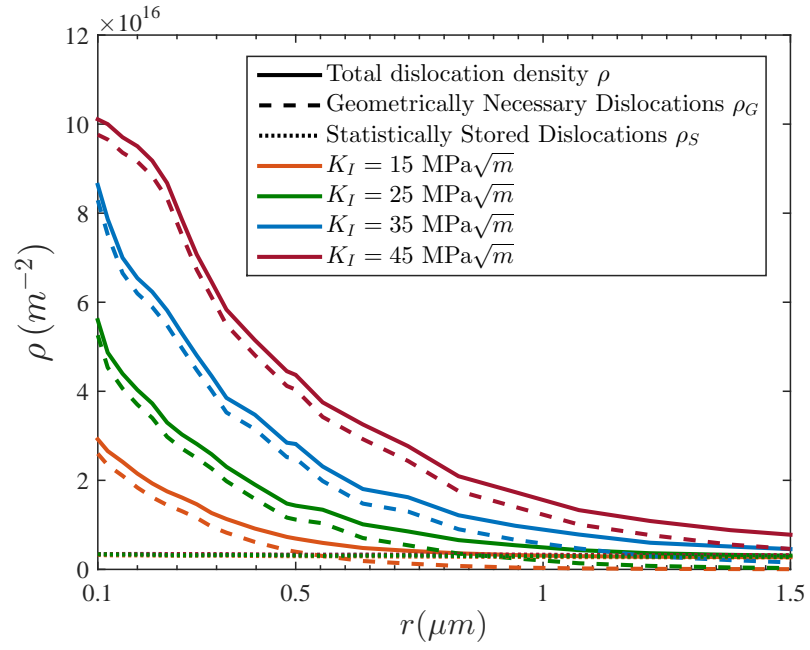
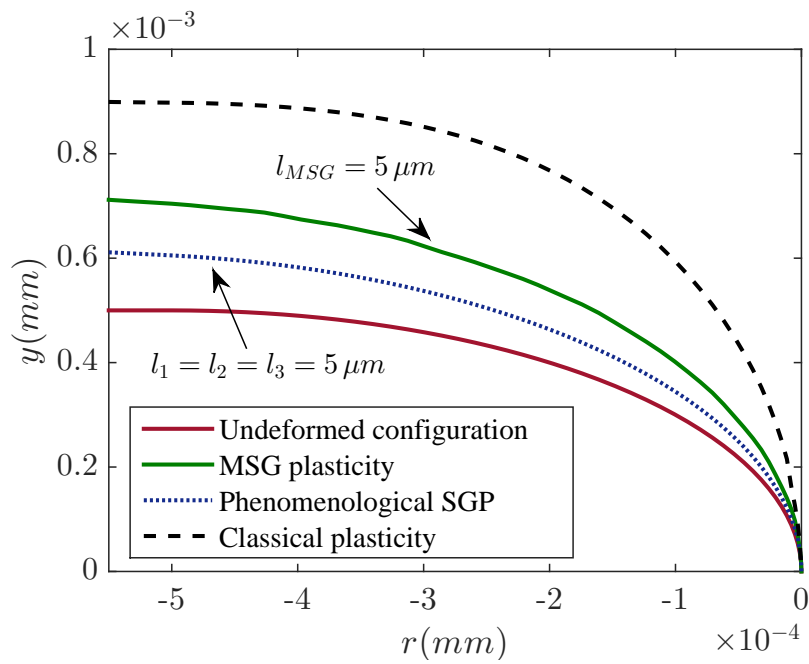


Figure 8.1: Numerical results of  $\sigma_H/\sigma_Y$  versus distance ahead of the blunted crack tip,  $r$ , for the range of  $K_I$  used in HEAC experiments with Monel K-500. Theories include: MSGP ( $l = 5 \mu m$ ), PSGP ( $l_1 = l_2 = l_3 = 5 \mu m$ ), and conventional plasticity.

Figure 8.2 shows MSGP-predicted GNDs density (from (8.10)) and the reduced crack tip profile in the opening ( $y$ ) direction for each SGP formulation. The  $\rho_S$  (Figure 8.2a) is determined from (2.8).



(a)



(b)

Figure 8.2: SGP predictions for Monel K-500 with  $l_{ref} = 5 \mu\text{m}$ : (a) MSGP predictions of  $\rho_S$  and  $\rho_G$  for the range of  $K_I$  used in the HEAC experiments, and (b) MSGP and PSGP predictions of blunt-crack opening shape for  $K_I = 15 \text{ MPa}\sqrt{\text{m}}$  compared to the profile from classic plasticity.

For HEAC modeling, crack tip  $\sigma_H$  is averaged over two distances,  $0.1 \mu\text{m} < r < 1 \mu\text{m}$  and  $0.1 \mu\text{m} < r < 2 \mu\text{m}$ , as justified in the Discussion, and values are given in Table 2, including results for a low strength

alloy [76].  $K_{TH}$  from (8.1) is predicted versus  $E_{APP}$  for the PSGP and MSGP-model values of  $\sigma_H/\sigma_Y$  (the average of the 1  $\mu\text{m}$  and 2  $\mu\text{m}$  intervals of  $r$ , Table 2).

Table 2: Large strain FE analysis predictions of  $\sigma_H/\sigma_Y$ , at  $r = 1$  or 2  $\mu\text{m}$  ahead of the blunted crack tip for conventional plasticity, and averaged between the blunted crack tip and  $r = 1$  or 2  $\mu\text{m}$  for two SGP formulations with  $l_{ref} = 5 \mu\text{m}$  for Monel K-500 and  $l_{ref} = 7 \mu\text{m}$  for AerMet<sup>TM</sup><sub>100</sub>.

$\sigma_H/\sigma_Y$	$K_I$ ( $\text{MPa}\sqrt{\text{m}}$ )	J <sub>2</sub> plasticity ( $r = 1, 2 \mu\text{m}$ )	MSGP ( $r = 1, 2 \mu\text{m}$ )	PSGP ( $r = 1, 2 \mu\text{m}$ )
AerMet <sup>TM</sup> <sub>100</sub> (Figure 8.4)	10	1.8 , 1.7	2.2 , 2.0	2.8 , 2.5
	20	1.4 , 1.6	3.4 , 3.1	4.6 , 4.1
	40	0.8 , 1.1	5.5 , 5.1	7.6 , 6.8
	80	0.5 , 0.8	8.6 , 8.1	14.0 , 13.2
Monel K-500 (Figure 8.1)	17.3	1.5 , 1.8	4.8 , 4.6	8.6 , 7.7
	50	1.0 , 1.1	7.1 , 6.7	16.8 , 16.5
Low Strength [76]	22.4	2.8 , 3.6	10.4 , 9.1	21.0 , 16.0

Results in Figure 8.3a are compared to experimental data for Monel K-500 in 0.6M NaCl solution [112, 180]. The 3-replicate measurements of  $K_{TH}$  at  $E_{APP}$  of  $-1.000 V_{SCE}$  are used to determine  $\alpha$ , which equals  $6.36 \text{ MPa}\sqrt{\text{m}}(\text{at frac H})^{-1}$  for PSGP-based  $\sigma_H$  ( $8.1\sigma_Y$ ) and  $37.59 \text{ MPa}\sqrt{\text{m}}(\text{at frac H})^{-1}$  for MSGP  $\sigma_H$  ( $4.7\sigma_Y$ ). The remaining constants in (8.1) were justified, including  $k_{IG}$  of  $0.880 \text{ MPa}\sqrt{\text{m}}$  from  $\gamma_S$  for Ni [180]. Since  $C_L$  is 1 to 50 wppm for Monel K-500 in NaCl solution [112],  $(1 - C_{L\sigma})$  is essentially 1.0 in (8.4). The PSGP and MSGP-based predictions of  $K_{TH}$  similarly agree with measured values over a range of  $E_{APP}$ ; only  $\alpha$  rises as crack tip  $\sigma_H$  falls. Each  $\alpha$  from the Figure 8.3a fit is used to calculate a  $C_{H\sigma-crit}$  through (8.8) with  $K_{TH}$  and  $da/dt_{II}$  measured at  $E_{APP}$  of  $-1.000 V_{SCE}$ . The  $da/dt_{II}$  is calculated from (8.2) and the results are given in Figure 8.3b. The PSGP and MSGP predictions of  $da/dt_{II}$  are essentially identical, and agree with measured  $da/dt_{II}$  at a single  $K_I$  of  $50 \text{ MPa}\sqrt{\text{m}}$  [112, 180]<sup>1</sup>.

<sup>1</sup> Filled points in Figure 8.3 represent 100% intergranular HEAC, while open points with upward arrows show those  $E_{APP}$  that did not produce intergranular HEAC for the highest-applied  $K_I$  [180]. The two points at  $E_{APP}$  (■) of  $-0.900$  and  $-0.800 V_{SCE}$  were associated with intergranular HEAC attributed to specimen-to-specimen variability in grain boundary-S segregation. This behavior was captured by higher  $\alpha$ , lower  $k_{IG}$ , and lower  $C_{H\sigma-crit}$  than used for the majority of  $K_{TH}$  and  $da/dt_{II}$  measurements in Figure 8.3. These parameter changes are consistent with grain boundary weakening due to S interaction with hydrogen.

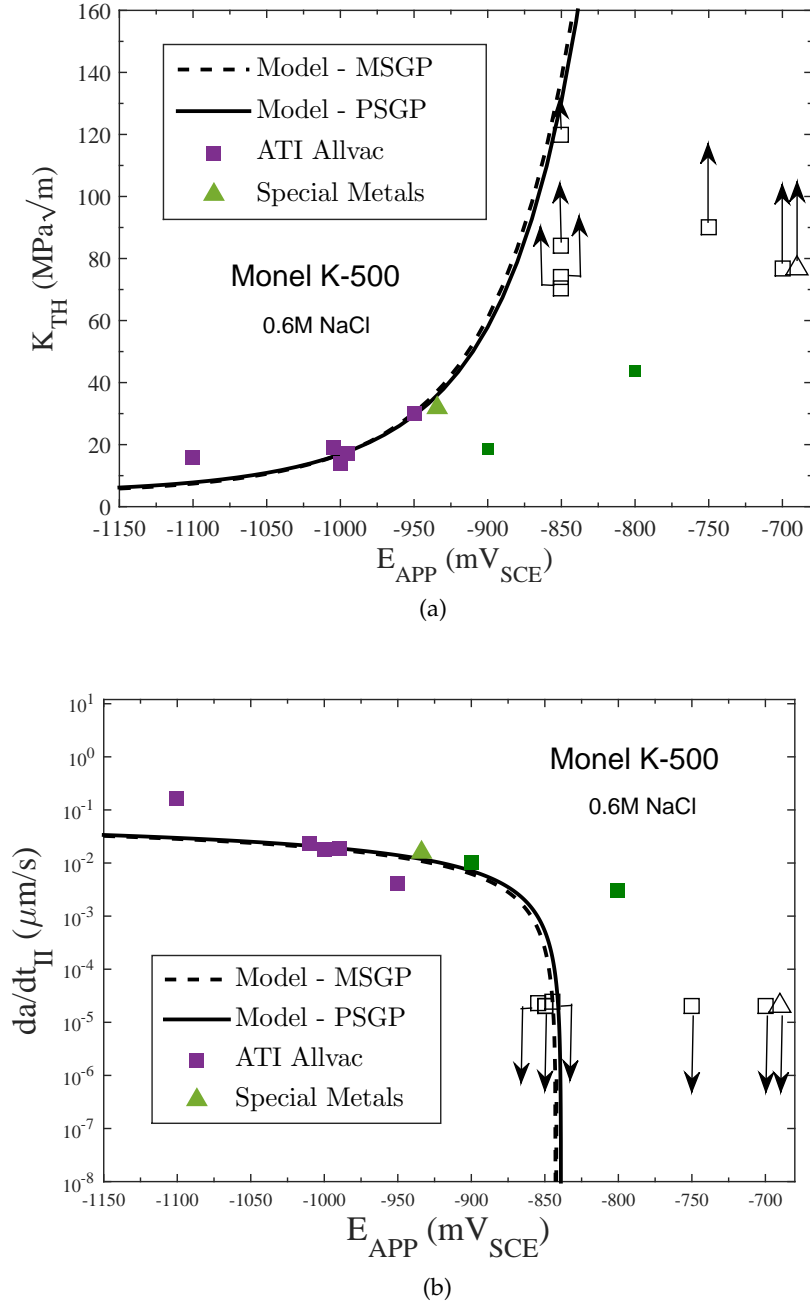


Figure 8.3: Hydrogen decohesion based predictions for Monel K-500 in 0.6M NaCl solution, calibrated by adjusting  $\alpha$  in (8.1) to fit the average of replicate experimental measurements of  $K_{TH}$  at  $E_{APP} = -1000 V_{SCE}$  for  $\sigma_H$  determined by PSGP (solid line,  $\sigma_H = 8.15\sigma_Y$ ,  $\alpha = 6.36 \text{ MPa}\sqrt{\text{m}} \text{ (at frac H)}^{-1}$  and  $C_{H\sigma\text{-crit}} = 407 \text{ wppm}$ ), as well as MSGP (dashed line,  $\sigma_H = 4.7\sigma_Y$ ,  $\alpha = 37.59 \text{ MPa}\sqrt{\text{m}} \text{ (at frac H)}^{-1}$  and  $C_{H\sigma\text{-crit}} = 68 \text{ wppm}$ ), each with  $l_{ref} = 5 \mu\text{m}$ ; (a)  $K_{TH}$  versus  $E_{APP}$ , and (b)  $da/dt_{II}$  versus  $E_{APP}$ . Other parameters are  $k_{IG} = 0.880 \text{ MPa}\sqrt{\text{m}}$  [180],  $D_{H\text{-EFF}} = 1 \cdot 10^{-10} \text{ cm}^2/\text{s}$  [183], and  $x_{crit} = 1 \mu\text{m}$ .

### 8.5.2 AerMet™<sub>100</sub> and Ferrium™M54

The crack tip hydrostatic stress distribution is computed for several  $K_I$  relevant to HEAC of AerMet™<sub>100</sub> and Ferrium™M54. Figure 8.4 shows  $\sigma_H/\sigma_Y$  versus  $r$  for MSGP ( $l_{ref} = 7 \mu\text{m}$ ), PSGP ( $l_{ref} = l_1 = l_2 = l_3 = 7 \mu\text{m}$ ), and classic plasticity. Stresses are given in Table 2, and show the same behavior as Monel K-500 (Figure 8.1) and a low strength alloy [76].

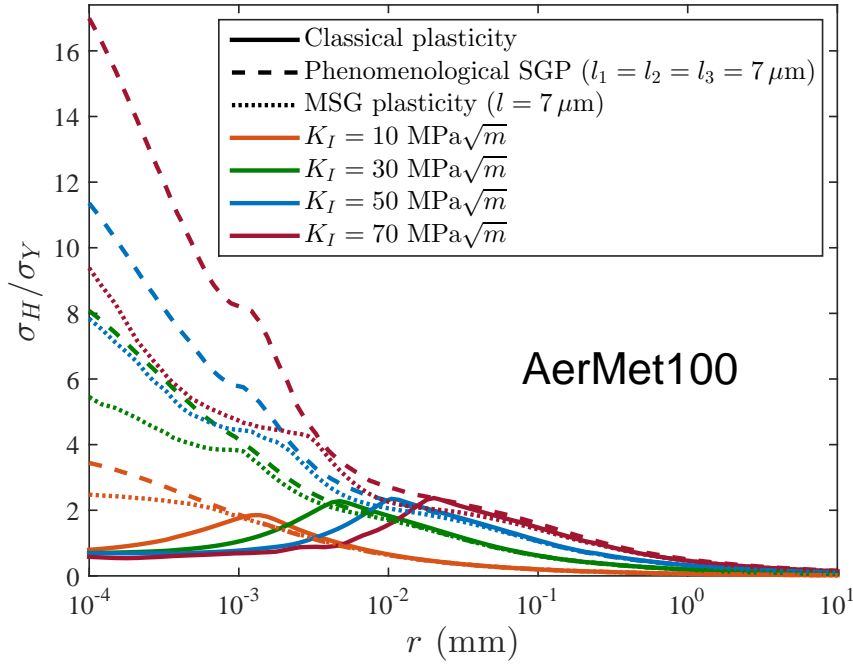


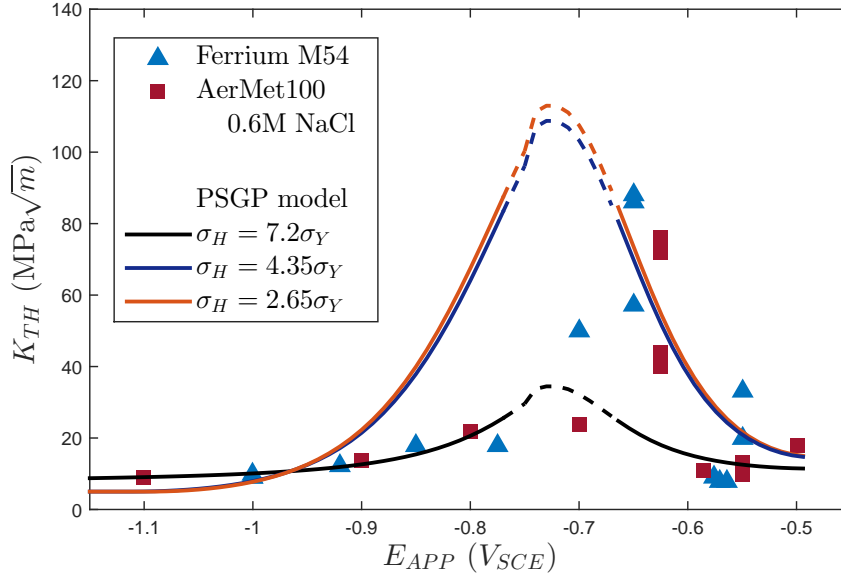
Figure 8.4: Numerical results of  $\sigma_H/\sigma_Y$  versus distance ahead of the blunted crack tip,  $r$ , for the range of  $K_I$  used in HEAC experiments with AerMet™<sub>100</sub>. Theories include: MSGP ( $l = 7 \mu\text{m}$ ), PSGP ( $l_1 = l_2 = l_3 = 7 \mu\text{m}$ ), and conventional plasticity.

$K_{TH}$  versus  $E_{APP}$  is predicted from (8.1) using crack tip hydrogen solubility from either the upper bound given by (8.6) and (8.7) or the lower-bound in (8.6); the results are given in Figures 8.5 and 8.6, respectively. Parts (a) and (b) of each figure show the PSGP and MSGP results, respectively. Three levels of averaged  $\sigma_H/\sigma_Y$  (Table 2) are examined corresponding to  $K_I$  of  $10 \text{ MPa}\sqrt{\text{m}}$ ,  $20 \text{ MPa}\sqrt{\text{m}}$ , and  $40 \text{ MPa}\sqrt{\text{m}}$ . The  $k_{IG}$  is  $1.145 \text{ MPa}\sqrt{\text{m}}$  for each steel, and the  $\alpha''$  and  $\beta'$  are identical to those used for Monel K-500 [180] and steel [170]. This Griffith toughness was estimated based on maximum modeled  $\gamma_S$  for a 100 surface of Fe ( $3.09 \text{ J/m}^2$  [59]) and Poisson's ratio of 0.29. This  $k_{IG}$  yielded a hydrogen-free  $K_{Ic}$  of  $224 \text{ MPa}\sqrt{\text{m}}$  through (8.1), which is reasonably higher than the microvoid-defect based  $K_{Ic}$  ( $130 \text{ MPa}\sqrt{\text{m}}$ ). However, the precise Griffith toughness for a lath or packet interface in the martensitic microstructure of AerMet™<sub>100</sub> is not known

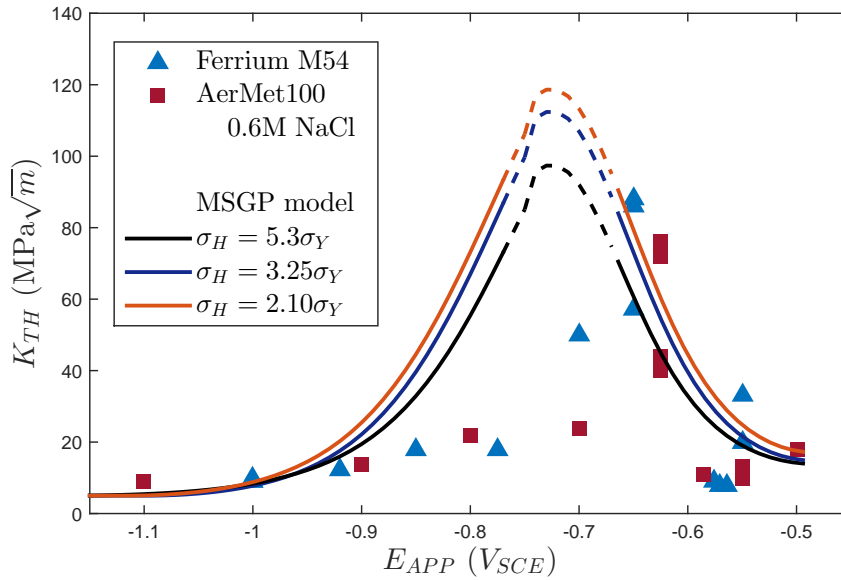
[181]. Each SGP prediction is given by a solid plus dashed curve, and compared to experimental measurements for AerMet<sup>TM</sup><sub>100</sub> and Ferrium<sup>TM</sup>M54 [182, 183]<sup>2</sup>. For each case examined, an average  $\alpha$  is calculated using the six experimental values of  $K_{TH}$  at  $E_{APP}$  of -0.900  $V_{SCE}$  and lower. This regime was selected because hydrogen solubility is well known through (8.6), HEAC is severe (measured  $K_{TH}$  varied between 9  $MPa\sqrt{m}$  and 14  $MPa\sqrt{m}$  with an average of 10.5  $MPa\sqrt{m}$ , and with 3 replicate values for Ferrium<sup>TM</sup>M54 are essentially equal at  $E_{APP}$  of -1.000  $V_{SCE}$ ), and HEAC is fully transgranular associated with martensite interface decohesion [181]. Average  $\alpha$  values are given in the captions of Figures 8.5 and 8.6. The dashed curves show the regime of  $E_{APP}$  where the  $K_{TH}$  model from (8.1) is expected to under-predict true  $K_{TH}$  for HEAC, as justified in the Discussion.

---

<sup>2</sup> The largest  $C_{H-Diff}$  is 6 wppm, and  $C_L$  is about 0.06 wppm, at the most cathodic  $E_{APP}$  examined. As such,  $C_{L\sigma}$  is 0.01 atom fraction H for the highest  $\sigma_H/\sigma_Y$  of 7.2 and the calculations in Figure 8.5 equate  $(1 - C_{L\sigma})$  in (8.4) to 1.

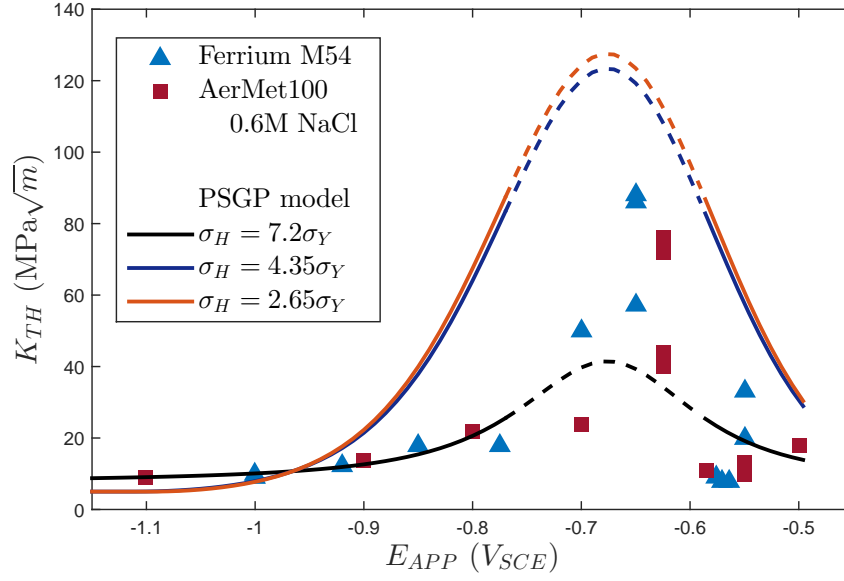


(a)

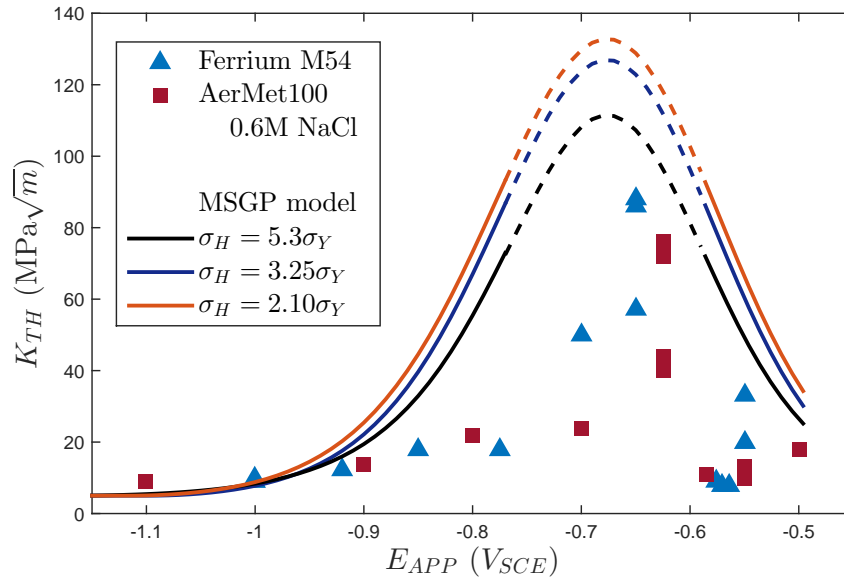


(b)

Figure 8.5: Predicted  $K_{TH}$  versus  $E_{APP}$  from (8.1) for AerMet<sup>TM</sup>100 and Ferrium<sup>TM</sup>M54 in 0.6M NaCl, calculated using upper bound  $C_{H,Diff}$  from (8.6) and (8.7), and calibrated by averaging  $\alpha$  by fitting to six  $K_{TH}$  values measured at  $E_{APP} \leq -0.9 V_{SCE}$ ;  $k_{IG} = 1.145 \text{ MPa}\sqrt{\text{m}}$  for each steel. The  $\sigma_H$  is estimated from either: (a) PSGP or (b) MSGP FE analysis at  $K$  of 10  $\text{MPa}\sqrt{\text{m}}$  (orange line: (a)  $\bar{\alpha} = 81.37 \text{ MPa}\sqrt{\text{m}}$  (at frac H)<sup>-1</sup> and (b)  $\bar{\alpha} = 161.81 \text{ MPa}\sqrt{\text{m}}$  (at frac H)<sup>-1</sup>), 20  $\text{MPa}\sqrt{\text{m}}$  (blue line: (a)  $\bar{\alpha} = 8.18 \text{ MPa}\sqrt{\text{m}}$  (at frac H)<sup>-1</sup> and (b)  $\bar{\alpha} = 35.64 \text{ MPa}\sqrt{\text{m}}$  (at frac H)<sup>-1</sup>) and 40  $\text{MPa}\sqrt{\text{m}}$  (black line: (a)  $\bar{\alpha} = 0.76 \text{ MPa}\sqrt{\text{m}}$  (at frac H)<sup>-1</sup> and (b)  $\bar{\alpha} = 2.65 \text{ MPa}\sqrt{\text{m}}$  (at frac H)<sup>-1</sup>). The  $\sigma_H/\sigma_Y$  listed on each plot increased as  $K_I$  rose from 10 to 20 to 40  $\text{MPa}\sqrt{\text{m}}$ .



(a)



(b)

Figure 8.6: Predicted  $K_{TH}$  versus  $E_{APP}$  from (8.1) for AerMet<sup>TM</sup>100 and Ferrium<sup>TM</sup>M54 in 0.6M NaCl, calculated using lower bound  $C_{H,Diff}$  from (8.6) and (8.7), and calibrated by averaging  $\alpha$  by fitting to six  $K_{TH}$  values measured at  $E_{APP} \leq -0.9 V_{SCE}$ ;  $k_{IG} = 1.145 \text{ MPa}\sqrt{\text{m}}$  for each steel. The  $\sigma_H$  is estimated from either: (a) PSGP or (b) MSGP FE analysis at  $K$  of  $10 \text{ MPa}\sqrt{\text{m}}$  (orange line: (a)  $\bar{\alpha} = 81.37 \text{ MPa}\sqrt{\text{m}}$  (at frac H)<sup>-1</sup> and (b)  $\bar{\alpha} = 161.81 \text{ MPa}\sqrt{\text{m}}$  (at frac H)<sup>-1</sup>),  $20 \text{ MPa}\sqrt{\text{m}}$  (blue line: (a)  $\bar{\alpha} = 8.18 \text{ MPa}\sqrt{\text{m}}$  (at frac H)<sup>-1</sup> and (b)  $\bar{\alpha} = 35.64 \text{ MPa}\sqrt{\text{m}}$  (at frac H)<sup>-1</sup>) and  $40 \text{ MPa}\sqrt{\text{m}}$  (black line: (a)  $\bar{\alpha} = 0.76 \text{ MPa}\sqrt{\text{m}}$  (at frac H)<sup>-1</sup> and (b)  $\bar{\alpha} = 2.65 \text{ MPa}\sqrt{\text{m}}$  (at frac H)<sup>-1</sup>). The  $\sigma_H/\sigma_Y$  listed on each plot increased as  $K_I$  rose from 10 to 20 to 40  $\text{MPa}\sqrt{\text{m}}$ .

The  $E_{APP}$  dependence of  $da/dt_{II}$  is predicted without any adjustable constants using independently established  $D_{H-EFF}$  [185] and  $x_{crit}$  [188]; results are shown for upper bound (Figure 8.7) and lower bound (Figure 8.8)  $C_{H,Diff}$ . PSGP ( $\sigma_H = 7.2\sigma_Y$ , solid line) and MSGP ( $\sigma_H = 5.3\sigma_Y$ , dashed line) predictions are shown in each plot, and compared to  $da/dt_{II}$  measured at  $K_I$  of  $40 \text{ MPa}\sqrt{\text{m}}$  [102, 181]. Each  $C_{H\sigma-crit}$  is calculated through (8.8), using the appropriate  $\alpha$  from the Figures 8.5 and 8.6 fits at  $K_I$  of  $40 \text{ MPa}\sqrt{\text{m}}$ , coupled with the average  $K_{TH}$  and average  $da/dt_{II}$  measured at  $E_{APP}$  of  $-1.000 \text{ V}_{SCE}$ . Downward arrows represent experiments where  $K_{TH}$  exceeded  $40 \text{ MPa}\sqrt{\text{m}}$ , and HEAC was not resolved; all other data are associated with transgranular HEAC [102, 181]. The predictions of the SGP-HEAC model in Figures 8.5 through 8.8 effectively capture the complex dependencies of  $K_{TH}$  and  $da/dt_{II}$  over a wide range of  $E_{APP}$ . Quality of fit and model consistency are considered in the Discussion.

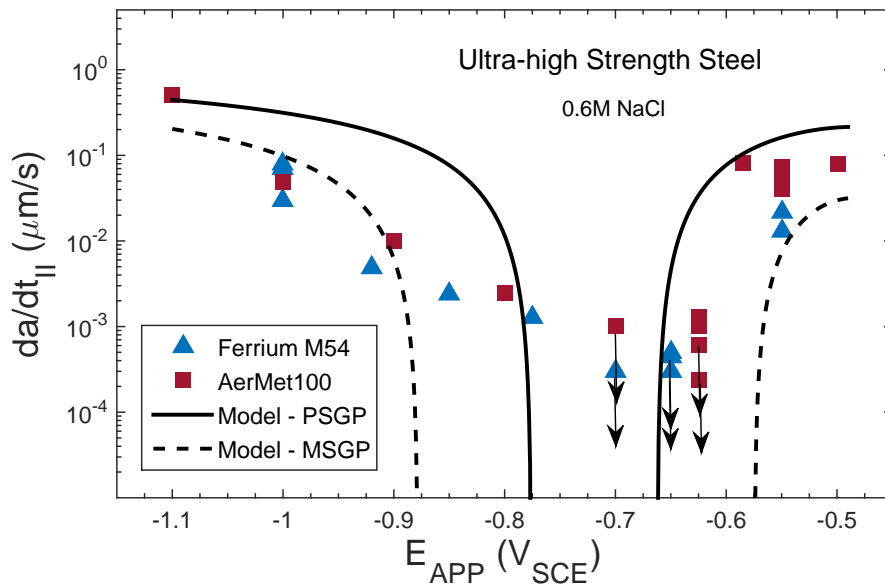


Figure 8.7:  $da/dt_{II}$  versus  $E_{APP}$  predicted from (8.2) with upper bound  $C_{H,Diff}$  from (8.6) and (8.7) for AerMet<sup>TM</sup>100 and Ferrium<sup>TM</sup>M54 in 0.6M NaCl. The  $\sigma_H$  is determined for  $K_I$  of  $40 \text{ MPa}\sqrt{\text{m}}$  using either PSGP (solid line,  $C_{H\sigma-crit} = 18867 \text{ wppm}$  for  $\sigma_H/\sigma_Y = 7.2$ ) or MSGP (dashed line,  $C_{H\sigma-crit} = 3056 \text{ wppm}$  for  $\sigma_H/\sigma_Y = 5.3$ ). Other parameters are  $k_{IG} = 1.145 \text{ MPa}\sqrt{\text{m}}$ .  $D_{H-EFF} = 1 \cdot 10^{-9} \text{ cm}^2/\text{s}$  [185] and  $x_{crit} = 1 \text{ }\mu\text{m}$  [188]

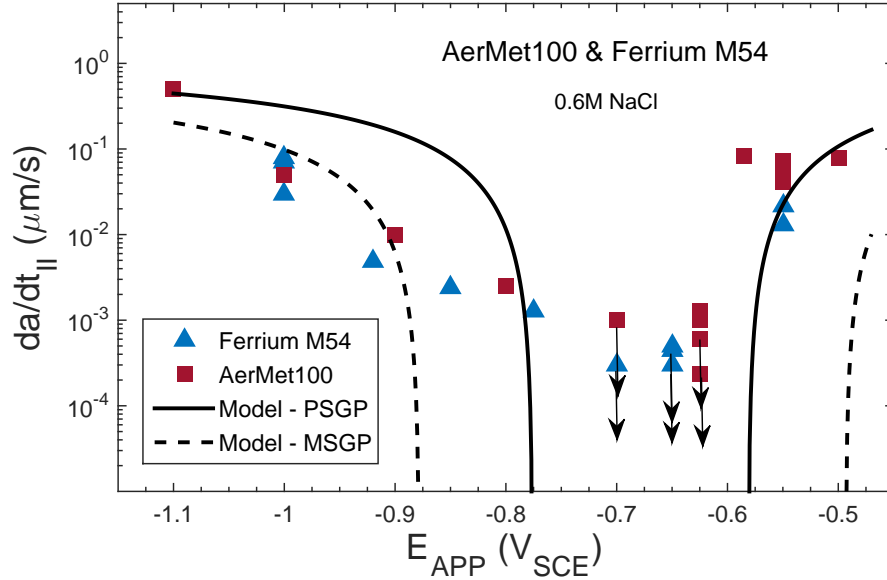


Figure 8.8:  $da/dt_{II}$  versus  $E_{APP}$  predicted from (8.2) with lower bound  $C_{H,Diff}$  from (8.6) for AerMet<sup>TM</sup><sub>100</sub> and Ferrium<sup>TM</sup><sub>M54</sub> in 0.6M NaCl. The  $\sigma_H$  is determined for  $K_I$  of 40 MPa $\sqrt{m}$  using either PSGP (solid line,  $C_{H\sigma-crit} = 18867$  wppm for  $\sigma_H/\sigma_Y = 7.2$ ) or MSGP (dashed line,  $C_{H\sigma-crit} = 3056$  wppm for  $\sigma_H/\sigma_Y = 5.3$ ). Other parameters are  $k_{IG} = 1.145$  MPa $\sqrt{m}$ .  $D_{H-EFF} = 1 \cdot 10^{-9}$  cm<sup>2</sup>/s [185] and  $x_{crit} = 1$   $\mu$ m [188]

## 8.6 DISCUSSION

### 8.6.1 SGP Impact on Hydrogen Cracking

SGP-enhanced large strain FE analysis results reveal a profound influence of GNDs on crack tip deformation for technologically important alloys. Specific simulation results in Figures 8.1, 8.2 and 8.4 establish the following effects attributed to MSGP and PSGP compared to classic plasticity analysis of a blunting crack tip.

- Crack tip stresses are substantially elevated, and the crack opening profile is reduced, due to a high-GNDs density.
- $\sigma_H$  levels from the 3-parameter PSGP model are substantially higher than those predicted by the MSGP formulation.
- The crack tip stress distribution from SGP rises and broadens with increasing  $K_I$ .
- GNDs density and  $\sigma_H$  are elevated over 1 to 20  $\mu$ m ahead of the crack tip, suggesting that SGP plays an important role in hydrogen cracking.

- The maximum in tensile stress with increasing distance from the crack tip is shifted to within 100 nm or less from the crack tip by SGP hardening. The magnitude of SGP-elevated  $\sigma_H/\sigma_Y$  decreases with increasing alloy strength.

Regression analysis of the PSGP simulation results (at  $K_I = 20 \text{ MPa}\sqrt{\text{m}}$ , averaged over the two intervals of  $r$  for the alloys in Table 2) yields  $\sigma_H/\sigma_{YS} = 6300/\sigma_{YS}$  (in MPa). The absolute value of crack tip  $\sigma_H$  is essentially constant (6300 MPa or  $\sim 0.035E$ ). The bounding distance where PSGP elevates crack tip tensile stresses falls from 8  $\mu\text{m}$  to 2.5  $\mu\text{m}$  (at  $K_I = 25 \text{ MPa}\sqrt{\text{m}}$ ) as  $\sigma_{YS}$  rises from 400 to 1725 MPa. The decreasing impact of SGP with increasing alloy flow strength (as well as decreasing  $K_I$ ) is consistent with infinitesimal-strain modeling [28] and explained as follows. Crack tip plastic strain rises steeply as  $r$  approaches the crack tip [101]; the magnitude and bounding distance of this distribution are reduced as  $\sigma_Y$  rises. Reduced gradient zone results in lower  $\rho_G$ , and a smaller SGP contribution to Taylor hardening, while  $\rho_S$  increases for higher strength alloys. These results show that it is imperative to account for the strain gradient in continuum modeling of HEAC and IHAC over a wide range of alloy strengths.

### 8.6.2 FPZ Definition

A critical distance is required to define crack tip  $\sigma_H$  to calculate  $C_{H\sigma}$  through (8.4)  $da/dt_{II}$  in (8.2). Classic plasticity equates this distance to the location of maximum stress [101, 133, 149, 162–169], as evident in Figures 8.1 and 8.4. The associated  $x_{\text{crit}}$  equals 6 to 13  $\mu\text{m}$  for Monel K-500 at  $K_I$  of 25 to 45  $\text{MPa}\sqrt{\text{m}}$  and 5 to 10  $\mu\text{m}$  for AerMet<sup>TM</sup><sub>100</sub> at  $K_I$  of 30 to 50  $\text{MPa}\sqrt{\text{m}}$ . In contrast, empirical analysis suggests that  $x_{\text{crit}}$  is about 1  $\mu\text{m}$  for alloys of different strengths and wide ranging  $K_I$  within Stage II [188]. This shorter distance is consistent with SGP model predictions of substantially elevated crack tip stress.

The SGP results suggest that  $x_{\text{crit}}$  is the location of the highest probability of hydrogen-assisted crack formation, governed by interaction of decreasing  $\sigma_H$  (and decreasing  $C_{H\sigma}$ ) with the increasing number of defect-based initiation sites within the FPZ; each with increasing  $r$ . The details of hydrogen-crack formation are not sufficiently defined to quantify  $x_{\text{crit}}$  following the approach used to model cleavage [190]. Electron microscopy suggests that HELP concentrates stress to promote interface HEDE [158]. Speculatively, the number of crack formation sites scales with  $\rho_G$  and interacts with  $C_{H\sigma}$  to establish  $x_{\text{crit}}$ . For Monel K-500, GNDs density from MSGP is above  $\rho_S$  for  $r$  up to 0.5  $\mu\text{m}$  at  $K_I$  of 15  $\text{MPa}\sqrt{\text{m}}$  and 2.2  $\mu\text{m}$  at 45  $\text{MPa}\sqrt{\text{m}}$  (Figure 8.2). Similar behavior is suggested for AerMet<sup>TM</sup><sub>100</sub>, since

$\sigma_H$  is elevated by MSGP for  $r$  of up to 1 to 6  $\mu\text{m}$  for HEAC relevant  $K_I$  of  $10 \text{ MPa}\sqrt{\text{m}}$  to  $40 \text{ MPa}\sqrt{\text{m}}$  (Figure 8.4).

### 8.6.3 Crack Growth Rate Modeling

As a proxy for statistical analysis in HEAC, an average of the two stress levels in Table 2 was used for each SGP model and  $K_I$ , and  $x_{\text{crit}}$  was taken as  $1.0 \mu\text{m}$ . Figures 8.7 and 8.8 show measured and model predicted  $da/dt_{II}$  agree precisely for AerMet<sup>TM</sup><sub>100</sub> at the most cathodic  $E_{\text{APP}}$  examined. Here, for the PSGP case, severe HEAC is diffusion controlled and the combination of independently measured  $D_{\text{H-EFF}}$  and  $x_{\text{crit}}$  of  $1.0 \mu\text{m}$  predicts measured  $da/dt_{II}$  through (8.2). Reasonable agreement is observed for Monel K-500 at the most cathodic  $E_{\text{APP}}$  below  $-1.000 V_{\text{SCE}}$  (Figure 8.3b); however,  $x_{\text{crit}}$  would have to equal  $0.35 \mu\text{m}$  for precise-model agreement with the single-highest  $da/dt_{II}$ . SGP modeling justifies an  $x_{\text{crit}}$  of order  $1 \mu\text{m}$  for HEAC, at least within the accuracy and relevance of measured  $D_{\text{H-EFF}}$  [191, 192].

The distributions of crack tip  $\sigma_H$  and  $\rho_G$  from SGP-FE analysis simulation can improve the accuracy of hydrogen diffusion models pertinent to HEAC and IHAC. The  $da/dt_{II}$  model in (8.2) does not explicitly include the effects of crack tip stress on hydrogen flux and dislocation trapping of hydrogen on  $D_{\text{H-EFF}}$  (typically from a stress-free hydrogen permeation experiment and approximate trapping analysis [191]). Sophisticated models address such complications [149, 168, 192]; however, these center on blunt-crack  $\sigma_H$  and  $\rho_S$  associated with plastic strain from classic plasticity [101]. In these models, the maximum crack tip  $\sigma_H$  provides a positive stress gradient ahead of the crack tip, which increases the flux of hydrogen from the tip surface to this maximum at  $x_{\text{crit}}$  [149, 167, 168, 187]. However,  $\sigma_H$  monotonically declines with increasing  $r$  due to SGP, at least for distances greater than  $100 \text{ nm}$  (Figures 8.1 and 8.4);  $d\sigma_H/dr$  is mildly negative for MSGP and more strongly for PSGP. The SGP-stress gradient will retard hydrogen diffusion ahead of the crack tip. Second, the predicted GNDs distribution due to SGP (Figure 8.2a) should provide dislocation sites for reversible-hydrogen trapping that reduces  $D_{\text{H-EFF}}$  within the FPZ. Provided the binding energy of hydrogen to GNDs structure is known, equilibrium trapping theory can estimate the effect of a GNDs distribution on the hydrogen diffusivity distribution relevant to the FPZ [173, 191].

SGP modeling (Table 2) establishes that crack tip tensile stress rises with increasing  $K_I$  for the MSGP and PSGP formulations, which appears to be at odds with  $K_I$  independent  $da/dt$  in Stage II [36, 159]. For example,  $\sigma_H$  rises from  $7.2\sigma_{YS}$  to  $16.7\sigma_{YS}$  as  $K_I$  increases

from  $40 \text{ MPa}\sqrt{\text{m}}$  to  $80 \text{ MPa}\sqrt{\text{m}}$  for AerMet<sup>TM</sup>100 (PSGP simulation, Table 2), but  $da/dt$  is constant [102, 181]. The hydrogen-diffusion model in (8.2) shows that  $da/dt_{II}$  depends on  $C_{H\sigma\text{-crit}}/C_{H\sigma}$ ; critically, this ratio is independent of  $K_I$  since each concentration is amplified by the same exponential dependence on  $\sigma_H$  through (8.3) and (8.4)<sup>3</sup>. Any  $K_I$  can be used; however, a lower  $K_I$  somewhat above  $K_{TH}$  reduces  $C_{H\sigma}$ . When  $C_{H\sigma}$  is large ( $\sim 0.5$  to  $1.0$  atom fraction H), stress due to lattice expansion from hydrogen in interstitial sites offsets the lattice dilating impact of  $\sigma_H$  [137, 193]. This issue is important for ultra-high strength steel, high  $K_I$ , and PSGP models (Table 2) where  $\sigma_H/\sigma_Y$  above 9 results in meaningless values of  $C_{H\sigma}$  exceeding 1.0 atom fraction of H in Fe.

#### 8.6.4 SGP-HEAC Model Validation

The results of the present investigation validate the integration of cutting edge SGP-FE analysis formulations with crack electrochemistry and two HEAC models to predict material-environment properties, specifically  $K_{TH}$  and  $da/dt_{II}$  as a function of environmental hydrogen activity. Models, with a single calibration constant, are validated over a broad range of applied polarization using precise experimental measurements of these HEAC properties. Particularly good agreement is reported for a Ni-Cu superalloy (Monel K-500) with cathodic  $E_{APP}$ . The comparison for AerMet<sup>TM</sup>100 and Ferrium<sup>TM</sup>54 steels is good, but hindered by crack mechanics and electrochemical uncertainties dictated by cathodic to anodic  $E_{APP}$ .

##### 8.6.4.1 Monel K-500

The SGP-based predictions of  $K_{TH}$  and  $da/dt_{II}$  versus  $E_{APP}$  quantitatively agree with experimental measurements for a single lot of Monel K-500 stressed under slow-rising  $K_I$  in 0.6M NaCl solution with cathodic polarization. Occluded-crack electrochemistry was previously detailed [112, 183], as was specimen variability due to grain boundary S segregation [180]. The one-length-parameter MSGP and three-term PSGP models of crack tip  $\sigma_H/\sigma_Y$  similarly predict the applied potential dependence of  $K_{TH}$  that agrees with experimental measurements over a range of cathodic  $E_{APP}$  (Figure 8.3a). Moreover,  $C_{H\sigma\text{-crit}}$  calculated from  $K_{TH}$ -calibrated  $\alpha$  predicts the  $E_{APP}$  dependence of  $da/dt_{II}$  that agrees equally well with experimental measurements for both MSGP and PSGP (Figure 8.3b). Since only  $\alpha$  was calibrated at a single-low  $E_{APP}$  ( $-1.000 \text{ V}_{SCE}$ ) to mo-

<sup>3</sup> This ratio is determined by calculation of  $C_{H\sigma}$  at any  $\sigma_H$  (or  $K_I$ ), followed by determination of  $\alpha$  in (8.1) and  $C_{H\sigma\text{-crit}}$  through (8.8) using the same  $\sigma_H$ . As a check for Monel K-500 with  $C_{H\sigma}$  calculated from (8.5) at  $E_{APP} = -1000 \text{ V}_{SCE}$ ,  $C_H/C_{H\sigma\text{-crit}} = 3.25$  for  $\sigma_H/\sigma_Y$  of 8.15 and  $C_H/C_{H\sigma\text{-crit}} = 3.01$  for  $\sigma_H/\sigma_Y$  of 4.70. This 10% difference in  $C_H/C_{H\sigma\text{-crit}}$  is not significant

del  $K_{TH}$ , with all other parameters in (8.2) ( $\alpha''$ ,  $\beta'$ , and  $k_{IG}$ ) justified elsewhere [180], and since no adjustable parameters were used to predict  $da/dt_{II}$ , the models represented by (8.1) and (8.2) are validated and consistent. The impact is clear; the wide-range dependence of HEAC properties on cathodic polarization is predicted with  $\alpha$  calibrated at a single  $E_{APP}$ . This prediction includes an accurate value of the technologically critical potential, above which HEAC is eliminated.

Considering classic plasticity for  $K_{TH}$  of  $17.3 \text{ MPa}\sqrt{\text{m}}$ ,  $\sigma_H/\sigma_{YS}$  is 1.5 at  $1 \text{ }\mu\text{m}$  ahead of the crack tip and 2.6 at the location ( $r = 3 \text{ }\mu\text{m}$ ) of the maximum stress (Figure 8.1). Predictions of  $K_{TH}$  versus  $E_{APP}$  using either of these  $\sigma_H$  levels agree with experimental values with  $\alpha$  of  $209.5 \text{ MPa}\sqrt{\text{m}} (\text{atom frac H})^{-1}$  ( $\sigma_H/\sigma_{YS} = 1.5$  and  $C_{H\sigma-crit}$  of 12.3 through (8.8)) or  $\alpha$  of  $116.0 \text{ MPa}\sqrt{\text{m}} (\text{atom frac H})^{-1}$  ( $\sigma_H/\sigma_{YS} = 2.6$  and  $C_{H\sigma-crit}$  of 22.2). These classic plasticity predictions are essentially identical to the SGP-based results in Figure 8.3a. However, the stress maximum in the classic plasticity model suggests that  $x_{crit}$  is 3 to 14  $\mu\text{m}$ , for  $K_I$  between 15 and 45  $\text{MPa}\sqrt{\text{m}}$ , rather than  $1 \text{ }\mu\text{m}$  justified by SGP. As such, classic plasticity-based prediction of  $da/dt_{II}$  is reduced by 3-fold to 14-fold at any  $E_{APP}$  compared to the SGP curves in Figure 8.3b. While  $K_{TH}$  modeling does not distinguish the most accurate crack tip stress field, the SGP models provide more accurate predictions of  $da/dt_{II}$  compared to classic plasticity. This behavior is governed by the smaller SGP-based  $x_{crit}$  of  $1 \text{ }\mu\text{m}$  and supports the relevance of crack tip stress elevation due to GNDs.

#### 8.6.4.2 *AerMet<sup>TM</sup>100 and Ferrium<sup>TM</sup>M54*

SGP-HEAC model predictions of  $K_{TH}$  and  $da/dt_{II}$  versus  $E_{APP}$  qualitatively agree with measurements for AerMet<sup>TM</sup>100 and Ferrium<sup>TM</sup>M54 stressed under slow-rising  $K_I$  in 0.6M NaCl solution, as shown in Figures 8.5 through 8.8. First, absolute values of  $K_{TH}$  at high potentials ( $> -0.600 \text{ V}_{SCE}$ ) are accurately predicted using the single  $\alpha$  calibrated at low  $E_{APP}$  (Figure 8.5). In each regime transgranular HEAC is severe. Agreement is quantitatively strong for the highest level of crack tip hydrostatic stress from the PSGP simulation in Figure 8.5a. Second, the window of  $E_{APP}$  between  $-0.600 \text{ V}_{SCE}$  and  $-0.800 \text{ V}_{SCE}$ , where  $K_{TH}$  rises sharply and  $da/dt_{II}$  falls toward zero, is captured, as governed by the minimum in  $C_{H-Diff}$  versus  $E_{APP}$  given by (8.6) and (8.7). Third, reasonable predictions of  $da/dt_{II}$  without any adjustable parameters, using  $C_{H\sigma-crit}$  calculated from  $\alpha$ , demonstrate the consistency of the HEAC models given by (8.1) and (8.2).

Interpretation of the fit between the various SGP-HEAC model predictions and experimental  $K_{TH}$  and  $da/dt_{II}$  measurements is complicated for the steels. Model assessment is demanding given the

change in occluded crack chemistry, which accompanies transition from cathodic to anodic polarization through the OCP of about  $-0.525 V_{SCE}$ . Electrochemical analysis of crack tip  $C_{H,Diff}$  is uncertain for  $E_{APP}$  above about  $-0.750 mV_{SCE}$  owing to limited crack chemistry measurements [182]. It is only possible to bound crack tip hydrogen solubility using (8.6) and (8.7), leading to the upper and lower bound predictions of  $K_{TH}$  (Figure 8.5 and 8.6) and  $da/dt_{II}$  (Figures 8.7 and 8.8). The best prediction of the  $E_{APP}$  dependence of these HEAC properties likely resides between these bounds. Second, the dashed parts of the predicted curves in Figures 8.5 and 8.6 show the regime of  $E_{APP}$  where  $C_{H-Diff}$  is less than 0.8 wppm and should promote mixed transgranular hydrogen-cracking and ductile microvoid fracture [138]. These dashed lines should under-predict measured  $K_{TH}$  since the HEAC model in (8.1) does not capture the added cracking resistance associated with ductile growth. Third,  $K_{TH}$  and low  $da/dt$  are difficult to measure when plasticity at higher  $K_I$  gives a false indication of low-rate crack extension from electrical potential measurement [181]. The variability of measured  $K_{TH}$  for  $-0.800 V_{SCE} < E_{APP} < -0.625 V_{SCE}$  is due in part to this limitation. Finally, surface reaction may interact with hydrogen diffusion for  $E_{APP}$  below about  $-0.750 V_{SCE}$  [194].  $da/dt_{II}$  from the hydrogen diffusion model in (8.2) is an upper bound when surface reaction rate is slow.

Given these considerations, Figures 8.5 through 8.8 establish that the best agreement between measured and predicted  $K_{TH}$  and  $da/dt_{II}$  is achieved over a wide range of  $E_{APP}$  for PSGP-based  $\sigma_H/\sigma_Y$  of 7.2. These figures suggest that  $\sigma_H$  as low as  $6.0\sigma_Y$  will provide similar-good predictions. However, lower crack tip stress levels ( $2.1 < \sigma_H/\sigma_Y < 5.3$ ) provide poor agreement between measured and modeled HEAC properties for either the upper or lower bound hydrogen solubilities. This behavior differs from the  $\sigma_H$  insensitivity of the HEAC predictions for Monel K-500 (Figure 8.3), and is due to the wider range of  $E_{APP}$  examined for the steels, as well as the absolute values of  $C_{H\sigma}$ , which can be very high for ultra-high strength steel. For this high  $\sigma_H$  regime, the bounded definition of crack tip hydrogen solubility in (8.6) and (8.7) is affirmed, as is particularly evident by comparison of the solid line predictions of  $da/dt_{II}$  versus  $E_{APP}$  above  $-0.800 V_{SCE}$  in Figures 8.7 and 8.8 (speculatively, crack growth rates for  $E_{APP}$  below  $-0.850 V_{SCE}$  are lower than the hydrogen-diffusion model prediction due to surface reaction rate limitation [194]). The  $K_{TH}$  versus  $E_{APP}$  predictions are mixed. Upper bound hydrogen solubility provides the absolute best agreement in  $K_{TH}$  for  $E_{APP}$  above about  $-0.600 V_{SCE}$  and below  $-0.700 V_{SCE}$  (Figure 8.5a), but the lower bound  $C_{H,Diff}$  relationship (Figure 8.6a) better captures the range of  $E_{APP}$  ( $-0.770$  to  $-0.585 V_{SCE}$ )

where the dashed line defines the lower bound on the variability in  $K_{TH}$  explained by plasticity-microvoid cracking and hindered crack growth resolution. It is likely that specimen to specimen differences are amplified for  $E_{APP}$  above about  $-0.800 V_{SCE}$  due to the strong sensitivity of crack tip hydrogen production and uptake to small changes in: (a) crack surface passivity (reduced by acidification and  $Cl^-$  intrusion), and/or (b) the magnitude of crack tip potential reduction below  $E_{APP}$  (due to increased crack tip occlusion from microscopic crack path tortuosity and corrosion product deposition) [182]. Crack chemistry modeling has not yet quantified such effects on  $C_{H,Diff}$  [165].

Considering classic plasticity analysis, the very low  $\sigma_H/\sigma_Y$  at  $x_{crit}$  of 1.0 to 2.0  $\mu m$  (0.8 to 1.8, Table 2), or at the location of maximum stress ( $r = 1.4$  to 12  $\mu m$ , Figure 8.4), provide poor predictions of  $K_{TH}$  and  $da/dt_{II}$  versus  $E_{APP}$ . Such predictions are similar to those from the lower  $\sigma_H/\sigma_Y$  SGP models in Figures 8.5 through 8.8, provided that  $\alpha$  is increased to  $475 \text{ MPa}\sqrt{m} (\text{atom frac H})^{-1}$ . Moreover,  $x_{crit}$  defined based on the  $\sigma_H$  maximum, predicts  $da/dt_{II}$  that are substantially below measured values. Overall, the comparisons in Figures 8.5 through 8.8 establish the necessity for high crack tip  $\sigma_H$  equal or above  $6\sigma_Y$ , in order to predict the wide-range  $E_{APP}$  dependencies of  $K_{TH}$  and  $da/dt_{II}$ . This result justifies the necessity for crack tip SGP and relevance of the three-parameter PSGP formulation. However, this finding is problematic for  $K_{TH}$  modeling because Table 2 shows that  $\sigma_H/\sigma_Y$  above 6 is only justified by the large strain FE-PSGP analysis for  $K_I$  of 35 to 40  $\text{MPa}\sqrt{m}$ . It is necessary to identify the cause of high crack tip stresses, sustained over  $r$  of  $\sim 1 \mu m$ , for low  $K_I$  below 20  $\text{MPa}\sqrt{m}$ .

It is difficult to justify very high crack tip stresses for ultra-high strength steels using the phenomenological blunt crack SGP approach per se. First, it is unlikely that the requirement for high crack tip stresses will be relaxed by changes in other aspects of the HEAC models. The parameters in the  $K_{TH}$  model ( $\alpha''$ ,  $\beta'$ , and  $k_{IG}$  in (8.1)) and  $da/dt_{II}$  model ( $D_H$  in (8.2)) were independently justified [112, 180, 183, 185] and are consistent with the original analysis by Gerberich and coworkers [137, 170, 186]. Second,  $l_i$  is a primary uncertainty in the PSGP and MSGP models. A specific value has not been reported for an ultra-high strength steel with an unrecrystallized fine-scale martensitic structure with high interfacial area [181] and high  $\rho_S$  ( $10^{16} m^{-2}$  [195]) without strain hardening. As such, an SGP-FE sensitivity study was conducted for a single  $K_I$  (20  $\text{MPa}\sqrt{m}$ ). In both SGP formulations,  $\sigma_H/\sigma_Y$  (at  $r < 2-5 \mu m$ ) rises as  $l_{ref}$  increases from 1 to 15  $\mu m$  (constant  $l_{ref}$  is assumed since different weighting for  $l_2$  and  $l_3$  has little influence in the

large strain PSGP models [76]). For example, at  $r = 1 \mu\text{m}$ ,  $\sigma_H/\sigma_Y$  rises from 2.1 to 3.5 for MSGP and from 1.8 to 3.8 for PSGP, as  $l_i$  increases from  $1 \mu\text{m}$  to  $15 \mu\text{m}$ . These  $\sigma_H$  elevations do not achieve 6 to 7-times  $\sigma_Y$ , extending over  $r$  of 1-2  $\mu\text{m}$ , that is necessary to accurately predict the  $E_{APP}$  dependency of  $K_{TH}$  (and  $da/dt_{II}$  for Stage II  $K_I$  below about  $30 \text{MPa}\sqrt{\text{m}}$ ). There is no indication that alternate values of  $l_1$ ,  $l_2$ , and  $l_3$  yield such high crack tip stresses.

Other approaches predict high crack tip stresses, but only over distances that are small compared to an  $\chi_{crit}$  of  $1 \mu\text{m}$  ahead of the crack tip. As an upper bound,  $\sigma_H$  from the singular terms of the plane strain elastic crack tip stress distribution only exceeds  $7\sigma_Y$  at  $r = 1 \mu\text{m}$  for  $K_I$  above  $33 \text{MPa}\sqrt{\text{m}}$ ; even singular-elastic stresses are not sufficient. Dislocation free zone (DFZ) models show that the net crack tip stress field is reduced below the singular-elastic field [171, 172]. The model represented by (8.1) is based on a DFZ approach, with the elastic crack tip stress field shielded by a pile-up of dislocations on a single slip plane coupled with a super-dislocation to capture “far field” plastic zone [170]. Very high crack tip  $\sigma_H/\sigma_Y$  was predicted, but only sustained over  $r$  less than 100 nm [137].

Enhancements to the continuum large strain elastic-plastic SGP-FE analysis could explain very high crack tip stresses extending  $\sim 1 \mu\text{m}$  ahead of the crack tip. The PSGP and MSGP stress fields (Figures 8.1 and 8.4) were calculated for a smoothly blunting crack [101]. SGP hardening is likely to be elevated for a geometrically “sharp” or irregular crack tip with reduced relaxation of the singularity. A tip that blunts to form a sharp corner could promote locally high stresses not relaxed by regular-geometric blunting [196]. Tip shape may be controlled by microstructural enforcement of the HEAC path, typically localized along austenite grain boundaries in Ni-superalloys and lath-martensite interfaces in modern ultra-high strength steels. Slip morphology, influenced by HELP [158], could impact crack tip shape. In situ loading and concurrent SEM stereo imaging of transgranular fatigue crack and intergranular HEAC tips demonstrated much less blunting for the latter [197]. Such research is required to establish the details of HEAC tip shape evolution over a range of  $K_I$ , and to build large strain SGP-based FE simulations of local crack tip stresses and GNDs density. Alternatively, microstructure-scale stresses can be elevated by slip morphology, dislocation substructure, and grain-elastic anisotropy [167]. Research is required to integrate local strain hardening due to SGP-GNDs with microstructure-scale stresses about a crack tip. This combination could lead to the high stresses and a micro-meter scale process zone necessary to model HEAC in complex alloys.

## 8.7 CONCLUSIONS

Large strain finite element analysis of crack tip stress, augmented by phenomenological and mechanism-based strain gradient plasticity formulations for a blunt crack, is integrated with electrochemical assessment of occluded-crack tip hydrogen solubility and hydrogen-decohesion based damage models to predict hydrogen assisted crack growth properties. Predictions agree with a robust data base for a high strength Ni superalloy and two modern ultra-high strength martensitic steels stressed in an aqueous hydrogen-producing environment. Conclusions are as follows.

- Large strain FE models establish a profound influence of SGP on crack tip stress and strain; GNDs density increases, crack tip stresses are elevated but do not exhibit a near-tip maximum, and crack opening is reduced compared to classic blunt-crack plasticity.
- The impact of SGP decreases with increasing alloy strength, but in all cases hydrostatic stress enhancement leads to locally high crack tip hydrogen concentration to enable damage; it is imperative to account for SGP hardening in modeling of hydrogen cracking.
- Integrated SGP, occluded-crack electrochemistry, and HEAC models effectively predict the dependencies of threshold stress intensity and hydrogen-diffusion limited Stage II crack growth rate on applied electrode potential for Monel K-500 and ultra-high strength steel (AerMet<sup>TM</sup>100 and Ferrium<sup>TM</sup>M54) in NaCl solution with a single calibration constant.
- For Monel with cathodic polarization,  $K_{TH}$  is accurately predicted using classic and SGP formulations of stress; however, Stage II crack growth rate is best predicted by the SGP descriptions that justify a critical distance of 1  $\mu\text{m}$  due to crack tip stress elevation from GNDs hardening.
- For AerMet<sup>TM</sup>100 and Ferrium<sup>TM</sup>M54, measured and modeled  $K_{TH}$  and  $da/dt_{II}$  quantitatively agree for cathodic and anodic potentials, within the bounds of somewhat uncertain crack tip H solubility, but only for crack tip  $\sigma_H/\sigma_Y$  of 6 to 8, which justifies SGP hardening and the relevance of a three-length PSGP model.
- Such high levels of crack tip  $\sigma_H/\sigma_Y$ , extending 1  $\mu\text{m}$  beyond the crack tip, are not sufficiently predicted by PSGP simulation for low  $K_I$  typical of  $K_{TH}$  for the steels. The necessary-high stress is speculatively attributed to SGP interacting with crack tip geometry and/or HELP-sensitive microstructure-scale stresses.

## CONCLUSIONS

---

### 9.1 ACHIEVEMENTS

A general purpose numerical framework to assess fracture and damage by means of gradient plasticity models has been developed. The main classes of [SGP](#) formulations have been successfully implemented, validated and used to address several applications of particular interest from the structural integrity perspective. Among the different numerical solutions employed, it is certainly worth remarking that two novel contributions have been presented. Namely, (i) an [X-FEM](#) scheme for mechanism-based [SGP](#) formulations and (ii) a general purpose [FE](#) implementation for gradient theories involving the plastic spin. The latter rests on two extremum principles and allows for an accurate modeling of both viscoplastic and rate independent material responses incorporating dissipative and energetic higher order terms. The former builds on [MSG](#) plasticity and takes advantage of its known asymptotic stress singularity to enrich the numerical solution. The investigation of crack tip fields reveals that the new enriched framework proposed significantly outperforms the standard [FE](#) solution, avoiding the convergence problems inherent to large element distortions and identifying a field where the use of the [X-FEM](#) could be of notable relevance.

The robustness of the aforementioned numerical framework is proven by investigating crack tip mechanics under load levels relevant to engineering practice, a very computationally demanding problem. Thus, the role of [GNDs](#) in fracture and damage has been thoroughly examined and the following achievements must be highlighted:

- Crack tip fields have been comprehensively characterized within a finite deformation framework.
- A thorough parametric study has been conducted, enabling to infer regimes where gradient effects are of significant relevance, as a function of material properties, constraint scenarios and applied loads.
- Predictions from different classes of [SGP](#) formulations have been compared, assessing the outcome on crack tip mechanics of the different constitutive prescriptions employed to account for [GNDs](#) in continuum modeling.

- The influence on crack tip fields of higher order energetic and dissipative contributions - a common feature among the majority of the most advanced **SGP** models - has been comprehensively examined.
- Hydrogen diffusion towards the crack tip has been modeled accounting for the influence of **GNDs** and the important implications of the results in the understanding of hydrogen embrittlement mechanisms extensively discussed.
- A novel **SGP**-based **HEAC** model has been developed, which has proven to be able to quantitatively predict hydrogen cracking thresholds and subcritical crack growth rates for a wide range of surface applied potentials.

It is therefore expected that the work developed during the present doctoral thesis will lead to a rational application of strain gradient models to serve as basis for prognosis of structural performance.

## 9.2 CONCLUDING REMARKS

The existence of **GNDs** ahead of the crack tip has been recognized since the early days of the development of **SGP** theories [3]. However, the role of strain gradients on fracture problems has not been properly assessed. In this work, crack tip mechanics are investigated by means of **SGP** within a finite deformation framework under conditions relevant for engineering practice. The results reveal a very strong effect of **GNDs** that could have important implications in fracture and damage modeling. Particularly,

- Large gradients of plastic strain in the vicinity of the crack promote local strain hardening, leading to crack tip stresses that are much larger than those predicted by means of classic plasticity.
- Due to the contribution of the plastic strain gradients to the work hardening of material, crack tip blunting is significantly attenuated, suppressing the local stress reduction intrinsic to conventional plasticity predictions. Consequently, the influence of **GNDs** increases largely when large strains are accounted for.
- The parametric study reveals, for material properties and load levels of interest for practical applications, a **GNDs**-dominated length of several tens of micrometers ahead of the crack and stress levels that can be up to 20-40 times the predictions of conventional theories close to the crack tip.

Results reveal a major influence of strain gradients, as the domain where **GNDs** significantly impact crack tip fields is of the order of the critical distance of many damage mechanisms. This is particularly the

case in hydrogen assisted cracking, where damage nucleates within a few microns to the crack tip and the hydrostatic stress plays a fundamental role. Hydrogen embrittlement has been investigated by means of SGP by first assessing the role of GNDs in hydrogen transport to the FPZ and subsequently modeling hydrogen-assisted cracking from a gradient-enhanced crack tip characterization. The following key issues must be highlighted:

- Very high levels of lattice hydrogen concentration are attained in the vicinity of the crack when GNDs are accounted for in the modeling. SGP predictions therefore suggest a predominant role of the HEDE mechanism, as large levels of reversibly-trapped hydrogen are also likely to be attained close to the crack tip due to the increased dislocation density associated with large gradients of plastic strain.
- Very promising predictions of the stress intensity factor threshold  $K_{TH}$  for cracking initiation and the stage II subcritical crack growth rate  $da/dt_{II}$  are obtained by means of an SGP-based HEAC model. A quantitative agreement is observed with experimental data of a Nickel superalloy and a very high strength steel for a wide range of environmental conditions.

The results of the present doctoral thesis will hopefully contribute to bridge the gap between macroscopic modeling of cracking and the atomistic mechanisms of fracture.

### 9.3 FUTURE WORK

The results highlight the need to comprehensively embrace SGP theories in the modeling of many damage mechanisms. Hence, future work will be mainly oriented to incorporate the influence of GNDs in continuum damage characterization. In this regard, it is necessary to remark that phenomenological modeling of micron-scale plasticity is a field in continuous development. Current efforts are devoted to (i) overcome the physical deficiencies of present SGP models [18], (ii) explore different forms of the free energy so as to consistently capture the behavior observed in the experiments [59] and (iii) link the length scale(s) with the underlying microstructure [198, 199]. The impact on fracture assessment of novel constitutive formulations must be investigated with the aim of improving crack tip characterization.

Encouraging results have been obtained in HEAC modeling when gradient effects are accounted for, but further research is needed to gain insight into the understanding of hydrogen embrittlement mechanisms. Particularly appealing topics for future research are

the kinetics of hydrogen trapping and the use of hydrogen-sensitive cohesive zone models under both monotonic and cyclic loading conditions.

Damage without the presence of hydrogen also deserves particular interest. Given the size of their domain of influence ahead of the crack, GNDs will most probably have a profound impact on probabilistic cleavage assessment [108] and ductile damage characterization [105, 106]. Regarding the latter, while a macroscopic yield criterion has been recently derived to capture size effects in void growth [200], assessment of practical applications is hindered by the absence of a complete numerical framework.

Other applications where GNDs are likely to play a major role are transformation induced plasticity (TRIP) steels (where the strengthening mechanisms cannot be captured by conventional theories [201]) and metal/ceramic functionally graded materials [202, 203].

A large theoretical and numerical literature has appeared seeking to encapsulate strain gradient effects into a theory of micron scale plasticity [22]. However, critical experiments are needed to achieve a major breakthrough in phenomenological gradient plasticity modeling. There is a strong need to develop novel experimental methodologies that will allow to measure the influence of GNDs in a number of configurations. In this regard, it seems particularly interesting to use small scale techniques (such as the Small Punch Test [204, 205]), which have shown through the years to be a reliable tool for estimating the mechanical properties of metallic materials.

## CONCLUSIONES

---

### 9.1 LOGROS

Se ha desarrollado un marco numérico de propósito general para examinar la fractura y el daño a partir de modelos de gradientes de deformación plástica. Así, las principales clases de formulaciones *SGP* se han implementado exitosamente, validado y empleado para analizar varias aplicaciones de particular interés para la integridad estructural. De entre las diferentes soluciones numéricas empleadas, cabe destacar la propuesta de dos novedosas contribuciones. Estas son, (i) una metodología *X-FEM* para las formulaciones *SGP* basadas en mecanismos y (ii) una implementación de propósito general para teorías de gradientes que incorporan el rotacional plástico por medio del método de los elementos finitos. Esta última se basa en dos principios de extremos y permite una modelización precisa tanto de un comportamiento viscoplástico del material como independiente de la velocidad de deformación, incorporando a su vez términos disipativos y energéticos de orden superior. La metodología *X-FEM* se basa en la teoría *MSG* y toma ventaja de su solución tensional asintótica para enriquecer la formulación numérica. El análisis de los campos tensionales en el frente de grieta revela una eficiencia mucho mayor que la de la solución convencional de elementos finitos, evitando así los problemas de convergencia inherentes a la distorsión de los elementos e identificando un campo donde el uso del *X-FEM* podría tener una importancia muy significativa.

La fiabilidad del marco numérico mencionado se demuestra con la modelización de probetas agrietadas bajo niveles de carga relevantes para casos prácticos ingenieriles, un problema muy exigente computacionalmente. Así, se investiga minuciosamente el papel de las dislocaciones geoméricamente necesarias en la fractura y el daño, destacando los siguientes logros:

- Los campos tensionales en el frente de grieta se han caracterizado exhaustivamente en el marco de la teoría de deformaciones finitas.
- Se ha llevado a cabo un completo estudio paramétrico, permitiendo así identificar las situaciones donde la influencia del gradiente es de particular importancia, en función de las propiedades del material, la constricción y la carga aplicada.

- Se ha establecido una comparativa entre las predicciones de las diferentes clases de formulaciones SGP, evaluando la influencia de las diferentes ecuaciones constitutivas empleadas para incorporar el efecto de las dislocaciones geoméricamente necesarias en la modelización de la fractura en el medio continuo.
- Se ha examinado minuciosamente la influencia de contribuciones energéticas y disipativas de orden superior - una característica común entre la mayoría de los modelos SGP más avanzados - en los campos tensionales mas allá de la punta de la grieta.
- Se ha modelizado la difusión de hidrógeno hacia la zona de proceso de fractura considerando la influencia de las dislocaciones geoméricamente necesarias y se han investigado en profundidad las importantes implicaciones de los resultados en la compresión de los mecanismos de fragilización por hidrógeno.
- Se ha desarrollado un nuevo modelo que, a partir de las teorías SGP, es capaz de predecir cuantitativamente el umbral de inicio del agrietamiento asistido por hidrógeno y la tasa de crecimiento subcrítica de la grieta en un amplio rango de potenciales externos.

Se espera por tanto que el trabajo desarrollado durante la presente tesis doctoral dé lugar a una aplicación racional de teorías de gradientes de deformación plástica en el análisis de la integridad de elementos estructurales.

## 9.2 CONCLUSIONES

La existencia de dislocaciones geoméricamente necesarias en la vecindad de la punta de la grieta es un hecho reconocido desde los inicios del desarrollo de teorías SGP [3]. Sin embargo, el papel de los gradientes de deformación en problemas de fractura no ha sido evaluado adecuadamente. En este trabajo se investiga el comportamiento mecánico en la punta de la grieta por medio de modelos SGP considerando grandes deformaciones y condiciones pertinentes para la práctica ingenieril. Los resultados revelan un efecto muy fuerte de las dislocaciones geoméricamente necesarias que podrían tener importantes implicaciones en la modelización de la fractura y el daño. Particularmente,

- La existencia de fuertes gradientes espaciales de deformación plástica en la vecindad de la grieta promueve un endurecimiento local, que se traduce en un nivel tensional mucho mayor que el estimado por medio de la plasticidad clásica.
- El enromamiento de la grieta disminuye significativamente debido a la contribución de los gradientes de deformación plástica

al trabajo de endurecimiento por deformación del material, suprimiendo así la reducción local de la tensión intrínseca a las predicciones de la plasticidad convencional. En consecuencia, la influencia de las dislocaciones geoméricamente necesarias se incrementa en gran medida cuando se consideran grandes deformaciones.

- El estudio paramétrico desarrollado revela, para propiedades del material y niveles de carga de interés para aplicaciones prácticas, una distancia mas allá de la punta de la grieta dominada por las dislocaciones geoméricamente necesarias de varias decenas de micrómetros. Además, el nivel tensional puede ser 20-40 veces superior a las predicciones de las teorías convencionales cerca de la punta de la grieta.

Los resultados obtenidos revelan una influencia importante de los gradientes de deformación, ya que el tamaño del dominio donde las dislocaciones geoméricamente necesarias tienen un impacto significativo es del orden de la distancia crítica de muchos mecanismos de daño. Este es particularmente el caso del agrietamiento asistido por hidrógeno, donde el daño se inicia a pocos micrómetros de la punta de la grieta y la tensión hidrostática desempeña un papel fundamental. La fragilización por hidrógeno es por consiguiente investigada por medio de modelos [SGP](#), evaluando en primer lugar el papel de las dislocaciones geoméricamente necesarias en el transporte de hidrógeno hacia la zona de proceso de fractura y modelizando a continuación el agrietamiento asistido por hidrógeno a partir de una caracterización de la grieta considerando el efecto gradiente. Entre otros aspectos, las siguientes cuestiones claves del estudio merecen especial mención:

- Se alcanzan niveles de concentración de hidrógeno en la red muy altos en la vecindad de la grieta cuando se incorpora la influencia de las dislocaciones geoméricamente necesarias en la modelización. Las predicciones basadas en modelos [SGP](#) sugieren por consiguiente un papel predominante del mecanismo de descohesión atomística, ya que muy posiblemente existan también altos niveles de hidrógeno atrapado de forma reversible cerca de la punta de la grieta a consecuencia de la mayor densidad de dislocaciones asociada a los gradientes de deformación plástica.
- Se obtienen estimaciones muy prometedoras del umbral del factor de intensidad de tensiones  $K_{TH}$  para el inicio del agrietamiento y de la velocidad subcrítica de crecimiento de grieta en la etapa II  $da/dt_{II}$  por medio de un modelo de agrietamiento asistido por el medio ambiente basado en teorías [SGP](#). Así, se

observa una concordancia cuantitativa con los datos experimentales para un amplio rango de condiciones ambientales en una superaleación de níquel y en un acero de muy alta resistencia.

Por consiguiente, se aspira a que los resultados de la presente tesis doctoral ayuden a cerrar la brecha entre la modelización macroscópica del agrietamiento y los mecanismos atomísticos de fractura.

### 9.3 TRABAJO FUTURO

Los resultados ponen de manifiesto la necesidad de adoptar sistemáticamente las teorías SGP en la modelización de numerosos mecanismos de daño. Así, el trabajo futuro estará orientado principalmente a incorporar la influencia de las dislocaciones geoméricamente necesarias en la caracterización del daño en el medio continuo. A este respecto, es necesario remarcar que la modelización fenomenológica de la plasticidad a escala micrométrica es un campo en continuo desarrollo. A día de hoy, los esfuerzos investigadores están principalmente orientados a (i) solventar las deficiencias físicas de los actuales modelos SGP [18], (ii) explorar diferentes expresiones de la energía libre que permitan capturar consistentemente el comportamiento observado en los experimentos [59] y (iii) enlazar los parámetros de escala con la microestructura subyacente [198, 199]. Es preciso investigar concienzudamente el impacto sobre la evaluación de la integridad estructural de las nuevas formulaciones constitutivas con el objetivo de mejorar la caracterización cuantitativa del comportamiento mecánico en la punta de la grieta.

Se han obtenido resultados alentadores en la predicción del agrietamiento asistido por hidrógeno cuando se incorpora la influencia de los gradientes de deformación en la modelización. Sin embargo, es necesario un mayor esfuerzo investigador para profundizar en la comprensión de los mecanismos de fragilización por hidrógeno. Temas particularmente atractivos para futuros trabajos son la cinética del atrapamiento de hidrógeno y el uso de formulaciones cohesivas sensibles a la concentración de hidrógeno, tanto para condiciones de carga monotónica como cíclica.

La evaluación del daño - sin la presencia de hidrógeno - también merece especial interés. Dado el tamaño del dominio de influencia de las dislocaciones geoméricamente necesarias mas allá de la punta de la grieta, éstas posiblemente tengan un impacto muy significativo en la caracterización probabilística de la fractura por clivaje [108] y en la modelización del daño dúctil [105, 106]. Al respecto de este último campo, aunque se ha derivado recientemente un criterio de plastificación macroscópica para capturar los efectos de escala en el crecimiento de microhuecos [200], la evaluación de aplicaciones

prácticas se ve obstaculizada por la ausencia de un completo marco numérico.

Otras aplicaciones donde las dislocaciones geoméricamente necesarias pueden jugar un papel fundamental son los aceros de transformación inducida por plasticidad (TRIP) - donde los mecanismos de fortalecimiento no pueden ser capturados por las teorías convencionales [201] - y los materiales funcionalmente graduados de matriz metálica [202, 203].

Un notable esfuerzo investigador ha ido destinado la formulación de modelos teóricos y su correspondiente implementación numérica para incorporar los efectos de los gradientes de deformaciones plásticas en una teoría de la plasticidad para la escala micrométrica [22]. Sin embargo, un avance significativo en el desarrollo de modelos fenomenológicos de gradientes de deformaciones plásticas requiere de la realización de experimentos críticos. Así, existe una fuerte necesidad de desarrollar nuevas metodologías experimentales que permitan medir la influencia de las dislocaciones geoméricamente necesarias en diversas configuraciones. En este sentido, parece particularmente interesante el uso de técnicas de ensayo de miniatura (como el ensayo de miniatura de punzonado [204, 205]) que han demostrado a través de los años ser una herramienta fiable para estimar las propiedades mecánicas de los metales.



## BIBLIOGRAPHY

---

- [1] W.D. Nix and H. Gao. «Indentation size effects in crystalline materials: a law for strain gradient plasticity.» In: *Journal of the Mechanics and Physics of Solids* 46 (1998), pp. 411–425. DOI: [10.1016/S0022-5096\(97\)00086-0](https://doi.org/10.1016/S0022-5096(97)00086-0).
- [2] L. Valdevit and J.W. Hutchinson. «Plasticity Theory at Small Scales.» In: *Encyclopedia of Nanotechnology* 2 (2012), pp. 2147–2154. DOI: [10.1007/978-90-481-9751-4\\_272](https://doi.org/10.1007/978-90-481-9751-4_272).
- [3] N.A. Fleck, G.M. Muller, M.F. Ashby, and J.W. Hutchinson. «Strain gradient plasticity: theory and experiment.» In: *Acta Metallurgica et materialia* 42 (1994), pp. 457–487. DOI: [10.1016/0956-7151\(94\)90502-9](https://doi.org/10.1016/0956-7151(94)90502-9).
- [4] J.S. Stölken and A.G. Evans. «A microbend test method for measuring the plasticity length scale.» In: *Acta Materialia* 46 (1998). DOI: [10.1016/S1359-6454\(98\)00153-0](https://doi.org/10.1016/S1359-6454(98)00153-0).
- [5] H. Gao and Y. Huang. «Geometrically necessary dislocation and size-dependent plasticity.» In: *Scripta Materialia* 48 (2003), pp. 113–118. DOI: [10.1016/S1359-6462\(02\)00329-9](https://doi.org/10.1016/S1359-6462(02)00329-9).
- [6] P. Gudmundson. «A unified treatment of strain gradient plasticity.» In: *Journal of the Mechanics and Physics of Solids* 52 (2004), pp. 1379–1406. DOI: [10.1016/j.jmps.2003.11.002](https://doi.org/10.1016/j.jmps.2003.11.002).
- [7] D. González, J. Alkorta, J.M. Martínez-Esnaola, and J. Gil Sevillano. «Numerical analysis of the indentation size effect using a strain gradient crystal plasticity model.» In: *Computational Materials Science* 82 (2014), pp. 314–319. DOI: [10.1016/j.commatsci.2013.10.004](https://doi.org/10.1016/j.commatsci.2013.10.004).
- [8] V.L. Berdichevskii and L.I. Sedov. «Dynamic theory of continuously distributed dislocations. Its relation to plasticity theory.» In: *Journal of Applied Mathematics and Mechanics* 31 (1967), pp. 989–1006. DOI: [10.1016/0021-8928\(67\)90203-1](https://doi.org/10.1016/0021-8928(67)90203-1).
- [9] E.C. Aifantis. «On the microstructural origin of certain inelastic models.» In: *Journal of Engineering Materials and Technology* 106 (1984), pp. 326–330. DOI: [10.1115/1.3225725](https://doi.org/10.1115/1.3225725).
- [10] E.C. Aifantis. «Strain gradient interpretation of size effects.» In: *International Journal of Fracture* 95 (1999), pp. 299–314. DOI: [10.1023/A:1018625006804](https://doi.org/10.1023/A:1018625006804).
- [11] N.A. Fleck and J.W. Hutchinson. «Strain gradient plasticity.» In: *Advances in applied mechanics* 33 (1997), pp. 295–361. DOI: [10.1016/S0065-2156\(08\)70388-0](https://doi.org/10.1016/S0065-2156(08)70388-0).

- [12] H. Gao, Y. Huang, W.D. Nix, and J.W. Hutchinson. «Mechanism-based strain gradient plasticity—I. Theory.» In: *Journal of the Mechanics and Physics of Solids* 47 (1999), pp. 128–152. DOI: [10.1016/S0022-5096\(98\)00103-3](https://doi.org/10.1016/S0022-5096(98)00103-3).
- [13] N.A. Fleck and J.W. Hutchinson. «A reformulation of strain gradient plasticity.» In: *Journal of the Mechanics and Physics of Solids* 49 (2001), pp. 2245–2271. DOI: [10.1016/S0022-5096\(01\)00049-7](https://doi.org/10.1016/S0022-5096(01)00049-7).
- [14] Y. Huang, S. Qu, K.C. Hwang, M. Li, and H. Gao. «A conventional theory of mechanism-based strain gradient plasticity.» In: *International Journal of Plasticity* 20 (2004), pp. 753–782. DOI: [10.1016/j.ijplas.2003.08.002](https://doi.org/10.1016/j.ijplas.2003.08.002).
- [15] M.E. Gurtin. «A gradient theory of small-deformation isotropic plasticity that accounts for the Burgers vector and for dissipation due to plastic spin.» In: *Journal of the Mechanics and Physics of Solids* 52 (2004), pp. 2545–2568. DOI: [10.1016/j.jmps.2004.04.010](https://doi.org/10.1016/j.jmps.2004.04.010).
- [16] M.E. Gurtin and L. Anand. «A theory of strain-gradient plasticity for isotropic, plastically irrotational materials. Part I: Small deformations.» In: *Journal of the Mechanics and Physics of Solids* 53 (2005), pp. 1624–1649. DOI: [10.1016/j.jmps.2004.12.008](https://doi.org/10.1016/j.jmps.2004.12.008).
- [17] M. Kuroda and V. Tvergaard. «An alternative treatment of phenomenological higher-order strain-gradient plasticity theory.» In: *International Journal of Plasticity* 26 (2010), pp. 507–515. DOI: [10.1016/j.ijplas.2009.09.001](https://doi.org/10.1016/j.ijplas.2009.09.001).
- [18] N.A. Fleck, J.W. Hutchinson, and J.R. Willis. «Guidelines for constructing strain gradient plasticity theories.» In: *Journal of Applied Mechanics* 82 (2015), 071002 (10 pages). DOI: [10.1115/1.4030323](https://doi.org/10.1115/1.4030323).
- [19] C.F. Niordson and J.W. Hutchinson. «On lower order strain gradient plasticity theories.» In: *European Journal of Mechanics - A/Solids* 22 (2003), pp. 771–778. DOI: [10.1016/S0997-7538\(03\)00069-X](https://doi.org/10.1016/S0997-7538(03)00069-X).
- [20] M. Kuroda and V. Tvergaard. «On the formulations of higher-order strain gradient crystal plasticity.» In: *Journal of the Mechanics and Physics of Solids* 56 (2008), pp. 1591–1608. DOI: [10.1016/j.jmps.2007.07.015](https://doi.org/10.1016/j.jmps.2007.07.015).
- [21] M.E. Gurtin and L. Anand. «Thermodynamics applied to gradient theories involving the accumulated plastic strain: the theories of Aifantis and Fleck and Hutchinson and their generalization.» In: *Journal of the Mechanics and Physics of Solids* 57 (2009), pp. 405–421. DOI: [10.1016/j.jmps.2008.12.002](https://doi.org/10.1016/j.jmps.2008.12.002).

- [22] J.W. Hutchinson. «Generalizing J 2 flow theory: Fundamental issues in strain gradient plasticity.» In: *Acta Mechanica Sinica* 28 (2012), pp. 1078–1086. DOI: [10.1007/s10409-012-0089-4](https://doi.org/10.1007/s10409-012-0089-4).
- [23] N.A. Fleck, J.W. Hutchinson, and J.R. Willis. «Strain gradient plasticity under non-proportional loading.» In: *Proceedings of the Royal Society A* 470 (2014), p. 20140267. DOI: [10.1098/rspa.2014.0267](https://doi.org/10.1098/rspa.2014.0267).
- [24] J.W. Hutchinson. «Plasticity at the micron scale.» In: *International Journal of Solids and Structures* 37 (2000), pp. 225–238. DOI: [10.1016/S0020-7683\(99\)00090-6](https://doi.org/10.1016/S0020-7683(99)00090-6).
- [25] G. Elssner, D. Korn, and M. Ruehle. «The influence of interface impurities on fracture energy of UHV diffusion bonded metal-ceramic bicrystals.» In: *Scripta Metallurgica et Materialia* 31 (1994), pp. 1037–1042. DOI: [10.1016/0956-716X\(94\)90523-1](https://doi.org/10.1016/0956-716X(94)90523-1).
- [26] D. Korn, G. Elssner, R.M. Cannon, and M. Rühle. «Fracture properties of interfacially doped Nb-A1 2 O 3 bicrystals: I, fracture characteristics.» In: *Acta materialia* 50 (2002), pp. 3881–3901. DOI: [10.1016/S1359-6454\(02\)00193-3](https://doi.org/10.1016/S1359-6454(02)00193-3).
- [27] Y. Wei and J.W. Hutchinson. «Steady-state crack growth and work of fracture for solids characterized by strain gradient plasticity.» In: *Journal of the Mechanics and Physics of Solids* 45 (1997), pp. 1253–1273. DOI: [10.1016/S0022-5096\(97\)00018-5](https://doi.org/10.1016/S0022-5096(97)00018-5).
- [28] U. Komaragiri, S. Agnew, R.P. Gangloff, and M. Begley. «The role of macroscopic hardening and individual length-scales on crack tip stress elevation from phenomenological strain gradient plasticity.» In: *Journal of the Mechanics and Physics of Solids* 56 (2008), pp. 3527–3540. DOI: [10.1016/j.jmps.2008.08.007](https://doi.org/10.1016/j.jmps.2008.08.007).
- [29] V. Tvergaard and C.F. Niordson. «Size effects at a crack-tip interacting with a number of voids.» In: *Philosophical Magazine* 88 (2008), pp. 3827–3840. DOI: [10.1080/14786430802225540](https://doi.org/10.1080/14786430802225540).
- [30] L.P. Mikkelsen and S. Goutianos. «Suppressed plastic deformation at blunt crack-tips due to strain gradient effects.» In: *International Journal of Solids and Structures* 46 (2009), pp. 4430–4436. DOI: [10.1016/j.ijsolstr.2009.09.001](https://doi.org/10.1016/j.ijsolstr.2009.09.001).
- [31] K.L. Nielsen, C.F. Niordson, and J.W. Hutchinson. «Strain gradient effects on steady state crack growth in rate-sensitive materials.» In: *Engineering Fracture Mechanics* 96 (2012), pp. 61–71. DOI: [10.1016/j.engfracmech.2012.06.022](https://doi.org/10.1016/j.engfracmech.2012.06.022).
- [32] H. Jiang, Y. Huang, Z. Zhuang, and K.C. Hwang. «Fracture in mechanism-based strain gradient plasticity.» In: *Journal of the Mechanics and Physics of Solids* 49 (2001), pp. 979–993. DOI: [10.1016/S0022-5096\(00\)00070-3](https://doi.org/10.1016/S0022-5096(00)00070-3).

- [33] S. Qu, Y. Huang, H. Jiang, and C. Liu. «Fracture analysis in the conventional theory of mechanism-based strain gradient (CMSG) plasticity.» In: *International Journal of Fracture* (2004), pp. 199–220. DOI: [10.1023/B:FRAC.0000047786.40200.f8](https://doi.org/10.1023/B:FRAC.0000047786.40200.f8).
- [34] Y. Wei and G. Xu. «A multiscale model for the ductile fracture of crystalline materials.» In: *International Journal of Plasticity* 21 (2005), pp. 2123–2149. DOI: [10.1016/j.ijplas.2005.04.003](https://doi.org/10.1016/j.ijplas.2005.04.003).
- [35] X. Pan and H. Yuan. «Applications of the element-free Galerkin method for singular stress analysis under strain gradient plasticity theories.» In: *Engineering Fracture Mechanics* 78 (2011), pp. 452–461. DOI: [10.1016/j.engfracmech.2010.08.024](https://doi.org/10.1016/j.engfracmech.2010.08.024).
- [36] R.P. Gangloff. «Hydrogen assisted cracking of high strength alloys.» In: *Comprehensive Structural Integrity*. Oxford: Elsevier, 2003. Chap. Volume 6: Environmentally Assisted Fatigue, pp. 1–194. DOI: [10.1016/B0-08-043749-4/06134-6](https://doi.org/10.1016/B0-08-043749-4/06134-6).
- [37] V. Tvergaard. «Effect of thickness inhomogeneities in internally pressurized elastic-plastic spherical shells.» In: *Journal of the Mechanics and Physics of Solids* 24 (1976), pp. 291–304. DOI: [10.1016/0022-5096\(76\)90027-2](https://doi.org/10.1016/0022-5096(76)90027-2).
- [38] X. Zhang and K. Aifantis. «Interpreting the internal length scale in strain gradient plasticity.» In: *Reviews on Advanced Materials Science* 41 (2015), pp. 72–83.
- [39] N.A. Fleck and J.W. Hutchinson. «A phenomenological theory for strain-gradient effects in plasticity.» In: *Journal of the Mechanics and Physics of Solids* 41 (1993), pp. 1825–1857. DOI: [10.1016/0022-5096\(93\)90072-N](https://doi.org/10.1016/0022-5096(93)90072-N).
- [40] P. Shrotriya, S.M. Allameh, J. Lou, T. Buchheit, and W.O. Soboyejo. «On the measurement of the plasticity length scale parameter in LIGA nickel foils.» In: *Mechanics of Materials* 35 (2003), pp. 233–243. DOI: [10.1016/S0167-6636\(02\)00273-9](https://doi.org/10.1016/S0167-6636(02)00273-9).
- [41] M.A. Haque and M.T.A. Saif. «Strain gradient effect in nanoscale thin films.» In: *Acta Materialia* 51 (2003), pp. 3053–3061. DOI: [10.1016/S1359-6454\(03\)00116-2](https://doi.org/10.1016/S1359-6454(03)00116-2).
- [42] Y.J. Ro, M.R. Begley, R.P. Gangloff, and S.R. Agnew. «Effect of aging on scale-dependent plasticity in aluminum alloy 2024.» In: *Materials Science and Engineering: A* 435–436 (2006), pp. 333–342. DOI: [10.1016/j.msea.2006.07.102](https://doi.org/10.1016/j.msea.2006.07.102).
- [43] X. Qian, S. Zhang, S. Swaddiwudhipong, and L. Shen. «Temperature dependence of material length scale for strain gradient plasticity and its effect on near-tip opening displacement.» In: *Fatigue & Fracture of Engineering Materials & Structures* 37 (2014), pp. 157–170. DOI: [10.1111/ffe.12096](https://doi.org/10.1111/ffe.12096).

- [44] G. Song, H. Yuming, L. Jian, L. Zhenkun, and L. Dabiao. «Individual strain gradient effect on torsional strength of electro-polished microscale copper wires.» In: *Scripta Materialia* 130 (2017), pp. 124–127. DOI: [10.1016/j.scriptamat.2016.11.029](https://doi.org/10.1016/j.scriptamat.2016.11.029).
- [45] S.P. Iliev, X. Chen, M.V. Pathan, and V.L. Tagarielli. «Measurements of the mechanical response of Indium and of its size dependence in bending and indentation.» In: *Materials Science and Engineering: A* 683 (2017), pp. 244–251. DOI: [10.1016/j.msea.2016.12.017](https://doi.org/10.1016/j.msea.2016.12.017).
- [46] Y. Huang, H. Gao, W.D. Nix, and J.W. Hutchinson. «Mechanism-based strain gradient plasticity—II. Analysis.» In: *Journal of the Mechanics and Physics of Solids* 48 (2000). DOI: [10.1016/S0022-5096\(99\)00022-8](https://doi.org/10.1016/S0022-5096(99)00022-8).
- [47] G.I. Taylor. «Plastic strain in metals.» In: *Journal of the Institute of Metals* 62 (1938), pp. 307–324.
- [48] P. Smyshlyaev and N.A. Fleck. «The role of strain gradients in the grain size effect in polycrystals.» In: *Journal of the Mechanics and Physics of Solids* 44 (1996), pp. 465–495. DOI: [10.1016/0022-5096\(96\)00009-9](https://doi.org/10.1016/0022-5096(96)00009-9).
- [49] C.F. Niordson and P. Redanz. «Size-effects in plane strain sheet-necking.» In: *Journal of the Mechanics and Physics of Solids* 52 (2004), pp. 2431–2454. DOI: [10.1016/j.jmps.2004.05.009](https://doi.org/10.1016/j.jmps.2004.05.009).
- [50] C.F. Niordson and V. Tvergaard. «Instabilities in power law gradient hardening materials.» In: *International Journal of Solids and Structures* 42 (2005), pp. 2259–2573. DOI: [10.1016/j.ijsolstr.2004.09.051](https://doi.org/10.1016/j.ijsolstr.2004.09.051).
- [51] C.F. Niordson and J.W. Hutchinson. «Non-uniform plastic deformation of micron scale objects.» In: *International Journal for Numerical Methods in Engineering* 56 (2003), pp. 961–975. DOI: [10.1002/nme.593](https://doi.org/10.1002/nme.593).
- [52] C. Truesdell and W. Noll. *The non-linear field theories of mechanics*. Springer, 1965. DOI: [10.1007/978-3-662-10388-3](https://doi.org/10.1007/978-3-662-10388-3).
- [53] M.E. Gurtin. «A gradient theory of single-crystal viscoplasticity that accounts for geometrically necessary dislocations.» In: *Journal of the Mechanics and Physics of Solids* 50 (2002), pp. 5–32. DOI: [10.1016/S0022-5096\(01\)00104-1](https://doi.org/10.1016/S0022-5096(01)00104-1).
- [54] S. Guha, S. Sangal, and S. Basu. «A review of higher order strain gradient theories of plasticity: Origins, thermodynamics and connections with dislocation mechanics.» In: *Sadhana* 40 (2015), pp. 1205–1240. DOI: [10.1007/s12046-015-0369-3](https://doi.org/10.1007/s12046-015-0369-3).

- [55] G.Z. Voyiadjis and B. Deliktas. «Mechanics of strain gradient plasticity with particular reference to decomposition of the state variables into energetic and dissipative components.» In: *International Journal of Engineering Science* 47 (2009), pp. 1405–1423. DOI: [10.1016/j.ijengsci.2009.05.013](https://doi.org/10.1016/j.ijengsci.2009.05.013).
- [56] E.C. Aifantis. «The physics of plastic deformation.» In: *International Journal of Plasticity* 3 (1987), pp. 211–247. DOI: [10.1016/0749-6419\(87\)90021-0](https://doi.org/10.1016/0749-6419(87)90021-0).
- [57] H.B. Mühlhaus and E.C. Aifantis. «A variational principle for gradient plasticity.» In: *International Journal of Solids and Structures* 28 (1991), pp. 845–857. DOI: [10.1016/0020-7683\(91\)90004-Y](https://doi.org/10.1016/0020-7683(91)90004-Y).
- [58] B. D. Reddy. «The role of dissipation and defect energy in variational formulations of problems in strain-gradient plasticity. Part 1: polycrystalline plasticity.» In: *Continuum Mechanics and Thermodynamics* 23 (2011), pp. 527–549. DOI: [10.1007/s00161-011-0194-9](https://doi.org/10.1007/s00161-011-0194-9).
- [59] L. Bardella and A. Panteghini. «Modelling the torsion of thin metal wires by distortion gradient plasticity.» In: *Journal of the Mechanics and Physics of Solids* 78 (2015), pp. 467–492. DOI: [10.1016/j.jmps.2015.03.003](https://doi.org/10.1016/j.jmps.2015.03.003).
- [60] E. Martínez-Pañeda, C.F. Niordson, and L. Bardella. «A finite element framework for distortion gradient plasticity with applications to bending of thin foils.» In: *International Journal of Solids and Structures* 96 (2016), pp. 288–299. DOI: [10.1016/j.ijsolstr.2016.06.001](https://doi.org/10.1016/j.ijsolstr.2016.06.001).
- [61] L. Bardella. «Size effects in phenomenological strain gradient plasticity constitutively involving the plastic spin.» In: *International Journal of Engineering Science* 48 (2010), pp. 550–568. DOI: [10.1016/j.ijengsci.2010.01.003](https://doi.org/10.1016/j.ijengsci.2010.01.003).
- [62] L.H. Poh and R.H.J. Peerlings. «The plastic rotation effect in an isotropic gradient plasticity model for applications at the meso scale.» In: *International Journal of Solids and Structures* 78-79 (2016), pp. 57–69. DOI: [10.1016/j.ijsolstr.2015.09.017](https://doi.org/10.1016/j.ijsolstr.2015.09.017).
- [63] J.F. Nye. «Some geometrical relations in dislocated crystals.» In: *Acta Metallurgica* 1 (1953), pp. 153–162. DOI: [10.1016/0001-6160\(53\)90054-6](https://doi.org/10.1016/0001-6160(53)90054-6).
- [64] L. Bardella. «A comparison between crystal and isotropic strain gradient plasticity theories with accent on the role of the plastic spin.» In: *European Journal of Mechanics - A/Solids* 28 (2009), pp. 638–646. DOI: [10.1016/j.euromechsol.2008.10.006](https://doi.org/10.1016/j.euromechsol.2008.10.006).

- [65] N.A. Fleck and J.R. Willis. «A mathematical basis for strain-gradient plasticity theory—Part I: Scalar plastic multiplier.» In: *Journal of the Mechanics and Physics of Solids* 57 (2009), pp. 161–177. DOI: [10.1016/j.jmps.2008.09.010](https://doi.org/10.1016/j.jmps.2008.09.010).
- [66] L. Bardella and A. Giacomini. «Influence of material parameters and crystallography on the size effects describable by means of strain gradient plasticity.» In: *Journal of the Mechanics and Physics of Solids* 56 (2008), pp. 2906–2934. DOI: [10.1016/j.jmps.2008.04.001](https://doi.org/10.1016/j.jmps.2008.04.001).
- [67] M.E. Gurtin and A. Needleman. «Boundary conditions in small-deformation, single-crystal plasticity that account for the burgers vector.» In: *Journal of the Mechanics and Physics of Solids* 53 (2005), pp. 1–31. DOI: [10.1016/j.jmps.2004.06.006](https://doi.org/10.1016/j.jmps.2004.06.006).
- [68] E. Bittencourt, A. Needleman, M.E. Gurtin, and E. Van der Giessen. «A comparison of nonlocal continuum and discrete dislocation plasticity predictions.» In: *Journal of the Mechanics and Physics of Solids* 51 (2003), pp. 281–310. DOI: [10.1016/S0022-5096\(02\)00081-9](https://doi.org/10.1016/S0022-5096(02)00081-9).
- [69] L.H. Poh. «Scale transition of a higher order plasticity model - A consistent homogenization theory from meso to macro.» In: *Journal of the Mechanics and Physics of Solids* 61 (2013), pp. 2692–2710. DOI: [10.1016/j.jmps.2013.09.004](https://doi.org/10.1016/j.jmps.2013.09.004).
- [70] L.H. Poh and V.T. Phan. «Numerical implementation and validation of a consistently homogenized higher order plasticity model.» In: *International Journal for Numerical Methods in Engineering* (in press) (2016). DOI: [10.1002/nme.5129](https://doi.org/10.1002/nme.5129).
- [71] K.C. Hwang, H. Jiang, Y. Huang, and H. Gao. «Finite deformation analysis of mechanism-based strain gradient plasticity: torsion and crack tip field.» In: *International Journal of Plasticity* 19 (2003), pp. 235–251. DOI: [10.1016/S0749-6419\(01\)00039-0](https://doi.org/10.1016/S0749-6419(01)00039-0).
- [72] E. Martínez-Pañeda and C. Betegón. «Modeling damage and fracture within strain-gradient plasticity.» In: *International Journal of Solids and Structures* 59 (2015), pp. 208–215. DOI: [10.1016/j.ijsolstr.2015.02.010](https://doi.org/10.1016/j.ijsolstr.2015.02.010).
- [73] M. Shi, Y. Huang, H. Jiang, K.C. Hwang, and M. Li. «The boundary-layer effect on the crack tip field in mechanism-based strain gradient plasticity.» In: *International Journal of Fracture* (2001), pp. 23–41. DOI: [10.1023/A:1013548131004](https://doi.org/10.1023/A:1013548131004).
- [74] S. Qu. «A conventional theory of mechanism-based strain gradient plasticity.» PhD Thesis. University of Illinois at Urbana-Champaign, 2004.

- [75] S. Kok, A.J. Beaudoin, and D.A. Tortorelli. «A polycrystal plasticity model based on the mechanical threshold.» In: *International Journal of Plasticity* 18 (2002), pp. 715–741. DOI: [10.1016/S0749-6419\(01\)00051-1](https://doi.org/10.1016/S0749-6419(01)00051-1).
- [76] E. Martínez-Pañeda and C.F. Niordson. «On fracture in finite strain gradient plasticity.» In: *International Journal of Plasticity* 80 (2016), pp. 154–167. DOI: [10.1016/j.ijplas.2015.09.009](https://doi.org/10.1016/j.ijplas.2015.09.009).
- [77] X. Pan and H. Yuan. «Computational assessment of cracks under strain-gradient plasticity.» In: *International Journal of Fracture* 167 (2010), pp. 235–248. DOI: [10.1007/s10704-010-9548-8](https://doi.org/10.1007/s10704-010-9548-8).
- [78] T. Elguedj, A. Gravouil, and A. Combescure. «Appropriate extended functions for X-FEM simulation of plastic fracture mechanics.» In: *Computer Methods in Applied Mechanics and Engineering* 195 (2006), pp. 501–515. DOI: [10.1016/j.cma.2005.02.007](https://doi.org/10.1016/j.cma.2005.02.007).
- [79] J.W. Hutchinson. «Singular behaviour at the end of a tensile crack in a hardening material.» In: *Journal of the Mechanics and Physics of Solids* (1968). DOI: [10.1016/0022-5096\(68\)90014-8](https://doi.org/10.1016/0022-5096(68)90014-8).
- [80] J.R. Rice and G.F. Rosengren. «Plane strain deformation near a crack tip in a power-law hardening material.» In: *Journal of the Mechanics and Physics of Solids* 16 (1968). DOI: [10.1016/0022-5096\(68\)90013-6](https://doi.org/10.1016/0022-5096(68)90013-6).
- [81] M. Duflot and S. Bordas. «A posteriori error estimation for extended finite elements by an extended global recovery.» In: *International Journal for Numerical Methods in Engineering* 76 (2008), pp. 1123–1138. DOI: [10.1002/nme.2332](https://doi.org/10.1002/nme.2332).
- [82] M. Duflot. «A study of the representation of cracks with level sets.» In: *International Journal for Numerical Methods in Engineering* 70 (2006), pp. 1261–1302. DOI: [10.1002/nme.1915](https://doi.org/10.1002/nme.1915).
- [83] T.P. Fries. «A corrected XFEM approximation without problems in blending elements.» In: *International Journal for Numerical Methods in Engineering* 75 (2008), pp. 503–532. DOI: [10.1002/nme.2259](https://doi.org/10.1002/nme.2259).
- [84] E. Martínez-Pañeda, S. Natarajan Cuesta, and S. Bordas. «Gradient plasticity crack tip characterization by means of the extended finite element method.» In: (submitted) (2016).
- [85] K.L. Nielsen and C.F. Niordson. «A 2D finite element implementation of the Fleck-Willis strain-gradient flow theory.» In: *European Journal of Mechanics - A/Solids* 41 (2013), pp. 134–142. DOI: [10.1016/j.euromechsol.2013.03.002](https://doi.org/10.1016/j.euromechsol.2013.03.002).

- [86] K.L. Nielsen and C.F. Niordson. «A numerical basis for strain-gradient plasticity theory: Rate-independent and rate-dependent formulations.» In: *Journal of the Mechanics and Physics of Solids* 63 (2014), pp. 113–127. DOI: [10.1016/j.jmps.2013.09.018](https://doi.org/10.1016/j.jmps.2013.09.018).
- [87] N.A. Fleck and J.R. Willis. «A mathematical basis for strain-gradient plasticity theory. Part II: Tensorial plastic multiplier.» In: *Journal of the Mechanics and Physics of Solids* 57 (2009), pp. 1045–1057. DOI: [10.1016/j.jmps.2009.03.007](https://doi.org/10.1016/j.jmps.2009.03.007).
- [88] P. Fredriksson and P. Gudmundson. «Size-dependent yield strength of thin films.» In: *International Journal of Plasticity* 21 (2005), pp. 1834–1854. DOI: [10.1016/j.ijplas.2004.09.005](https://doi.org/10.1016/j.ijplas.2004.09.005).
- [89] C.F. Niordson and B.N. Legarth. «Strain gradient effects on cyclic plasticity.» In: *Journal of the Mechanics and Physics of Solids* 58 (2010), pp. 542–557. DOI: [10.1016/j.jmps.2010.01.007](https://doi.org/10.1016/j.jmps.2010.01.007).
- [90] M.I. Idiart, V.S. Deshpande, N.A. Fleck, and J.R. Willis. «Size effects in the bending of thin foils.» In: *International Journal of Engineering Science* 47 (2009), pp. 1251–1264. DOI: [10.1016/j.ijengsci.2009.06.002](https://doi.org/10.1016/j.ijengsci.2009.06.002).
- [91] J Ostien and K Garikipati. «A discontinuous Galerkin method for an incompatibility-based strain gradient plasticity theory.» In: *IUTAM Symposium on Theoretical, Computational and Modeling Aspects of Inelastic Media*. Springer, 2008, pp. 217–226. DOI: [10.1007/978-1-4020-9090-5\\_20](https://doi.org/10.1007/978-1-4020-9090-5_20).
- [92] C.F. Niordson and J.W. Hutchinson. «Basic strain gradient plasticity theories with application to constrained film deformation.» In: *Journal of Mechanics of Materials and Structures* 6 (2011), pp. 395–416. DOI: [10.2140/jomms.2011.6.395](https://doi.org/10.2140/jomms.2011.6.395).
- [93] J.W. Hutchinson. «Linking scales in fracture mechanics.» In: ed. by B.L. Karihaloo, Y.W. Mai, M.I. Ripley, and R.O. Ritchie. *Advances in Fracture Research*. Amsterdam: Pergamon Press, 1997, pp. 1–14.
- [94] H. Yuan and J. Chen. «Analysis of size effects based on lower-order gradient plasticity model.» In: *Computational Materials Science* 19 (2000), pp. 143–157. DOI: [10.1016/S0927-0256\(00\)00149-X](https://doi.org/10.1016/S0927-0256(00)00149-X).
- [95] S. Swaddiwudhipong, J. Hua, K.K. Tho, and Z.S. Liu. «Finite element modelling for materials with size effect.» In: *Modelling and Simulation in Materials Science and Engineering* 14 (2006), pp. 1127–1137. DOI: [10.1088/0965-0393/14/7/002](https://doi.org/10.1088/0965-0393/14/7/002).
- [96] S. Swaddiwudhipong, K.K. Tho, J. Hua, and Z.S. Liu. «Mechanism-based strain gradient plasticity in  $C^0$  axisymmetric element.» In: *International Journal of Solids and Structures* 43 (2006), pp. 1117–1130. DOI: [10.1016/j.ijsolstr.2005.05.026](https://doi.org/10.1016/j.ijsolstr.2005.05.026).

- [97] G. Papazafeiropoulos, M. Muñoz-Calvente, and E. Martínez-Pañeda. «Abaqus2Matlab: a suitable tool for finite element post-processing.» In: (submitted) (2017).
- [98] C. Betegón and J.W. Hancock. «Two-parameter characterization of elastic-plastic crack-tip fields.» In: *Journal of Applied Mechanics* 58 (1991), pp. 104–110. DOI: [10.1115/1.2897135](https://doi.org/10.1115/1.2897135).
- [99] Y.-Y. Wang. «A two-parameter characterization of elastic-plastic crack-tip fields and applications to cleavage fracture.» PhD Thesis. Massachusetts Institute of Technology, 1991.
- [100] T. Hughes and J. Winget. «Finite rotation effects in numerical integration of rate constitutive equations arising in large-deformation analysis.» In: *International Journal for Numerical Methods in Engineering* 15 (1980), pp. 1862–1867. DOI: [10.1002/nme.1620151210](https://doi.org/10.1002/nme.1620151210).
- [101] R.M. McMeeking. «Finite deformation analysis of crack-tip opening in elastic-plastic materials and implications for fracture.» In: *Journal of the Mechanics and Physics of Solids* 25 (1977), pp. 357–381. DOI: [10.1016/0022-5096\(77\)90003-5](https://doi.org/10.1016/0022-5096(77)90003-5).
- [102] Y. Lee and R.P. Gangloff. «Measurement and Modeling of Hydrogen Environment-Assisted Cracking of Ultra-High-Strength Steel.» In: *Metallurgical and Materials Transactions A* 38 (2007), pp. 2174–2190. DOI: [10.1007/s11661-006-9051-z](https://doi.org/10.1007/s11661-006-9051-z).
- [103] C. Betegón, I. Peñuelas, and J.J. del Coz. «Numerical analysis of the influence of material mismatching in the transition curve of welded joints.» In: *Engineering Fracture Mechanics* 75 (2008), pp. 3464–3482. DOI: [10.1016/j.engfracmech.2007.05.005](https://doi.org/10.1016/j.engfracmech.2007.05.005).
- [104] C.C. Chu and A. Needleman. «Void nucleation effects in biaxially stretched sheets.» In: *Journal of Engineering Materials and Technology* 102 (1980), pp. 249–256. DOI: [10.1115/1.3224807](https://doi.org/10.1115/1.3224807).
- [105] A.L. Gurson. «Plastic flow and fracture behaviour of ductile materials incorporating void nucleation, growth and coalescence.» PhD Thesis. Brown University, 1975.
- [106] V. Tvergaard and A. Needleman. «Analysis of the cup-cone fracture in a round tensile bar.» In: *Acta Metallurgica* 32 (1984), pp. 157–169. DOI: [10.1016/0001-6160\(84\)90213-X](https://doi.org/10.1016/0001-6160(84)90213-X).
- [107] P.F. Thomason. *Ductile fracture of metals*. Oxford: Pergamon Press, 1990.
- [108] X. Qian, S. Zhang, and S. Swaddiwudhipong. «Calibration of Weibull parameters using the conventional mechanism-based strain gradient plasticity.» In: *Engineering Fracture Mechanics* 78 (2011), pp. 1928–1944. DOI: [10.1016/j.engfracmech.2011.03.010](https://doi.org/10.1016/j.engfracmech.2011.03.010).

- [109] N.A. Fleck. «Finite element analysis of plasticity-induced crack closure under plane strain conditions.» In: *Engineering Fracture Mechanics* 25 (1986), pp. 441–449. DOI: [10.1016/0013-7944\(86\)90258-4](https://doi.org/10.1016/0013-7944(86)90258-4).
- [110] B. Liu, Y. Huang, M. Li, K.C. Hwang, and C. Liu. «A study of the void size effect based on the Taylor dislocation model.» In: *International Journal of Plasticity* 21 (2005), pp. 2107–2122. DOI: [10.1016/j.ijplas.2005.03.016](https://doi.org/10.1016/j.ijplas.2005.03.016).
- [111] K.R. Cooper, L.M. Young, R.P. Gangloff, and R.G. Kelly. «The electrode potential dependence of environment-assisted cracking of AA 7050.» In: *Materials Science Forum* 331-337 (2000), pp. 1625–1634. DOI: [10.4028/www.scientific.net/MSF.331-337.1625](https://doi.org/10.4028/www.scientific.net/MSF.331-337.1625).
- [112] R.P. Gangloff, H.M. Ha, J.T. Burns, and J.R. Scully. «Measurement and modeling of hydrogen environment-assisted cracking in Monel K-500.» In: *Metallurgical and Materials Transactions A* 45 (2014), pp. 3814–3834. DOI: [10.1007/s11661-014-2324-z](https://doi.org/10.1007/s11661-014-2324-z).
- [113] Y. Wei, X. Qiu, and K.C. Hwang. «Steady-state crack growth and fracture work based on the theory of mechanism-based strain gradient plasticity.» In: *Engineering Fracture Mechanics* 71 (2004), pp. 107–125. DOI: [10.1016/S0013-7944\(03\)00065-1](https://doi.org/10.1016/S0013-7944(03)00065-1).
- [114] M.R. Begley and J.W. Hutchinson. «The mechanics of size-dependent indentation.» In: *Journal of the Mechanics and Physics of Solids* 46 (1998), pp. 2049–2068. DOI: [10.1016/S0022-5096\(98\)00018-0](https://doi.org/10.1016/S0022-5096(98)00018-0).
- [115] M.E. Gurtin. «On the plasticity of single crystals: free energy, microforces, plastic-strain gradients.» In: *Journal of the Mechanics and Physics of Solids* 48 (2000), pp. 989–1036. DOI: [10.1016/S0022-5096\(99\)00059-9](https://doi.org/10.1016/S0022-5096(99)00059-9).
- [116] L. Anand, M. Gurtin, S. Lele, and C. Gething. «A one-dimensional theory of strain-gradient plasticity: formulation, analysis, numerical results.» In: *Journal of the Mechanics and Physics of Solids* 53 (2005), pp. 1789–1826. DOI: [10.1016/j.jmps.2005.03.003](https://doi.org/10.1016/j.jmps.2005.03.003).
- [117] J.G. Swadener, E.P. George, and G.M. Pharr. «The correlation of the indentation size effect measured with indenters of various shapes.» In: *Journal of the Mechanics and Physics of Solids* 50 (2002), pp. 681–694. DOI: [10.1016/S0022-5096\(01\)00103-X](https://doi.org/10.1016/S0022-5096(01)00103-X).
- [118] Y. Xiang and J.J. Vlassak. «Bauschinger and size effects in thin-film plasticity.» In: *Journal of the Mechanics and Physics of Solids* 54 (2006), pp. 5449–5460. DOI: [10.1016/j.actamat.2006.06.059](https://doi.org/10.1016/j.actamat.2006.06.059).

- [119] G.Z. Voyiadjis and R.K. Abu Al-Rub. «Gradient plasticity theory with a variable length scale parameter.» In: *International Journal of Solids and Structures* 42 (2005), pp. 3998–4029. DOI: [10.1016/j.ijsolstr.2004.12.010](https://doi.org/10.1016/j.ijsolstr.2004.12.010).
- [120] K. Danas, V.S. Deshpande, and N.A. Fleck. «Size effects in the conical indentation of an elasto-plastic solid.» In: *Journal of the Mechanics and Physics of Solids* 60 (2012), pp. 1605–1625. DOI: [10.1016/j.jmps.2012.05.002](https://doi.org/10.1016/j.jmps.2012.05.002).
- [121] S. Forest and N. Guéinichault. «Inspection of free energy functions in gradient crystal plasticity.» In: *Acta Mechanica Sinica* 29 (2013), pp. 763–772. DOI: [10.1007/s10409-013-0088-0](https://doi.org/10.1007/s10409-013-0088-0).
- [122] V. Tvergaard and J.W. Hutchinson. «The relation between crack growth resistance and fracture process parameters in elastic-plastic solids.» In: *Journal of the Mechanics and Physics of Solids* 40 (1992), pp. 1377–1397. DOI: [10.1016/0022-5096\(92\)90020-3](https://doi.org/10.1016/0022-5096(92)90020-3).
- [123] X.-P. Xu and A. Needleman. «Void nucleation by inclusion debonding in a crystal matrix.» In: *Modelling and Simulation in Materials Science and Engineering* 1 (1999), pp. 111–132. DOI: [10.1088/0965-0393/1/2/001](https://doi.org/10.1088/0965-0393/1/2/001).
- [124] V.S. Deshpande, A. Needleman, and E. Van der Giessen. «Discrete dislocation modeling of fatigue crack propagation.» In: *Acta Materialia* 50 (2002), pp. 831–846. DOI: [10.1016/S1359-6454\(01\)00377-9](https://doi.org/10.1016/S1359-6454(01)00377-9).
- [125] V. Tvergaard, C.F. Niordson, and J.W. Hutchinson. «Material size effects on crack growth along patterned wafer-level Cu–Cu bonds.» In: *International Journal of Mechanical Sciences* 68 (2013), pp. 270–276. DOI: [10.1016/j.ijmecsci.2013.01.027](https://doi.org/10.1016/j.ijmecsci.2013.01.027).
- [126] J.C.J. Schellekens and R. de Borst. «On the numerical integration of interface elements.» In: *International Journal for Numerical Methods in Engineering* 36 (1993), pp. 43–66. DOI: [10.1002/nme.1620360104](https://doi.org/10.1002/nme.1620360104).
- [127] G.T. Camacho and M. Ortiz. «Computational modelling of impact damage in brittle materials.» In: *International Journal of Solids and Structures* 33 (1996), pp. 2899–2938. DOI: [10.1016/0020-7683\(95\)00255-3](https://doi.org/10.1016/0020-7683(95)00255-3).
- [128] J. Segurado and J. Llorca. «A new three-dimensional interface finite element to simulate fracture in composites.» In: *International Journal of Solids and Structures* 41 (2004), pp. 2977–2993. DOI: [10.1016/j.ijsolstr.2004.01.007](https://doi.org/10.1016/j.ijsolstr.2004.01.007).

- [129] J. Lemonds and A Needleman. «Finite element analyses of shear localization in rate and temperature dependent solids.» In: *Mechanics of Materials* 5 (1986), pp. 339–361. DOI: [10.1016/0167-6636\(86\)90039-6](https://doi.org/10.1016/0167-6636(86)90039-6).
- [130] S.R. Chowdhury and R. Narasimhan. «A cohesive finite element formulation for modelling fracture and delamination in solids.» In: *Sadhana* 25 (2000), pp. 561–587. DOI: [10.1007/BF02703506](https://doi.org/10.1007/BF02703506).
- [131] N.A. Fleck and J.R. Willis. «Strain gradient plasticity: energetic or dissipative?» In: *Acta Mechanica Sinica* 31 (2015), pp. 465–472. DOI: [10.1007/s10409-015-0468-8](https://doi.org/10.1007/s10409-015-0468-8).
- [132] J. Sanchez, S.F. Lee, M.A. Martin-Rengel, J. Fulla, C. Andrade, and J. Ruiz-Hervías. «Measurement of hydrogen and embrittlement of high strength steels.» In: *Engineering Failure Analysis* 59 (2016), pp. 467–477. DOI: [10.1016/j.engfailanal.2015.11.001](https://doi.org/10.1016/j.engfailanal.2015.11.001).
- [133] S. Serebrinsky, E.A. Carter, and M. Ortiz. «A quantum-mechanically informed continuum model of hydrogen embrittlement.» In: *Journal of the Mechanics and Physics of Solids* 52 (2004), pp. 2403–2430. DOI: [10.1016/j.jmps.2004.02.010](https://doi.org/10.1016/j.jmps.2004.02.010).
- [134] I. Scheider, M. Pfuff, and W. Dietzel. «Simulation of hydrogen assisted stress corrosion cracking using the cohesive model.» In: *Engineering Fracture Mechanics* 75 (2008), pp. 4283–4291. DOI: [10.1016/j.engfracmech.2007.10.002](https://doi.org/10.1016/j.engfracmech.2007.10.002).
- [135] A. Alvaro, V. Olden, and O.M. Akselsen. «3D cohesive modelling of hydrogen embrittlement in the heat affected zone of an X70 pipeline steel.» In: *International Journal of Hydrogen Energy* 38 (2013), pp. 7539–7549. DOI: [10.1016/j.ijhydene.2013.02.146](https://doi.org/10.1016/j.ijhydene.2013.02.146).
- [136] A. Alvaro, V. Olden, and O.M. Akselsen. «3D cohesive modelling of hydrogen embrittlement in the heat affected zone of an X70 pipeline steel - Part II.» In: *International Journal of Hydrogen Energy* 39 (2014), pp. 3528–3541. DOI: [10.1016/j.ijhydene.2013.12.097](https://doi.org/10.1016/j.ijhydene.2013.12.097).
- [137] W.W. Gerberich, R.A. Oriani, M.-J. Lji, X. Chen, and T. Foecke. «The necessity of both plasticity and brittleness in the fracture thresholds of iron.» In: *Philosophical Magazine A* 63 (1991), pp. 363–376. DOI: [10.1080/01418619108204854](https://doi.org/10.1080/01418619108204854).
- [138] R.L.S. Thomas, J.R. Scully, and R.P. Gangloff. «Internal hydrogen embrittlement of ultrahigh-strength AERMET 100 steel.» In: *Metallurgical and Materials Transactions A* 34 (2003), pp. 327–344. DOI: [10.1007/s11661-003-0334-3](https://doi.org/10.1007/s11661-003-0334-3).
- [139] R.P. Gangloff. *Critical issues in hydrogen assisted cracking of structural alloys*. Tech. rep. University of Virginia, 2005.

- [140] P. Sofronis and R.M. McMeeking. «Numerical analysis of hydrogen transport near a blunting crack tip.» In: *Journal of the Mechanics and Physics of Solids* 37 (1989), pp. 317–350. DOI: [10.1016/0022-5096\(89\)90002-1](https://doi.org/10.1016/0022-5096(89)90002-1).
- [141] B. Klusemann, B. Svendsen, and H. Vehoff. «Modeling and simulation of deformation behavior, orientation gradient development and heterogeneous hardening in thin sheets with coarse texture.» In: *International Journal of Plasticity* 50 (2013), pp. 109–125. DOI: [10.1016/j.ijplas.2013.04.004](https://doi.org/10.1016/j.ijplas.2013.04.004).
- [142] R.P. Gangloff and B.P. Somerday. *Gaseous hydrogen embrittlement of materials in energy technologies*. Vol. 1. Cambridge: Woodhead Publishing, 2012.
- [143] A. Turnbull. «Perspectives on hydrogen uptake, diffusion and trapping.» In: *International Journal of Hydrogen Energy* 40 (2015), pp. 16961–16970. DOI: [10.1016/j.ijhydene.2015.06.147](https://doi.org/10.1016/j.ijhydene.2015.06.147).
- [144] V. Olden, C. Thaulow, R. Johnsen, E. Østby, and T. Berstad. «Influence of hydrogen from cathodic protection on the fracture susceptibility of 25%Cr duplex stainless steel – Constant load SENT testing and FE-modelling using hydrogen influenced cohesive zone elements.» In: *Engineering Fracture Mechanics* 76 (2009), pp. 827–844. DOI: [10.1016/j.engfracmech.2008.11.011](https://doi.org/10.1016/j.engfracmech.2008.11.011).
- [145] S.X. Mao and M. Li. «Mechanics and thermodynamics on the stress and hydrogen interaction in crack tip stress corrosion: experiment and theory.» In: *Journal of the Mechanics and Physics of Solids* 46 (1998), pp. 1125–1137. DOI: [10.1016/S0022-5096\(97\)00054-9](https://doi.org/10.1016/S0022-5096(97)00054-9).
- [146] C.V. Di Leo and L. Anand. «Hydrogen in metals: a coupled theory for species diffusion and large elastic-plastic deformations.» In: *Journal of the Mechanics and Physics of Solids* 31 (2013), pp. 1037–1042. DOI: [10.1016/j.ijplas.2012.11.005](https://doi.org/10.1016/j.ijplas.2012.11.005).
- [147] V. Olden, C. Thaulow, R. Johnsen, E. Østby, and T. Berstad. «Application of hydrogen influenced cohesive laws in the prediction of hydrogen induced stress cracking in 25%Cr duplex stainless steel.» In: *Engineering Fracture Mechanics* 75 (2008), pp. 2333–2351. DOI: [10.1016/j.engfracmech.2007.09.003](https://doi.org/10.1016/j.engfracmech.2007.09.003).
- [148] Z. Huang, Q. Shi, F. Chen, and Y. Shi. «FEM simulation of the hydrogen diffusion in X80 pipeline steel during stacking for slow cooling.» In: *Acta Metallurgica Sinica* 27 (2014), pp. 416–421. DOI: [10.1007/s40195-014-0073-z](https://doi.org/10.1007/s40195-014-0073-z).
- [149] A. Taha and P. Sofronis. «A micromechanics approach to the study of hydrogen transport and embrittlement.» In: *Engineering Fracture Mechanics* 68 (2001), pp. 803–837. DOI: [10.1016/S0013-7944\(00\)00126-0](https://doi.org/10.1016/S0013-7944(00)00126-0).

- [150] C. Ayas, N.A. Fleck, and V.S. Deshpande. «Hydrogen embrittlement of a bimaterial.» In: *Mechanics of Materials* 80 (2015), pp. 193–202. DOI: [10.1016/j.mechmat.2014.06.002](https://doi.org/10.1016/j.mechmat.2014.06.002).
- [151] E. Martínez-Pañeda, C.F. Niordson, and R.P. Gangloff. «Strain gradient plasticity-based of hydrogen environment assisted cracking.» In: *Acta Materialia* 117 (2016), pp. 321–332. DOI: [10.1016/j.actamat.2016.07.022](https://doi.org/10.1016/j.actamat.2016.07.022).
- [152] *Modeling across scales: a roadmapping study for connecting materials models and simulations across length and time scales*. Tech. rep. Warrendale, PA: The Minerals, Metals and Materials Society, 2015.
- [153] R.C. McClung, M.P. Enright, W. Liang, K. Chan, J. Moody, W.T. Wu, R. Shankar, W. Luo, J. Oh, and S. Fitch. «Integration of manufacturing process simulation with probabilistic damage tolerance analysis of aircraft engine components.» In: *53rd AIAA/ASME/ASCE/AHS/ASC Structures, Structural Dynamics and Materials Conference, Honolulu, Hawaii, Paper No. AIAA 2012-1528*. 2012.
- [154] J.M. Papazian, E.L. Anagnostou, S.J. Engel, D. Hoitsma, J. Madsen, R.P. Silberstein, G. Welsh, and J.B. Whiteside. «A structural integrity prognosis system.» In: *Engineering Fracture Mechanics* 76 (2009), pp. 620–632. DOI: [10.1016/j.engfracmech.2008.09.007](https://doi.org/10.1016/j.engfracmech.2008.09.007).
- [155] P.L. Andresen and F.P. Ford. «Prediction of stress corrosion cracking (SCC) in nuclear power systems.» In: ed. by V.S. Raja and T. Shoji. *Stress Corrosion Cracking, Theory and Practice*. Cambridge: Woodhead Publishing Limited, 2011, pp. 651–713.
- [156] R.P. Gangloff. «Probabilistic fracture mechanics simulation of stress corrosion cracking using accelerated laboratory testing and multi-scale modeling.» In: *Corrosion* (in press) (2016). DOI: [10.5006/1920](https://doi.org/10.5006/1920).
- [157] R.A. Oriani. «Hydrogen, the versatile embrittler.» In: *Corrosion* 4 (1987), pp. 390–397. DOI: [10.5006/1.3583875](https://doi.org/10.5006/1.3583875).
- [158] I.M. Robertson, P. Sofronis, A. Nagao, M.L. Martin, S. Wang, D.W. Gross, and K.E. Nygren. «Hydrogen embrittlement understood.» In: *Metallurgical and Materials Transactions B* 46 (2015), pp. 1085–1103. DOI: [10.1007/s11663-015-0325-y](https://doi.org/10.1007/s11663-015-0325-y).
- [159] R.P. Wei. *Fracture mechanics: integration of mechanics, materials science and chemistry*. New York: Cambridge University Press, 2010.
- [160] R.P. Gangloff and B.P. Somerday. *Gaseous hydrogen embrittlement of materials in energy technologies*. Vol. 2. Cambridge: Woodhead Publishing, 2012.

- [161] M. Dadfarnia, A. Nagao, S. Wang, M.L. Martin, B.P. Somerday, and P. Sofronis. «Recent advances on hydrogen embrittlement of structural materials.» In: *International Journal of Fracture* 196 (2015), pp. 223–243. DOI: [10.1007/s10704-015-0068-4](https://doi.org/10.1007/s10704-015-0068-4).
- [162] K.N. Akhurst and T.J. Baker. «The threshold stress intensity for hydrogen-induced crack growth.» In: *Metallurgical Transactions A* 12 (1981), pp. 1059–1070. DOI: [10.1007/BF02643487](https://doi.org/10.1007/BF02643487).
- [163] P. Novak, R. Yuan, B.P. Somerday, P. Sofronis, and R.O. Ritchie. «A statistical, physical-based, micro-mechanical model of hydrogen-induced intergranular fracture in steel.» In: *Journal of the Mechanics and Physics of Solids* 58 (2010), pp. 206–226. DOI: [10.1016/j.jmps.2009.10.005](https://doi.org/10.1016/j.jmps.2009.10.005).
- [164] M. Dadfarnia, B.P. Somerday, P.E. Schembri, P. Sofronis, J.W. Foulk III, K.A. Nibur, and D.K. Balch. «On modeling hydrogen-induced crack propagation under sustained load.» In: *JOM* 66 (2014), pp. 1390–1398. DOI: [10.1007/s11837-014-1050-8](https://doi.org/10.1007/s11837-014-1050-8).
- [165] D. Lee, Y. Huang, and J.D. Achenbach. «A reformulation of strain gradient plasticity.» In: *Proceedings of the Royal Society A* 471 (2015), p. 20140703. DOI: [10.1098/rspa.2014.0703](https://doi.org/10.1098/rspa.2014.0703).
- [166] M.M. Hall and D.M. Symons. «Hydrogen assisted fracture model for low potential stress corrosion cracking of Ni-Cr-Fe Alloys.» In: ed. by R.H. Jones. *Chemistry and Electrochemistry of Stress Corrosion Cracking*. Warrendale, PA: The Minerals, Metals and Materials Society, 2001, pp. 447–466.
- [167] Q. Wu and M.A. Zikry. «Prediction of diffusion assisted hydrogen embrittlement failure in high strength martensitic steels.» In: *Journal of the Mechanics and Physics of Solids* 85 (2015), pp. 143–159. DOI: [10.1016/j.jmps.2015.08.010](https://doi.org/10.1016/j.jmps.2015.08.010).
- [168] A.H.M. Krom, R.W.J. Koers, and A. Bakker. «Hydrogen transport near a blunting crack tip.» In: *Journal of the Mechanics and Physics of Solids* (1999), pp. 971–992. DOI: [10.1016/S0022-5096\(98\)00064-7](https://doi.org/10.1016/S0022-5096(98)00064-7).
- [169] J.R. Rice. «Mechanics aspects of stress corrosion cracking and hydrogen embrittlement.» In: ed. by R.W. Staehle. *Stress Corrosion Cracking and Hydrogen Embrittlement of Iron Base Alloys*. Houston: NACE International, 1977, pp. 11–15.
- [170] W.W. Gerberich. «Modeling hydrogen induced damage mechanisms in metals.» In: ed. by R.P. Gangloff and B.P. Somerday. *Gaseous Hydrogen Embrittlement of Materials in Energy Technologies*. Vol. 2. Cambridge: Woodhead Publishing Limited, 2012, pp. 209–246.

- [171] S.M. Ohr. «Dislocation-crack interaction.» In: *Journal of Physics and Chemistry of Solids* 48 (1987), pp. 1007–1014. DOI: [10.1016/0022-3697\(87\)90116-8](https://doi.org/10.1016/0022-3697(87)90116-8).
- [172] J. Chen and S. Kitaoka. «Distribution of dislocations at a mode I crack tip and their shielding effect.» In: *International Journal of Fracture* 100 (1999), pp. 307–320. DOI: [10.1023/A:1018681016860](https://doi.org/10.1023/A:1018681016860).
- [173] J.P. Hirth. «Effects of hydrogen on the properties of iron and steel.» In: *Metallurgical Transactions A* 11 (1980), pp. 861–890. DOI: [10.1007/BF02654700](https://doi.org/10.1007/BF02654700).
- [174] T.Y. Zhang and J.E. Hack. «The equilibrium concentration of hydrogen atoms ahead of a mixed mode I-mode III crack tip in single crystal iron.» In: *Metallurgical and Materials Transactions A* 30 (1999), pp. 155–159. DOI: [10.1007/s11661-999-0203-9](https://doi.org/10.1007/s11661-999-0203-9).
- [175] M.R. Begley, J.A. Begley, and C.M. Landis. «Continuum mechanics modeling of hydrogen embrittlement.» In: ed. by R.P. Gangloff and B.P. Somerday. *Gaseous Hydrogen Embrittlement of Materials in Energy Technologies*. Vol. 2. Cambridge: Woodhead Publishing Limited, 2012, pp. 286–325.
- [176] R.H. Dauskardt, M. Lane, Q. Ma, and N. Krishna. «Adhesion and debonding of multi-layer thin film structures.» In: *Engineering Fracture Mechanics* 61 (1998), pp. 141–162. DOI: [10.1016/S0013-7944\(98\)00052-6](https://doi.org/10.1016/S0013-7944(98)00052-6).
- [177] N.C. Broedling, A. Hartmaier, and H. Gao. «Fracture toughness of layered structures: embrittlement due to confinement of plasticity.» In: *Engineering Fracture Mechanics* 75 (2008), pp. 3743–3754. DOI: [10.1016/j.engfracmech.2007.10.014](https://doi.org/10.1016/j.engfracmech.2007.10.014).
- [178] S. Brinckmann and T. Siegmund. «Computations of fatigue crack growth with strain gradient plasticity and an irreversible cohesive zone model.» In: *Engineering Fracture Mechanics* 75 (2008), pp. 2276–2294. DOI: [10.1016/j.engfracmech.2007.09.007](https://doi.org/10.1016/j.engfracmech.2007.09.007).
- [179] E. Martínez-Pañeda, S. del Busto, C.F. Niordson, and C. Betegón. «Strain gradient plasticity modeling of hydrogen diffusion to the crack tip.» In: *International Journal of Hydrogen Energy* 41 (2016), pp. 10265–10274. DOI: [10.1016/j.ijhydene.2016.05.014](https://doi.org/10.1016/j.ijhydene.2016.05.014).
- [180] J.T. Burns, Z.D. Harris, J.D. Dolph, and R.P. Gangloff. «Measurement and modeling of hydrogen environment-assisted cracking in a Ni-Cu-Al-Ti superalloy.» In: *Metallurgical and Materials Transactions A* 47 (2016), pp. 990–997. DOI: [10.1007/s11661-015-3315-4](https://doi.org/10.1007/s11661-015-3315-4).

- [181] G.L. Pioszak. «Metallurgical control of stress corrosion cracking in ultra-high strength stainless steel.» PhD Thesis. University of Virginia, 2015.
- [182] B.A. Kehler and J.R. Scully. «Predicting the effect of applied potential on crack tip hydrogen concentration in low-alloy martensitic steels.» In: *Corrosion* 5 (2008), pp. 465–477. DOI: [10.5006/1.3278484](https://doi.org/10.5006/1.3278484).
- [183] J. Ai, H. Ha, R.P. Gangloff, and J.R. Scully. «Hydrogen diffusion and trapping in a precipitation-hardened nickel-copper–aluminum alloy Monel K-500 (UNS N05500).» In: *Acta Materialia* 61 (2013), pp. 3186–3199. DOI: [10.1016/j.actamat.2013.02.007](https://doi.org/10.1016/j.actamat.2013.02.007).
- [184] D. Li, J.R. Gangloff, and J.R. Scully. «Hydrogen trap states in ultrahigh-strength AERMET 100 steel.» In: *Metallurgical and Materials Transactions A* 35 (2004), pp. 849–864. DOI: [10.1007/s11661-004-0011-1](https://doi.org/10.1007/s11661-004-0011-1).
- [185] D. Figueroa and M.J. Robinson. «Hydrogen transport and embrittlement in 300 M and AerMet100 ultra high strength steels.» In: *Corrosion Science* 52 (2010), pp. 1593–1602. DOI: [10.1016/j.corsci.2010.01.001](https://doi.org/10.1016/j.corsci.2010.01.001).
- [186] H. Huang and W.W. Gerberich. «Quasi-equilibrium modeling of the toughness transition during semibrittle cleavage.» In: *Acta Metallurgica et Materialia* 42 (1994), pp. 639–647. DOI: [10.1016/0956-7151\(94\)90260-7](https://doi.org/10.1016/0956-7151(94)90260-7).
- [187] P. Doig and G.T. Jones. «A model for the initiation of hydrogen embrittlement cracking at notches in gaseous hydrogen environments.» In: *Metallurgical Transactions A* 8 (1977), pp. 1993–1998. DOI: [10.1007/BF02646573](https://doi.org/10.1007/BF02646573).
- [188] R.P. Gangloff. «Diffusion control of hydrogen environment embrittlement in high strength alloys.» In: ed. by N.R. Moody. *Hydrogen Effects on Material Behavior and Corrosion Deformation Interactions*. Warrendale, PA: The Minerals, Metals and Materials Society, 2003, pp. 477–497.
- [189] E. Akiyama, M. Wang, S. Li, Z. Zhang, Y. Kimura, N. Uno, and K. Tsuzaki. «Studies of the evaluation of hydrogen embrittlement property of high-strength steels with consideration of the effect of atmospheric corrosion.» In: *Metallurgical and Materials Transactions A* 44 (2012), pp. 1290–1300. DOI: [10.1007/s11661-012-1403-2](https://doi.org/10.1007/s11661-012-1403-2).
- [190] T. Lin, A.G. Evans, and R.O. Ritchie. «A statistical model of brittle fracture by transgranular cleavage.» In: *Journal of the Mechanics and Physics of Solids* 34 (1986), pp. 477–497. DOI: [10.1016/0022-5096\(86\)90013-X](https://doi.org/10.1016/0022-5096(86)90013-X).

- [191] A. Turnbull. «Hydrogen diffusion and trapping in metals.» In: ed. by R.P. Gangloff and B.P. Somerday. *Gaseous Hydrogen Embrittlement of Materials in Energy Technologies*. Vol. 2. Cambridge: Woodhead Publishing Limited, 2012, pp. 89–128.
- [192] J. Toribio and V. Kharin. «A generalised model of hydrogen diffusion in metals with multiple trap types.» In: *Philosophical Magazine* 95 (2015), pp. 3429–3451. DOI: [10.1080/14786435.2015.1079660](https://doi.org/10.1080/14786435.2015.1079660).
- [193] W.C. Johnson and J.Y. Huh. «Thermodynamics of stress-induced interstitial redistribution in body-centered cubic metals.» In: *Metallurgical and Materials Transactions A* 34 (2003), pp. 2819–2825. DOI: [10.1007/s11661-003-0183-0](https://doi.org/10.1007/s11661-003-0183-0).
- [194] J.R. Scully and P.J. Moran. «The influence of strain on hydrogen entry and transport in a high strength steel in sodium chloride solution.» In: *Journal of the Electrochemical Society* 135 (1988), pp. 1337–1348. DOI: [10.1149/1.2095978](https://doi.org/10.1149/1.2095978).
- [195] S. Takebayashi, T. Kunieda, N. Yoshinaga, K. Ushioda, and S. Ogata. «Comparison of the dislocation density in martensitic steels evaluated by some X-ray diffraction methods.» In: *ISIJ International* 50 (2010), pp. 875–882. DOI: [10.2355/isijinternational.50.875](https://doi.org/10.2355/isijinternational.50.875).
- [196] K.J. Handerhan and W.M. Garrison Jr. «A study of crack tip blunting and the influence of blunting behavior on the fracture toughness of ultra high strength steels.» In: *Acta Metallurgica et Materialia* 40 (1992), pp. 1337–1355. DOI: [10.1016/0956-7151\(92\)90435-H](https://doi.org/10.1016/0956-7151(92)90435-H).
- [197] B.P. Somerday, L.M. Young, and R.P. Gangloff. «Crack tip mechanics effects on environment-assisted cracking of beta-titanium alloys in aqueous NaCl.» In: *Fatigue & Fracture of Engineering Materials & Structures* 23 (2000), pp. 39–58. DOI: [10.1046/j.1460-2695.2000.00243.x](https://doi.org/10.1046/j.1460-2695.2000.00243.x).
- [198] S. Chakravarthy and W.A. Curtin. «Stress-gradient plasticity.» In: *Proceedings of the National Academy of Sciences* 108 (2011), pp. 15716–15720. DOI: [10.1073/pnas.1107035108](https://doi.org/10.1073/pnas.1107035108).
- [199] S.S. Shishvan and A.-H. Asghari. «Particle size effect in metal matrix composites: a study by the continuum theory of stress gradient plasticity.» In: *Journal of Composite Materials* 50 (2016), pp. 1717–1723. DOI: [10.1177/0021998315595708](https://doi.org/10.1177/0021998315595708).
- [200] V. Monchiet and G. Bonnet. «A Gurson-type model accounting for void size effects.» In: *International Journal of Solids and Structures* 50 (2013), pp. 320–327. DOI: [10.1016/j.ijsolstr.2012.09.005](https://doi.org/10.1016/j.ijsolstr.2012.09.005).

- [201] L. Mazzoni-Leduc, T. Pardoen, and T.J. Massart. «Analysis of size effects associated to the transformation strain in TRIP steels with strain gradient plasticity.» In: *European Journal of Mechanics A/Solids* 29 (2010), pp. 132–142. DOI: [10.1016/j.euromechsol.2009.08.001](https://doi.org/10.1016/j.euromechsol.2009.08.001).
- [202] E. Martínez-Pañeda and R. Gallego. «Numerical analysis of quasi-static fracture in functionally graded materials.» In: *International Journal of Mechanics and Materials in Design* 11 (2015), pp. 405–424. DOI: [10.1007/s10999-014-9265-y](https://doi.org/10.1007/s10999-014-9265-y).
- [203] A. Nazari. «Modeling fracture toughness of ferritic and austenitic functionally graded steel based on the strain gradient plasticity theory.» In: *Computational Materials Science* 50 (2011), pp. 3238–3244. DOI: [10.1016/j.commatsci.2011.06.008](https://doi.org/10.1016/j.commatsci.2011.06.008).
- [204] E. Martínez-Pañeda, T.E. García, and C. Rodríguez. «Fracture toughness characterization through notched small punch test specimens.» In: *Materials Science and Engineering: A* 657 (2016), pp. 422–430. DOI: [10.1016/j.msea.2016.01.077](https://doi.org/10.1016/j.msea.2016.01.077).
- [205] E. Martínez-Pañeda, I.I. Cuesta, I. Peñuelas, A. Díaz, and J.M. Alegre. «Damage modeling in Small Punch Test specimens.» In: *Theoretical and Applied Fracture Mechanics* 86A (2016), pp. 51–60. DOI: [10.1016/j.tafmec.2016.09.002](https://doi.org/10.1016/j.tafmec.2016.09.002).

## VITA

Emilio Martínez Pañeda was born in 1987, in Oviedo (Spain). He earned a 5 year BEng. & MEng. degree in Industrial Engineering from the University of Oviedo in 2011 and an MSc degree in Structural Engineering from the University of Granada in October 2012. During his MSc studies, Martínez Pañeda conducted research in the mechanics of functionally graded materials [Int. J. Mech. Mater. Des. 11, pp. 405-424] under the supervision of Prof. Rafael Gallego. Immediately after graduation he started working at the University of Oviedo as a Research Assistant under the supervision of Prof. Covadonga Betegón. In the year 2013 he started his PhD studies and was awarded a predoctoral fellowship by the University of Oviedo (ranked 2<sup>nd</sup> in Engineering). Martínez Pañeda carries out research activities in the fields of mechanics of materials and computational solid mechanics, with particular emphasis on the modeling of size effects in metal plasticity and fracture and damage assessment. Besides working on topics closely related with his doctoral thesis, he has also conducted research on novel small scale testing methodologies [Mater. Sci. Eng. A, 657, pp. 422-430; Theor. Appl. Fract. Mech. 86A, pp. 51-60].

Martínez Pañeda has held visiting scholar positions at several Universities such as the Technical University of Denmark (host: C. Niordson), the University of Luxembourg (host: S. Bordas) or the University of Cambridge (host: N. Fleck) and he is actively involved in many international collaborations. He is currently a member of the European Structural Integrity Society (ESIS), the European Community on Computational Methods in Applied Sciences (ECCOMAS) and the International Association for Computational Mechanics (IACM). He has delivered several invited talks and seminars in various international conferences and research institutions. He is author or co-author of numerous scientific publications in international referred journals in the field of solid mechanics.

In July 2016 Martínez Pañeda will start working as a postdoctoral fellow in the Technical University of Denmark after being selected in the competitive H.C. Ørsted program.